Technische Universität München
Physik Department
Max-Planck-Institut für Astrophysik

Multi-Dimensional Relativistic Simulations of Core-Collapse Supernovae with Energy-Dependent Neutrino Transport

Bernhard Müller

Vollständiger Abdruck der von der Fakultät für Physik der Technischen Universität München zur Erlangung des akademischen Grades eines

Doktors der Naturwissenschaften (Dr. rer. nat.)

genehmigten Dissertation.

Vorsitzender:		Univ.-Prof. Dr. L. Oberauer
Prüfer der Dissertation:		
	1.	Priv.-Doz. Dr. H.-Th. Janka
	2.	Univ.-Prof. Dr. M. Ratz

Die Dissertation wurde am 26.03.2009 bei der Technischen Universität München eingereicht und durch die Fakultät für Physik am 07.05.2009 angenommen.

Contents

1. Introduction

1.1. Supernova research – The beginnings

Spectacular celestial events have always managed to spell-bind human imagination, and the appearance of a new star, or *stella nova* ranks among the most prominent of these. However, it was only in the late 16th century that these phenomena became the object of scientific study in any modern sense, and that their astrological interpretation as *omina*, portending commotions in the terrestrial sphere, began to give way to a more dispassionate view. Two supernovae in the constellation of Cassiopeia in 1572 and in the constellation of Ophiuchis in 1604, documented by such eminent astronomers as Tycho Brahe and Johannes Kepler, were important catalysts for the development of modern astronomy during this era. The heavens were a domain of the supernatural no longer; they were soon found to be subject to the same laws of nature that apply on earth, and henceforth belonged to the realm of physics. Kepler's treatise *De stella nova* on the supernova of 1604 constitutes a milestone in this process, discussing such bold questions as "*an iam olim extiterit materia corpusque novi sideris*"[1] [31] that undermined the very foundations of the established Aristotelian cosmology of the middle ages[2].

Of course, Kepler's work, openly described on the frontispiece as " *ἐνδόξοις καὶ παραδόξοις plenus*" [3], was still largely based on philosophical speculation, and the physical origin of supernovae remained unclear for another 300 years. It was only in the 1930s that Baade and Zwicky [3] first distinguished them from common novae, and "*advance[d] the view that a super-nova* [sic] *represents the transition of an ordinary star into a neutron star*" [4]. The discovery of a pulsar (i.e. a magnetized rotating neutron star) in the Crab nebula [152, 172] which had already been identified as the remnant of the historical supernova of 1054 [76, 119], provided a striking confirmation for their hypothesis.

---

[1] "Whether the matter and body of the new star had already existed before."

[2] This is not meant to imply that medieval and early Renaissance cosmology was *solidly* Aristotelian before the astronomical discoveries of the 16th century. Moreover, we do not attempt to evaluate the extent (which has sometimes been exaggerated) of the philosophical repercussions of these findings beyond the immediate realm of natural science.

[3] This phrase is highly ambiguous, probably deliberately so. It can be interpreted both as "full of glorious and strange things" or "full of accepted and contradictory opinions"

1.2. The modern paradigm and the quest for the explosion mechanism

Apart from the fact that a sub-class of supernovae (so-called "Ia's", which will not be discussed in this thesis) are now believed to originate from the thermonuclear explosion of accreting or merging white dwarfs, our current understanding of supernovae is still based on the model outlined by Baade and Zwicky [4], albeit with many elaborations after decades of intensive research: Except for those of type Ia, they originate from the collapse of stars more massive than $\approx 8M_\odot$. After going through successive stages of nuclear burning, such stars finally form cores composed of iron-group nuclei ("iron cores") that are supported by the degeneracy pressure of electrons. At the edge of the core, silicon burning remains active and continually increases the mass of the core, until it comes close to the Chandrasekhar limit of roughly $1.4M_\odot$.

At that point, photo-disintegration of heavy nuclei and electron capture reactions initiate the dynamical collapse[4] of the core. During the collapse, matter becomes more and more neutron-rich due to electron captures on heavy nuclei and (at higher densities) on free protons. As these processes also reduce the electron fraction Y_e (defined as the number of electrons per baryon), they result in a pressure reduction and further accelerate the collapse. However, the neutrinos emitted during this process of "deleptonization" escape from the collapsing core only at densities $\lesssim 10^{12}$ g cm^{-3}. At higher densities, the mean free path of neutrinos becomes significantly smaller than the radius of the core due to coherent scattering on heavy nuclei. At that stage, neutrinos no longer escape the core, but are advected along with the fluid (a phenomenon known as "trapping"). Thermodynamical and chemical equilibrium between electrons and neutrinos is then quickly established. After trapping, the electron fraction changes only slightly, and the collapse continues almost adiabatically beyond nuclear densities until it is stopped by the stiffening of the equation of state due to repulsive interactions between nucleons. The rebounding, or "bounce" of the inner core launches a pressure wave that steepens into a shock wave at the edge of core.

Although the initial energy of this "prompt shock" is of the order of the observed explosion energies of core-collapse supernovae ($\simeq 10^{51}$ erg) it cannot trigger the explosion directly. As it propagates outwards, its energy is spent for the dissociation of heavy nuclei in the infalling matter into free nucleons, which consumes roughly 1.5×10^{52} erg/$M_\odot$. The shock is further weakened when it reaches layers with densities lower than $\lesssim 10^{12}$ g cm^{-3}, and rapid deleptonization (which also associated with an energy loss) occurs in the region behind the shock as it becomes transparent to neutrinos. Within a few milliseconds, the outward motion of post-shock matter ceases. However, the shock front continues to be pushed outwards as more and more infalling matter is piled ("accreted") onto the newly-formed "proto-neutron star". Typically, the outward-moving "accretion shock" starts to recede again a few tens of ms later after having reached a radius of $\approx 100\ldots200$km. According to the most promising model (the "delayed neutrino-driven mechanism" [191]), it

---

[4] It should be noted that for stars only slightly more massive than $8M_\odot$, the collapse may already occur when the core is still composed of O, Ne and Mg [136, 137].

is revived by the deposition of energy in the so-called "gain-region" by neutrinos emitted from the proto-neutron star after several hundreds of milliseconds, and then dynamically propagates through the outer layers of the star, which are expelled in its wake. It should be pointed out, of course, that this model is still not finally and generally established; a few alternative suggestions are mentioned in Chapter 6.

However, in most of the modern sophisticated computer simulations in *spherical symmetry* the delayed-neutrino driven mechanism fails to trigger an explosion[5], and hence multi-dimensional effects are believed to be of vital importance for the explosion mechanism. Convection, both inside the proto-neutron star and in the gain region may aid neutrino heating, either by increasing the neutrino luminosity, or by providing a means of efficient heat transfer from the inner part of the gain region (where neutrino heating is strongest) to the layers immediately behind the shock. The neutrino heating efficiency is also enhanced by another recently discovered instability of the shock to non-radial deformations, the "standing accretion-shock instability" (SASI) [11].

Nowadays, the evolution of core-collapse supernovae towards the explosion during the phase after bounce ("post-bounce phase") is studied with the help of sophisticated numerical models that need to take all the relevant physical ingredients into account, i.e. hydrodynamics, self-gravity, the equation of state of dense nuclear matter, nuclear burning, neutrino matter-interactions, and neutrino transport (which is particularly challenging). The most sophisticated codes handle neutrino transport by using multi-group methods (i.e. methods in which the neutrino spectrum is explicitly discretized instead of assuming a thermal distribution) of different complexity; some of them even rely on a discretization of the Boltzmann equation [21, 25, 106, 110, 121, 151, 201]. However, in all multi-dimensional simulations of the post-bounce phase, the hydrodynamics has been treated in the Newtonian approximation, although some effects of relativistic gravity can be included [116, 151]. During the past few years, the primary focus has been on multi-dimensional hydrodynamical effects and the microphysics (nuclear equation of state, neutrino physics), and their influence during the post-bounce phase. Some spectacular progress has been made on this front: Successful explosions in which hydrodynamical instabilities play a major role have been reported (among others) by Buras et al. [20], Marek et al. [117], Burrows et al. [26], and Bruenn et al. [17], and other questions connected to supernova explosion, e.g. about supernova nucleosynthesis, can now be discussed on the basis of self-consistent models (see, e.g., [75, 149, 187]).

1.3. Core collapse and general relativity

However, relativistic gravity has been something of sideshow in this quest for the explosion mechanism during the recent years. This is rather surprising, as it was realized [142, 182] very soon after the concept of neutron stars had been first proposed that such

---

[5] Progenitors with O-Ne-Mg cores [91] are the one notable exception. In the case of more massive progenitors, it has been suggested that a phase transition to quark matter at relatively low densities may help in launching a neutrino-driven explosion [158]; but whether the details of this suggestion withstand future scrutiny is unclear.

extremely compact objects need to be described within a relativistic framework. Core-collapse supernovae are thus a fascinating laboratory for the strong-field regime of *general relativity* (GR). In particular, they have long been considered as promising sources for *gravitational waves*, which are produced by the aspherical motion of matter, e.g. by convection in the post-bounce phase, or by the collapse of rotating, aspherically deformed iron cores. Although gravitational wave emission can be studied approximately in the Newtonian limit, it is obvious that an exact treatment of general relativity in the core collapse problem is most desirable for this particular aspect. However, general relativity is also of large relevance for the post-bounce phase, according to simulations with neutrino transport in *spherical symmetry*: Relativistic simulations show the proto-neutron star to be significantly more compact and hotter than in the Newtonian case, and this in turn leads to larger neutrino luminosities, which can, of course, play a crucial role in the delayed mechanism described in the previous section. The stronger gravitational field also influences the propagation of the shock directly. General relativity is thus an essential ingredient for the entire supernova problem (see, e.g., Bruenn et al. [17] for a more thorough discussion in the case of spherical symmetry). Even if it turned out that it were not crucial for the success of the delayed neutrino-driven mechanism, it could still have a great impact on important details of the post-bounce evolution, such as the time of the explosion (early/late), and on (potential) observables like the final mass of the neutron star, the explosion energy, or the products of nucleosynthesis.

However, modern supernova codes featuring sophisticated neutrino transport methods do not take the effects of general relativity into account in a rigorous manner (see Chapter 6 for more details) for a simple reason: The numerical treatment of general relativistic hydrodynamics is beset with tremendous difficulties, compared to the Newtonian case: On the one hand, the equations of relativistic hydrodynamics are much more complicated than their Newtonian counterparts, so that comparable numerical methods were often developed years or decades later. On the other hand, the non-linear gravitational field equations have proved notoriously difficult to evolve. While these obstacles can be quite easily overcome in the special case of spherical symmetry, multi-dimensional relativistic hydrodynamics codes for self-gravitating systems (like core-collapse supernovae) have only become available during the last one-and-a-half decades. This was achieved, unfortunately, at the expense of neglecting other integral aspects of the supernova problem, such as neutrino transport, or the nuclear equation of state. Consequently, multi-dimensional relativistic simulations of stellar core collapse cannot yet address the post-bounce phase and the explosion mechanism with any accuracy, where these issues are of vital importance. Instead, their use has been confined to the phases of collapse and bounce, and their primary target was the gravitational wave emission from rotational collapse, where first attempts at incorporating some essential microphysics (e.g. deleptonization) in a very approximative manner have recently been made [34, 44–46, 143, 144]. However, no general relativistic code for core collapse presently includes a detailed treatment of neutrino transport that is even remotely comparable to the sophisticated multi-group methods in the most advanced Newtonian codes. Similarly elaborate methods for general relativistic neutrino transport have not been developed so far.

1.4. Aims of this thesis

From the foregoing, it should be clear that both the "Newtonian approach" described in Sec. 1.2 and the "relativistic approach" described in Sec. 1.3 have severe shortcomings. Both approaches neglect or over-simplify important physical effects that are properly captured by the other: It would clearly be desirable to combine the strengths of the Newtonian approach – i.e. an accurate treatment of the microphysics and the neutrino transport – and of the general relativistic approach. This is precisely what we set out to do in this thesis. In order to achieve this aim we generalize the thoroughly tested neutrino transport code VERTEX [21, 151] to the relativistic case, and integrate it into the GR hydrodynamics code CoCoNuT [41, 43]. With the new combined VERTEX-CoCoNuT code, we are able to conduct the first multi-dimensional simulations of core-collapse supernova with sophisticated neutrino transport *and* an accurate treatment of general relativistic hydrodynamics, and to provide some answers to questions that neither the "Newtonian" nor the "relativistic" approach have hitherto been able to address reliably: Does the inclusion of general relativity influence the development of convection and the standing accretion shock instability? Does it have any bearing on the explosion mechanism? What are the observable gravitational wave signatures from the collapse phase and the post-bounce phase?

1.5. Organization of this thesis

In our thesis, we approach these questions in the following manner: In Chapter 2, we introduce the governing equations of general relativistic radiation hydrodynamics, along with some remarks on the numerical methods, and generalize the Newtonian ray-by-ray-plus neutrino transport method of Buras et al. [21] to the relativistic case. Some important improvements to the numerical methods hitherto used in VERTEX and CoCoNuT, which greatly enhance the efficiency and accuracy of the combined VERTEX-CoCoNuT code, are described in more detail in Chapter 3. We present tests of the new code in spherical symmetry in Chapter 4, including a comparison with the relativistic neutrino transport code AGILE-BOLTZTRAN and the Newtonian PROMETHEUS-VERTEX code. Applications of our multi-dimensional relativistic radiation hydrodynamics code are discussed in Chapters 5 and 6: In Chapter 5, we analyze the collapse of rotating iron-cores, while Chapter 6 addresses the post-bounce phase, focusing on aspects relevant for the delayed neutrino-driven explosion mechanism, such as neutrino emission, convection and the standing-accretion shock instability. Finally, we attempt a brief summary of our results in Chapter 7 and outline possible future extensions of our work.

2. General Relativistic Radiation Hydrodynamics

2.1. Overview

Our approach to radiation hydrodynamics relies on the the variable Eddington factor technique as implemented in the VERTEX code by Rampp and Janka [151] for spherically symmetric problems, and its generalization to the multi-dimensional case within the ray-by-ray-plus approximation of Buras et al. [21]. In this chapter, we provide a relativistic formulation of the methods of Rampp and Janka [151] and Buras et al. [21], and elaborate on their implementation in VERTEX and in the GR hydrodynamics code CoCoNuT [40, 41, 43]. On occasion, reference to the corresponding Newtonian case is made to highlight important differences; however, for the complete set of equations the reader should refer to Appendix C. We also discuss the quality of our approximation to the full six-dimensional general relativistic neutrino transport problem.

Note that geometrized units are used throughout this chapter, i.e. both the speed of light and the gravitational constant are set to unity: $G = c = 1$. Greek indices run from 0 to 3, Latin indices from $1 to 3$.

2.2. Hydrodynamics

In general relativity, the hydrodynamic evolution of a perfect fluid is governed by two conservation equations for the baryonic rest mass current J^μ and the stress-energy tensor $T^{\mu\nu}$,

$$\nabla_\mu J^\mu = 0, \quad \nabla_\nu T^{\mu\nu} = 0, \tag{2.1}$$

where ∇_ν denotes the covariant derivative. For a perfect fluid, J^μ and $T^{\mu\nu}$ can be expressed in terms of the baryon rest-mass density ρ in the local fluid frame, the four-velocity u^μ, the pressure, the specific enthalpy $h = 1 + \epsilon + P/\rho$ (where ϵ is the specific internal energy density, and P is the pressure), and the four-metric $g_{\mu\nu}$,

$$J^\mu = \rho u^\mu, \quad T^{\mu\nu} = \rho h u^\mu u^\nu + P g^{\mu\nu}. \tag{2.2}$$

For the metric, we adopt the Arnowitt-Deser-Misner (ADM) 3 + 1 formalism [102] of general relativity to foliate the spacetime into spacelike hypersurfaces. In this approach, the four-dimensional line element $\mathrm{d}s^2 = g_{\mu\nu}\,\mathrm{d}x^\mu\,\mathrm{d}x^\nu$ is written as follows,

$$\mathrm{d}s^2 = -\alpha^2 + \gamma_{ij}\left(\mathrm{d}x^i + \beta^i \mathrm{d}t\right)\left(\mathrm{d}x^j + \beta^j \mathrm{d}t\right), \tag{2.3}$$

where α is the lapse function, β^i is the shift vector, and γ_{ij} is the induced three-metric on each hypersurface. Using this decomposition of the four-metric, the equations of hydrodynamics can be formulated in the frame of an Eulerian observer[1] moving orthogonally to the spacelike hypersurfaces, i.e. with a four-velocity $n^\mu = (\alpha^{-1}, \alpha^{-1}\beta^i)$. As in Banyuls et al. [5], we introduce the following conserved variables[2],

$$D = \rho W, \quad S^i = \rho h W^2 v^i, \tau = \rho h W^2 - P - D, \tag{2.4}$$

where $v^i = u^i/(\alpha u^0) + \beta^i/\alpha$ is the three-velocity in the Eulerian frame, and W is the corresponding Lorentz factor $W = 1/\sqrt{1 - v_i v^i}$. The equations of GR hydrodynamics in flux-conservative form then read,

$$\begin{aligned}
\frac{\partial \sqrt{\gamma} \rho W}{\partial t} + \frac{\partial \sqrt{-g} \rho W \hat{v}^i}{\partial x^i} &= 0, &(2.5)\\
\frac{\partial \sqrt{\gamma} \rho h W^2 v_j}{\partial t} + \frac{\partial \sqrt{-g}\left(\rho W v_j \hat{v}^i + \delta^i_j P\right)}{\partial x^i} &= \frac{1}{2}\sqrt{-g} T^{\mu\nu} \frac{\partial g_{\mu\nu}}{\partial x^j} + \left(\frac{\partial \sqrt{\gamma} S_j}{\partial t}\right)_C, &(2.6)\\
\frac{\partial \sqrt{\gamma}\tau}{\partial t} + \frac{\partial \sqrt{-g}\left(\tau \hat{v}^i + P v^i\right)}{\partial x^i} &= \alpha \sqrt{-g}\left(T^{\mu 0} \frac{\partial \ln \alpha}{\partial x^\mu} - T^{\mu\nu}\Gamma^0_{\mu\nu}\right) + \left(\frac{\partial \sqrt{\gamma}\tau}{\partial t}\right)_C. &(2.7)
\end{aligned}$$

Here, $\hat{v}^i$ is defined as $\hat{v}^i = v^i - \beta^i/\alpha$, and g and γ are the determinants of the four-metric $g_{\mu\nu}$ and the three-metric γ_{ij}, respectively. Different from the purely hydrodynamic case discussed by [5], the RHSs of Eqs. (2.6) and (2.7) contain source terms for the exchange of momentum and energy with neutrinos (denoted by a subscript "C") in addition to the gravitational and geometric source terms. These source terms will be specified in Sec. 2.4.5.

Eqs. (2.5) to (2.7) must be supplemented by an additional equation expressing the conservation of electron number in the absence of weak interactions (which will be discussed separately),

$$\frac{\partial \sqrt{\gamma} \rho W Y_e}{\partial t} + \frac{\partial \sqrt{-g} \rho W Y_e \hat{v}^i}{\partial x^i} = \left(\frac{\partial \sqrt{\gamma} \rho W Y_e}{\partial t}\right)_C, \tag{2.8}$$

where Y_e is the electron fraction (number of electrons minus number of positrons per baryon). The change of the electron number due to neutrino emission or absorption is accounted for by the source term on the RHS, in a similar fashion as energy and momentum exchange with neutrinos in Eqs. (2.6) and (2.7).

---

[1] Since the terminology in the existing literature on relativistic hydrodynamics and radiative transfer is not uniform, we add some remarks on this issue here. The "frame" of an observer (or a class of observers) is an orthonormal tetrad field whose time-like base vector coincides with the four-velocity of the observer. We shall use the terms "Eulerian frame" (as in [5]) or "lab frame" (as in [124]) interchangeably to denote the frame of an Eulerian observer as described in the main body of the text. It is important to note that such an Eulerian observer is *not* a fixed-coordinate observer unless the shift vector vanishes.

[2] D, S_i and τ can be obtained form J^μ and $T^{\mu\nu}$ using n^μ and the projection operator $\perp^\mu_\nu$ onto the three-hypersurfaces: $D = n_\mu J^\mu$, $S^i = \perp^i_\mu n_\nu T^{\mu\nu}$, and $\tau = n_\mu n_\nu T^{\mu\nu} - D$.

Since we are dealing with a multi-component fluid whose composition is not uniquely determined by the thermodynamic state (ρ, T, Y_e) unless nuclear statistical equilibrium (NSE) applies, additional conservation equations for the mass fractions X_k of protons, neutrons, α-particles and heavier nuclei are also needed,

$$\frac{\partial \sqrt{\gamma} \rho W X_k}{\partial t} + \frac{\partial \sqrt{-g} \rho W X_k \hat{v}^i}{\partial x^i} = 0. \tag{2.9}$$

Finally, the pressure and the composition (in the NSE regime) in Eqs. (2.6,2.7,2.9) have to be provided by an equation of state (EoS).

We rely on the CoCoNuT code [41, 43] to solve the equations of relativistic hydrodynamics in spherical polar coordinates by means of a high-resolution shock-capturing (HRSC) scheme, employing piecewise parabolic (PPM) reconstruction [35], an approximate Riemann solver, and second-order Runge-Kutta timestepping. Our method of choice for the Riemann solver is a new hybrid HLLC/HLLE scheme in CoCoNuT along the lines of Quirk [150], combining the high resolution of the HLLC solver [123, 183] with the robustness of the HLLE solver [50, 68] against odd-even decoupling near grid-aligned shocks [89, 109, 150, 176]. Our most recent simulations also use a reformulated energy equation instead of Eq. (2.7) to improve total energy conservation (see Sec. 3.1 for details), and a reformulated momentum equation instead of Eq. (2.6) (see Appendix B). In order to treat the advection equations for the nuclear mass fractions, we have added a simplified version of the consistent multi-fluid advection (CMA) method by Plewa and Müller [147]. Moreover, the computational performance of the code has been improved significantly by enhancing parallelism in the axisymmetric (2D) mode. In the Newtonian case, we use the PROMETHEUS code [62, 63], which is based on essentially the same methods, but differs from CoCoNuT in several respects (apart from its Newtonian character): an exact iterative Riemann solver is used instead of HLLC, second-order time accuracy is achieved by a single-step midpoint method, and multi-dimensional problems are handled by Strang splitting. As for the equation of state, we have used the EoS of Lattimer and Swesty [100] for the high-density regime in all the simulations presented in this thesis. Low-density matter (with $\rho < 6 \times 10^7$ g cm$^{-3} \ldots 10^{11}$ g cm^{-3}, depending on the exact model setup) is treated as an ideal gas composed of nucleons, nuclei, leptons and radiation; in this regime various prescriptions are used to determine the NSE composition (where applicable) or composition changes due to nuclear burning [21, 114, 151].

2.3. Metric equations – The Conformal Flatness Condition

The CoCoNuT code solves Einstein's field equation using the conformal flatness condition (CFC), which was introduced by Isenberg [77] and first used in a dynamical context by Wilson et al. [193]. In the CFC approximation, the spatial three-metric is assumed to be conformally flat [3], i.e. it is obtained from the flat three-metric[4] $\hat{\gamma}_{ij}$ by a conformal transformation $\gamma_{ij} = \phi^4 \hat{\gamma}_{ij}$, where ϕ is the conformal factor, thus reducing the number of independent metric quantities to five. As a consequence, the four constraint equations for the metric in the ADM formalism, combined with a slicing condition, determine the metric completely. In our case, we use maximal slicing, i. e. we require the trace of the extrinsic curvature K^{ij} to vanish: $K = K^i_i = 0$. We then obtain a set of five non-linear elliptic equations for α, ϕ, and β^i,

$$\begin{aligned}
\hat{\Delta}\Phi &= -2\pi\phi^5 \left(E + \frac{K_{ij}K^{ij}}{16\pi}\right), & (2.10)\\
\hat{\Delta}(\alpha\Phi) &= 2\pi\alpha\phi^5 \left(E + 2S + \frac{7K_{ij}K^{ij}}{16\pi}\right), & (2.11)\\
\hat{\Delta}\beta^i &= 16\pi\alpha\phi^4 S^i + 2\phi^{10} K^{ij} \hat{\nabla}_j \left(\frac{\alpha}{\Phi^6}\right) - \frac{1}{3}\hat{\nabla}^i \hat{\nabla}_j \beta^j, & (2.12)
\end{aligned}$$

where $\hat{\Delta}$ and $\hat{\nabla}$ are the Laplace and covariant derivative operators for a flat three-space. The total matter-energy density $E = \tau + D$, the three-momentum density S_i and the trace $S = \gamma_{ij} S^{ij}$ of the spatial components S_{ij} of the stress-energy tensor (as measured by an Eulerian observer) appear in the non-linear source terms on the right-hand side, and comprise contribution both from matter and (neutrino) radiation. For the matter component we obtain,

$$E = \rho h W^2 - P, \tag{2.13}$$

$$S = \rho h W^2 v^2 + 3P, \tag{2.14}$$

$$S^i = \rho h W^2 v^i, \tag{2.15}$$

while for neutrinos,

$$E = S = 4\pi W^2 \left(J + 2v_r H + v_r^2 K\right), \tag{2.16}$$

$$S_1 = 4\pi\phi^{-2} W^2 \left[H\left(1 + v_r^2\right) + v_r \left(J + K\right)\right], \tag{2.17}$$

$$S_2 = S_3 = 0, \tag{2.18}$$

in our approximation. Here, J, H, and K denote the zeroth, first and second moments of the neutrino radiation intensity in the comoving frame (see section 2.4), and $v_r = \phi^2 v^1$.

We solve the CFC equations (2.10), (2.11), and (2.12) using a fixed point iteration scheme as described in Dimmelmeier et al. [43]; i.e. during each iteration step, the non-linear source terms are updated, and the Laplace operators on the left-hand side of the equations are inverted by means of a multipole expansion (cf. [131]). While this method suffers from a somewhat low convergence rate compared to the spectral nonlinear Poisson solver of Dimmelmeier et al. [43], the underlying algorithm is more

---

[3] We note in passing that this assumption can always be fulfilled by an appropriate gauge choice for a spherically symmetric spacetime, and no approximations to the ADM equations are actually made by using CFC in that case. See section 2.5 for more details.

[4] Thus, in spherical polar coordinates we have $\hat{\gamma}_{ij} = \mathrm{diag}\left(1, r^2, r^2 \sin^2\theta\right)$.

easily amenable to parallelization, which is a critical issue for multi-dimensional neutrino transport simulations.

In our Newtonian simulations with PROMETHEUS, the treatment of self-gravity is much simpler, since only the (linear) Poisson equation

$$\hat{\Delta}\Phi = 4\pi G\rho \tag{2.19}$$

needs to be solved. Correction terms to Φ may be added to account for certain general relativistic effects at a reasonable level of accuracy [116, 128]. We will refer to this strategy as "pseudo-Newtonian", "pseudo-relativistic", or "effective potential" approach.

2.4. Neutrino transport in CFC spacetime

2.4.1. Overview

Up to now, all self-consistent numerical simulations of neutrino transport in core collapse supernovae are based on the assumptions i) that a semi-classical treatment of kinetic theory is applicable, and ii) that neutrino oscillations need not to be taken into account (see [30, 174, 199] for a discussion of the more general case). In our approach to the transport problem, we retain those assumptions, although they may be invalid under certain specific circumstances (cf. Sec. 2.5). Under this proviso, the evolution of the invariant neutrino distribution function f (the number of neutrinos per phase-space volume $\mathrm{d}^3x\,\mathrm{d}^3p$) is governed by the relativistic Boltzmann equation for massless or ultra-relativistic particles, which reads

$$p^\mu \frac{\partial f}{\partial x^\mu} + \frac{\mathrm{d}p^i}{\mathrm{d}\lambda}\frac{\partial f}{\partial p^i} = \mathfrak{C} \tag{2.20}$$

in any coordinate basis. Here, f and the collision term $\mathfrak{C}$ depend on the spacetime coordinates x^μ and the four-momentum vector p^μ (obeying the mass-shell constraint $p_\mu p^\mu = 0$) as measured in the associated holonomic base ∂_μ; λ is the affine parameter.

In general, Eq. (2.20) describes a six-dimensional time-evolution problem, which can be scaled down considerably by using the ray-by-ray-plus approximation [21] in the following manner: First, the equations of neutrino transport are formulated for the spherically symmetric case (sections 2.4.2 to 2.4.5), thus reducing the overall dimensionality from six to three. By working with a finite number (i.e. two) of angular moments of the Boltzmann equation, yet another dimension can be eliminated. The additional *space* dimensions are then taken into account by solving these equations independently on different radial "rays" with direction $\mathbf{n}$ (corresponding to the angular zones of the polar grid), assuming rotational symmetry around $\mathbf{n}$ for the neutrino distribution function. In addition, certain terms from the full transport equations are taken into account to avoid unphysical behaviour in the optically thick regime (section 2.4.6).

2.4.2. Boltzmann equation in spherical symmetry

The precise form of Eq. (2.20) in a spherically symmetric spacetime has been discussed in various places in the literature [32, 108, 120, 162]; it depends on the adopted gauge and slicing conditions, and on the tetrad basis used in momentum space. In our case, the spacetime metric is of the CFC type with $\beta_1 = \phi^4 \beta^r$ and $\beta_2 = \beta_3 = 0$,

$$\mathrm{d}s^2 = -\alpha(t,r)^2 + \phi(t,r)^4 \left[(\mathrm{d}r + \beta_r(t,r)\ \mathrm{d}t)^2 + r^2 \mathrm{d}\theta^2 + r^2 \sin^2\theta\, \mathrm{d}\varphi^2 \right]. \tag{2.21}$$

Furthermore, we carry out a transformation to the orthonormal frame comoving with the fluid, in which the collision integral $\mathfrak{C}$ can be expressed most conveniently; the expressions for the collision integral provided in Appendix A of Rampp and Janka [151] thus remain valid. With the velocity field chosen as

$$\left(v^1, v^2, v^3\right) = \left(\phi^{-2} v_r(t,r), 0, 0\right), \tag{2.22}$$

a possible choice for the basis vectors of such a frame is given by,

$$\begin{aligned}
\mathbf{e_0} &= \alpha^{-1} W\, \partial_t + W \left(\phi^{-2} v_r - \alpha^{-1}\beta_r\right) \partial_r, && (2.23)\\
\mathbf{e_1} &= \alpha^{-1} v_r W\, \partial_t + W \left(\phi^{-2} - \alpha^{-1}\beta_r v_r\right) \partial_r, && (2.24)\\
\mathbf{e_2} &= \phi^{-2} r^{-1}\, \partial_\theta, && (2.25)\\
\mathbf{e_3} &= \phi^{-2} r^{-1} \sin^{-1}\theta\, \partial_\varphi. && (2.26)
\end{aligned}$$

In spherical symmetry, the distribution function f depends only on t, r, the comoving frame energy $\varepsilon = \mathbf{p} \cdot \mathbf{e}_0$ (where $\mathbf{p}$ is the neutrino four-momentum) and the angle cosine $\mu = \mathbf{p} \cdot \mathbf{e}_1 / \mathbf{p} \cdot \mathbf{e_0}$, and obeys the following PDE (see Appendix A for a brief sketch of the derivation):

$$\begin{aligned}
&W \left[\frac{\xi}{\alpha} \left(\frac{\partial f}{\partial t} - \beta_r \frac{\partial f}{\partial r} \right) + \frac{\nu}{\phi^2} \frac{\partial f}{\partial r} \right] - \\
&\quad \frac{\varepsilon W^3}{r \alpha \phi^3} \frac{\partial f}{\partial \varepsilon} \left\{ v_r^2 \phi \left[\beta_r \phi \left(2r \frac{\partial \phi}{\partial r} - \psi \phi \right) + r \left(-\mu \frac{\partial \alpha}{\partial r} + \mu^2 \phi^2 \frac{\partial \beta_r}{\partial r} - \frac{\partial \phi^2}{\partial t} \right) \right] + \right. \\
&\quad v_r^3 \left[r \mu \phi \left(-\mu \frac{\partial \alpha}{\partial r} + \frac{\partial \beta_r \phi^2}{\partial r} - \frac{\partial \phi^2}{\partial t} \right) - \psi \frac{\alpha}{\phi} \frac{\partial r \phi^2}{\partial r} \right] + \beta_r \phi^3 \left(-\psi - r\mu \frac{\partial v_r}{\partial r} \right) + \\
&\quad \phi \left[r\mu \left(\mu\alpha \frac{\partial v_r}{\partial r} + \frac{\partial \alpha}{\partial r} + \phi^2 \left(-\mu \frac{\partial \beta_r}{\partial r} + \frac{\partial v_r}{\partial t} \right) \right) + r \frac{\partial \phi^2}{\partial t} - r \beta_r \frac{\partial \phi^2}{\partial r} \right] + \\
&\quad \left. v_r \alpha \left[\phi \left(\psi + r\mu \frac{\partial v_r}{\partial r} \right) + 2r\psi \frac{\partial \phi}{\partial r} + \phi^2 \left(\mu \frac{\partial v_r}{\partial t} - \frac{\partial \beta_r}{\partial r} \right) + \frac{\partial \phi^2}{\partial t} \right] \right\} + \\
&\quad \frac{W^3 \left(1 - \mu^2\right)}{r \alpha \phi^3} \frac{\partial f}{\partial \mu} \left\{ \alpha \left[\phi \left(\frac{\xi}{W^2} - r\nu \frac{\partial v_r}{\partial r} \right) + 2r \frac{\xi}{W^2} \frac{\partial \phi}{\partial r} \right] + \right. \\
&\quad \left. \phi \left[\beta \phi^2 \left(r\xi \frac{\partial v_r}{\partial r} - \frac{\nu}{W^2} \right) - \frac{r}{W^2} \left(\xi \frac{\partial \alpha}{\partial r} - \nu \phi^2 \frac{\partial \beta_r}{\partial r} \right) - r\xi\phi^2 \frac{\partial v_r}{\partial t} \right] \right\} = \mathfrak{C}\left[f\right],
\end{aligned} \tag{2.27}$$

where $\nu = \mu + v_r$, $\xi = 1 + \mu v_r$ and $\psi = 1 - \mu^2$. It should be noted that our result is analytically equivalent to the one obtained by Mezzacappa and Matzner [120] for the same gauge and slicing conditions. The transfer equation for the radiation intensity $\mathcal{I} = h^{-3} c^{-2} \varepsilon^3 f$ can be obtained by exploiting the relation $\varepsilon^3 \partial f / \partial \varepsilon = \partial \left(f \varepsilon^3 \right) / \partial \varepsilon - 3\varepsilon^2 f$, and is omitted here for the sake of brevity.

2.4.3. Exact moment equations for CFC metric in spherical symmetry

Multiplying Eq. (2.27) by $h^{-3}c^{-2}\varepsilon^{3}$ and taking the zeroth and first angular moment yields the moment equations in a spherically symmetric CFC spacetime, resulting in

$$
\begin{aligned}
&\frac{\partial W\left(\hat{J}+v_r\hat{H}\right)}{\partial t}+\frac{\partial}{\partial r}\left[\left(W\frac{\alpha}{\phi^2}-\beta_r v_r\right)\hat{H}+\left(W v_r\frac{\alpha}{\phi^2}-\beta_r\right)\hat{J}\right]- \\
&\quad\frac{\partial}{\partial\varepsilon}\left\{W\varepsilon\hat{J}\left[\frac{1}{r}\left(\beta_r-\frac{\alpha v_r}{\phi^2}\right)+2\left(\beta_r-\frac{\alpha v_r}{\phi^2}\right)\frac{\partial\ln\phi}{\partial r}-2\frac{\partial\ln\phi}{\partial t}\right]+\right. \\
&\quad W\varepsilon\hat{H}\left[v_r\left(\frac{\partial\beta_r\phi^2}{\partial r}-2\frac{\partial\ln\phi}{\partial t}\right)-\frac{\alpha}{\phi^2}\frac{\partial\ln\alpha W}{\partial r}+\alpha W^2\left(\beta_r\frac{\partial v_r}{\partial r}-\frac{\partial v_r}{\partial t}\right)\right]- \\
&\quad\left.\varepsilon\hat{K}\left[\frac{\beta_r W}{r}-\frac{\partial\beta_r W}{\partial r}+W v_r r\frac{\partial}{\partial r}\left(\frac{\alpha}{r\phi^2}\right)+W^3\left(\frac{\alpha}{\phi^2}\frac{\partial v_r}{\partial r}+v_r\frac{\partial v_r}{\partial t}\right)\right]\right\}- \\
&\quad W\hat{J}\left[\frac{1}{r}\left(\beta_r-\frac{\alpha v_r}{\phi^2}\right)+2\left(\beta_r-\frac{\alpha v_r}{\phi^2}\right)\frac{\partial\ln\phi}{\partial r}-2\frac{\partial\ln\phi}{\partial t}\right]- \\
&\quad W\hat{H}\left[v_r\left(\frac{\partial\beta_r\phi^2}{\partial r}-2\frac{\partial\ln\phi}{\partial t}\right)-\frac{\alpha}{\phi^2}\frac{\partial\ln\alpha W}{\partial r}+\alpha W^2\left(\beta_r\frac{\partial v_r}{\partial r}-\frac{\partial v_r}{\partial t}\right)\right]+ \\
&\quad\hat{K}\left[\frac{\beta_r W}{r}-\frac{\partial\beta_r W}{\partial r}+W v_r r\frac{\partial}{\partial r}\left(\frac{\alpha}{r\phi^2}\right)+W^3\left(\frac{\alpha}{\phi^2}\frac{\partial v_r}{\partial r}+v_r\frac{\partial v_r}{\partial t}\right)\right]=\alpha\hat{C}^{(0)},
\end{aligned}
\tag{2.28}
$$

for the energy equation; and the momentum equation reads,

$$
\begin{aligned}
&\frac{\partial W\left(\hat{H}+v_r\hat{K}\right)}{\partial t}+\frac{\partial}{\partial r}\left[\left(W\frac{\alpha}{\phi^2}-\beta_r v_r\right)\hat{K}+\left(W v_r\frac{\alpha}{\phi^2}-\beta_r\right)\hat{H}\right]- \\
&\quad\frac{\partial}{\partial\varepsilon}\left\{W\varepsilon\hat{H}\left[\frac{1}{r}\left(\beta_r-\frac{\alpha v_r}{\phi^2}\right)+2\left(\beta_r-\frac{\alpha v_r}{\phi^2}\right)\frac{\partial\ln\phi}{\partial r}-2\frac{\partial\ln\phi}{\partial t}\right]+\right. \\
&\quad W\varepsilon\hat{K}\left[v_r\left(\frac{\partial\beta_r\phi^2}{\partial r}-2\frac{\partial\ln\phi}{\partial t}\right)-\frac{\alpha}{\phi^2}\frac{\partial\ln\alpha W}{\partial r}+\alpha W^2\left(\beta_r\frac{\partial v_r}{\partial r}-\frac{\partial v_r}{\partial t}\right)\right]- \\
&\quad\left.\varepsilon\hat{L}\left[\frac{\beta_r W}{r}-\frac{\partial\beta_r W}{\partial r}+W v_r r\frac{\partial}{\partial r}\left(\frac{\alpha}{r\phi^2}\right)+W^3\left(\frac{\alpha}{\phi^2}\frac{\partial v_r}{\partial r}+v_r\frac{\partial v_r}{\partial t}\right)\right]\right\}+ \\
&\quad\left(\hat{J}-\hat{K}\right)\left[v_r\left(\frac{\beta_r}{r}-\frac{\partial\beta_r}{\partial r}\right)+\frac{\partial}{\partial r}\left(\frac{W\alpha}{\phi^2}\right)-\frac{W\alpha}{r\phi^2}+W^3\left(\frac{\partial v_r}{\partial t}-\beta_r\frac{\partial v_r}{\partial r}\right)\right]+ \\
&\quad\left(\hat{H}-\hat{L}\right)\left[\frac{W^3\alpha}{\phi^2}\frac{\partial v_r}{\partial r}+\frac{\beta W}{r}-\frac{\partial\beta W}{\partial r}-W v_r r\frac{\partial}{\partial r}\left(\frac{\alpha}{r\phi^2}\right)+\frac{\partial W}{\partial t}\right]- \\
&\quad W\hat{H}\left[\frac{1}{r}\left(\beta_r-\frac{\alpha v_r}{\phi^2}\right)+2\left(\beta_r-\frac{\alpha v_r}{\phi^2}\right)\frac{\partial\ln\phi}{\partial r}-2\frac{\partial\ln\phi}{\partial t}\right]- \\
&\quad W\hat{K}\left[v_r\left(\frac{\partial\beta_r\phi^2}{\partial r}-2\frac{\partial\ln\phi}{\partial t}\right)-\frac{\alpha}{\phi^2}\frac{\partial\ln\alpha W}{\partial r}+\alpha W^2\left(\beta_r\frac{\partial v_r}{\partial r}-\frac{\partial v_r}{\partial t}\right)\right]+ \\
&\quad\hat{L}\left[\frac{\beta_r W}{r}-\frac{\partial\beta_r W}{\partial r}+W v_r r\frac{\partial}{\partial r}\left(\frac{\alpha}{r\phi^2}\right)+W^3\left(\frac{\alpha}{\phi^2}\frac{\partial v_r}{\partial r}+v_r\frac{\partial v_r}{\partial t}\right)\right]=\alpha\hat{C}^{(1)}.
\end{aligned}
\tag{2.29}
$$

Here, the angular moments J, H, K and L of the specific intensity are given by,

$$\{J, H, K, L\} = \frac{1}{2}\int\limits_{-1}^{1} \mathrm{d}\mu\, \mu^{0,1,2,3}\mathcal{I}, \tag{2.30}$$

while $C^{(0)}$ and $C^{(1)}$ are the corresponding zeroth and first moment of the collision integral. Note that Eqs. (2.28) and (2.29) are written in terms of the densitized moments $\hat{J}$, $\hat{H}$, $\hat{K}$ and $\hat{L}$ (where $\hat{X} = \sqrt{\gamma}X$) which contain the square root of the determinant of the three-metric as an additional factor, in order to better reflect the underlying law of energy conservation. The virtue of such a formulation is more apparent in the equations governing the evolution of the neutrino number density and flux,

$$\begin{aligned}
&\frac{\partial W\left(\hat{\mathcal{J}} + v_r\hat{\mathcal{H}}\right)}{\partial t} + \frac{\partial}{\partial r}\left[\left(W\frac{\alpha}{\phi^2} - \beta_r v_r\right)\hat{\mathcal{H}} + \left(W v_r\frac{\alpha}{\phi^2} - \beta_r\right)\hat{\mathcal{J}} + \right] - \\
&\quad\frac{\partial}{\partial \varepsilon}\left\{W\varepsilon\hat{\mathcal{J}}\left[\frac{1}{r}\left(\beta_r - \frac{\alpha v_r}{\phi^2}\right) + 2\left(\beta_r - \frac{\alpha v_r}{\phi^2}\right)\frac{\partial \ln\phi}{\partial r} - 2\frac{\partial \ln\phi}{\partial t}\right] + \right.\\
&\quad W\varepsilon\hat{\mathcal{H}}\left[v_r\left(\frac{\partial\beta_r\phi^2}{\partial r} - 2\frac{\partial\ln\phi}{\partial t}\right) - \frac{\alpha}{\phi^2}\frac{\partial\ln\alpha W}{\partial r} + \alpha W^2\left(\beta_r\frac{\partial v_r}{\partial r} - \frac{\partial v_r}{\partial t}\right)\right] - \\
&\quad\left.\varepsilon\hat{\mathcal{K}}\left[\frac{\beta_r W}{r} - \frac{\partial\beta_r W}{\partial r} + W v_r r\frac{\partial}{\partial r}\left(\frac{\alpha}{r\phi^2}\right) + W^3\left(\frac{\alpha}{\phi^2}\frac{\partial v_r}{\partial r} + v_r\frac{\partial v_r}{\partial t}\right)\right]\right\} = \alpha\hat{\mathcal{C}}^{(0)}
\end{aligned} \tag{2.31}$$

$$\begin{aligned}
&\frac{\partial W\left(\hat{\mathcal{H}} + v_r\hat{\mathcal{K}}\right)}{\partial t} + \frac{\partial}{\partial r}\left[\left(W\frac{\alpha}{\phi^2} - \beta_r v_r\right)\hat{\mathcal{K}} + \left(W v_r\frac{\alpha}{\phi^2} - \beta_r\right)\hat{\mathcal{H}} + \right] - \\
&\quad\frac{\partial}{\partial \varepsilon}\left\{W\varepsilon\hat{\mathcal{H}}\left[\frac{1}{r}\left(\beta_r - \frac{\alpha v_r}{\phi^2}\right) + 2\left(\beta_r - \frac{\alpha v_r}{\phi^2}\right)\frac{\partial \ln\phi}{\partial r} - 2\frac{\partial \ln\phi}{\partial t}\right] + \right.\\
&\quad W\varepsilon\hat{\mathcal{K}}\left[v_r\left(\frac{\partial\beta_r\phi^2}{\partial r} - 2\frac{\partial\ln\phi}{\partial t}\right) - \frac{\alpha}{\phi^2}\frac{\partial\ln\alpha W}{\partial r} + \alpha W^2\left(\beta_r\frac{\partial v_r}{\partial r} - \frac{\partial v_r}{\partial t}\right)\right] - \\
&\quad\left.\varepsilon\hat{\mathcal{L}}\left[\frac{\beta_r W}{r} - \frac{\partial\beta_r W}{\partial r} + W v_r r\frac{\partial}{\partial r}\left(\frac{\alpha}{r\phi^2}\right) + W^3\left(\frac{\alpha}{\phi^2}\frac{\partial v_r}{\partial r} + v_r\frac{\partial v_r}{\partial t}\right)\right]\right\} + \\
&\quad\left(\hat{\mathcal{J}} - \hat{\mathcal{K}}\right)\left[v_r\left(\frac{\beta_r}{r} - \frac{\partial\beta_r}{\partial r}\right) + \frac{\partial}{\partial r}\left(\frac{W\alpha}{\phi^2}\right) - \frac{W\alpha}{r\phi^2} + W^3\left(\frac{\partial v_r}{\partial t} - \beta_r\frac{\partial v_r}{\partial r}\right)\right] + \\
&\quad\left(\hat{\mathcal{H}} - \hat{\mathcal{L}}\right)\left[\frac{W^3\alpha}{\phi^2}\frac{\partial v_r}{\partial r} + \frac{\beta W}{r} - \frac{\partial\beta W}{\partial r} - W v_r r\frac{\partial}{\partial r}\left(\frac{\alpha}{r\phi^2}\right) + \frac{\partial W}{\partial t}\right] = \alpha\hat{\mathcal{C}}^{(1)},
\end{aligned} \tag{2.32}$$

where $\{\mathcal{J}, \mathcal{H}, \mathcal{K}, \mathcal{L}, \mathcal{C}\} = \{\varepsilon^{-1}J, \varepsilon^{-1}H, \varepsilon^{-1}K, \varepsilon^{-1}L, \varepsilon^{-1}C\}$. Apart from the collision integral, no source terms appear in the neutrino number Eq. (2.31); thus, a finite-volume discretization exactly conserves the total neutrino number measured in the laboratory (coordinate) frame

$$\int \mathrm{d}^3x\, \sqrt{\gamma}N_{\mathrm{eul}} = \frac{4\pi}{c}\int \mathrm{d}^3x\, \mathrm{d}\varepsilon\, \sqrt{\gamma}W\left(\mathcal{J} + v_r\mathcal{H}\right), \tag{2.33}$$

in the absence of neutrino-matter interactions. As a consequence, numerical conservation of lepton number can be achieved with an appropriate conservative treatment of the flux terms in the neutrino moment equations and the source term for the electron fraction.

With a few minor exceptions, the numerical solution of the neutrino moment equations in our code proceeds exactly as described by Rampp and Janka [151]. Eqs. (2.28) and (2.29) are written in a conservative finite-difference form using second-order space discretization on a staggered mesh and backward differencing in time; only the neutrino advection terms

$$\frac{\partial}{\partial r}\left[\left(W\frac{\alpha}{\phi^2}v_r-\beta_r\right)\hat{J}\right],\quad \frac{\partial}{\partial r}\left[\left(W\frac{\alpha}{\phi^2}v_r-\beta_r\right)\hat{H}\right],a \tag{2.34}$$

are discretized with upwind differences in space and central differences in time. Unlike Rampp and Janka [151], we use a special second-order finite difference representation for the terms governing advection in energy space to guarantee that *both* energy and lepton number are conserved (see Sec. 3.2). The higher moments K and L are computed from the variable Eddington factors f_K and f_L obtained from the solution of a model Boltzmann equation (cf. Sec. 2.4.4) as $K = f_K J$ and $L = f_L J$ where necessary. Finally, the moment equations are supplemented by two additional equations for the operator-split update of the specific internal energy and the electron fraction due to neutrino-matter interactions,

$$\left(\frac{\partial\epsilon}{\partial t}\right)_\nu = -\frac{4\pi\alpha}{\rho W}\int_0^\infty \mathrm{d}\varepsilon \sum C_\nu^{(0)}, \tag{2.35}$$

$$\left(\frac{\partial Y_e}{\partial t}\right)_\nu = -\frac{4\pi\alpha m_\mathrm{B}}{\rho W}\int_0^\infty \mathrm{d}\varepsilon \left(\mathcal{C}_{\nu_e}^{(0)}-\mathcal{C}_{\bar{\nu}_e}^{(0)}\right), \tag{2.36}$$

where the factor αW^{-1} takes care of the conversion from proper time to coordinate time. The resulting non-linear system of equations for $\mathcal{J}$, $\mathcal{H}$, ϵ and Y_e is then solved by Newton-Raphson iteration. As in [151], we treat μ and τ neutrinos and their antiparticles as a single species, and solve the corresponding moment equations separately from the (fully coupled) moment equations for the transport of electron neutrinos and antineutrinos.

2.4.4. Model Boltzmann equation

In the variable Eddington factor technique, the closure relations required for Eqs. (2.28) and (2.29) are extracted from the formal solution of a model Boltzmann equation, with the moments of the neutrino distribution function occurring in the collision integral taken from the solution of the moment equation in an iterative procedure [24, 124, 151]. Since the model Boltzmann equation is only used to compute *normalized* moments of the radiation intensity, it is sufficient to consider a strongly simplified equation version of Eq. (2.27). We therefore neglect terms containing the shift vector or derivatives of the metric functions α and ϕ in Eq. (2.27), as well as higher-order terms $\mathcal{O}(v_r^2)$ in the radial velocity. Furthermore, we set $\nu = \mu$ and $\xi = 1$ in the terms for advection in energy space. However, the radial advection term is kept exactly as in the full equation. The model transfer equation for the radiation intensity thus obtained reads,

$$\begin{aligned}
&\frac{\partial \mathcal{I}}{\partial t} + \left(\frac{\alpha v_r}{\phi^2} - \beta_r\right)\frac{\partial f}{\partial r} + \frac{\alpha\mu}{\phi^2}\frac{\partial f}{\partial r} + \mathcal{I}\left[\left(3-\mu^2\right)\frac{\alpha v_r}{r\phi^2} + \left(1+\mu^2\right)\alpha\phi^2\frac{\partial v_r}{\partial r} + 2\alpha\mu\frac{\partial v_r}{\partial t}\right] - \\
&\quad \frac{\partial \mathcal{I}}{\partial \varepsilon}\left\{\varepsilon\left[\left(1-\mu^2\right)\frac{\alpha v_r}{r\phi^2} + \mu^2\frac{\alpha}{\phi^2}\frac{\partial v_r}{\partial r} + \alpha\mu\frac{\partial v_r}{\partial t}\right]\right\} + \frac{\alpha\left(1-\mu^2\right)}{r\phi^2}\frac{\partial \mathcal{I}}{\partial \mu} + \\
&\quad \frac{\partial}{\partial \mu}\left\{\left(1-\mu^2\right)\left[\mu\left(\frac{\alpha v_r}{r\phi^2} - \frac{\alpha}{\phi^2}\frac{\partial v_r}{\partial r}\right) - \mu\alpha\frac{\partial v_r}{\partial t}\right]\mathcal{I}\right\} = C\left[\mathcal{I}\right]. \qquad (2.37)
\end{aligned}$$

Here, $C\left[\mathcal{I}\right]$ denotes the collision term in the transfer equation, which is related to the collision term $\mathfrak{C}$ in the Boltzmann equation (2.27) by $C\left[\mathcal{I}\right] = \varepsilon^3 h^{-3} c^{-2}\mathfrak{C}[f]$. Aside from the appearance of prefactors containing the metric functions α and ϕ and of the radial shift β_r in the advection term, Eq. (2.37) is identical to the flat-space transfer equation in the $\mathcal{O}(v/c)$-approximation. Therefore, the same solution method as in Rampp and Janka [151] can be employed, i.e. the radial advection term and the energy derivatives in Eq. (2.37) are treated by a conservative interpolation procedure and a time-explicit upwind scheme respectively, while the tangent-ray method [124, 205] is used for the remaining terms.

2.4.5. Source terms

Once the solution of the moment equations is known, the source terms Q_{Y_e} Q_E, and Q_M for electron number, energy, and momentum in the local fluid frame can be computed from the zeroth and first angular moments $C^{(0)}$ and $C^{(1)}$ of the collision integral,

$$Q_{Y_e} = \left(\frac{\mathrm{d}\rho Y_e}{\mathrm{d}\lambda}\right)_C = -4\pi m_{\mathrm{B}}\int_0^\infty \mathrm{d}\varepsilon\,\left(\mathcal{C}^{(0)}_{\nu_e} - \mathcal{C}^{(0)}_{\bar{\nu}_e}\right), \qquad (2.38)$$

$$Q_E = \left(\frac{\mathrm{d}\rho\varepsilon}{\mathrm{d}\lambda}\right)_C = -4\pi\int_0^\infty \mathrm{d}\varepsilon\,\sum C^{(0)}_\nu, \qquad (2.39)$$

$$Q_M = -4\pi\int_0^\infty \mathrm{d}\varepsilon\,\sum C^{(1)}_\nu. \qquad (2.40)$$

To obtain the correct transformation to the Eulerian frame (in which the equations of hydrodynamics are solved), we note that the covariant source terms s and q^μ which account for neutrino interactions in the continuity equation for the electron number density and in the equations of hydrodynamics,

$$\nabla_\mu\left(\rho Y_e u^\mu\right) = s, \quad \nabla_\nu T^{\mu\nu} = q^\mu, \qquad (2.41)$$

can be expressed as a coordinate-independent scalar and vector in terms of Q_{Y_e}, Q_E, and Q_M:

$$s = Q_{Y_e}, \quad q^\mu = Q_E\mathbf{e_0} + Q_M\mathbf{e_1}. \qquad (2.42)$$

After carrying out a Lorentz transformation [5] back to the Eulerian frame and recasting the resulting equations into conservative form, we obtain the following source terms for the conserved Eulerian quantities that appear in Eqs. (2.6), (2.7) and (2.8):

$$\left(\frac{\partial\sqrt{\gamma}S_1}{\partial t}\right)_C = \sqrt{\gamma}W\left(v_r Q_E + Q_M\right). \tag{2.43}$$

$$\left(\frac{\partial\sqrt{\gamma}\tau}{\partial t}\right)_C = \sqrt{\gamma}W\left(Q_E + v_r Q_M\right). \tag{2.44}$$

$$\left(\frac{\partial\sqrt{\gamma}\rho W Y_e}{\partial t}\right)_C = \sqrt{\gamma}W Q_{Y_e} \tag{2.45}$$

Note that we have multiplied the source terms by the metric $\sqrt{\gamma}$, because it is the densitized variables $\sqrt{\gamma}S_i$, $\sqrt{\gamma}\tau$ and $\sqrt{\gamma}DY_e$ that are actually evolved in Eqs. (2.6), (2.7) and (2.8). This is possible because the metric factor $\sqrt{\gamma}$ is obviously not changed by neutrino interactions.

2.4.6. Ray-by-ray-plus approach for axisymmetric problems

As noted by Rampp and Janka [151], a treatment of neutrino transport in spherical symmetry (as described in Secs. 2.4.3 to 2.4.5) can be extended to the multi-dimensional case by assuming that all the involved physical quantities depend only parametrically on the coordinates θ and ϕ (using spherical polar coordinates), while neglecting any lateral derivatives in the full three-dimensional moment equations. However Buras et al. [21] pointed out that the lateral advection of neutrinos in the optically thick regime and the non-radial components of the neutrino pressure gradient need to be taken into account to avoid unphysical convective activity in the proto-neutron star. In general relativity the additional advection terms in the moment equations are,

$$\left(\frac{\partial\sqrt{\gamma}W\left(J+v_r H\right)}{\partial t}\right)_{\mathrm{adv}} + \frac{\partial\alpha\sqrt{\gamma}W\hat{v}^2\left(J+v_r H\right)}{\partial\theta} = 0 \tag{2.46}$$

$$\left(\frac{\partial\sqrt{\gamma}W\left(H+v_r K\right)}{\partial t}\right)_{\mathrm{adv}} + \frac{\partial\alpha\sqrt{\gamma}W\hat{v}^2\left(H+v_r K\right)}{\partial\theta} = 0, \tag{2.47}$$

which are solved in an operator-split step before the radial transport sweep. We also include terms for the compressional heating of the neutrino due to lateral motions, which are added to the moment equations (2.28) and (2.29) when performing the radial transport sweep,

$$\left(\frac{\partial\sqrt{\gamma}\left(J+v_r H\right)}{\partial t}\right)_{\mathrm{comp}} = -\frac{\partial\alpha\sqrt{\gamma}W\hat{v}^2}{\partial\theta}\frac{J-K}{2} - \frac{\partial}{\partial\varepsilon}\left(\varepsilon\frac{\partial\alpha\sqrt{\gamma}W\hat{v}^2}{\partial\theta}\frac{J-K}{2}\right) \tag{2.48}$$

$$\left(\frac{\partial\sqrt{\gamma}\left(H+v_r K\right)}{\partial t}\right)_{\mathrm{comp}} = -\frac{\partial\alpha\sqrt{\gamma}W\hat{v}^2}{\partial\theta}\frac{K-L}{2} - \frac{\partial}{\partial\varepsilon}\left(\varepsilon\frac{\partial\alpha\sqrt{\gamma}W\hat{v}^2}{\partial\theta}\frac{H-L}{2}\right) \tag{2.49}$$

---

[5] Since we consider a purely radial velocity field at this stage, the Lorentz transformation of a four-vector from the comoving frame to the Eulerian frame simply reads: $(q^0, q^1, q^2, q^3) \rightarrow W(q^0 + v_r q^1, q^1 + v_r q^0, q^2, q^3)$

It should be noted that gravitational redshift associated with lateral motion is still neglected here; however, this is a tiny effect in typical supernova environments due to the relatively small asphericity of the gravitational field.

The lateral component of the neutrino pressure gradient appears as a source term for the component S_2 of the fluid momentum density,

$$\left(\frac{\partial\sqrt{\gamma}S_2}{\partial t}\right)_{\text{lat}} = -\sqrt{-g}\frac{\partial P_\nu}{\partial\theta}, \tag{2.50}$$

where we assume that the neutrino pressure is given by $P_\nu = 4/3\pi J$ in the optically thick regime. Since the acceleration four-vector due to the neutrino pressure gradient must be orthogonal to the four-velocity of the fluid, the source term in the energy equation (work exerted on the fluid) is given by,

$$\left(\frac{\partial\sqrt{\gamma}\tau}{\partial t}\right)_{\text{lat}} = -\sqrt{-g}v^2\frac{\partial P}{\partial\theta}. \tag{2.51}$$

Finally, contrary to the Newtonian case, the covariant source vector q^μ has to be transformed to the Eulerian frame by a Lorentz boost which includes the non-radial velocity components. Q_E and Q_M now enter differently into the source term for S_1, and additional source terms for S_2 and S_3 appear,

$$\left(\frac{\partial\sqrt{\gamma}S_1}{\partial t}\right)_C = \sqrt{\gamma}\left[Wv_1Q_E + Q_M\left(1 + v_1v_r\frac{W-1}{v_iv^i}\right)\right], \tag{2.52}$$

$$\left(\frac{\partial\sqrt{\gamma}S_2}{\partial t}\right)_C = \sqrt{\gamma}\left[Wv_2Q_E + Q_Mv_2v^r\frac{W-1}{v_iv^i}\right], \tag{2.53}$$

$$\left(\frac{\partial\sqrt{\gamma}S_3}{\partial t}\right)_C = \sqrt{\gamma}\left[Wv_3Q_E + Q_Mv_3v_r\frac{W-1}{v_iv^i}\right]. \tag{2.54}$$

While the new terms in Q_M are of order $\mathcal{O}(v^2)$ and can usually be neglected, all the terms in Q_E are of order $\mathcal{O}(v)$ and need to be included to ensure the correct evolution of the specific internal energy ϵ. This is particularly crucial for rapidly rotating configurations, where the rotational velocity v_ϕ can reach a significant fraction of c.

2.5. Quality of our approximation

Our relativistic ray-by-ray-plus method entails several approximations, which fall into three categories, viz., approximations in the treatment i) of the microphysics (EoS, neutrino interactions, etc.), ii) of neutrino transport, and iii) of the gravitational field equations. Concerning the microphysics, we rely on the same up-to-date description as the non-relativistic PROMETHEUS-VERTEX code, which includes a number of additional neutrino reactions compared to the "standard" set of neutrino opacities used by Bruenn [12] (see [19, 22, 67, 78, 99, 115] for the extensions to the standard opacities). Neutrino oscillations are presently neglected despite the fact that the classical MSW effect and collective neutrino-antineutrino flavour oscillations may possibly have an important bearing at least on the observable neutrino properties. However, considering that our understanding of the latter phenomenon is by no means complete, and that the classical MSW effect is only relevant far outside the supernova core, it is doubtful whether the physics of neutrino oscillations is *dynamically* relevant for the supernova problem at all. Moreover, no self-consistent dynamical simulations including these effects have been carried out so far; recent studies have contented themselves with post-processing progenitor or simulation data [48, 111]. Thus, our treatment of neutrino physics, while certainly not complete, is state-of-the-art for dynamical supernova simulations, and the same is true for the three high-density equations of state (Lattimer&Swesty [100], Shen [167], Wolff&Hillebrandt [74]) available in our code.

Handling the neutrino transport with the "ray-by-ray-plus" scheme of Buras et al. [21] introduces approximations on two different levels: First, the variable Eddington factor technique is not strictly equivalent to full Boltzmann transport even in spherical symmetry, since only a simplified "model" Boltzmann equation is solved to provide the closure for the moment equations. This shortcoming is mitigated by the fact that comparisons with analytic solutions [151] and with Boltzmann solvers based on the S_N-method [107] show that the approximate solution is entirely adequate in many cases. Second, the "ray-by-ray-plus" approach ignores the lateral propagation (but not the lateral advection) of neutrinos. However, the analysis of [21] at least suggests that this approximation does not affect the heating in the gain layer dramatically, and therefore captures the overall dynamics during the proto-neutron star accretion phase and also during the subsequent wind phase quite adequately. Unfortunately, no detailed comparison of the "ray-by-ray-plus" method with true multi-angle transport or alternative approaches, like multi-group flux-limited diffusion (MGFLD), which would allow us to better assess the quality of our method, is available as yet. So far, the different approaches to multi-dimensional transport hitherto pursued by supernova modellers all have their individual strengths and weaknesses: the only true multi-angle [110, 145] simulations for example, have been carried out at the expense of neglecting inelastic scattering reactions, and MGFLD has been shown to smear out lateral variations of the radiation field quite considerably [145], while the "ray-by-ray-plus" method probably tends to overestimate such variations. Still, simulations with ray-by-ray transport show effects that are qualitatively similar to those seen by Ott et al. [145] with multi-angle transport. At any rate, ray-by-ray transport can also be classified as a state-of-the-art method in the field, notwithstanding the fact that is certainly limited too scenarios where the anisotropies in the matter distribution (at least out to the neutrinosphere) do not become exceedingly large. Compared to other radiative transfer methods used in multi-dimensional *relativistic* simulations up to now – like the deleptonization scheme of Liebendörfer [103], which was first used in GR by Ott et al. [144], or the grey two-moment formalism (using the Eddington approximation) by Farris et al. [54] – it is a much more ambitious and accurate approach to neutrino transport in core collapse supernovae.

Given the limitations of the "ray-by-ray-plus" method, the use of the CFC approximation to the gravitational field equations is quite natural: CFC breaks down for strongly deformed, rapidly rotating matter configurations, where the "ray-by-ray-plus"method is not applicable anyway – there is little to be gained by a more accurate treatment of general relativity in that regime. It is noteworthy, however, that the the CFC approximation has been found to be very accurate for a wide range of (sometimes extreme) astrophysical scenarios, such as rapidly rotating neutron stars [36], rigidly rotating disks [92], and rotational core collapse [33, 44, 143, 144, 169]. In the core collapse scenario, CFC still appears to be adequate [66] for the extremely rapidly rotating models of Shibata and Sekiguchi [170]; even toroidally deformed neutron stars obviously pose little problem to CFC. These facts indicate that in typical supernova simulations, where the neutron star rotates moderately at most, CFC will not be the weakest link in the chain of approximations, and that, at least for our purpose, GR effects are treated correctly in our code. All in all, VERTEX-CoCoNuT can thus be regarded as a truly relativistic radiation hydrodynamics code for core collapse supernovae, featuring a sophisticated neutrino transport scheme and an up-to-date treatment of the microphysics.

3. Improved Numerical Methods

In the last chapter, we already commented on the numerical methods used in the VERTEX-CoCoNuT code. Most of these methods are abundantly documented in the literature or in the papers on VERTEX [21, 151] and CoCoNuT [41, 43], and we therefore refrain from describing them in detail. However, our implementation of the equations of hydrodynamics and neutrino transport in VERTEX-CoCoNuT differs from the CoCoNuT and VERTEX codes in some important points, namely in the treatment of the relativistic energy equation (2.7), and in the treatment of the Doppler and gravitational redshift terms in the neutrino moment equations (2.28) and (2.29). Since the new implementation in VERTEX-CoCoNuT significantly improves either the numerical accuracy and (in the case of the "Doppler" terms) the computational efficiency of the code, we discuss these details at some length in this chapter. Furthermore, our reformulation of the energy equation and the new scheme for the "Doppler" terms can be applied in a more general context, and may be found useful in other hydrodynamics and neutrino transport codes, relativistic and Newtonian alike.

3.1. Energy Conservation in Newtonian and Relativistic Hydrodynamics

3.1.1. Importance of energy conservation in the supernova problem

Conservative discretization schemes for the Euler equations of gas dynamics are one of the cornerstones in modern computational astrophysics, both because they have appealing mathematical properties [101], and because they conserve important integral quantities (total rest mass, total energy, etc.) to machine precision. Unfortunately, the standard formulation of the Euler equations for self-gravitating fluids is not strictly conservative despite the fact that there exists an integral conservation law for the total kinetic, internal, and potential energy for any *localized*[1] matter distribution.

In the supernova problem, the non-conservative formulation of gravitational source terms in the Euler equations raises some critical questions: Can a secular drift of the total energy on the order of 10^{51} erg over a few 100 ms (which is a typical value for many simulations [26, 106, 133]) have a qualitative influence on the propagation of the shock and the development of the explosion, as the explosion energy is typically of the same order? Is there an appreciable effect in the first few seconds of the neutron star cooling

---

[1] This restriction is crucial, and has tangible implications: It is not possible, for example, to formulate a conservation law for the energy in a general cosmological context [175].

phase? The former question may probably be answered in the negative, because the accumulated error in the gravitational energy liberated during the collapse of the iron core and the contraction of the proto-neutron star makes itself felt primarily as a small excess or deficit (on the percent level or below) in the internal energy of the compact central object (which contains most of the mass on the grid), and not as a large relative error in the region around the shock. This also suggests that the energy conservation error due to the use of effective potentials (for which total energy conservation does not hold [116]) should not affect the post-bounce phase seriously. There is also some empirical evidence for this line of reasoning, since energy conservation in the shells above the neutron star has been discussed quantitatively and found to be adequate for an explosion model of an $8.8 M_\odot$ star [82]. On the other hand, a secular drift of the total energy can qualitatively affect neutron star cooling in the post-explosion phase: Once spurious generation of energy due to numerical inaccuracies outweighs the slowly decreasing neutrino losses, the proto-neutron star does not cool any longer (such an effect was actually observed in one of our pseudo-Newtonian simulations).

In order to alleviate the problems associated with the non-conservative character of gravitational source terms in the energy equation, we have developed an alternative scheme for treating the energy equation that significantly decreases the secular drift of the total energy. The new scheme can easily be integrated into any Eulerian finite-volume method, and is applicable (with only small variations) both in Newtonian and relativistic hydrodynamics. In the Newtonian case, it also works with effective gravitational potentials that do not obey the Poisson equation, and is very useful even then despite the fact that total energy is not conserved analytically, since the purely numerical drift is often much larger than the conservation error stemming from the pseudo-relativistic potential.

3.1.2. Energy equation in Newtonian hydrodynamics

Description of the algorithm

Usually the energy equation for a self-gravitating fluid is written as,

$$\frac{\partial e}{\partial t} + \frac{\partial \left(e + P\right) v^i}{\partial x^i} = -\rho v^i \frac{\partial \Phi}{\partial x^i}. \tag{3.1}$$

Here, $e = \rho v^2/2 + \rho\epsilon$ is the total energy density, P is the pressure, v^i is the fluid velocity, ρ is the (baryonic) mass density, and ϵ is the specific internal energy. Although Eq. (3.1) is not written in the form of a pure conservation equation, there is a conservation law for the volume integral of the total (i.e. kinetic, internal, and potential) energy (see, e.g., [171]): In order to obtain this integral conservation law, we absorb the source term $-\rho v^i \partial\Phi/\partial x^i$ into the flux term on the LHS,

$$\frac{\partial e}{\partial t} + \frac{\partial \left(e + P + \rho\Phi\right) v^i}{\partial x^i} = \Phi \frac{\partial \rho v^i}{\partial x^i}, \tag{3.2}$$

and use the continuity equation $\partial\rho/\partial t + \nabla \cdot (\rho \mathbf{v}) = 0$ to eliminate the divergence of the mass flux in the new source term,

$$\frac{\partial e}{\partial t} + \frac{\partial \left(e + P + \rho\Phi\right) v^i}{\partial x^i} = -\Phi \frac{\partial \rho}{\partial t}. \tag{3.3}$$

Integrating Eq. (3.3) over the entire spatial domain then yields,

$$\begin{aligned} \int \frac{\partial e}{\partial t}\,\mathrm{d}V &= -\int \Phi \frac{\partial \rho}{\partial t}\,\mathrm{d}V = 4\pi \int \Phi \frac{\partial \Delta\Phi}{\partial t}\,\mathrm{d}V = -4\pi \int \nabla\Phi \frac{\partial \nabla\Phi}{\partial t}\,\mathrm{d}V = \\ &= -2\pi \frac{\partial}{\partial t} \int \nabla\Phi \cdot \nabla\Phi\,\mathrm{d}V = 2\pi \frac{\partial}{\partial t} \int \Phi\Delta\Phi\,\mathrm{d}V = -\frac{1}{2}\frac{\partial}{\partial t} \int \rho\Phi\,\mathrm{d}V. \end{aligned} \tag{3.4}$$

Here, we have used Green's first identity, the Poisson equation $\Delta\Phi = 4\pi G\rho$, and the fact that the surface integral,

$$\int \Phi\nabla\Phi\,\mathrm{d}A, \tag{3.5}$$

vanishes if the domain of integration is extended to infinity. Eq. (3.4) implies that the total energy is conserved,

$$\int \left(e + \frac{1}{2}\rho\Phi\right) \mathrm{d}V = \mathrm{const.} \tag{3.6}$$

However, the *discretized* representation of the total energy,

$$E_{\mathrm{tot}} = \sum_{i,j,k} \left(e_{i,j,k} + \frac{1}{2}\rho_{i,j,k}\Phi_{i,j,k}\right) \Delta V_{i,j,k}, \tag{3.7}$$

will not be automatically conserved, if the numerical implementation of the gravitational source term is based on Eq. (3.1), because the discretized source term cannot be manipulated in the same fashion as in the steps from Eq. (3.1) to (3.3). One way to eliminate any secular drift of the total energy resulting from this, and to avoid the unwanted consequences described in Sec. 3.1.1, would be to use a strictly conservative form of the energy equation [138],

$$\frac{\partial}{\partial t}\left[e + \rho\Phi + \frac{1}{8\pi G}\left(\frac{\partial\Phi}{\partial x^i}\right)^2\right] + \frac{\partial}{\partial x^i}\left[\left(e + P + \rho\Phi\right) v^i + \frac{1}{4\pi G}\Phi\frac{\partial^2\Phi}{\partial t\,\partial x^i}\right] = 0 \tag{3.8}$$

Unfortunately, this form of the energy equation has several drawbacks: the "gravitational self-energy" contribution $1/(8\pi G)\left(\partial\Phi/\partial x^i\right)^2$ to the total energy density can exceed the kinetic, internal, and binding energy of the matter by a large factor, resulting in considerable round-off errors in these quantities. Furthermore, the flux term contains a mixed spatial and temporal derivative, which may introduce numerical inaccuracies. It is also impossible to formulate an analogue of Eq. (3.8) for the effective relativistic potentials commonly used in PROMETHEUS-VERTEX [116, 128] because these do not obey the Poisson equation.

However, there is a simple and efficient solution to the problem of numerical energy conservation that avoids these shortcomings and requires only a minimal modification of the "standard" scheme based on Eq. (3.1). The starting point is the reformulation of the energy equation in Eq. (3.2),

$$\frac{\partial e}{\partial t}+\frac{\partial\left(e+P+\rho\Phi\right)v^i}{\partial x^i}=\Phi\frac{\partial\rho v^i}{\partial x^i}.$$

Using the continuity equation, the divergence of ρv^i can be replaced by the time derivative of the density, which is in turn partially absorbed in the time derivative of $\rho\Phi$,

$$\frac{\partial\left(e+\rho\Phi\right)}{\partial t}+\frac{\partial\left(e+P+\rho\Phi\right)v^i}{\partial x^i}=\rho\frac{\partial\Phi}{\partial t}. \tag{3.9}$$

The remaining source term now contains the time derivative of the gravitational potential. Eq. (3.9) can be conveniently solved with an operator-split scheme in three steps.

Step 1: First, the equations of hydrodynamics are solved with the additional potential energy terms $\rho\Phi$, where Φ itself is kept constant,

$$\frac{\partial\left(e+\rho\Phi\right)}{\partial t}+\frac{\partial\left(e+P+\rho\Phi\right)v^i}{\partial x^i}=0, \Phi=\text{const.} \tag{3.10}$$

Since $\rho\Phi$ may be considerably larger than the internal energy density e, using $e+\rho\Phi$ as conserved quantity instead of e may lead to large round-off errors in e and produce unwanted numerical noise (in particular spurious entropy loss or production). To circumvent this problem, the time derivative $\partial\rho\Phi/\partial t$ can be re-expressed in terms of the mass flux (as $\Phi=$ const.), i.e. $\partial\rho\Phi/\partial t=\Phi\partial\rho/\partial t=-\Phi\nabla\cdot(\rho\mathbf{v})$,

$$\frac{\partial e}{\partial t}+\frac{\partial\left(e+P+\rho\Phi\right)v^i}{\partial x^i}-\frac{\partial\rho v^i}{\partial x^i}\Phi=0, \Phi=\text{const.} \tag{3.11}$$

The value $e^{(n+1/3)}$ of the energy density after the first fractional step can be obtained by integrating Eq. (3.11) over the cell volume V. It is instructive to compare the final formula for the update of e with "standard" implementations of the gravitational source term. Working with forward differences in time [2], we now have

$$e^{(n+1/3)}=e^{(n)}-\frac{\Delta t}{V}\left[\int_{\partial V}\left(e+P\right)\mathbf{v}\cdot d\mathbf{A}+\sum_k\int_{A_k}\left(\Phi_c-\Phi_k\right)\rho\mathbf{v}\cdot d\mathbf{A}_k\right], \tag{3.12}$$

(where A_k denotes the k-th cell interface, while Φ_c and Φ_k are the cell-centre and -interface values of Φ) instead of,

$$e^{(n+1/3)}=e^{(n)}-\frac{1}{V}\int_{\partial V}\left(e+P\right)\mathbf{v}\cdot d\mathbf{A}-\nabla\Phi\cdot\rho\mathbf{v} \tag{3.13}$$

Since $\int\left(\Phi_k-\Phi_c\right)d\mathbf{A}_k/V$ is the component of $\nabla\Phi$ pointing into the direction of $d\mathbf{A}_k$, the update prescription (3.12) can be viewed as an alternative version of (3.13), in which

---

[2] First-order forward differences are only adopted for illustration at this point. The implementation in higher-order time integration schemes is straightforward.

the cell-averaged mass flux $\rho\mathbf{v}$ has been replaced by an average of the mass flux at cell interfaces. *Thus, gravitational energy is only released or stored when mass is actually exchanged between different cells.* This is the key ingredient for eliminating a secular drift of the total energy.

When the gravitational field is stationary, no further fractional steps are required, and the value of e after one full time-step is just $e^{(n+1)} = e^{(n+1/3)}$. If the gravitational potential varies with time, two additional steps are necessary once Φ has been updated from its old value $\Phi^{(n)}$ to $\Phi^{(n+1)}$ at the end of the time-step.

Step 2: In order to ensure that Eq. (3.10) is fulfilled, the energy density $e^{(n+2/3)}$ after the second fractional step must be calculated according to,

$$e^{(n+2/3)} = e^{(n+1/3)} + \rho^{(n+1)}\left(\Phi^{(n)} - \Phi^{(n+1)}\right). \tag{3.14}$$

Step 3: Finally, the source term $\rho\partial\Phi/\partial t$ has to be accounted for in a third step,

$$\frac{\partial\left(e+\rho\Phi\right)}{\partial t} = \rho\frac{\partial\Phi}{\partial t}. \tag{3.15}$$

If centred differences in time are used to obtain second-order accuracy, the energy density at the end of the time-step reads,

$$e^{(n+1)} = e^{(n+2/3)} + \frac{1}{2}\left(\rho^{(n)} + \rho^{(n+1)}\right)\left(\Phi^{(n+1)} - \Phi^{(n)}\right). \tag{3.16}$$

Steps 2 and 3 can easily be combined into a compact formula for the update of e after each recalculation of the gravitational potential:

$$e^{(n+1)} = e^{(n+1/3)} + \frac{1}{2}\left(\rho^{(n)} - \rho^{(n+1)}\right)\left(\Phi^{(n+1)} - \Phi^{(n)}\right). \tag{3.17}$$

Condition for the exact conservation of energy

Under certain conditions, the scheme described in Sec. 3.1.2 conserves the total energy exactly. To demonstrate this for the special case of a spherical polar grid, we consider the total energy balance after each sub-step of the algorithm: Steps 1 and 2 conserve the (discretized) total volume integral of $e + \rho\Phi$, provided that the flux $(e + P + \rho\Phi)\mathbf{v}$ vanishes at the boundaries of the computational domain,

$$\sum_{i,j,k}\left(e^{(n+2/3)}_{(i,j,k)} + \rho^{(n+1)}_{(i,j,k)}\Phi^{(n+1)}_{(i,j,k)}\right)\Delta V_{i,j,k} = \sum_{i,j,k}\left(e^{(n)}_{(i,j,k)} + \rho^{(n)}_{(i,j,k)}\Phi^{(n)}_{(i,j,k)}\right)\Delta V_{i,j,k}. \tag{3.18}$$

If e is then updated according to Eq. (3.16), we obtain, by combination with Eq. (3.18),

$$\sum_{i,j,k}\left(e^{(n+1)}_{(i,j,k)} + \rho^{(n+1)}_{(i,j,k)}\Phi^{(n+1)}_{(i,j,k)}\right)\Delta V_{i,j,k} = \tag{3.19}$$

$$\sum_{i,j,k}\left[e^{(n)}_{(i,j,k)} + \frac{1}{2}\left(\rho^{(n)}_{(i,j,k)}\Phi^{(n)}_{(i,j,k)} - \rho^{(n+1)}_{(i,j,k)}\Phi^{(n)}_{(i,j,k)} + \rho^{(n+1)}_{(i,j,k)}\Phi^{(n+1)}_{(i,j,k)} + \rho^{(n)}_{(i,j,k)}\Phi^{(n+1)}_{(i,j,k)}\right)\right]\Delta V_{i,j,k}.$$

Hence, the total energy after the $(n+1)$-th time-step is according to the definition in Eq. (3.7),

$$E_{\mathrm{tot}}^{(n+1)} = E_{\mathrm{tot}}^{(n)} + \sum_{i,j,k} \rho_{(i,j,k)}^{(n)} \Phi_{(i,j,k)}^{(n+1)} \Delta V_{i,j,k} - \sum_{i,j,k} \rho_{(i,j,k)}^{(n+1)} \Phi_{(i,j,k)}^{(n)} \Delta V_{i,j,k}, \tag{3.20}$$

The sums on the RHS quantify the violation of total energy conservation during one time-step. If they were replaced by integrals, we could manipulate them using Green's first identity and the Poisson equation $\nabla \cdot \nabla \Phi = 4\pi G \rho$ to obtain an exact cancellation:

$$\begin{aligned} &\int \rho^{(n)} \Phi^{(n+1)} \,\mathrm{d}V - \int \rho^{(n+1)} \Phi^{(n)} \,\mathrm{d}V = \qquad (3.21)\\ &4\pi G \int \left(\nabla \Phi^{(n)}\right) \cdot \left(\nabla \Phi^{(n+1)}\right) \mathrm{d}V - 4\pi G \int \left(\nabla \Phi^{(n+1)}\right) \cdot \left(\nabla \Phi^{(n)}\right) \mathrm{d}V = 0. \end{aligned}$$

Using a special finite-difference representation of the Poisson equation, we can manipulate the sums in Eq. 3.20 in very much the same way as by applying Green's first identity. Let us assume that the source density $4\pi\rho$ is expressed as the divergence of the gravitational acceleration $\mathbf{g}$ in the following natural manner,

$$\begin{aligned} 4\pi\rho\Delta V_{(i,j,k)} &= g_{(i+1/2,j,k)} \Delta A_{(i+1/2,j,k)} - g_{(i-1/2,j,k)} \Delta A_{(i-1/2,j,k)}, \\ &+ g_{(i,j+1/2,k)} \Delta A_{(i,j+1/2,k)} - g_{(i,j-1/2,k)} \Delta A_{(i,j-1/2,k)}, \\ &+ g_{(i,j,k+1/2)} \Delta A_{(i,j,k+1/2)} - g_{(i,j,k-1/2)} \Delta A_{(i,j,k-1/2)}. \end{aligned} \tag{3.22}$$

Here, $\Delta A_{(i+1/2,j,k)}$ denotes the area of the interface between the cells (i,j,k) and $(i+1,j,k)$, and $g_{(i+1/2,j,k)}$ denotes the perpendicular component of $\mathbf{g}$ thereon; $\Delta A_{(i,j+1/2,k)}$, etc. are defined analogously. Let us further suppose that $g_{(i+1/2,j,k)}$ is obtained by multiplying the difference $\Phi_{(i+1,j,k)} - \Phi_{(i,j,k)}$ by a time-independent factor $c_{i,j,k}$, as in the following natural finite-difference representation of $\mathbf{g}$,

$$g_{(i+1/2,j,k)} = c_{i,j,k} \left(\Phi_{(i+1,j,k)} - \Phi_{(i,j,k)}\right) = \frac{1}{r_i - r_{i+1}} \left(\Phi_{(i+1,j,k)} - \Phi_{(i,j,k)}\right) \tag{3.23}$$

$$g_{(i,j+1/2,k)} = d_{i,j,k} \left(\Phi_{(i,j+1,k)} - \Phi_{(i,j,k)}\right) = \frac{1}{r_i \left(\theta_j - \theta_{j+1}\right)} \left(\Phi_{(i,j+1,k)} - \Phi_{(i,j,k)}\right) \tag{3.24}$$

$$g_{(i,k+1/2)} = e_{i,j,k} \left(\Phi_{(i,j,k+1)} - \Phi_{(i,j,k)}\right) = \frac{1}{r_i \sin\theta_j \left(\varphi_k - \varphi_{k+1}\right)} \left(\Phi_{(i,j,k+1)} - \Phi_{(i,j,k)}\right) \tag{3.25}$$

At the outer boundary, we may set $g_{(m+1/2,j,k)} = \Phi_{(m,j,k)} r_m / r_{m+1/2}^2$ to obtain the correct monopole moment of the gravitational field.

The first sum term in the energy balance equation (3.20) can now be written as

$$\begin{aligned} \sum_{i,j,k} \rho_{(i,j,k)}^{(n)} \Phi_{(i,j,k)}^{(n+1)} \Delta V_{i,j,k} = & \sum_{i,j,k} \left[\left(g_{(i+1/2,j,k)}^{(n)} \Delta A_{(i+1/2,j,k)} - g_{(i-1/2,j,k)}^{(n)} \Delta A_{(i-1/2,j,k)} \right) \Phi_{(i,j,k)}^{(n+1)} \right. \\ & + \left(g_{(i,j+1/2,k)}^{(n)} \Delta A_{(i,j+1/2,k)} - g_{(i,j-1/2,k)}^{(n)} \Delta A_{(i,j-1/2,k)} \right) \Phi_{(i,j,k)}^{(n+1)} \\ & \left. + \left(g_{(i,j,k+1/2)}^{(n)} \Delta A_{(i,j,k+1/2)} - g_{(i,j,k-1/2)}^{(n)} \Delta A_{(i,j,k-1/2)} \right) \Phi_{(i,j,k)}^{(n+1)} \right] \Delta V_{i,j,k}. \end{aligned} \tag{3.26}$$

Via summation by parts[3], we arrive at an expression that is completely symmetric with respect to the time indices n and $n+1$:

$$\begin{aligned}\sum_{i,j,k} \rho^{(n)}_{(i,j,k)} \Phi^{(n+1)}_{(i,j,k)} \Delta V_{i,j,k} \quad = \quad & \sum_{i=1,M-1} \sum_{j=1,N-1} \sum_{k=1,O} g^{(n)}_{(i,j+1/2,k)} \Delta A_{(i,j+1/2,k)} g^{(n+1)}_{(i,j+1/2,k)} \\ & + \sum_{i=1,M} \sum_{j=1,N-1} \sum_{k=1,O} g^{(n)}_{(i,j+1/2,k)} \Delta A_{(i,j+1/2,k)} g^{(n+1)}_{(i,j+1/2,k)} \\ & + \sum_{i=1,M} \sum_{j=1,N} \sum_{k=1,O-1} g^{(n)}_{(i,j,k+1)} \Delta A_{(i,j+1/2,k)} g^{(n+1)}_{(i,j+1/2,k)} \\ & + \sum_{j=1,N} \sum_{k=1,O} g^{(n)}_{(m+1/2,j,k)} \Delta A_{(m+1/2,j,k)} g^{(n+1)}_{(m+1/2,j,k)}. \end{aligned} \tag{3.27}$$

In effect, we have obtained a finite-difference analogue of Green's first identity with non-vanishing surface contributions. The second sum in (3.20) can be rearranged in precisely the same way and thus cancels the first sum exactly. Hence, the total internal, kinetic and gravitational energy is conserved exactly,

$$E^{(n+1)}_{\mathrm{tot}} = E^{(n)}_{\mathrm{tot}}. \tag{3.28}$$

3.1.3. Energy equation in general relativity

In general relativity, the situation is somewhat different from the Newtonian case: At first sight, the fact that no sources appear in the local conservation law $\nabla_\nu T^{\mu\nu} = 0$ for the stress-energy tensor $T^{\mu\nu}$ might suggest that the energy and momentum equations can be formulated in a strictly flux-conservative form (i.e. without sources). However, an integral conservation law can only be formulated (via Gauss' theorem) for divergence-free vector fields on a differentiable and orientable manifold [175, 186]; such fields can in general be constructed from the energy momentum tensor only if there exists a Killing vector field[4]. On the other hand, a conservation law can be formulated for the sum of $T^{\mu\nu}$ and the Landau-Lifshitz pseudo-tensor $t^{\mu\nu}$ of the gravitational field [98, 175],

$$\frac{\partial\,(-g)\,(T^{\mu\nu} + t^{\mu\nu})}{\partial x^\nu} = 0, \tag{3.29}$$

Unfortunately, the practical use of Eq. (3.29) is limited because t is a complicated (and non-unique) function of the metric and its derivatives. Furthermore, it is impossible to interpret $t^{\mu 0}$ as the local energy-momentum vector density of the gravitational field due to its non-uniqueness and non-tensorial character; only the integral

---

[3] Note that in spherical polar coordinates some "surface contributions" vanish since $A_{(1/2,j,k)} = A_{(i,1/2,k)} = A_{(1/2,N-1/2,k)} = 0$, $\Phi_{(i,j,0)} = \Phi_{(i,j,O)}$, and $\Phi_{(i,j,O+1)} = \Phi_{(i,j,1)}$.

[4] Special cases comprise: i) the flat Minkowski spacetime with ten Killing fields (implying the conservation of energy, momentum and angular momentum), ii) stationary spacetimes with a time-like Killing field (implying energy conservation), and iii) axisymmetric spacetimes with a space-like Killing field that creates an $SO(2)$ isometry group (implying the conservation of one angular momentum component).

$E_{\mathrm{ADM}} = \int \left(T^{\mu 0} + t^{\mu 0}\right) \mathrm{d}V$ (known as ADM energy) over the entire spatial domain in an asymptotically flat spacetime has a well-defined physical meaning. In general, Eq. (3.29) will only be useful for special gauge choices and symmetry assumptions, where the resulting source-free energy equation is not overly complicated (see e.g. [104, 154]). The total volume integral E_{ADM} (which can also be expressed in different ways) is, of course, an important *diagnostic* quantity for assessing the quality of energy conservation in a numerical code.

Because of these obstacles we construct an improved scheme for the energy equation in a similar way as in the Newtonian case and do not attempt to eliminate source terms from the energy equation altogether. We start from the formulation used by Dimmelmeier et al. [46],

$$\frac{\partial \sqrt{\gamma}\tau}{\partial t} + \frac{\partial \sqrt{-g}\left(\tau \hat{v}^i + P v^i\right)}{\partial x^i} = \sqrt{-g}\left[T^{00}\left(K_{ij}\beta^i\beta^j - \beta^i \frac{\partial \alpha}{\partial x^i}\right) + T^{0i}\left(2K_{ij}\beta^j - \frac{\partial \alpha}{\partial x^i}\right) + T^{ij}K_{ij}\right]. \tag{3.30}$$

For convenience, we add the continuity equation, and subsume most of the source terms on the RHS under the variable Q to arrive at an equation very similar to Eq. (3.1),

$$\frac{\partial \sqrt{\gamma}\left(\tau + D\right)}{\partial t} + \frac{\partial \sqrt{-g}\left(\tau \hat{v}^i + D\hat{v}^i + P v^i\right)}{\partial x^i} = -\sqrt{-g}\left[\left(\tau + D\right)\hat{v}^i + P v^i\right]\frac{\partial \alpha}{\partial x^i} + Q. \tag{3.31}$$

The first source term on the RHS corresponds closely to the Newtonian source term $\rho v^i \partial\Phi/\partial x^i$. It is the product of the total energy flux (rest mass flux in Newtonian gravity) and the flat-space gradient of the lapse function (corresponding to the Newtonian potential). This source term can be eliminated by multiplying Eq. (3.31) by α,

$$\alpha\frac{\partial \sqrt{\gamma}\left(\tau + D\right)}{\partial t} + \alpha\frac{\partial \sqrt{-g}\left(\tau \hat{v}^i + D\hat{v}^i + P v^i\right)}{\partial x^i} = -\alpha\sqrt{-g}\left[\left(\tau + D\right)\hat{v}^i + P v^i\right]\frac{\partial \alpha}{\partial x^i} + \alpha Q, \tag{3.32}$$

and by pushing the lapse function into the space and time derivatives,

$$\frac{\partial \sqrt{\gamma}\alpha\left(\tau + D\right)}{\partial t} + \frac{\partial \sqrt{-g}\alpha\left(\tau \hat{v}^i + D\hat{v}^i + P v^i\right)}{\partial x^i} = \sqrt{\gamma}\left(\tau + D\right)\frac{\partial \alpha}{\partial t} + \alpha Q. \tag{3.33}$$

Again, the new source term $\left(\tau + D\right)\partial\alpha/\partial t$ corresponds closely to $\rho\partial\Phi/\partial t$ in the Newtonian case. Since it is numerically advantageous to separate the baryonic mass contributions to the total energy (due to the reduction of round-off errors), we subtract the continuity equation, and finally arrive at the following alternative energy equation:

$$\frac{\partial}{\partial t}\left[\sqrt{\gamma}\alpha\left(\tau + D\right) - \sqrt{\gamma}D\right] + \frac{\partial}{\partial x^i}\left[\sqrt{-g}\left(\alpha\tau\hat{v}^i + \alpha D\hat{v}^i - D\hat{v}^i + \alpha P v^i\right)\right] = \sqrt{\gamma}\left(\tau + D\right)\frac{\partial \alpha}{\partial t} + \alpha Q. \tag{3.34}$$

The numerical solution within a finite-volume scheme can again be split into three sub-steps, the first of which consists in solving the energy equation (including only αQ as source term) while keeping the lapse function α fixed,

$$\frac{\partial}{\partial t}\left[\sqrt{\gamma}\alpha\tau + \sqrt{\gamma}\left(\alpha - 1\right)D\right] + \frac{\partial}{\partial x^i}\left[\sqrt{-g}\left(\alpha\tau\hat{v}^i + \alpha D\hat{v}^i - D\hat{v}^i + \alpha P v^i\right)\right] = \alpha Q. \tag{3.35}$$

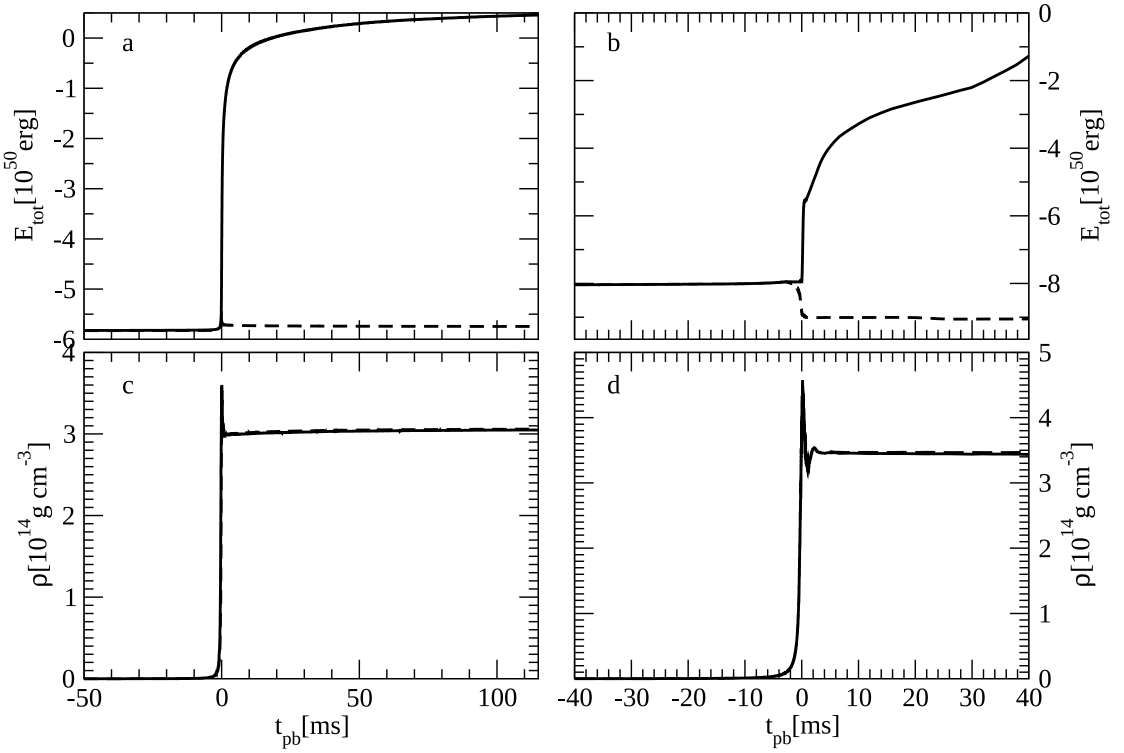

Figure 3.1.: Total energy (panels a and b) and central density (panels c and d) for core collapse runs with CoCoNuT and PROMETHEUS, both in Newtonian gravity. The CoCoNuT run (panels a and c) has been carried out using the deleptonization scheme of Liebendörfer [103], and the progenitor model s20.0 of Woosley et al. [196]; the energy lost in the form of neutrinos is added to the total energy budget. The adiabatic collapse (except for nuclear burning) of the $15M_\odot$ model s15s7b2 of Woosley and Weaver [195] simulated with PROMETHEUS is shown in panels b and d. Results obtained with the "standard" and improved scheme for the energy equation are drawn as solid and dashed lines, respectively.

In order to avoid working with $\sqrt{\gamma}\alpha\tau + \sqrt{\gamma}\,(\alpha - 1)\,D$ as conserved quantity, we note that the change in $\sqrt{\gamma}\,(\alpha - 1)\,D$ inside a cell volume V during the time-step Δt can be expressed in terms of the integral of the flux $D\hat{v}^i$ over the cell boundary $A = \partial V$. The finite-volume version of the energy equation for this cell can therefore be written as,

$$\begin{aligned}\int_V \alpha\sqrt{\gamma}\tau^{(n+1/3)}\,\mathrm{d}V &= \int_V \alpha\sqrt{\gamma}\tau^{(n)}\,\mathrm{d}V + \Delta t\left[-\int_{\partial V}\sqrt{\gamma}\alpha^2\left(\tau\hat{v}^i + Pv^i\right)\,\mathrm{d}A\right.\\ &\left.-\int_{\partial V}\sqrt{\gamma}\alpha\,(\alpha-1)\,D\hat{v}^i\,\mathrm{d}A + (\alpha-1)\int_{\partial V}\alpha\sqrt{\gamma}D\hat{v}^i\,\mathrm{d}A + \int_V \alpha Q\right].\end{aligned} \tag{3.36}$$

The surface integrals in the second line of Eq. (3.36) can be combined into a single term containing the difference between the lapse function α_c at the cell centre and the lapse

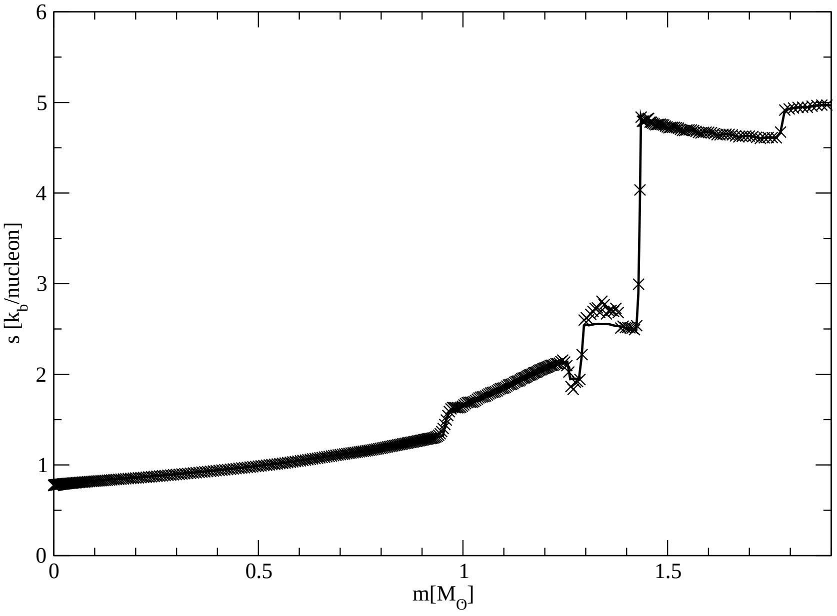

Figure 3.2.: Entropy versus enclosed mass for the adiabatic collapse of model s15s7b2 at a time of 1.2 ms before bounce (crosses) compared to the entropy profile of the initial model. The entropy changes at $m \approx 1.3 M_\odot$ are caused by silicon burning, and by the transition to the high-density EoS regime.

function α_k at the k-th cell interface,

$$\begin{aligned}\int_V \sqrt{\gamma}\tau^{(n+1/3)}\,\mathrm{d}V &= \int_V \sqrt{\gamma}\tau^{(n)}\,\mathrm{d}V + \Delta t \int_V Q\,\mathrm{d}V + \Delta t \int_V \alpha Q \\ &\quad -\frac{\Delta t}{\alpha}\left[\int_{\partial V} \sqrt{\gamma}\alpha^2 \left(\tau \hat{v}^i + P v^i\right)\,\mathrm{d}A + \sum_k \int_{A_k} \sqrt{\gamma}\alpha_k \left(\alpha_c - \alpha_k\right)\,\mathrm{d}A\right].\end{aligned} \tag{3.37}$$

This formulation requires only a minimal modification of the scheme for the unmodified energy equation (3.30).

In a second step, the lapse function is updated, while the conserved quantity $\sqrt{\gamma}\left[\tau + (\alpha - 1) D\right]$ is kept constant,

$$\frac{\partial}{\partial t}\left[\alpha\hat{\tau} + (\alpha - 1)\hat{D}\right] = 0. \tag{3.38}$$

Note that it is convenient to work with the densitized quantities $\hat{\tau} = \sqrt{\gamma}\tau$ and $\hat{D} = \sqrt{\gamma}D$ here because $\sqrt{\gamma}$ may be updated at the same time as α. The discretized version of Eq. (3.38),

$$\alpha^{(n+1)}\hat{\tau}^{(n+2/3)} + \left(\alpha^{(n+1)} - 1\right)\hat{D}^{(n+1)} = \alpha^{(n)}\hat{\tau}^{(n+1/3)} + \left(\alpha^{(n)} - 1\right)\hat{D}^{(n+1)}, \tag{3.39}$$

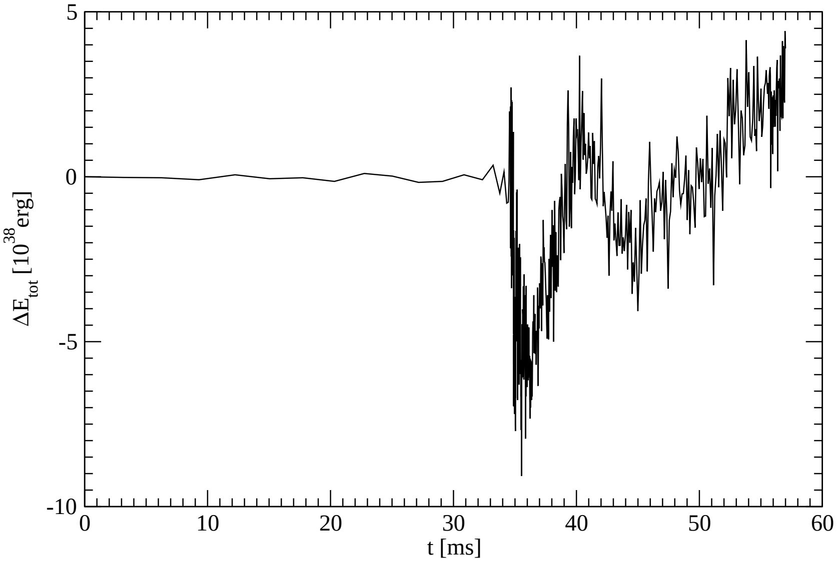

Figure 3.3.: Violation of total energy conservation for the collapse simulation of a 4/3-polytrope with the TVD test code. Initially the total energy of the polytrope is -1.08×10^{51} erg.

has the solution,

$$\sqrt{\gamma}\tau^{(n+2/3)} = \sqrt{\gamma}\tau^{(n+1/3)} + \left(\tau^{(n+1/3)} + D^{(n+1)}\right)\left(\frac{\alpha^{(n)}}{\alpha^{(n+1)}} - 1\right). \tag{3.40}$$

In a third operator-split step, the source term containing $\sqrt{\gamma}\,(\tau + D)\,\partial\alpha/\partial t$ in Eq. (3.34) is taken care of,

$$\frac{\partial}{\partial t}\left[\sqrt{\gamma}\alpha\tau + \sqrt{\gamma}\,(\alpha - 1)\,D\right] = \sqrt{\gamma}\,(\tau + D)\,\frac{\partial\alpha}{\partial t}. \tag{3.41}$$

As in the Newtonian case, the second and third step can be merged, and if centred differences in time are used, τ has to be updated according to,

$$\hat{\tau}^{(n+1)} = \hat{\tau}^{(n+1/3)} + \frac{\hat{\tau}^{(n+1/3)} + \hat{\tau}^{(n)} + D^{(n+1)} + D^{(n)}}{2}\frac{\alpha^{(n)} - \alpha^{(n-1)}}{\alpha^{(n)}}. \tag{3.42}$$

3.1.4. Numerical tests

To illustrate the virtues of the new scheme for the energy equation, we have conducted several numerical tests in spherical symmetry with different codes. Newtonian core collapse simulations have been carried out with PROMETHEUS, the Newtonian version of CoCoNuT and a self-written second-order accurate hydrodynamics code employing TVD reconstruction and the Kurganov-Tadmor central scheme [95].

The PROMETHEUS run follows the adiabatic collapse of the progenitor model s15s7b2 of Woosley and Weaver [195] to a central density of 10^{13} g cm^{-3} with a quasi-Lagrangian

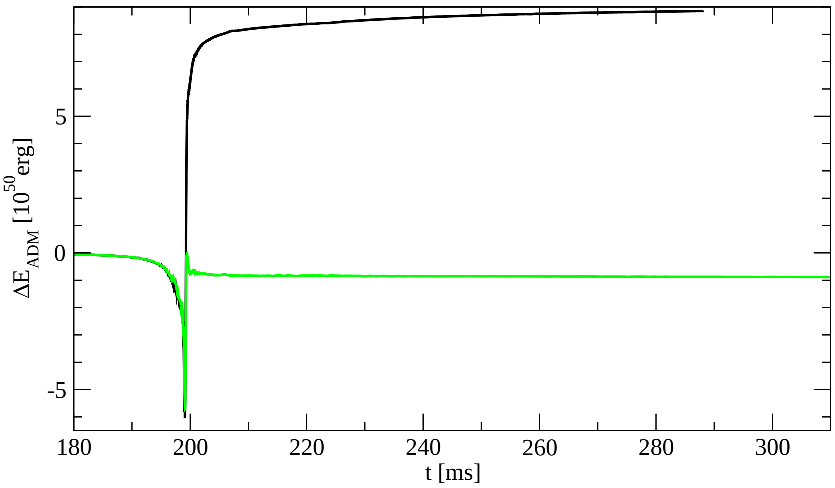

Figure 3.4.: Violation of ADM energy conservation for a general relativistic core collapse run with CoCoNuT with the "standard" scheme (black) and the improved scheme (green) for the relativistic energy equation. The run has been carried out using the parameterized $Y_e(\rho)$ trajectory of Liebendörfer [103], and the progenitor model s20.0 of Woosley et al. [196]. Neutrino energy losses are neglected.

grid. After that point, the grid is fixed, and the new scheme is switched on. The right upper panel of Fig. 3.1 shows that the new implementation still produces a residual violation of energy conservation of about 10^{50} erg around bounce. However, the total energy changes by less than 6×10^{48} erg after $t_{\mathrm{pb}} = 10$ ms, which is a considerable improvement compared to the old implementation, where the accumulated error reaches several 10^{50} erg within 40 ms after bounce. The reduction of the numerical error is of little relevance dynamically: the proto-neutron settles down at a slightly higher central density, which is consistent with the smaller total energy obtained with the new scheme. In order to demonstrate that by evolving e instead of $e + \rho\Phi$ round-off errors in the internal energy and the specific entropy can be kept small as we claimed, we also show entropy profiles of the model at the beginning of the simulation and shortly before bounce in Fig.3.2. Apart from small changes in the outer region of the core (at $m \approx 1.3 M_\odot$), which are, however, due to nuclear burning, the entropy is conserved to very good accuracy.

Total energy is conserved to even greater accuracy in a completely Eulerian simulation of the collapse of model s20.0 of Woosley et al. [196] using the Newtonian version of CoCoNuT and the deleptonization scheme of Liebendörfer [103]. If neutrino energy losses are correctly taken into account (which is trivial in the non-relativistic case), our new scheme conserves the total energy to an accuracy of 2×10^{49} erg at bounce, but reduces the secular drift after $t_{\mathrm{pb}} = 10$ ms to less than 2×10^{48} erg. In the same simulation with the "standard" implementation of gravity, energy conservation is violated by 6×10^{50} erg, i.e. the new scheme reduces the error by an order of magnitude. However, the effect on the dynamical evolution is small, as in the simulation with PROMETHEUS, with a minimal increase in the final central density of the proto-neutron star due to the new implementation.

Although a change of the total energy by around 3% as in the CoCoNuT simulation is probably more than satisfactory for core collapse simulations, this level of accuracy still does not exhaust the full potential of our new scheme, which can in principle conserve the total energy exactly as explained in Sec. 3.1.2. In order to verify this, we have simulated the collapse of a 4/3-polytrope with our self-written TVD test code using the hybrid equation of state of Janka et al. [83]. The gravitational potential and acceleration are calculated according to Eq. (3.22) and (3.23), hence the condition for exact energy conservation is satisfied. Fig. 3.3 shows that the total energy changes by less than 10^{39} erg (!), which corresponds to a relative error of less than 10^{-12} in terms of the initial energy ($E_{\mathrm{tot,i}} = -1.08 \times 10^{51}$ erg) and less than 10^{-14} in terms of the internal energy at the end of the simulation. Thus our improved scheme can indeed preserve the total energy almost to machine precision provided that the gravitational potential is determined appropriately.

In addition to these tests in Newtonian gravity, we have also simulated the collapse of model s20.0 in general relativity using CoCoNuT. We employ the Liebendörfer scheme for deleptonization with one minor modification: While reducing Y_e according to a $Y_e(\rho)$-parameterization, we neglect energy losses due to neutrino emission, because this simplifies the total energy budget considerably. Ideally, we would expect the ADM energy E_{ADM}, which can be written as,

$$E_{\mathrm{ADM}} = -2\pi \int \left(\Phi^5 \rho h W^2 - P + \frac{K_{ij} K^{ij}}{16\pi} \right) \mathrm{d}V, \tag{3.43}$$

in a CFC spacetime, to be conserved in such a situation. Fig. 3.4 shows that E_{ADM} is not perfectly conserved either with the "standard" scheme or with the new scheme. In both cases, conservation is violated by $|\Delta E_{\mathrm{ADM}}| \approx 6 \times 10^{50}$ erg around bounce, which is not surprising considering the complicated non-linear nature of the field equation and the appearance of gravitational self-energy terms in the sources and in the ADM energy. However, $|\Delta E_{\mathrm{ADM}}|$ settles down to a value of less than 10^{50} erg within 1 ms after bounce in the simulation using our new scheme, and the secular drift is only 10^{49} erg for the next 100 ms afterwards. The old scheme, on the other hand, leads to a violation of around 9×10^{50} erg and a small but clearly visible drift of E_{ADM} during the post-bounce phase.

The relativistic test thus confirms our findings in Newtonian gravity: Our reformulation considerably improves numerical energy conservation in simulations of self-gravitating systems. The secular drift during the quasi-stationary PNS evolution not completely eliminated in all cases, but can be easily reduced by an order of magnitude, which demonstrates the usefulness of our new scheme particularly for long-time simulations covering many dynamical time-scales.

3.2. Simultaneous Conservation of Energy and Lepton Number

While the monochromatic moment equation (2.28,2.29) and (2.31,2.32) for neutrino energy and number transport are analytically equivalent, a flux-conservative discretization of either pair of equations does not necessarily guarantee neutrino number (or, in the presence of neutrino-matter interactions, lepton number) and energy conservation simultaneously. The reason for this problem, which is inherent to spectral neutrino transport in the comoving frame, can be understood by comparing the analytic and discretized forms of the Doppler and gravitational redshift terms (denoted by a subscript "D") in the moment equations. In the neutrino energy equation these terms can be written as

$$\left(\frac{\partial J}{\partial t}\right)_D = \frac{\partial \varepsilon w J}{\partial \varepsilon} - wJ, \tag{3.44}$$

where the advection "velocity" in energy space w is a function of the velocities, metric functions, and the Eddington factors $f_H = H/J$, $f_K = K/J$, and $f_L = L/J$. To obtain the corresponding term in the equation for the monochromatic neutrino number density $\mathcal{J} = J/\varepsilon$, we divide by ε and apply the product rule,

$$\left(\frac{\partial \mathcal{J}}{\partial t}\right)_\mathrm{D} = \frac{\partial wJ}{\partial \varepsilon} + \frac{wJ}{\varepsilon} - \frac{wJ}{\varepsilon} = \frac{\partial wJ}{\partial \varepsilon} = \frac{\partial \varepsilon w \mathcal{J}}{\partial \varepsilon}.$$

The Doppler term in the neutrino number equation is thus a pure flux derivative term and cancels out if the equation is integrated over ε to obtain the evolution equation for the total neutrino number density. On the other hand, if the energy equation is discretized with backward differences in time and a flux-conservative form for the energy advection term,

$$\left(\frac{J_i^{n+1}\Delta\varepsilon_i - J_i^n \Delta\varepsilon_i}{\Delta t}\right)_\mathrm{D} = \varepsilon_{i+1/2} w_{i+1/2} J_{i+1/2}^{n+1} - \varepsilon_{i-1/2} w_{i-1/2} J_{i-1/2}^{n+1} - w_i J_i^{n+1} \Delta\varepsilon_i, \tag{3.45}$$

the discretized Doppler term for $\mathcal{J}$ reads,

$$\begin{aligned}
\left(\frac{\mathcal{J}_i^{n+1}\Delta\varepsilon_i - \mathcal{J}_i^n \Delta\varepsilon_i}{\Delta t}\right)_\mathrm{D} &= \frac{\varepsilon_{i+1/2}}{\varepsilon_i} w_{i+1/2} J_{i+1/2}^{n+1} - \frac{\varepsilon_{i-1/2}}{\varepsilon_i} w_{i-1/2} J_{i-1/2}^{n+1} - w_i J_i^{n+1} \frac{\Delta\varepsilon_i}{\varepsilon_i} \\
&= w_{i+1/2}\varepsilon_{i+1/2} \mathcal{J}_{i+1/2}^{n+1} - w_{i-1/2}\varepsilon_{i-1/2} \mathcal{J}_{i-1/2}^{n+1} - w_i J_i^{n+1} \frac{\Delta\varepsilon_i}{\varepsilon_i} \\
&\quad + \frac{\varepsilon_{i+1/2} - \varepsilon_i}{\varepsilon_i} w_{i+1/2} J_{i+1/2}^{n+1} + \frac{\varepsilon_i - \varepsilon_{i-1/2}}{\varepsilon_i} w_{i-1/2} J_{i-1/2}^{n+1}.
\end{aligned} \tag{3.46}$$

Thus, the source term in the neutrino number equation does *not* vanish in the discretized form of the equations, unless the last three terms in Eq. (3.46) cancel. Different methods have been proposed to recover the property of neutrino number conservation [12, 106]. In the original version of VERTEX [151] the problem is overcome by solving both the monochromatic moment equations for the neutrino energy density and flux (J, H), and the number density and flux $(\mathcal{J}, \mathcal{H})$ for electron neutrinos and antineutrinos *simultaneously*, but there are significant drawbacks to this approach: first, the mean energy $J/\mathcal{J}$ within a given energy zone $[\varepsilon_{i-1/2}, \varepsilon_{i+1/2}]$ is not constrained to the cell-centre value ε_i and may even move beyond the cell boundaries if $\mathcal{J}$ is treated as an independent quantity. Moreover, the solution of the equations by the Newton-Raphson method involves the inversion of square matrix blocks of size $4 \times N_\varepsilon + 2$ instead of $2 \times N_\varepsilon + 2$ for neutrino energy transport alone, which makes the Newton-Raphson iteration almost eight times more expensive.

Fortunately, the Doppler terms in the moment equations for neutrino energy transport can be discretized in such a way as to guarantee neutrino energy and number conservation simultaneously. For example, in a rather simple approach the interface values $J^{n+1}_{i+1/2}$ could be computed iteratively from J_i and $J_{i-1/2}$ using the condition

$$\frac{\varepsilon_{i+1/2} - \varepsilon_i}{\varepsilon_i} w_{i+1/2} J^{n+1}_{i+1/2} = w_i J_i \frac{\Delta\varepsilon_i}{\varepsilon_i} - \frac{\varepsilon_i - \varepsilon_{i-1/2}}{\varepsilon_i} w_{i-1/2} J^{n+1}_{i-1/2}, \tag{3.47}$$

so that the last three terms in Eq. (3.46) would indeed cancel. However, since this scheme allows large violations of the monotonicity condition $J_i < J_{i+1/2} < J_{i+1}$, the resulting algorithm would be rather unstable. To construct a stable scheme, we need to impose a weaker condition on the interface fluxes $F = \varepsilon w J$, i.e. we only require the source term in the frequency-integrated neutrino number equation to vanish:

$$\left(\frac{\mathcal{J}^{n+1}_{\mathrm{tot}} - \mathcal{J}^{n}_{\mathrm{tot}}}{\Delta t}\right)_{\mathrm{D}} = \sum_i \left(\frac{\varepsilon_{i+1/2}}{\varepsilon_i} w_{i+1/2} J^{n+1}_{i+1/2} - \frac{\varepsilon_{i-1/2}}{\varepsilon_i} w_{i-1/2} J^{n+1}_{i-1/2} - w_i J^{n+1}_i \frac{\Delta\varepsilon_i}{\varepsilon_i} \right) = 0. \tag{3.48}$$

In order to find interface fluxes $F_{i+1/2} = \varepsilon_{i+1/2} w_{i+1/2} J^{n+1}_{i+1/2}$ that fulfil this condition, we first rearrange the sum in Eq. (3.48) in the following manner:

$$\begin{aligned}
\left(\frac{\mathcal{J}^{n+1}_{\mathrm{tot}} - \mathcal{J}^{n}_{\mathrm{tot}}}{\Delta t}\right)_{\mathrm{D}} = \; & \ldots - \frac{F_{i-3/2}}{\varepsilon_{i-1}} - w_i J^{n+1}_{i-1} \frac{\Delta\varepsilon_{i-1}}{\varepsilon_{i-1}} + \frac{F_{i-1/2}}{\varepsilon_{i-1}} & (3.49)\\
& - \frac{F_{i-1/2}}{\varepsilon_i} - w_i J^{n+1}_i \frac{\Delta\varepsilon_i}{\varepsilon_i} + \frac{F_{i+1/2}}{\varepsilon_i} & \\
& - \frac{F_{i+1/2}}{\varepsilon_{i+1}} - w_i J^{n+1}_{i+1} \frac{\Delta\varepsilon_{i+1}}{\varepsilon_{i-1}} + \frac{F_{i+3/2}}{\varepsilon_{i+1}} - \ldots & \\
= \; & \ldots + \left(\frac{1}{\varepsilon_{i-2}} - \frac{1}{\varepsilon_{i-1}}\right) F_{i-3/2} - w_i J^{n+1}_{i-1} \frac{\Delta\varepsilon_{i-1}}{\varepsilon_{i-1}} & \\
& + \left(\frac{1}{\varepsilon_{i-1}} - \frac{1}{\varepsilon_i}\right) F_{i-1/2} - w_i J^{n+1}_i \frac{\Delta\varepsilon_i}{\varepsilon_i} & (3.50)\\
& + \left(\frac{1}{\varepsilon_i} - \frac{1}{\varepsilon_{i+1}}\right) F_{i+1/2} - w_i J^{n+1}_i \frac{\Delta\varepsilon_{i+1}}{\varepsilon_{i+1}} + \ldots . &
\end{aligned}$$

Next we split the fluxes into "left" and "right" components which are assigned to the adjacent energy zones,

$$F_{i+1/2} = F^L_i + F^R_{i+1}, \tag{3.51}$$

and again rewrite the frequency-integrated Doppler term in the discretized neutrino number equation:

$$\begin{aligned}\left(\frac{\mathcal{J}^{n+1}_{\mathrm{tot}}-\mathcal{J}^{n}_{\mathrm{tot}}}{\Delta t}\right)_{\mathrm{D}} &= \ldots+\left[\left(\frac{1}{\varepsilon_{i-2}}-\frac{1}{\varepsilon_{i-1}}\right)F^R_{i-1}-w_i J^{n+1}_{i-1}\frac{\Delta\varepsilon_{i-1}}{\varepsilon_{i-1}}+\left(\frac{1}{\varepsilon_{i-1}}-\frac{1}{\varepsilon_{i}}\right)F^L_{i-1}\right] \\ &+\left[\left(\frac{1}{\varepsilon_{i-1}}-\frac{1}{\varepsilon_{i}}\right)F^R_{i}-w_i J^{n+1}_{i}\frac{\Delta\varepsilon_{i}}{\varepsilon_{i}}+\left(\frac{1}{\varepsilon_{i}}-\frac{1}{\varepsilon_{i+1}}\right)F^L_{i}\right] \qquad (3.52)\\ &+\left[\left(\frac{1}{\varepsilon_{i}}-\frac{1}{\varepsilon_{i+1}}\right)F^R_{i+1}-w_i J^{n+1}_{i+1}\frac{\Delta\varepsilon_{i+1}}{\varepsilon_{i+1}}+\left(\frac{1}{\varepsilon_{i+1}}-\frac{1}{\varepsilon_{i+2}}\right)F^L_{i+1}\right]+\ldots\end{aligned}$$

If F^R and F^L are chosen such that each of the square brackets in Eq. (3.52) vanishes, no source term in the frequency-integrated neutrino number equation appears, and hence the total lepton number is also conserved[5].

The condition we obtain for the "left" and "right" fluxes,

$$\left(\frac{1}{\varepsilon_{i-1}}-\frac{1}{\varepsilon_{i}}\right)F^R_{i}+\left(\frac{1}{\varepsilon_{i}}-\frac{1}{\varepsilon_{i+1}}\right)F^L_{i}=w_i J^{n+1}_{i}\frac{\Delta\varepsilon_{i}}{\varepsilon_{i}}, \qquad (3.53)$$

only fixes the (weighted) sum of F_R and F_L, so we are still free to specify the ratio F_R/F_L to obtain steeper flux profiles in the high-energy tail of the spectrum, where J_i decreases rapidly with the zone index i. To this end, we parameterize F_R and F_L by a weighting factor ξ_i,

$$F^L_i = \frac{w_i\Delta\varepsilon_i}{1-\varepsilon_i\varepsilon^{-1}_{i+1}}J^{n+1}_i\xi_i, \qquad (3.54)$$

$$F^R_i = \frac{w_i\Delta\varepsilon_i}{\varepsilon_i\varepsilon^{-1}_{i-1}-1}J^{n+1}_i\left(1-\xi_i\right). \qquad (3.55)$$

Here, ξ is defined as a function of the zeroth angular moment $j = Jh^3c^2/\varepsilon^3$ of the neutrino distribution function at zone interfaces (obtained as weighted geometric mean of j in the adjacent zones), and a steepness parameter α,

$$\xi_i=\frac{j^{\alpha}_{i+1/2}}{j^{\alpha}_{i-1/2}+j^{\alpha}_{i+1/2}}. \qquad (3.56)$$

Only the lowest energy zone constitutes an exception, since the condition that $F(\varepsilon=0)$ should vanish requires $\xi_1=1$. For the steepness parameter, we typically set $\alpha=1/2$ or $\alpha=1$; both choices result in a second-order accurate scheme [6].

---

[5] Strictly speaking, this statement holds only as long as the non-linear moment equations are solved exactly. In practice, the time-critical Newton-Raphson iteration is terminated once a specified accuracy in the solution is reached, and a sufficiently low tolerance level must be chosen to guarantee long-time conservation of lepton number.

[6] Second-order accuracy can be proved by means of a Taylor series expansion, but this involves lengthy calculations that are omitted here.

The rationale for this seemingly complicated procedure for determining the weighting factor can be illustrated as follows: First, we specialize to the case of a logarithmic grid as used in VERTEX [7], so that Eqs. (3.54) and (3.55) simplify to,

$$\begin{aligned} F_i^L &= w_i \varepsilon_{i+1/2} J_i^{n+1} \xi_i && (3.57) \\ F_i^R &= w_i \varepsilon_{i-1/2} J_i^{n+1} (1-\xi_i) \,. && (3.58) \end{aligned}$$

In regions where J_i varies mildly with i, ξ is close to 1/2, and hence the total interface flux is approximately given by the arithmetic mean of the flux in the adjacent cells,

$$F_{i+1/2} = F_i^L + F_{i+1}^R \approx \frac{w_i J_i^{n+1} + w_{i+1} J_{i+1}^{n+1}}{2}. \qquad (3.59)$$

On the other hand, in the high-energy tail of the spectrum J_i drops rapidly with increasing i, i.e. $J_{i+1} \ll J_i$. Assuming that the spectrum can be approximated by a Fermi-Dirac distribution (with a small chemical potential in the sense that $\mu \ll \varepsilon_i$), J_i is given in terms of the inverse temperature β and a normalization factor k as,

$$J_i \approx k e^{-\beta \varepsilon_i} \varepsilon_i^3, \qquad (3.60)$$

and the weighting factor is approximately,

$$\xi \approx e^{-\beta \Delta \varepsilon_i} \ll 1. \qquad (3.61)$$

In this case the flux components read,

$$\begin{aligned} F_i^L &= w_i \varepsilon_{i+1/2} k e^{-\beta(\varepsilon_i + \alpha \Delta \varepsilon_i)} \varepsilon_i^3, && (3.62) \\ F_i^R &= w_i \varepsilon_{i-1/2} k e^{-\beta \varepsilon_i} \varepsilon_i^3. && (3.63) \end{aligned}$$

Bearing in mind that ε^3 varies far more slowly than $e^{-\beta\varepsilon}$ in the steep tail of the spectrum, we obtain

$$F_i^L \approx w_i \varepsilon_{i+1/2} k J_{i+1/2}, \quad \left|F_i^R\right| \approx \left|w_i \varepsilon_{i-1/2} k J_i\right| \ll \left|F_{i-1}^L\right|, \quad F_{i+1/2} \approx F_i^L \qquad (3.64)$$

for $\alpha = 1/2$, while for $\alpha = 1$ we have,

$$F_i^L \approx w_i \varepsilon_{i+1/2} k J_{i+1}, \quad F_i^R \approx w_i \varepsilon_{i-1/2} k J_i \quad F_{i+1/2} \approx (w_i + w_{i+1}) \varepsilon_{i+1/2} k J_{i+1}. \quad (3.65)$$

Thus, in the case of $\alpha = 1/2$, the effective interface value of J appearing in the fluxes is given by the weighted *geometric* mean of J in the adjacent zones; for $\alpha = 1$ it is twice the minimum value in either zone, which corresponds more closely (but not exactly) to the weighted *harmonic* mean. Since $\alpha = 1$ generally reduces the absolute values of the fluxes, the resulting scheme is somewhat more robust than for $\alpha = 1/2$, i.e. the Newton-Raphson iteration fails to convergence less frequently.

---

[7] More precisely, the zone interfaces and centres are chosen as follows: $\varepsilon_{i+1/2} = \Delta\varepsilon_0 \lambda^i$ (for $i \in \{1, \ldots, N\}$), $\varepsilon_{-1/2} = 0$, and $\varepsilon_i = \frac{1}{2}\left(\varepsilon_{i-1/2} + \varepsilon_{i+1/2}\right)$. Here, N is the number of energy zones, $\Delta\varepsilon_0$ is the width of the first zone, and $\lambda > 1$ is an adjustable parameter.

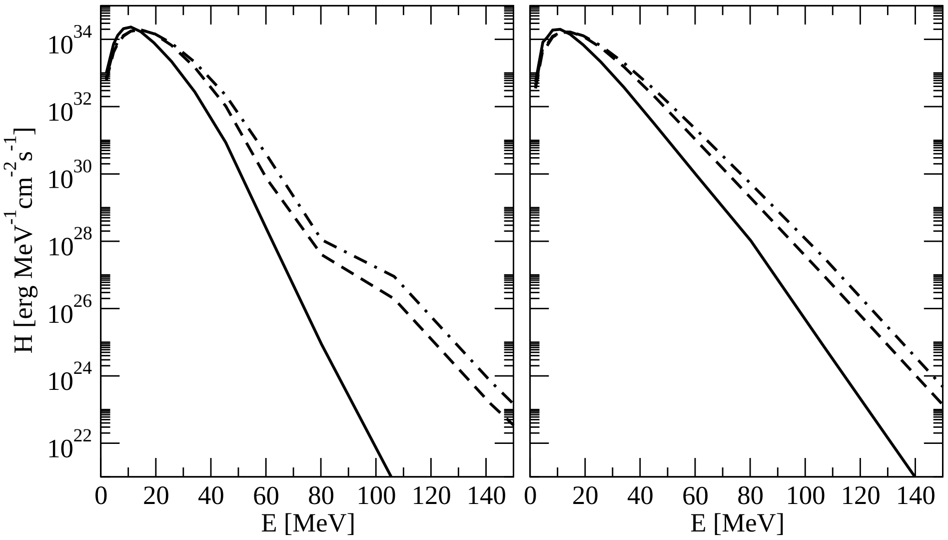

Figure 3.5.: Spectral energy flux of electron neutrino (solid), electron anti-neutrinos (dashed) and μ/τ (dash-dotted) neutrinos from the simulation of a cooling neutron star with PROMETHEUS-VERTEX. All quantities are measured at $r = 400$ km in the comoving frame. The left panel shows spectra from 1 s after bounce, obtained with the Doppler treatment of Rampp and Janka [151]. The spectra in the right panel (from $t_{\mathrm{pb}} = 1.5$ s were obtained with our new conservative Doppler scheme using "harmonic" ($\alpha = 1/2$) interpolation. Aside from some secular changes of the electron neutrino spectrum, the main difference if the elimination of the dip in the $\bar{\nu}_e$- and ν_μ/ν_τ spectra at the neutrino energy $E \approx 80$ MeV.

"Harmonic" interpolation with $\alpha = 1$ has another welcome side effect in addition to the improved robustness of the scheme: The method of geometric interpolation (also in the original scheme of Rampp and Janka [151]) suffers from a mild "kink" instability, that may produce an unphysical dip in the neutrino spectra. In a long-time simulation of the neutron star cooling phase with PROMETHEUS-VERTEX, in which our new scheme was switched on about 1 s after bounce, we found that "harmonic" interpolation eliminates such a dip, as shown in Fig. 3.5. Because of the favourable stability properties and the smoother neutrino spectra, we preferably work with $\alpha = 1$, but $\alpha = 1/2$ is also a viable choice. The simulations conducted so far also indicate that the new scheme conserves lepton number about as accurately as the original treatment of Rampp and Janka [151][8]; even for time-steps as large as $\Delta = 3 \times 10^{-5}$ ms the relative change of the total lepton number per time step is no larger than a few 10^{-8}.

---

[8] Note that the extraordinary accuracy of 10^{-11} per time-step for lepton number conservation mentioned by Rampp and Janka [151] is typically only achieved during the initial phase of the collapse. In practice, the violation of lepton number conservation per time-step during the later phases of the evolution is higher also with the scheme of Rampp and Janka [151].

4. Code Tests in Spherical Symmetry

4.1. Simple test problems – Radiating spheres

Stationary solutions for the propagation of radiation from a central source into vacuum furnish one of the simplest kinds of test problems in radiation hydrodynamics. Although not overly challenging *per se*, they provide a useful consistency check for the numerical implementation of the relativistic neutrino moment equations. The principle underlying these tests may be illustrated by considering the neutrino energy equation Eq. (2.28) in flat space, assuming stationarity and specializing to the laboratory frame (where $v_r \equiv 0$),

$$\frac{1}{r^2}\frac{\partial\left(r^2 H_{\mathrm{eul}}\right)}{\partial r} = C^{(0)}. \tag{4.1}$$

Outside the central source (which may be chosen as a homogeneous isothermal sphere of radius R with vanishing scattering opacity and frequency-independent absorption opacity as a very simple case), the collision integral vanishes, and hence the lab frame luminosity remains constant,

$$L_{\mathrm{eul}} = 16\pi^2 H_{\mathrm{eul}} r^2 = \mathrm{const.} \tag{4.2}$$

Likewise, since no energy-exchanging reactions occur, and since all the Doppler terms in the moment equations vanish, the mean energy of the radiation is independent of the radius r in the vacuum region,

$$\langle\varepsilon\rangle_{\mathrm{eul}} = H/\mathcal{H} = \mathrm{const.} \tag{4.3}$$

The luminosity and mean energy as measured by moving observers can be constructed from the transformation properties of the radiation moments J, H, and K (see, e.g., Mihalas and Weibel Mihalas [124]). Since $J = H = K$ for $r \gg R$, we have

$$LW^2\left(1+v_r^2+2v_r\right) = L\frac{1+v_r}{1-v_r} = \mathrm{const.}, \quad \langle\varepsilon\rangle\, W\left(1+v_r\right) = \mathrm{const.}, \tag{4.4}$$

for the luminosity $L = 16\pi^2/cH$ and the mean energy $\langle\varepsilon\rangle$ in the frame of a moving observer. We have compared the numerical solution obtained with VERTEX-CoCoNuT to this analytical solution for the case of a radiating sphere with $R = 4$ km and an observer velocity field with a peak value of $v = -0.2c$ at $r = 150$ km,

$$v_r = \begin{cases} 0, & r < 135\ \mathrm{km} \\ -0.2c\,\frac{r-135\ \mathrm{km}}{15\ \mathrm{km}}, & 135\ \mathrm{km} \leq r < 150\ \mathrm{km} \\ -0.2c\left(\frac{150\ \mathrm{km}}{r}\right)^2, & 150\mathrm{km} \leq r \end{cases} \tag{4.5}$$

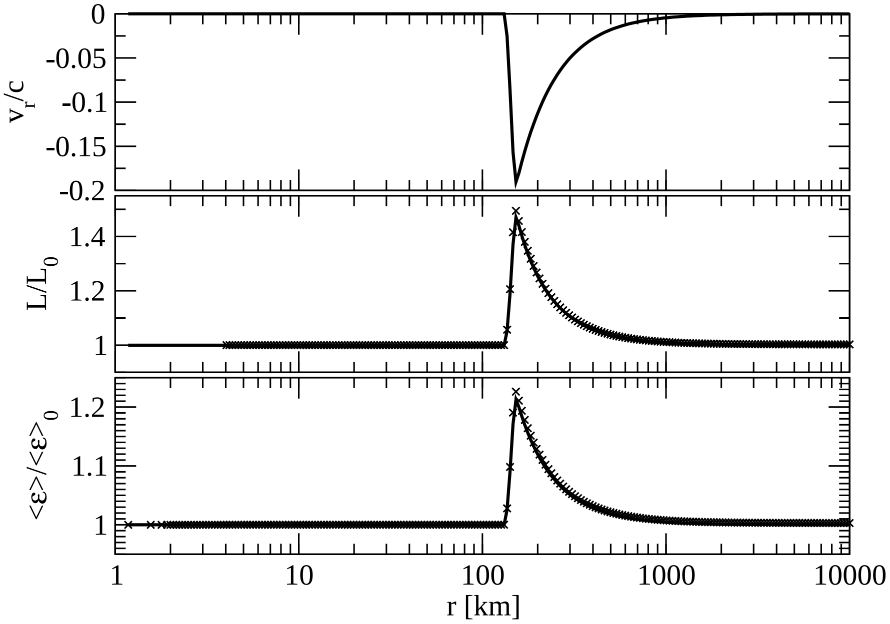

Figure 4.1.: Radial velocity, luminosity and mean energy (both in the moving observer frame) for test problem 1. Crosses indicate the results obtained with VERTEX-CoCoNuT, the analytic solutions are drawn as solid lines.

This setup ("test problem 1") mimics the velocity profile typically encountered in the accretion phase of core collapse supernovae with a strong shock discontinuity at radii of order ≈ 100 km. Fig. 4.1 shows that the numerical solution is in excellent agreement with Eq. (4.4), with a maximum deviation of less than 2%. Considering that the finite-difference representation of the moment equations has not been specifically tuned to reproduce the analytic result, and that the energy grid is rather coarse ($\Delta\varepsilon/\varepsilon \approx 0.28$), the accuracy achieved by VERTEX-CoCoNuT seems more than adequate, and indicates that the velocity-dependent terms in the moment equations have been correctly implemented.

The implementation of the gravitational redshift terms can be tested in a similar fashion: We now consider the propagation of radiation from an isothermal sphere in a curved spacetime, assuming that the metric is diagonal and isotropic, i.e. $\mathrm{d}s^2 = -\alpha^2 \mathrm{d}t^2 + \phi^4 \left(\mathrm{d}r^2 + r^2 \mathrm{d}\theta^2 + \sin^2\theta \mathrm{d}\phi^2\right)$. The frequency-integrated neutrino energy and number equations (obtained from Eqs. (2.28) and (2.29) after setting $\beta_r \equiv v_r \equiv 0$ and $W \equiv 1$) can then be solved directly in the vacuum region,

$$\alpha\phi^4 \mathcal{H} r^2 = \text{const.}, \quad \alpha^2\phi^4 H r^2 = \text{const.}, \quad \alpha \langle\varepsilon\rangle = \text{const.} \tag{4.6}$$

To test our numerical scheme, we have chosen a lapse function $\alpha(r)$ from a pseudo-relativistic core collapse simulation with VERTEX-PROMETHEUS (with a minimum value of $\alpha(0) \approx 0.72$), thus mimicking a potential well of similar strength as in real applications. For convenience, the conformal factor ϕ is set to $\phi = \sqrt{\alpha^{-1}}$ as in the weak-field limit. Again, the luminosity and mean energy are in very good agreement with the analytic results for this test case ("test problem 2"), as shown in Fig. 4.2. The redshift-corrected luminosity[1] $L = \alpha \left(16\pi\alpha\phi^4 H r^2\right)$, which should be constant outside the radiating sphere for our specific choice for α and ϕ, is in fact constant to within 0.02%.

Test problem 1 and 2 can be easily combined to serve as more stringent check for the implementation of the moment equations (as more and more non-vanishing terms enter), if we consider non-Eulerian observers in a curved spacetime. The redshift-corrected luminosity and mean energy as measured by an observer moving with a velocity v_r then obey the following simple equations,

$$\alpha\phi^4 \frac{1+v_r}{1-v_r} L = \text{const.}, \quad W\alpha \left(1+v_r\right) \langle\varepsilon\rangle = \text{const.}. \tag{4.7}$$

With the same choice for v_r, α, and ϕ as in test problem 1 and 2, VERTEX-CoCoNuT once more reproduces the analytic solution to very good accuracy (see Fig. 4.3).

4.2. Core collapse in spherical symmetry

While the performance of VERTEX-CoCoNuT for the simple test problems presented in the last section is reassuring, only a comparison with existing one-dimensional general relativistic neutrino transport codes can serve as a true shakedown test for future applications in "uncharted territory" (i.e. multi-dimensional GR neutrino transport). Fortunately, such codes are available [104–106, 201]; and a detailed comparison of the relativistic AGILE-BOLTZTRAN (AGILE for short) and the pseudo-relativistic PROMETHEUS-VERTEX code has already been carried out by Liebendörfer et al. [107] and Marek et al. [116]. Since Liebendörfer et al. [107] provides a useful framework for assessing the quality of a newly developed code, we have repeated their run G15 with VERTEX-CoCoNuT, and have compared our results to those obtained with AGILE. As the neutrino transport module in VERTEX-CoCoNuT is largely identical to that in PROMETHEUS-VERTEX (apart from the underlying moment equations), there is an additional payoff from this testing strategy: in a number of cases, the origin of the differences between the three codes can be pinpointed more accurately with a third code available. In total, our analysis encompasses four different simulations[2] of model G15 with AGILE, CoCoNuT, and PROMETHEUS (with two different choices for the gravitational potential).

---

[1] The uncorrected relativistic luminosity in a CFC spacetime, i.e. the energy passing through a sphere around the origin of radius r per unit coordinate time is just $16\pi\alpha\phi^4 H r^2$. If the spacetime is static, gravitational redshift corrections can be taken into account analytically by including another factor α.

[2] The data from the AGILE and PROMETHEUS-VERTEX (case R) runs have been taken from the online material provided in the electronic version of [107]. The PROMETHEUS-VERTEX (case A) run has been carried out using the latest version of that code.

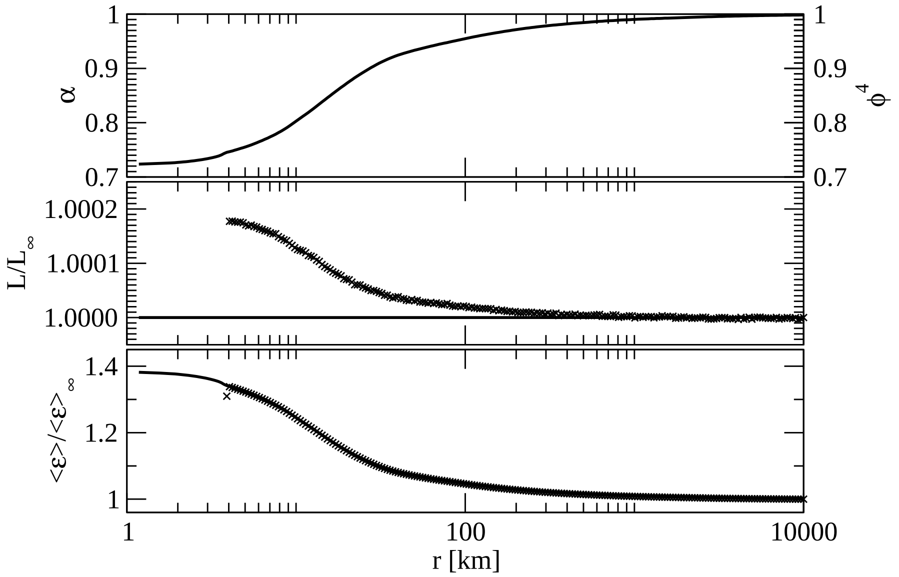

Figure 4.2.: Lapse function, luminosity and mean energy (both in the frame of an Eulerian observer) for test problem 2. Crosses indicate the results obtained with VERTEX-CoCoNuT, the analytic solutions are drawn as solid lines.

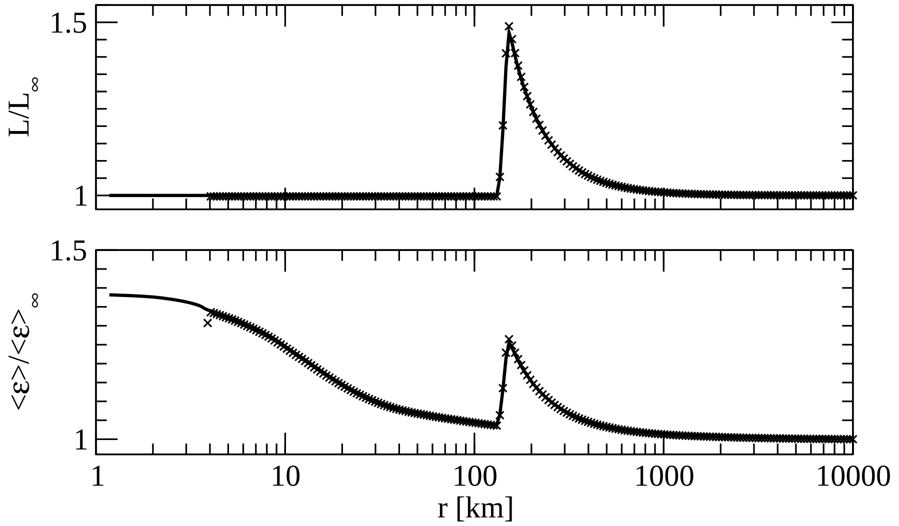

Figure 4.3.: Luminosity and mean energy (both in the moving observer frame) for test problem 3. Crosses indicate the results obtained with VERTEX-CoCoNuT, the analytic solutions are drawn as solid lines.

Following Liebendörfer et al. [107] as closely as possible, we launch our simulation from the $15M_\odot$ progenitor s15s7b2 of Woosley and Weaver [195], and use the same set of neutrino interactions rates[3]. Our treatment of the EoS differs slightly from both AGILE and PROMETHEUS-VERTEX for this test run: While using the EoS of Lattimer and Swesty [100] above a threshold density of 6×10^7 g cm^{-3}, nuclear burning is switched off below 3×10^7 g cm^{-3} (as in AGILE), and the composition of the progenitor is advected with the fluid (different from AGILE, which considers only one nucleus, ^{28}Si, in that regime). Between those transition densities, the composition is taken from a 17-species NSE table[4]. An Eulerian grid was used both for the hydrodynamics and the neutrino transport (400 and 234 zones, respectively), and the same energy resolution as in PROMETHEUS-VERTEX (17 zones) was chosen.

Although the microphysical input is almost identical in all three codes, it is crucial to bear in mind that they differ considerably from each other in their approach to neutrino radiation hydrodynamics before proceeding with a comparison of their results: AGILE solves the relativistic Boltzmann equations directly by means of a discrete-angle (S_N) method, and relies on an artificial viscosity scheme with an adaptive (moving) grid for the hydrodynamics. PROMETHEUS-VERTEX employs a variable Eddington factor technique for the neutrino transport and the PPM method for solving the equations of hydrodynamics; it uses a number of approximations to incorporate general relativistic effects, while remaining essentially a Newtonian code. The key element of its GR treatment is a modification of the Newtonian gravitational potential that leads to the same hydrostatic stellar structure equation (TOV equation) as in general relativity (PROMETHEUS-VERTEX "case R") or to a sightly modified TOV equation that improves the agreement with the relativistic case[5] ("case A"). VERTEX-CoCoNuT, while based on the same approach as PROMETHEUS-VERTEX, accounts for general relativistic effects exactly in spherical symmetry (apart from the computation of the Eddington factors). However, the PPM scheme in CoCoNuT is somewhat less accurate than that in PROMETHEUS due to the use of an approximate Riemann solver (only HLLE for this run). Moreover, the two relativistic codes CoCoNuT and AGILE differ in their choice of gauge and slicing conditions: ambiguities arising from this fact must be handled carefully.

While the conversion from the isotropic radial coordinate r_iso used in CoCoNuT to the areal (circumferential) radius r used by Liebendörfer et al. [107] is straightforward ($r = \phi^2 r_\mathrm{iso}$), the identification of time slices for the comparison of radial profiles of density, luminosity, etc. is non-trivial. In principle, a complete reconstruction of the entire spacetime would be necessary to allow for a rigorous comparison of the code output. Since the data provided in Liebendörfer et al. [107] is insufficient for such a reconstruction, we are forced to identify time slices by the elapsed coordinate time t (i.e. proper time for a non-moving observer at infinity). This is actually less critical than it

---

[3] The details of the implementation differ, however: In particular, both VERTEX codes simplify the physics in the μ/τ-neutrino sector by not treating neutrinos and anti-neutrinos separately.

[4] This procedure has been adopted to ensure that material in grids cells passing from the high-density to the low-density regime has a physically reasonable composition

[5] For a heuristic motivation of the modifications in Case A, see Marek et al. [117].

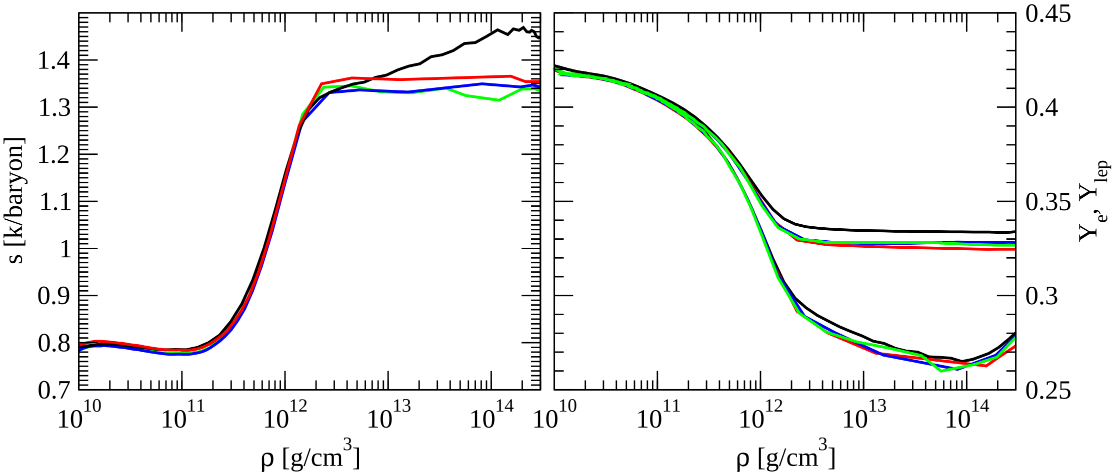

Figure 4.4.: Comparison of the entropy per baryon s (left panel), the electron fraction Y_e, and the lepton fraction Y_{lep} during collapse in AGILE-BOLTZTRAN (black), VERTEX-CoCoNuT (green), and VERTEX-PROMETHEUS (red and blue for the effective potentials R and A) 3 ms after bounce. A somewhat lower central electron and lepton fraction compared to AGILE is seen for the VERTEX codes. After trapping, the central entropy is conserved to good accuracy in VERTEX-CoCoNuT.

might appear if we synchronize the different codes at bounce and use the post-bounce time t_{pb} as time coordinate, because the system soon settles down to a quasi-stationary state for which the slicing conditions in AGILE and CoCoNuT are identical to very good approximation. However, even during collapse, the time slices in CoCoNuT and AGILE remain in sync quite well despite the different form of the metric equations; the elapsed coordinate time at bounce differs only by 5 ms. This would suggest that the spacetime slicings in both codes are rather similar, and that they remain synchronized also after the bounce. Backed by these findings, we can undertake a detailed comparison of the simulations in CoCoNuT and AGILE (and, of course, also in PROMETHEUS) during the collapse, bounce, and post-bounce phase.

Relativistic effects are of minor importance until the late stages of collapse when the density reaches several 10^{13} g cm^{-3}; only then do the infall velocity v and the compactness parameter M/R of the iron core reach values of the order of 0.1 (in relativistic units). Consequently, the three codes are in excellent agreement during most of the collapse phase. Slight differences in the evolution of the central electron and lepton fraction around trapping (i.e. at a density of a few 10^{12} g cm^{-3}) can be discerned in Fig. 4.4. Since the VERTEX-based codes consistently produce somewhat lower values, it is likely that this difference stems from small differences in the treatment of the neutrino interaction rates. It should be noted that the new VERTEX-CoCoNuT code conserves the central lepton fraction and entropy to very good accuracy, thus passing another important test.

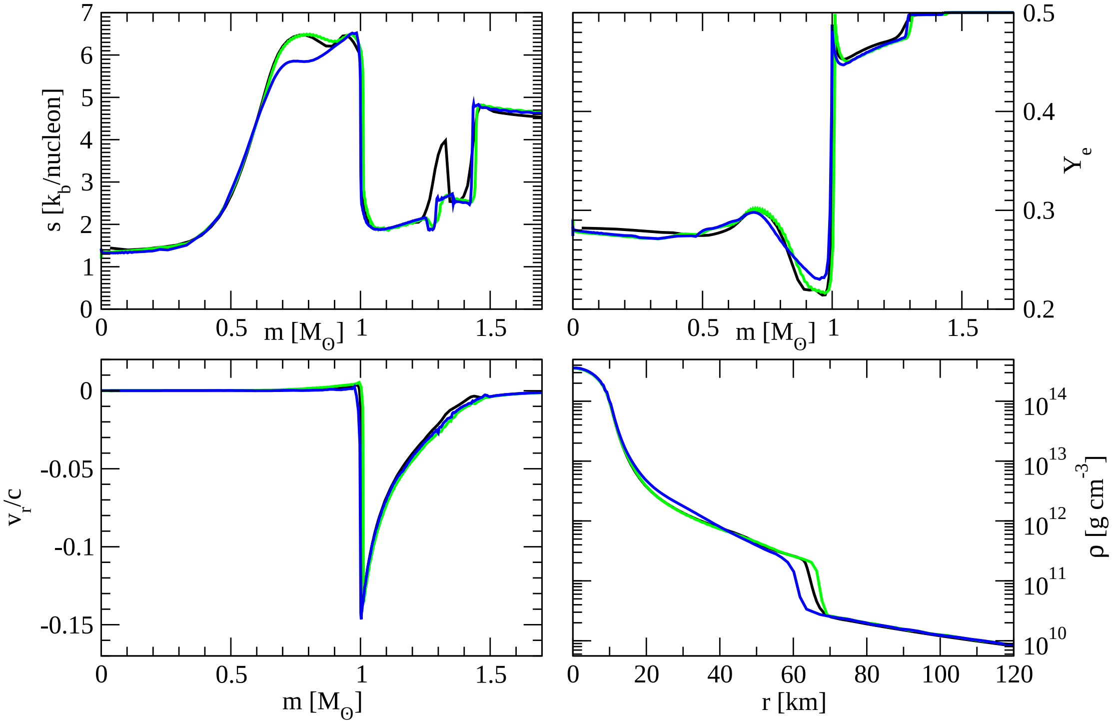

Figure 4.5.: Profiles of the specific entropy s (upper left), the electron fraction Y_e (upper right), the radial velocity v_r (bottom left), and the density ρ (bottom right) for model G15, obtained with different neutrino transport codes: AGILE-BOLTZTRAN (black), VERTEX-CoCoNuT (green), and VERTEX-PROMETHEUS (case A) (blue). For the sake of clarity, case R is not shown; the profiles are very similar to case A.

The good agreement between the different codes persists until shock formation (defined as the instant when the specific entropy inside the sonic point first reaches $3k_b$/nucleon), which occurs at an enclosed mass of $0.53M_\odot$ in AGILE, CoCoNuT and PROMETHEUS (case A), and at a slightly smaller mass of $0.49M_\odot$ in PROMETHEUS (case R). Interestingly, important special relativistic effects can be seen shortly after bounce (Fig. 4.5): Within 3 ms the shock has propagated to the mass shell $m \approx 1.0M_\odot$. The velocity profile for the best effective potential (case A) of Marek et al. [116] still matches the profiles from AGILE and CoCoNuT perfectly, but the entropy profile left behind by the shock differs appreciably. As long as the shock travels through an optically thick medium (to neutrinos), the post-shock entropy is higher by up to $0.5k_B$ in the relativistic case (AGILE, CoCoNuT), indicating that the shock is initially stronger. The post-shock velocity and the velocity jump across the shock indeed remain larger in CoCoNuT than in PROMETHEUS out until $m \approx 0.9M_\odot$ – velocity profiles from AGILE during the relevant phase are not available from Liebendörfer et al. [107], unfortunately.

On the other hand, the compression (i.e. the ratio of the post- and pre-shock densities

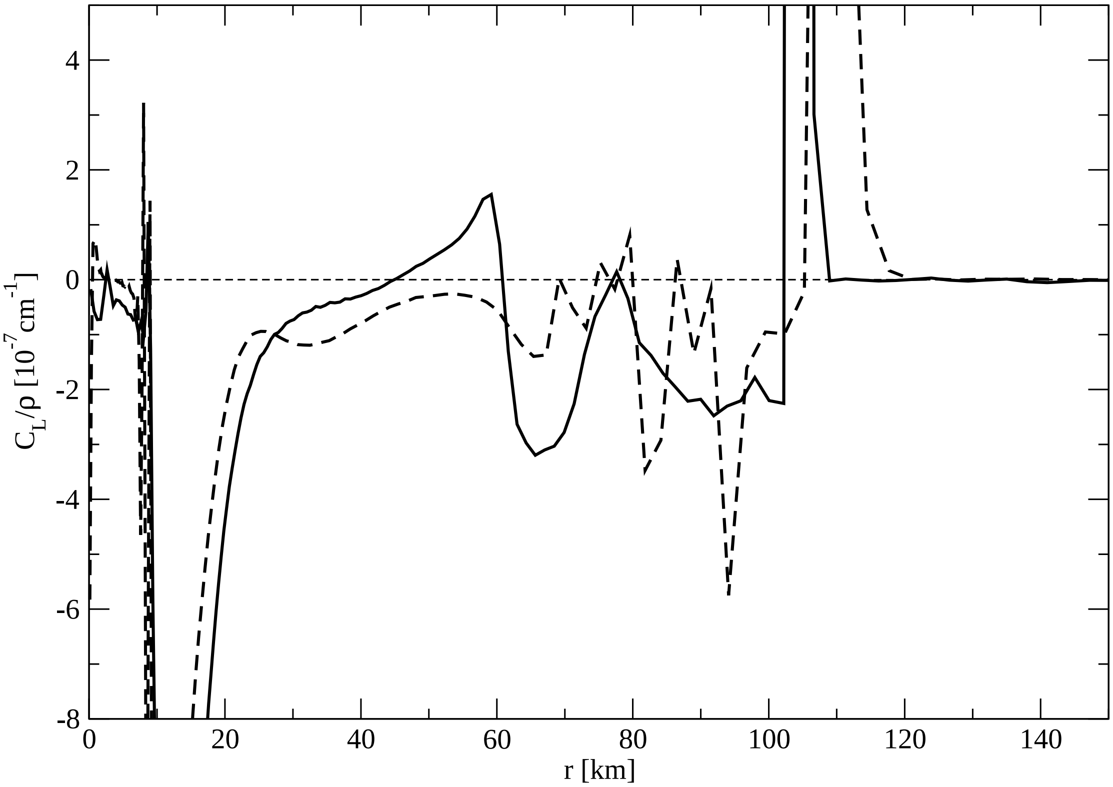

Figure 4.6.: Ledoux criterion 20 ms after bounce for the relativistic VERTEX-CoCoNuT run (solid) and for the pseudo-relativistic VERTEX-PROMETHEUS (case A) run (dashed). For convenience, C_L is scaled to the local baryonic mass density ρ. The region between $r = 45$ km and $r = 60$ km is convectively unstable in the CoCoNuT run, while no extended unstable region is present in the PROMETHEUS run.

ρ_s and ρ_p) is higher in strong relativistic shocks than in the Newtonian case[6] [84]. Combined with the initially higher entropy production in the shock, this leads to stronger neutrino emission as soon as the shock moves into semi-transparent layers at lower densities, which accounts for the lower electron fraction around $m = 0.9 M_\odot$, and also explains why the second hump in the entropy profile between $0.9 M_\odot$ and $1.0 M_\odot$ is less pronounced in AGILE and CoCoNuT[7]. The effects of relativistic shock propagation are also visible in the density stratification between the proto-neutron star and the shock, which is more shallow in the region outside $r \approx 25$ km ($m \approx 0.7$). Such small differences may seem unimportant in the case of a spherically symmetric problems – in

---

[6] In Newtonian hydrodynamics, the maximal compression for a given adiabatic index γ is $\rho_\mathrm{s}/\rho_\mathrm{p} = (\gamma+1)/(\gamma-1)$.

[7] Contrary to the statement in Liebendörfer et al. [107], the lower electron fraction cannot be explained by the fact that the deleptonization during shock breakout occurs at an earlier instant in AGILE than in PROMETHEUS, since the lower electron fraction around $m = 0.9 M_\odot$ persists for quite some time.

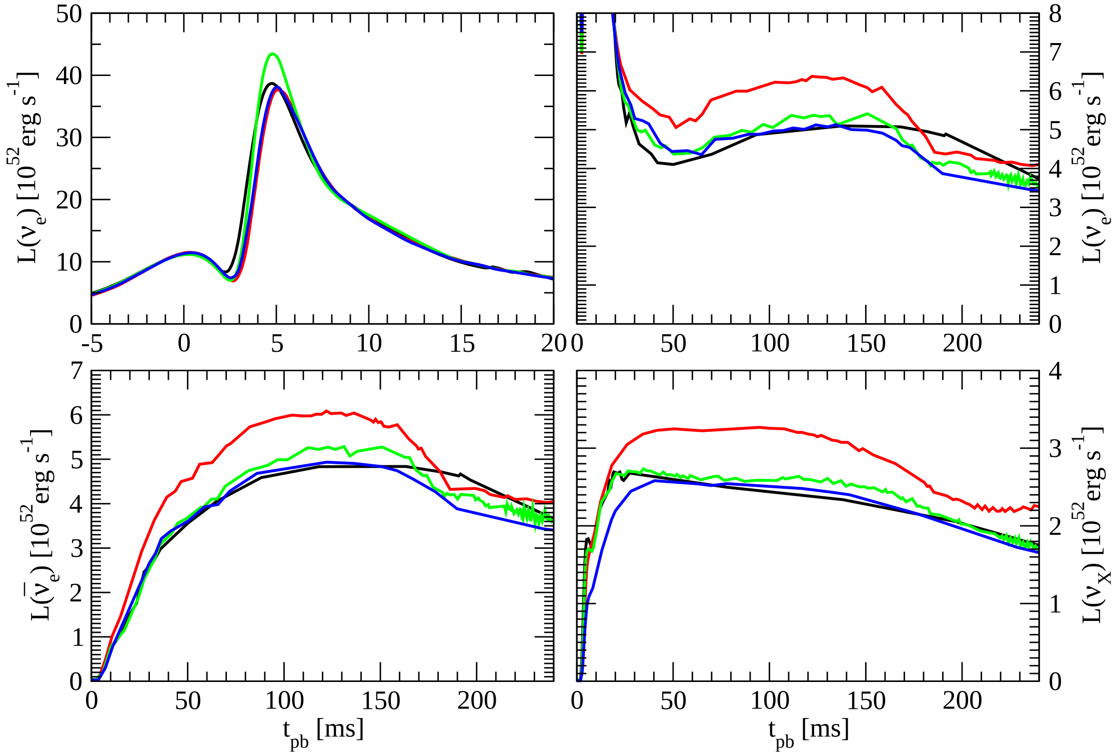

Figure 4.7.: Neutrino luminosities for model G15 obtained with AGILE-BOLTZTRAN (black), VERTEX-CoCoNuT (green), and VERTEX-PROMETHEUS (red and blue for the effective potentials R and A) as measured by an observer at $r = 500$ km in the comoving frame. Electron neutrino luminosities are shown in the upper panels, electron anti-neutrino and μ/τ neutrino luminosities in the left and right lower panel.

particular when they are washed out after a few tens of ms – but they can be crucial in multi-dimensional simulations, where they can affect the growth of hydrodynamic instabilities. Our 1D simulations already give a strong indication that this is indeed the case: Convective instability is expected if the Schwarzschild-Ledoux criterion C_L cp. [163], which is given in terms of the density ρ, the pressure P, and the specific internal energy density ϵ by

$$C_L = \frac{\partial \rho\,(1+\epsilon)}{\partial r} - \frac{1}{c_s^2}\frac{\partial P}{\partial r}, \tag{4.8}$$

in the relativistic case [180], or

$$C_L = \frac{\partial \rho}{\partial r} - \frac{1}{c_s^2}\frac{\partial P}{\partial r}, \tag{4.9}$$

in Newtonian hydrodynamics, is positive[8]. Fig. 4.6 reveals a convectively unstable layer at $r \approx 50$ km with a thickness of more than 10 km at a time of 20 ms after bounce in

---

[8] Note that the Schwarzschild-Ledoux criterion reduces to the simple Schwarzschild criterion $C_S =$

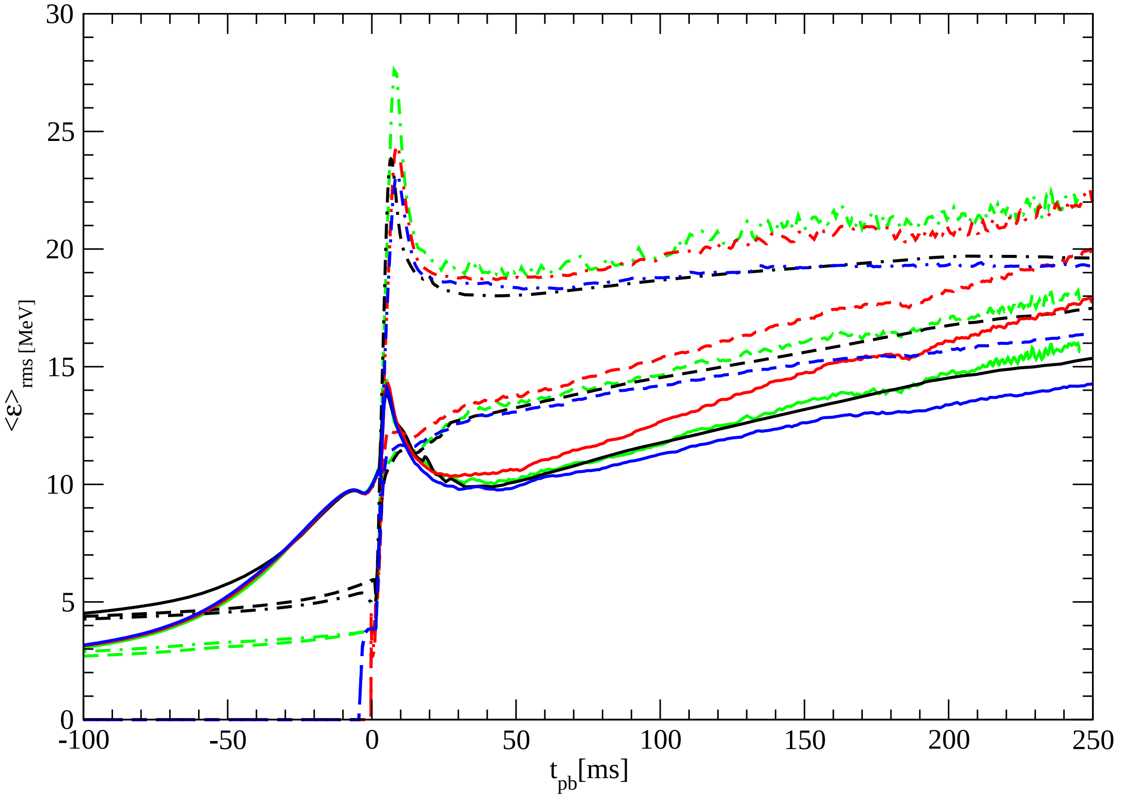

Figure 4.8.: Neutrino rms energies for model G15 obtained with AGILE-BOLTZTRAN (black), VERTEX-CoCoNuT (green), and VERTEX-PROMETHEUS (red and blue for the effective potentials R and A), sampled at $r = 500$ km in the comoving frame. Electron neutrino, electron anti-neutrino, and μ/τ neutrino luminosities are shown as solid, dashed, and dotted lines, respectively.

the CoCoNuT run, which is not present in the VERTEX run. Since the underlying effect should always produce a more shallow density stratification in the region of the Y_e-trough, prompt post-shock convection can thus be expected to develop more easily in truly relativistic simulations, regardless of the progenitor structure and the microphysical input (see Chapter 6 for further discussion).

The stronger deleptonization in the region around $m = 0.9 M_\odot$ also leads to a visibly different evolution of the electron neutrino luminosities during the neutronization burst (first panel of Fig. 4.7). Although the peak luminosity $L_\mathrm{burst} \approx 3.8 \times 10^{53}$ erg s^{-1} in PROMETHEUS (case A and R) agrees well with the one in AGILE, the radiated energy between $t_\mathrm{pb} = 1$ ms and $t_\mathrm{pb} = 8$ ms is smaller by a around 10%. Conversely, the total

---

$\mathrm{d}s/\mathrm{d}r$ for a chemically homogeneous fluid. The alternative form $C_L = \mathrm{d}s/\mathrm{d}r\,(\partial\rho/\partial s)_{P,Y_\mathrm{lep}} + \mathrm{d}Y_\mathrm{lep}/\mathrm{d}r\,(\partial\rho/\partial Y_\mathrm{lep})_{s,P}$ [21] can *not* be applied in the relativistic case. However, the relativistic Ledoux criterion can be expressed in terms of the spatial derivative of s and Y_lep in the following manner, $C_L = \mathrm{d}s/\mathrm{d}r\,(\partial(\rho+\rho\epsilon)/\partial s)_{P,Y_\mathrm{lep}} + \mathrm{d}Y_\mathrm{lep}/\mathrm{d}r\,(\partial(\rho+\rho\epsilon)/\partial Y_\mathrm{lep})_{s,P}$.

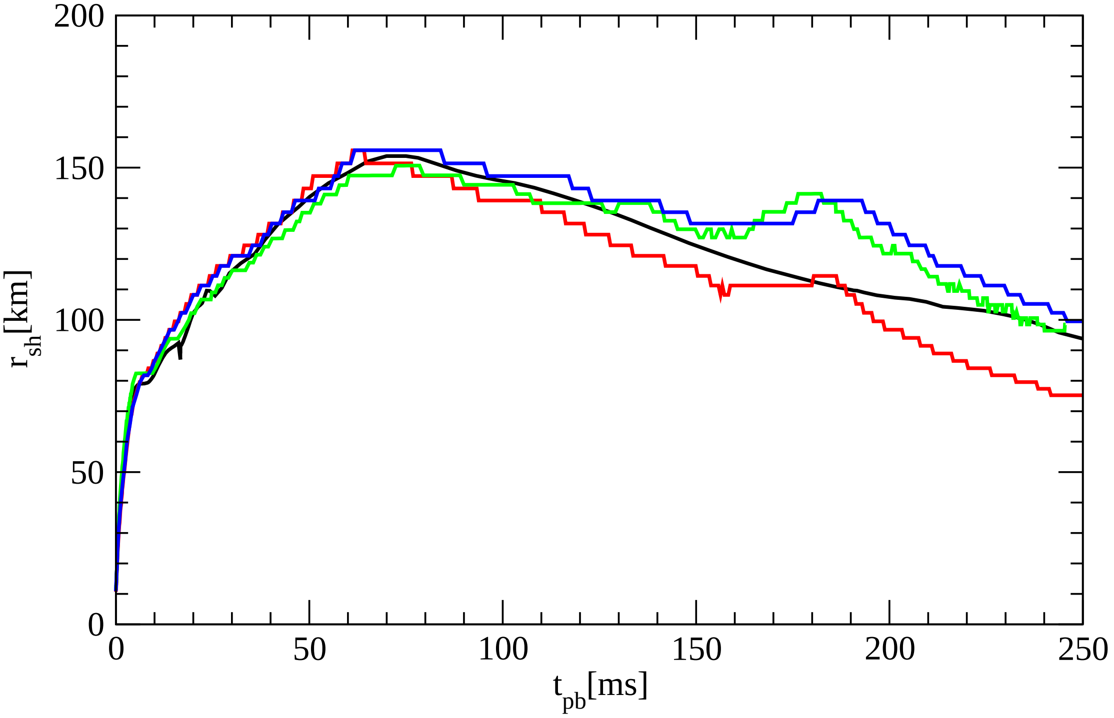

Figure 4.9.: Time evolution of the shock position for model G15 in AGILE-BOLTZTRAN (black), VERTEX-CoCoNuT (green), and VERTEX-PROMETHEUS with the effective potentials A and R (blue, red).

energy radiated in ν_e-s in CoCoNuT during the burst is in perfect agreement with AGILE despite the higher peak value of $L_{\mathrm{burst}} \approx 4.3 \times 10^{53}$ erg s^{-1}. The different shape of the burst in AGILE and CoCoNuT is probably due to the choice of the radial grid, or the different accuracy of the discretization scheme (first order vs. second order in space), which both influence the numerical diffusivity of the transport scheme and thus lead to a different degree of smearing during the propagation of the neutrino burst to the observer radius $r = 500$ km (cp. [106] for an analysis of the broadening of the burst). The treatment of the model Boltzmann equation in VERTEX-CoCoNuT may also be an important factor, either because of the approximations in the tangent ray-scheme (which may affect the transition from the optically thick to the optically thin regime) or because of the superior angular resolution of the tangent-ray scheme at large radii compared to the S_N-method used in AGILE, but these factors probably play a minor role.

The post-bounce evolution of the luminosity of all neutrino flavours (see also Fig. 4.7) is again very similar in CoCoNuT and AGILE. During the first 150 ms after bounce the luminosities in CoCoNuT tend to be slightly higher than in AGILE. The agreement is about as good as for PROMETHEUS (case A) and significantly better than for case R, where the strength of the gravitational potential and hence the accretion luminosity is

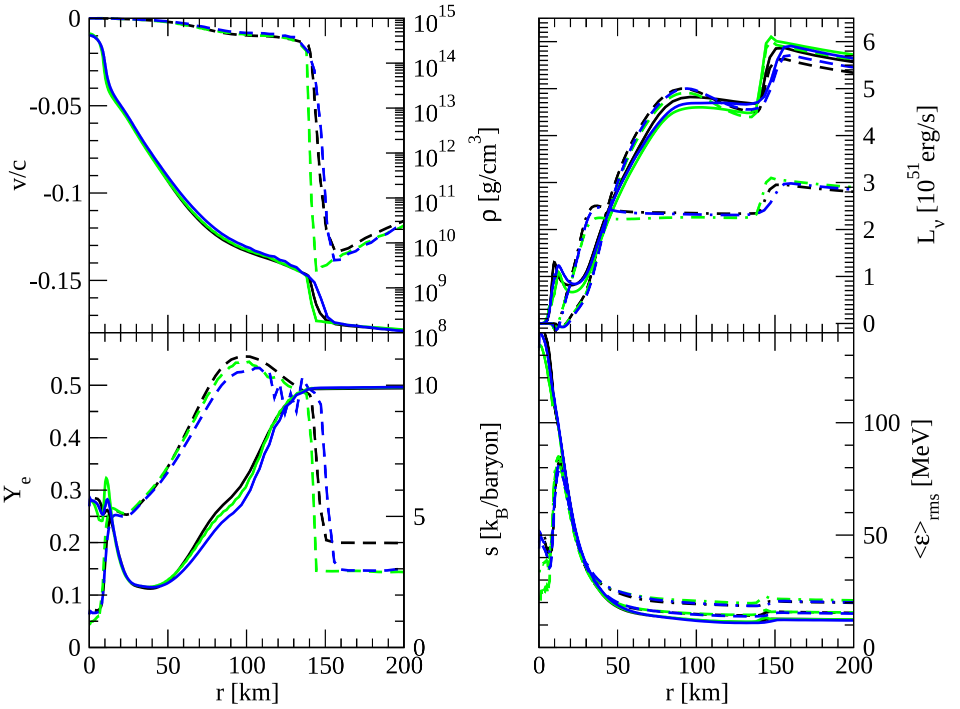

Figure 4.10.: Radial profiles of the velocity v (dashed lines), the density ρ (solid lines, upper left), the electron fraction Y_e (solid lines), the specific entropy s (dashed lines, bottom left), the neutrino luminosity (upper right), and the neutrino rms energy (bottom right) in AGILE-BOLTZTRAN (black), VERTEX-CoCoNuT (green), and VERTEX-PROMETHEUS with the effective potential A (blue) at a post-bounce time of 100 ms. Neutrino luminosities and energies are sampled at a circumferential radius of $r = 500$ km, and are given in the comoving frame; solid lines are used for electron neutrinos, dashed lines for electron anti-neutrinos, and dash-dotted lines for μ/τ neutrinos.

considerably overestimated. While PROMETHEUS (case A) is always very close to both CoCoNuT and AGILE, it is interesting to note that only the two last-named codes show a very abrupt transition from the fast rise in the ν_μ/ν_τ luminosity until $t_{pb} = 20$ ms to the subsequent plateau phase. The small differences between CoCoNuT and AGILE are well within the range expected for different codes (cp. the Newtonian run N13 in [107]) or even for one code at different resolutions (cp. [113]). As in PROMETHEUS, there is a noticeable drop in the luminosities of all flavours (ν_e and $\bar{\nu}_e$ in particular) between $t_{\mathrm{pb}} =$ 150 ms and $t_{\mathrm{pb}} = 200$ ms – i.e. at a time, when the shock reaches the oxygen-rich silicon shell – which is far less pronounced in AGILE due to the different treatment of the nuclear composition in the low-density regime and the possible superiority of the Riemann solver methods in PROMETHEUS and CoCoNuT in following the composition discontinuity at the Si-SiO-interface.

There is also good agreement between the three codes concerning the spectral prop-

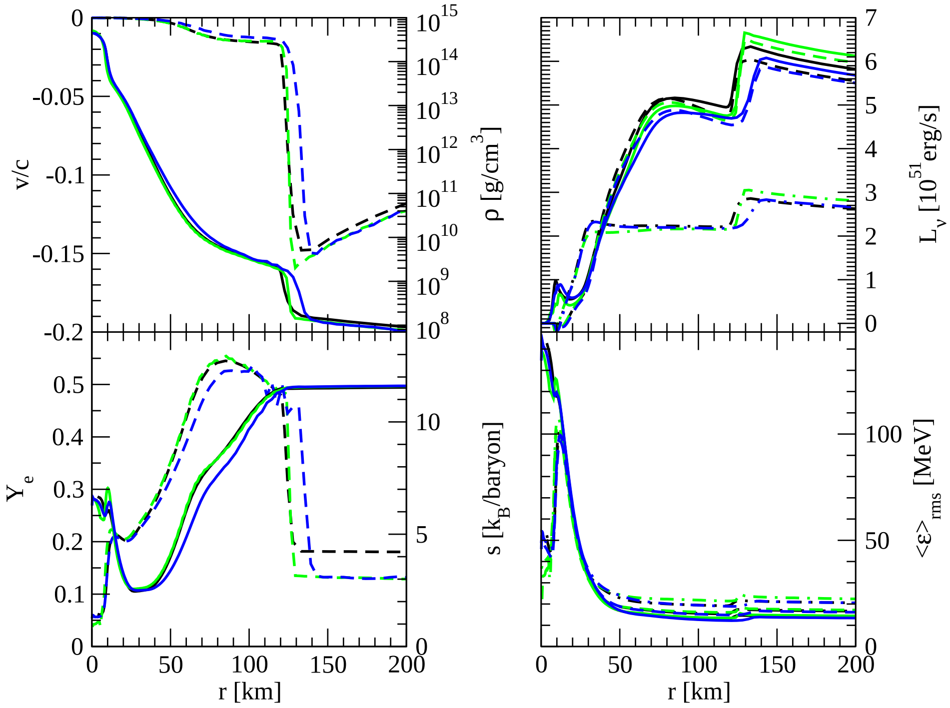

Figure 4.11.: Radial profiles of the velocity v (dashed lines), the density ρ (solid lines, upper left), the electron fraction Y_e (solid lines), the specific entropy s (dashed lines, bottom left), the neutrino luminosity (upper right), and the neutrino rms energy (bottom right) in AGILE-BOLTZTRAN (black), VERTEX-CoCoNuT (green), and VERTEX-PROMETHEUS with the effective potential A (blue) at a post-bounce time of 150 ms. Neutrino luminosities and energies are sampled at a circumferential radius of $r = 500$ km, and are given in the comoving frame; solid lines are used for electron neutrinos, dashed lines for electron anti-neutrinos, and dash-dotted lines for μ/τ neutrinos.

erties of the emitted neutrinos (Fig. 4.8). The root mean square (rms) energies of electron neutrino and anti-neutrinos as measured by an observer at $r = 500$ km (in the comoving frame) in CoCoNuT differ from those obtained with AGILE by 1 MeV at most. For electron neutrinos and anti-neutrinos the agreement is significantly better than in PROMETHEUS (case R and A), where the rms energies are either over- or underestimated. On the other hand, the μ and τ neutrinos are somewhat more energetic in CoCoNuT than in AGILE throughout the entire post-bounce evolution, whereas PROMETHEUS (case A) is very close to AGILE. Given the fact that the agreement in the electron neutrino sector is worse than for μ and τ neutrinos for case A, and that the luminosity of μ and τ neutrinos during the first 40 ms after bounce rises much more slowly than in AGILE, it is likely that the excellent matching of ν_μ/ν_τ rms energies between case A and AGILE is due to a cancellation of the error introduced by the approximate treatment of general relativity (leading to lower rms energies) and differences in the implementation of ν_μ/ν_τ interactions rates (leading to higher rms energies). We are therefore inclined to believe that the higher rms energy of μ and τ neutrinos in CoCoNuT is not indicative of a bug in our relativistic transport code.

Similar luminosities and spectral properties already suggest similar neutrino loss rates in the cooling zone and similar heating rates in the gain region, therefore the dynamical evolution of the proto-neutron star and the accretion shock in CoCoNuT and AGILE should not be very different either. Fig. 4.9 shows that this is indeed the case: Until $t_{\mathrm{pb}} = 150$ ms the accretion shock in CoCoNuT is very close to the one in AGILE; the radial deviation corresponds to only one or two grid zones. Interestingly, there is a brief transient period of shock stagnation at $t_{\mathrm{pb}} \approx 7$ ms (lasting a few ms) both in AGILE and CoCoNuT, which is absent, or at least much less pronounced in PROMETHEUS (cases A and R). It is conceivable that this feature is connected to the different relativistic and Newtonian form of the jump conditions, and to the slightly higher energy loss in electron neutrinos during the burst in the GR simulations. In all simulations, the maximum shock radius of $r_{\mathrm{max}} \approx 150$ km is reached at $t_{\mathrm{pb}} = 60\ \mathrm{ms} \ldots 80$ ms. Afterwards the shock position in CoCoNuT lies somewhere in between the two PROMETHEUS runs until $t_{\mathrm{pb}} \approx 150$ ms, and is a little closer to AGILE than either of them. The CoCoNuT and PROMETHEUS runs then show a transient phase of shock expansion when the infalling Si-SiO interface reaches the accretion front; this feature is absent in AGILE (as explained before) because of the different nuclear composition of low-density material. At later times ($t_{\mathrm{pb}} > 220$ ms), the shock in CoCoNuT again recedes to the same radius as the shock in AGILE. The overall shock trajectory in PROMETHEUS (case A) is very similar to the one in CoCoNuT (but not for case R), which indicates that the effects of general relativity can still be adequately captured by an effective gravitational potential in one-dimensional simulations.

The very close overall agreement between CoCoNuT, AGILE and PROMETHEUS (case A) and the even better agreement between CoCoNuT and AGILE is also evident in Figs. 4.10 and 4.11, which show radial profiles of selected physical quantities at 100 ms and 150 ms after bounce. There are only minute differences in the velocity profiles produced by the three codes; the shock front seems to be resolved a little more sharply in CoCoNuT, but this is probably incidental, since the sharpness of the jump changes slightly as the shock slowly moves from zone to zone. The density profile behind the shock is still slightly more shallow in AGILE and CoCoNuT than in PROMETHEUS (case A) outside $r \approx 70$ km, but the effects of genuinely relativistic shock propagation in the early post-bounce phase have been largely washed out. This can also be seen in the entropy profiles, which are very similar during this phase, except for the fact that PROMETHEUS (case A) seems to give slightly lower entropies in the gain region. Interestingly, we now find the deleptonization behind the shock to be somewhat more effective in PROMETHEUS (case A), contrary to the situation near shock breakout. The luminosity and neutrino rms energy profiles show some visible, but not worrisome differences between the three codes; e.g. the jump at the shock is generally a little larger in CoCoNuT than in AGILE, which is to be expected however, since there are small differences in the pre- and post-shock velocities. Considering that the three codes use different radial grids (and in the case of AGILE also a different grid in energy space), such small discrepancies seem unavoidable and are probably not to be ascribed to coding errors in any them.

Having thus analysed and compared the $G15$ runs with three different supernova codes, we may draw several important conclusions. First, VERTEX-CoCoNuT emerges as a reliable 1D neutrino transport code that gives results very similar to the relativistic AGILE-BOLTZTRAN code despite the disparity of methods used in both codes, and allows simulations of the post-bounce phase over several hundreds of ms. Second, there is also excellent agreement between the codes PROMETHEUS-VERTEX (case A) and VERTEX-CoCoNuT, which use identical neutrino physics and the same basic neutrino transport algorithm. This implies that the good performance of PROMETHEUS-VERTEX (case A) in comparison with genuinely relativistic codes is not the result of a fortunate cancellation of inaccuracies in the description of general relativistic effects. For simulations in spherical symmetry, the use of an effective relativistic potential in an otherwise Newtonian code may thus be completely adequate. Finally, there is evidence for the importance of general relativistic effects in *multi-dimensional* simulations, which require a more accurate GR treatment than hitherto available in neutrino transport simulations. Our findings indicate that post-shock convection may be facilitated in full GR as the result of a significantly different density stratification behind the accretion front at early times. There is a clear need to proceed to multi-dimensional simulations in VERTEX-CoCoNuT to address the consequences of this.

5. Applications I: Collapse of Rotating Iron Cores

As the tests of VERTEX-CoCoNuT in spherical symmetry have demonstrated the reliability of the new code, we can now proceed to multi-dimensional simulations. In this chapter, we focus on multi-dimensional effects during the collapse phase, which have been a major topic in astrophysical relativity since the 1960s, when it was recognized that the rotational (and hence *aspherical*) collapse and bounce of iron cores would be a promising source of gravitational waves [188, 190]. For a long time, this subject could only be approached by analytical approximations (e.g. [139, 155–157, 164, 181]). Although the first relativistic code for spherical collapse (without neutrino transport and extremely simplified microphysics) was already developed in the late 1960s by May and White [118], it took another 30 years before the first general relativistic simulations of rotational core collapse could be carried out [41, 42] using the CFC approximation [77, 193] for the spacetime, because the evolution of the Einstein field equations proved notoriously difficult. As an intermediate step, gravitational wave emission from rotational collapse was studied numerically in the Newtonian approximation [57, 127, 200, 206], and although many of the findings of these works had to be revised as relativistic simulations became available, they provided a useful framework for the classification of gravitational wave signals from the bounce: Zwerger and Müller [206] distinguished three different signal types: type I originates from the bounce of a core at supranuclear densities due to the stiffening of the equation of state ("regular bounce"), and exhibits a single dominant peak with negative amplitude, followed by "ring-down" oscillations. Type II originates from multiple bounces at subnuclear densities due to centrifugal braking (a scenario already suggested by Shapiro and Lightman [166]), and exhibits multiple negative amplitude peaks of similar magnitude. "Rapid regular bounces" at supranuclear densities give rise to type III signals, which are characterized by a positive amplitude peak and a strong suppression of the ring-down signal. These different signal types were also observed in relativistic simulations [42, 169], but centrifugally supported bounces were found to occur much more rarely than in Zwerger and Müller [206].

With the exception of Mönchmeyer et al. [127], rotational core collapse was studied using extremely simple equations of state, i.e. a polytropic EoS[1], or, at best, the "hybrid" equation of state of Janka et al. [83], and neutrino emission during the collapse was disregarded altogether. As a trade-off for the exact treatment of general relativ-

---

[1] For a polytropic equation of state, the pressure is given in terms of the density by a simple power law $P \propto \rho^\Gamma$, where Γ is the polytropic exponent

Model	Progenitor	Neutrino interactions	A [10^8 cm]	$\Omega_{\mathrm{c,i}}$ [rad s^{-1}]
G15a1o1	s15s7b2	simplified	50.0	0.45
G15a1o5	s15s7b2	simplified	50.0	1.01
G15a1o7	s15s7b2	simplified	50.0	1.43
G15a1o9	s15s7b2	simplified	50.0	1.91
G15a1o13	s15s7b2	simplified	50.0	2.71
G15a2o5	s15s7b2	simplified	1.0	2.40
G15a2o9	s15s7b2	simplified	1.0	4.56
s15a1o1	s15.0	full	50.0	0.45
s15a1o5	s15.0	full	50.0	1.01
s15a1o7	s15.0	full	50.0	1.43
s15a1o9	s15.0	full	50.0	1.91
s15a1o13	s15.0	full	50.0	2.71
s15a2o5	s15.0	full	1.0	2.40
s15a2o9	s15.0	full	1.0	4.56

Table 5.1.: Summary of rotating core collapse models. The table indicates the progenitor model, the set of neutrino interaction rates (simplified, or the full VERTEX set), the length scale A for differential rotation, and the initial angular velocity $\Omega_{\mathrm{c,i}}$ at the centre. For convenience, the model nomenclature follows Dimmelmeier et al. [46] closely; the tag aXoY used for encoding the parameter A of differential rotation and the initial angular velocity is taken over directly from their paper.

ity that had finally been achieved, the elaborate treatment of the equation of state the neutrino transport had been sacrificed. The situation changed somewhat in 2007, when Dimmelmeier et al. [44] and Ott et al. [143] presented the first relativistic core collapse simulations with a modern nuclear equation of state and a parameterized "deleptonization scheme" for neutrino emission suggested by Liebendörfer [103]. These authors found [44–46, 143, 144], that, as a consequence of deleptonization, the gravitational wave signal is exclusively of type I according to the classification of Mönchmeyer et al. [127] and Zwerger and Müller [206], and is associated with a single bounce. Type II signals, arising from multiple bounces of the core at sub-nuclear densities due to centrifugal forces, or type III signals from the bounce of a rapidly collapsing and rather small inner core were not seen at all. It has also been claimed that the GW spectra exhibit a robust spectral peak in the frequency region of 700 . . . 750Hz for a wide range of progenitor models and rotation rates, which could greatly facilitate the detection of GW signals from core-collapse events by means of frequency narrow-banding. Only for extremely rapidly rotating models that undergo a single centrifugal bounce at sub-nuclear densities (but still produce type I signals) this degeneracy is broken, and the signal frequencies are shifted downwards. There also seems to be a very strong and uniform correlation between the gravitational wave amplitude and the rotational state of the core at bounce

[46], a result which may prove a great asset for the analysis of future observations.

However, while this constitutes an important step towards unifying general relativistic hydrodynamics and sophisticated methods for neutrino transport, the Liebendörfer scheme [103] employed by these authors is by no means comparable to the elaborate multi-group methods now routinely used in Newtonian supernova simulations, and even depends on input from these. It assumes, based on the observations of Müller and Hillebrandt [129] and Liebendörfer [103] in spherically symmetric simulations with sophisticated neutrino transport, that the deleptonization of the core can be described in terms of a more or less universal parameterization of the electron fraction Y_e as a function of the density ρ. As we shall argue later, it is by no means clear whether this approximation is still valid for strongly rotating progenitor cores. Thus, it is doubtful whether the recent findings concerning gravitational wave emission from rotational collapse are to be taken as final conclusions, or whether a more accurate treatment of neutrino transport would change the picture.

With the new VERTEX-CoCoNuT code, we are, for the first time, in a position to model the general relativistic collapse of strongly rotating iron cores with an up-to-date neutrino transport scheme and thereby to check the results of [44–46, 143, 144]. In this chapter, we address not only the gravitational wave signals emanating from rotational collapse, but also attempt a critical evaluation of the approximate neutrino treatment of Liebendörfer [103] in the context of strong rotation.

5.1. Investigated models

In order to study the effects of rotation on the collapse of iron cores, we have carried out 14 axisymmetric simulations with VERTEX-CoCoNuT. Since multi-dimensional models of rotating progenitor stars are as yet unavailable (with the exception of white dwarfs undergoing accretion-induced collapse [203]), we start our simulations from the spherically symmetric progenitor models s15s7b2 of Woosley and Weaver [195] and s15.0 of Woosley et al. [196], on which we impose a specified rotation profile. Although there are already "1+1/2"-dimensional stellar evolution calculations that include rotation [70, 71], this method has the advantage of allowing for an arbitrary, exploratory variation of the initial rotation rate. It must be stressed that none of the initial models thus constructed is in rotational equilibrium (which is also true for the models in [70, 71]), and that the influence of rotation during the progenitor evolution is neglected.

The rotation profile of the initial models is specified by the central angular velocity $\Omega_{\mathrm{c,i}}$ and the length scale A of differential rotation according to the following rotation law[2],

$$\Omega_i = \Omega_{\mathrm{c,i}} \frac{A^2}{A^2 + r^2 \sin^2 \theta}. \tag{5.1}$$

This rotation law gives a nearly flat rotation profile for $r \sin\theta \lesssim A$, a quadratic fall-off with the distance $r \sin\theta$ to the rotation axis for $r \sin\theta \gg A$, and is in accordance with

---

[2] Note that the Newtonian formulation is adequate for the progenitor model. For the relativistic version, see, e.g., Komatsu et al. [93], and cp. [53].

the Rayleigh stability criterion for rotating fluids [178].

Both progenitor models have been simulated with seven different rotation profiles, with the central angular velocity ranging from 0.45 rad s^{-1} to 4.56 rad s^{-1}, and assuming either almost uniform rotation (the a1 series with $A = 5.0 \times 10^9$ cm) or considerable differential rotation (the a2 series with $A = 1.0 \times 10^8$ cm). All the initial models are summarized in Table 5.1. It should be noted that the G15 series based on the progenitor s15s7b2 has been simulated using the same reduced set of neutrino opacities as for model G15 in Chapter 4 to allow for a direct comparison, while the full set of neutrino opacities has been used for the s15 series. Since the emission of electron anti-neutrinos and μ/τ-neutrinos only becomes important in the post-bounce phase, we exclusively consider electron neutrinos in the rotational core collapse runs. The EoS of Lattimer and Swesty [100] has been used in all cases. We also note that the seven rotation profiles are a subset of those considered by Dimmelmeier et al. [46] for the progenitor s15.0, which greatly facilitates a comparison with that particular study. All models have been simulated on a spherical polar grid with 400 × 64 (radial × angular) zones covering 180°.

5.2. Collapse dynamics and shock formation

The gravitational wave signal from the bounce is intimately connected to the dynamics of the collapse, which determines the waveform type, the amplitude, and the dominant frequency by setting the properties (specifically, the mass and the rotational state) of the homologously collapsing inner core. Dimmelmeier et al. [44, 45, 46] showed that the dynamics of core collapse with deleptonization can be understood in terms of the theory of collapsing polytropes [65, 197, 198], and could provide a convincing explanation for the generic gravitational wave signals they found in their simulations. In order to assess the validity of their findings, we therefore briefly review their arguments, and thereby also provide a framework for the analysis of our own results.

Dimmelmeier et al. [44] attempted to interpret the effects of deleptonization in terms of a reduction of the "effective" adiabatic index γ_{eff} [44, 185] of the fluid,

$$\gamma_{\mathrm{eff}} = \gamma_{\mathrm{EoS}} + \frac{4}{3}\frac{1}{Y_e}\frac{\delta Y_e}{\delta \ln \rho} + \frac{1}{P}\frac{\delta P_\nu}{\delta \rho} + \Delta\gamma_{\mathrm{GR}}. \tag{5.2}$$

Here, $\delta/\delta\rho$ denotes the absolute derivative with respect to the density along the trajectory of a given mass element, and P_ν is the neutrino pressure in the optically thick regime. The effects of the stronger gravitational field in general relativity are approximately taken into account by including a correction term $\Delta\gamma_{\mathrm{GR}} \approx -0.015$. Taking an average γ_{EoS} of 1.32 in the dynamically relevant regime of densities ($10^{12} \ldots 10^{14}$ g cm^{-3}), Dimmelmeier et al. [44] obtained an effective adiabatic index of $\gamma_{\mathrm{eff}} \approx 1.29$. They were thus able to explain the absence of multiple centrifugal bounces (which they found to occur only for $\gamma_{\mathrm{eff}} \gtrsim 1.31$) as a consequence of deleptonization.

In order to facilitate a more intuitive physical understanding of the suppression of multiple bounces, it is instructive to reformulate the explanation of Dimmelmeier et al. [44] slightly by considering the mass of the inner core as the crucial quantity for the

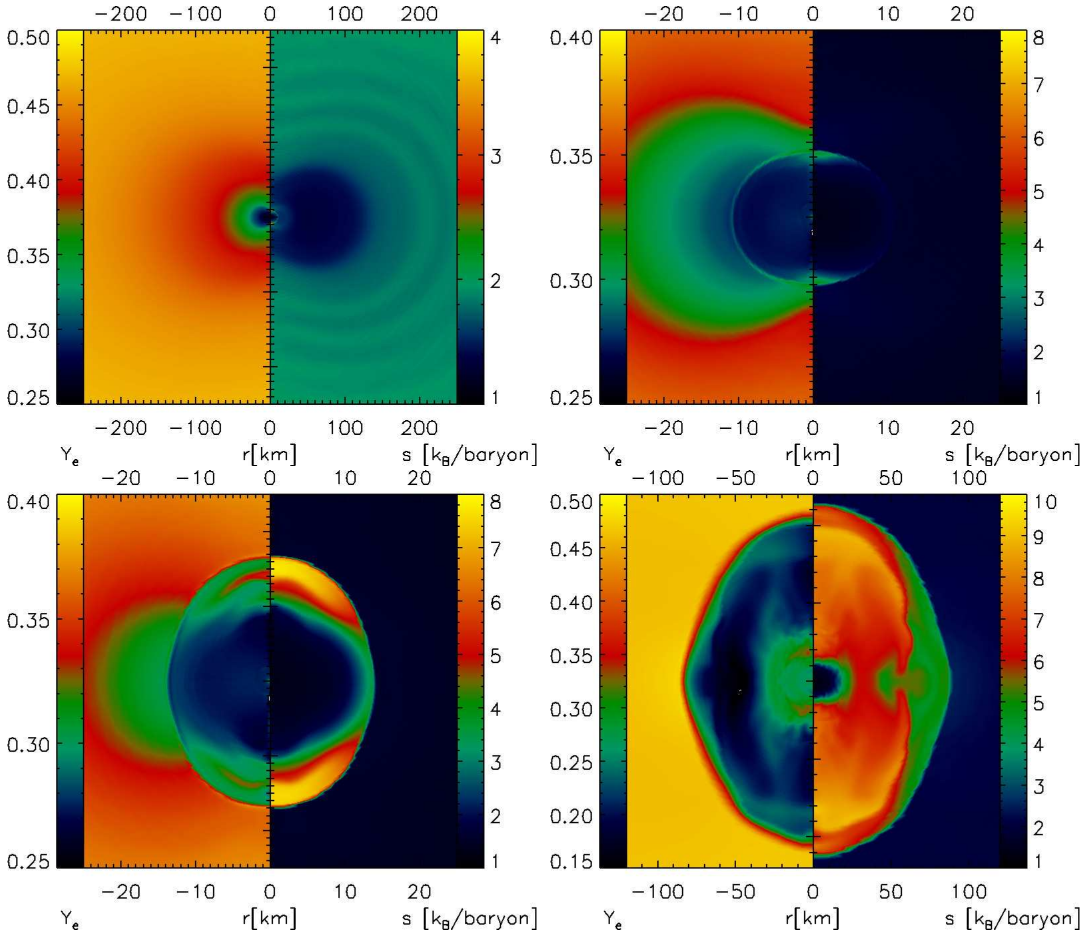

Figure 5.1.: Snapshots of the electron fraction Y_e (left half of panels) and the specific entropy s for model G15a2o9. The top panels show the situation 0.3 ms before bounce on different radial scales, the bottom left panel shows the moment of bounce, and the bottom left panel depicts the situation 5.5 ms after bounce. Note that we define the bounce as the moment when the post-shock entropy first exceeds $3k_b$/nucleon *in the equatorial plane.*

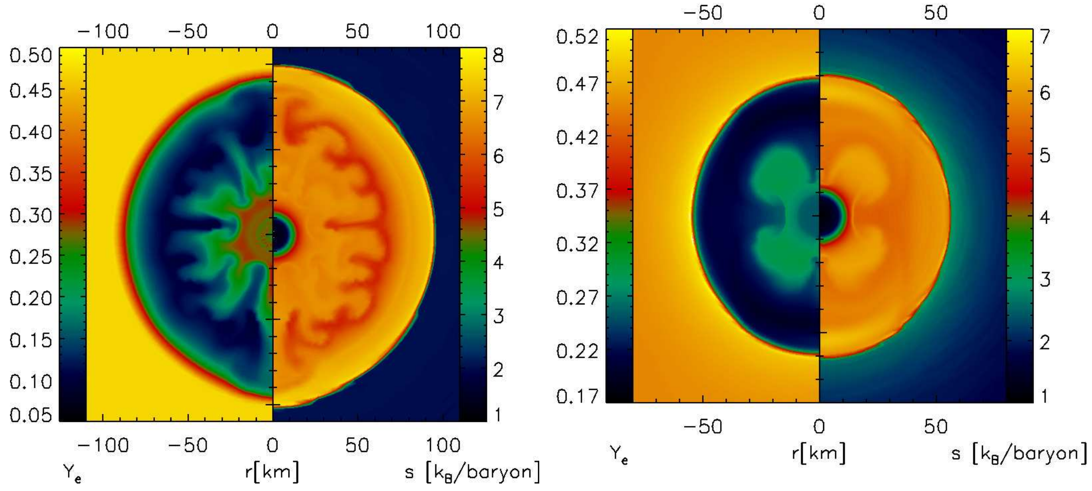

Figure 5.2.: Snapshots of the electron fraction Y_e (left half of panels) and the specific entropy s for model G15a1o1 (left panel) at $t_{\mathrm{pb}} = 14$ ms and for model s15a1o1 (right) panel at $t_{\mathrm{pb}} = 5$ ms. While a larger number of convective plumes develops in the post-shock region of model G15a1o1, model s15a1o1 shows only two large lobes and a broad downflow in the equatorial plane.

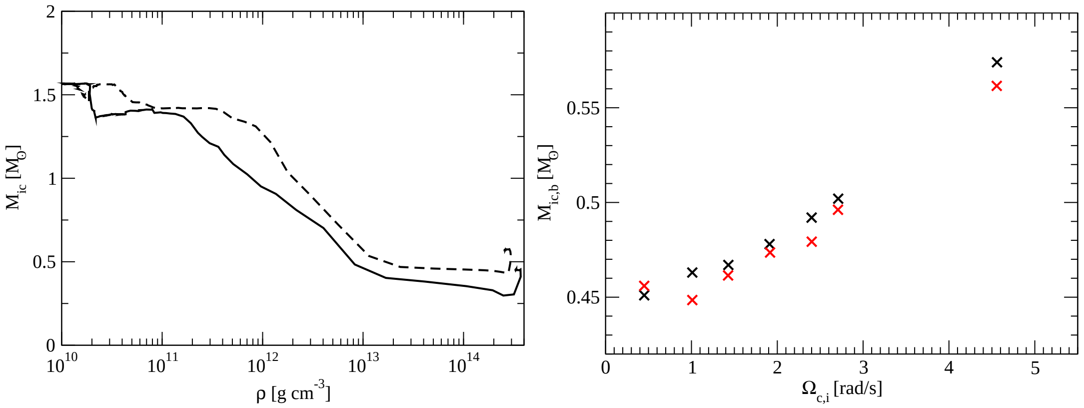

Figure 5.3.: Left panel: Mass M_{ic} of the homologously collapsing inner core as a function of the central density ρ_{c} during the collapse of models s15a1o1 (solid line) and s15a2o9 (dashed line). Right panel: Mass $M_{\mathrm{ic,b}}$ of the inner core at bounce as a function of the initial central angular velocity $\Omega_{\mathrm{c,i}}$ for the s15 series. Results obtained with neutrino transport are marked as black crosses, while the results obtained in Ref. [46] with the deleptonization scheme of [103] are shown as red crosses.

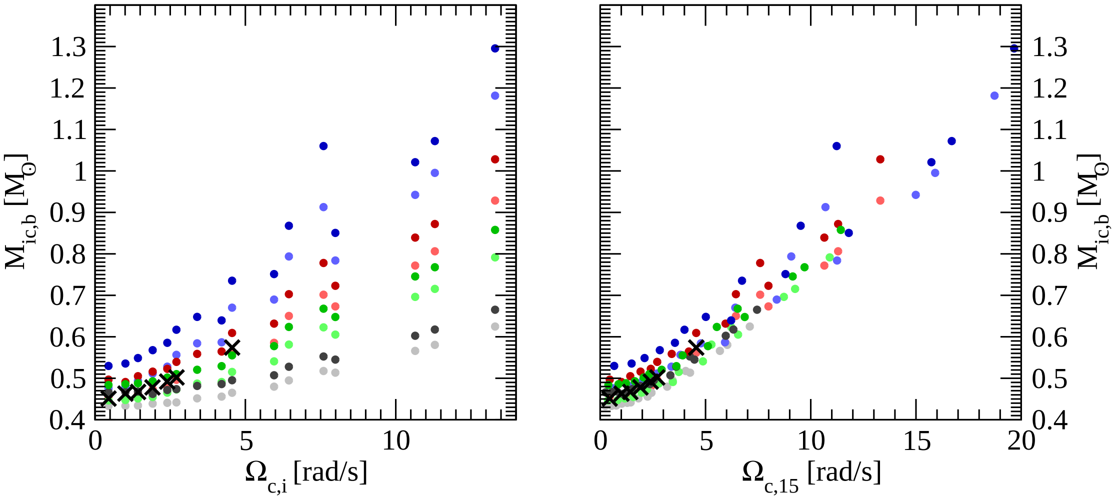

Figure 5.4.: Left panel: Mass $M_{\mathrm{ic,b}}$ of the inner core at bounce as a function of the central angular velocity $\Omega_{\mathrm{c,i}}$ of the initial model for different progenitors (s11.2: grey, s15.0: red, s20.0: green, s40.0: blue) from Woosley et al. [196], and for two different equations of state (Lattimer&Swesty: light shades, Shen EoS [167]: dark shades). In addition to the data taken from Dimmelmeier et al. [46], (filled circles) the results for the s15 series as simulated with VERTEX-CoCoNuT are also shown as black crosses. Right panel: Same as left panel, but with the rescaled angular velocity $\Omega_{\mathrm{c,15}}$ instead of $\Omega_{\mathrm{c,i}}$.

dynamics of the collapse. Since the outer shells of a rotating progenitor possess higher specific angular momentum (a natural consequence of the Rayleigh criterion), it is obvious that for a centrifugal bounce to occur, the inner core must be sufficiently massive, i.e. it must still include shells with large angular momentum when the core reaches the bounce density. Empirically, one finds [46] that the inner core mass must exceed $\approx 0.8 M_\odot$ for a centrifugal bounce to occur. Since rotation slows down the collapse and thus increases the mass of the inner core, such values can be reached in principle: Using the parameterized deleptonization prescription of Liebendörfer [103], one finds empirically [46] that the critical value for the initial angular velocity at the centre is rather high ($\gtrsim 6$ rad s^{-1}). Moreover, since the collapse does not proceed adiabatically below the trapping density, a significant amount of the gravitational energy released during the collapse is lost completely in the form of neutrinos, and the energy stored as rotational and internal energy is not sufficiently large to allow for a strong re-expansion of the core even if the collapse is halted at subnuclear densities. Thus, only a single centrifugal bounce followed by some ring-down oscillations occurs (instead of multiple bounces) even in the case of extremely strong rotation. On the other hand, the core mass typically remains higher than $0.45 M_\odot$, which precludes the rapid collapse required for type III signals. The mass of the inner core is thus the key factor in determining the bounce behaviour and the gravitational waveform type, and serves as a useful diagnostic quantity for assessing the accuracy of the deleptonization scheme of Liebendörfer [103].

Before analysing our models, it is expedient to discuss why a simple deleptonization scheme might not be applicable to rotational collapse. The fact that Y_e is given by a "universal"[3] progenitor-independent function of the density during the collapse phase, implies that the derivative $\mathrm{d}Y_e/\mathrm{d}\ln\rho$ must be a function of the density only,

$$\frac{\mathrm{d}Y_e}{\mathrm{d}\ln\rho} = \frac{\mathrm{d}Y_e}{\mathrm{d}\ln\rho}(\rho). \tag{5.3}$$

The derivative $\mathrm{d}Y_e/\mathrm{d}\ln\rho$ can be written as the ratio of the net electron capture rate $\mathrm{d}Y_e/\mathrm{d}t$ and the compression rate $\mathrm{d}\ln\rho/\mathrm{d}t$,

$$\frac{\mathrm{d}Y_e}{\mathrm{d}\ln\rho} = \frac{\mathrm{d}Y_e}{\mathrm{d}t}\left(\frac{\mathrm{d}\ln\rho}{\mathrm{d}t}\right)^{-1}. \tag{5.4}$$

However, the compression rate $\mathrm{d}\ln\rho/\mathrm{d}t$ does *not* depend on the density alone for homologous collapse, but also on the position of a mass element in the core; at a given density it is highest in the outer regions of the homologous inner part (as will be illustrated later). The higher compression rate must be compensated by a proportionally higher electron capture rate if condition (5.3) should hold. This is easily conceivable, if we consider, e.g., the rate of electron capture on free protons[4], which scales as (see e.g. [165]),

$$\frac{\mathrm{d}Y_e}{\mathrm{d}t} \propto -Y_p\mu_e^5. \tag{5.5}$$

In the limit of high degeneracy, the electron chemical potential depends only on ρY_e, while the proton number fraction Y_p also depends strongly on the specific entropy s. Since s is slightly higher in the outer regions of the core, this could in principle account for the higher electron capture rates posited by our argument. In any case, the proposed "universality" of the function $Y_e(\rho)$ must be the result of a delicate balance between the variation of the compression rate and the electron capture rate in different regions of the core (and also in different progenitors).

Based on these considerations, it is easy to see why the "universal" relation between Y_e and ρ in the core might be broken in the case of rotational collapse: The stabilizing effect of centrifugal forces, which can even halt the collapse at sub-nuclear densities, can be expected to decrease the compression rate $\mathrm{d}\ln\rho/\mathrm{d}t$ significantly[5], thus spoiling the balance between $\mathrm{d}\ln\rho/\mathrm{d}t$ and the electron capture rate, which only depends on the thermodynamic state variables (e.g. entropy and electron fraction) at a given density and is *not* influenced by rotation. If this were the case, rotating cores could undergo

---

[3] The function $Y_e(\rho)$ *does* of course depend on the choice of neutrino interaction rates. It can only be "universal" in the sense that it does not depend on the progenitor model, the rotational state and is valid for the entire collapsing core.

[4] A similar line of reasoning can be applied in the case of heavy nuclei.

[5] This would affect the *entire* inner core, and not just its outer regions where most of the angular momentum is located: Since the material in the inner core remains in sonic contact, centrifugal forces in its outer regions slow down the collapse of its central region as well.

significantly stronger deleptonization than non-rotating ones, and, since this implies a reduction of the mass of the homologous core, the dynamics of the collapse could be strongly affected. However, it cannot be determined *a priori* whether stronger deleptonization is important dynamically, and it is therefore advisable to discuss the dynamics of the collapse separately before investigating deleptonization in rotating cores *per se*.

We begin our analysis of the collapse and bounce phase with Fig. 5.1, which shows snapshots of the electron fraction and the matter entropy at three different times around bounce for model G15a2o9, i.e. for a model with the highest initial rotation rate considered in this chapter. The upper panels depict the situation 0.3 ms before bounce. At this time, the entropy behind the nascent shock (on the polar axis) first reaches $3k_b$/baryon – the usual criterion for the moment of shock formation in spherical symmetry (cp. Sec. 4.2). Around the equator, however, the shock has not formed yet as a consequence of the aspherical infall: Matter in the polar region lacks centrifugal support because of its lower specific angular momentum and therefore falls faster than matter near the equatorial plane. This can clearly be seen in the upper left panel, where the aspherically deformed isocontours of the entropy allow the identification of matter originating from the same mass shell in the progenitor. It takes another 0.3 ms for the shock to form in the equatorial plane (lower left panel); for our rotating models we define this as the "moment of bounce". Initially, the shock exhibits a strong *prolate* deformation, which subsists for the first few ms after bounce (lower right panel). 5.5 ms after bounce a high entropy bubble has developed in each of the polar regions, while the shock front begins to bulge outwards near the equator due to the high specific angular momentum of the newly accreted matter. Such a behaviour has already been observed in early simulations of rotational core collapse in Newtonian gravity [127, 129]. Interestingly, the shock expansion in the equatorial plane produces a localized region of convective instability, which is, however, quite dissimilar to the region of prompt post-shock convection seen in non-rotating models (which will be discussed in Chapter 6), inasmuch as only a single Rayleigh-Taylor mushroom develops. Although rotation locally acts as a stabilizing influence against convection [178], it can obviously trigger convection in the post-shock region indirectly through the propagation of the shock. Since we see indications of a large-scale convective overturn in most of our models (e.g. also in s15a2o9), early post-shock convection may be more prevalent than claimed by Dimmelmeier et al. [46], who observed it only for slow rotation[6]. Nonetheless, it may be more adequate to speak of partially stabilized post-shock convection for the more rapidly rotating models because of the peculiar morphology of the convective flow. There is of course a continuous transition to the more familiar type of convection that is dominated by high angular wavenumbers, as evinced by Fig. 5.2, which shows the electron fraction and entropy for the slowly rotating models G15a1o1 and s15a1o1 during the early post-bounce phase. Model s15a1o1 exhibits large-scale convective overturn with two downflows along the polar axes, while post-shock convection in model G15a1o1 is very similar to the

---

[6] Unfortunately, a direct comparison with Dimmelmeier et al. [46] is not possible, because they did not discuss post-shock convection in detail, and only singled out models where it contributes significantly to the gravitational wave signal.

non-rotating models that will be discussed in the next chapter.

Because of the aspherical formation of the shock, the definition of the mass of the inner core at bounce is ambiguous and can potentially mar the comparison with the parameterized models of [44–46, 143, 144]. We therefore cling to the definition used by Dimmelmeier et al. [46] (which was not explicitly stated in their paper, unfortunately), and use their data for a comparison[7]. For each angular direction, we define the location $r_s(\theta)$ of the sonic point as the smallest radial coordinate for which the radial velocity equals the local sound speed,

$$|v_r(r_s(\theta), \theta)| = c_s(r_s(\theta), \theta). \tag{5.6}$$

Once the shock has formed, $r_s(\theta)$ gives the angle-dependent shock position[8]. In addition, we introduce the radius $r_3(\theta)$ where the entropy reaches $3k_b$/baryon, and define the (baryonic) mass of the inner core as,

$$M_{\mathrm{ic}} = 2\pi \int_0^\pi \int_0^{\min(r_s(\theta), r_3(\theta))} \sqrt{\gamma}\rho W \,\mathrm{d}\theta \,\mathrm{d}r. \tag{5.7}$$

In other words, M_{ic} is the total baryonic mass inside the sonic surface (or inside the shock afterwards) with a specific entropy of less than $3k_b$/baryon. The mass $M_{\mathrm{ic,b}}$ of the inner core at bounce is then obtained from $M_{\mathrm{ic}}(t)$ using the aforementioned definition of the bounce as the instant when the post-shock entropy in the equatorial plane reaches $3k_b$/baryon.

Dimmelmeier et al. [46] found a roughly quadratic dependence of $M_{\mathrm{ic,b}}$ on the initial central angular velocity $\Omega_{\mathrm{c,i}}$ of the core, and our sophisticated neutrino transport simulations tend to confirm this claim. The right panel of Fig. 5.3 shows the mass of the inner core at bounce as a function of the $\Omega_{\mathrm{c,i}}$ for the s15 series as obtained with VERTEX-CoCoNuT, compared to results obtained with Liebendörfer's deleptonization prescription. The differences are relatively small: The results of Dimmelmeier et al. [46] deviate by less than $0.015 M_\odot$ (or 4%) from ours. This give further credence to the argument against gravitational wave signals of type III from rapid regular bounces: It appears that stronger deleptonization due to the slowing-down of the collapse by centrifugal forces does not occur, or at least not at such a level that the mass of the inner core is changed significantly compared to the the Liebendörfer scheme. It should also be pointed out that the increase of $M_{\mathrm{ic,b}}$ is not an artifact of the somewhat arbitrary definition of the time of bounce. The left panel of Fig. 5.3 illustrates that M_{ic} is higher for a rapidly rotating model (s15a2o9) than for a slowly rotating one (s15a1o1) throughout the entire collapse phase (cp. also Fig.6 in [44]).

However, the simulations carried out with VERTEX-CoCoNuT so far still leave some unanswered questions concerning the validity of the results obtained with the Liebendörfer scheme: So far, a direct comparison with ray-by-ray-transport could only be carried out for one two progenitors (s15.0 and s15s7b2) of the same mass, one equation

---

[7] We are indebted to H. Dimmelmeier for providing the relevant information

[8] Of course, the angle-dependent shock radius $r_{\mathrm{sh}}(\theta)$ can be different from $r_s(\theta)$ in general, but during the early post-bounce phase both quantities are identical.

of state, and for an initial angular velocity lower than $\approx 1/3$ of the highest values considered by Dimmelmeier et al. [46]. Sophisticated neutrino transport simulations of extremely rapidly rotating models are possible in principle, but are currently limited to the stage of shock formation near the polar axes. Tests conducted so far have shown that some of the pre-shock material at densities $\lesssim 10^{12}$ g cm^{-3} is exposed to neutrino heating (specifically by absorption of electron neutrinos) for a sufficiently long time to reach values of Y_e considerably higher than 0.5, and even exceeding the boundaries of the EoS table of Lattimer&Swesty. While this is an indication that models with $\Omega_{\mathrm{c,i}} > 5$ rad s^{-1} may yet show unexpected behaviour very different from simulations with the Liebendörfer scheme, a quantitative analysis is precluded by the limitations of the EoS at this stage.

Fortunately, the alleged progenitor dependence of $M_{\mathrm{ic,b}}$ [46] can already be discussed — at least to some degree — without conducting further simulations of rotational core collapse. Dimmelmeier et al. [46] found that $M_{\mathrm{ic,b}}$ varies considerably between different progenitor models, and that the progenitor dependence is considerably amplified for high initial rotation rates, as shown in the left panel of Fig. 5.4 (cp. also Fig. 4 in [46], which is virtually identical). These are actually two different aspects, and ought to be addressed separately. Concerning the variation of the inner core mass in the non-rotational limit, there is evidence that the Liebendörfer scheme overestimates the dependence on the progenitor model. In order to demonstrate this, we have conducted spherically symmetric core-collapse simulations with CoCoNuT, using either the VERTEX transport module, or the Liebendörfer deleptonization scheme with the same parameterization of $Y_e(\rho)$ as in Dimmelmeier et al. [46]. In both cases, the simulations have been conducted on a grid with 400 radial zones. Resolution effects, which could possibly skew our comparison with Dimmelmeier et al. [46] (who used only 250 radial zones) are thus eliminated. The results (see Table 5.2) show a spread of $M_{\mathrm{ic,b}}$ of $\approx 0.045 M_\odot$ or $\approx 10\%$ for the Liebendörfer scheme, whereas $M_{\mathrm{ic,b}}$ is virtually independent of the progenitor in the full transport simulations with VERTEX-CoCoNuT. As an aside, we note that the values obtained from our spherical simulations with the Liebendörfer scheme are almost identical to the inner core masses of the most slowly rotating models of Dimmelmeier et al. [46]. Hence, their results should not be gravely affected by resolution effects, and their values for $M_{\mathrm{ic,b}}$ are probably converged to within $\approx 0.01 M_\odot$ or better.

The convergence of different progenitors to an identical inner core mass in the spherically symmetric VERTEX-CoCoNuT runs suggests a feedback mechanism that the Liebendörfer prescription does not properly account for. The increase of the inner core mass with the progenitor mass that is observed with the Liebendörfer scheme may not seem surprising at first: more massive progenitors tend to have higher central entropies, and the concomitant finite-temperature effects on the pressure could produce slightly more massive cores. However, the Liebendörfer scheme does not take into account that higher entropies also imply higher electron capture rates (i.e. stronger deleptonization), which would have the opposite effect on the inner core mass. Furthermore, the Liebendörfer prescription cannot reproduce another feedback effect either: The relative contribution of electron captures on free protons to the total number of capture events is larger for higher entropies at a given density. Since electron captures on protons

Progenitor	VERTEX-CoCoNuT	Liebendörfer scheme
s11.2	0.46	0.435
s15.0	0.46	0.46
s20.0	0.46	0.45
s40.0	0.46	0.48

Table 5.2.: Mass $M_{\mathrm{ic,b}}$ of the inner core at bounce in spherically symmetric simulations with VERTEX-CoCoNuT and with the Liebendörfer scheme for different progenitors.

tend to decrease the entropy, while electron capture reactions on nuclei contribute to its increase, initial entropy differences between different progenitor cores may actually be reduced during collapse. The overestimation of the progenitor dependence of $M_{\mathrm{ic,b}}$ may thus indicate some genuine weaknesses of the Liebendörfer scheme.

On the other hand, the amplification of the progenitor dependence in the case of rotational collapse found by Dimmelmeier et al. [46] need not be ascribed to shortcomings of the Liebendörfer scheme. Instead, it can be adequately understood as an artifact of the parameterization of the initial rotational state of the progenitor core: The central angular velocity constantly increases during collapse because of angular momentum conservation, and its initial value during a simulation is therefore not an appropriate parameter for a comparison between initial models of different compactness – only the specific angular momentum of the infalling matter in the stellar core is conserved, and could be used as parameter for such a comparison directly. Alternatively, one could compare the central angular velocity for a specified central density instead of the specific angular momentum. This can be done rather easily, if we bear in mind that the inner core contracts homologously: Conservation of mass dictates that the density scales with R^{-3}, where R is the radius of the core, while the specific angular momentum $l = \Omega r^2$ scales with R^2. The central angular velocity thus increases with the central density according to,

$$\Omega_{\mathrm{c}} \propto \rho_{\mathrm{c}}^{2/3}, \tag{5.8}$$

at least during the early phase of collapse. We may therefore conveniently rescale the angular velocity of any pre-collapse model to the central density of a specified reference model, e.g. s15.0, in order to obtain a more useful measure for the initial rotational state,

$$\Omega_{\mathrm{c},15} = \Omega_{\mathrm{c,i}} \left(\frac{\rho_{\mathrm{c,s15.0}}}{\rho_{\mathrm{c}}} \right)^{2/3}. \tag{5.9}$$

The right panel of Fig. 5.4 shows that the mass of the inner core does *not* vary significantly more strongly with the progenitor model than in the case of spherical collapse if the rotational state of the initial model is specified by the rescaled angular velocity $\Omega_{\mathrm{c},15}$. At the very least, the large variation of up to $0.6 M_{\odot}$ for the highest values of $\Omega_{\mathrm{c,i}}$ is drastically reduced. Nonetheless, future simulations with full neutrino transport should re-address the progenitor dependence of $M_{\mathrm{ic,b}}$ in the case of rotational collapse to

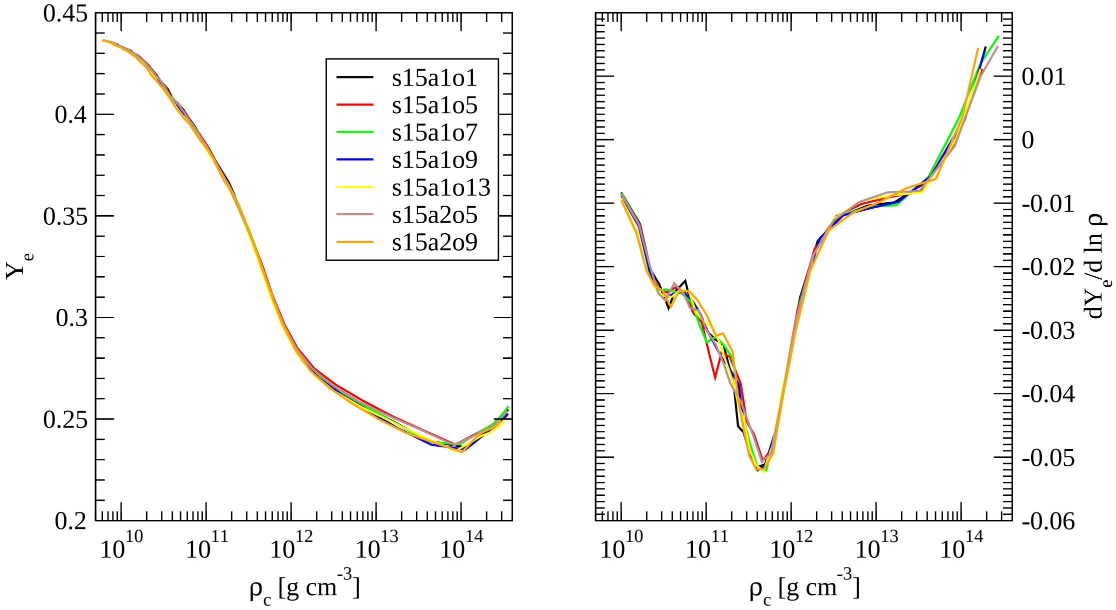

Figure 5.5.: Evolution of the central electron fraction Y_e (left panel) and the derivative $\mathrm{d}Y_e/\mathrm{d}\ln\rho$ (right panel) as a function of the central density ρ_c for the seven models of the s15 series.

determine whether the convergence of different progenitors to the same inner core mass might be even as perfect as for spherical collapse.

5.3. Rotational collapse and deleptonization

As discussed in the previous section, Liebendörfer's deleptonization prescription obviously captures the dynamics of rotational core collapse rather adequately. We shall now show that the underlying assumption of a universal relation between Y_e and ρ is indeed fulfilled remarkably well for the rotation rates considered in our study. Fig. 5.5 illustrates this for the *central* electron fraction: For the seven models of the s15 series with different initial rotation rates, the central Y_e is spread only over a narrow band of $\Delta Y_e \lesssim 0.01$, which is comparable to the spread between different progenitors in spherically symmetric simulations [46]. Apparently, the balance between the electron capture rate and the matter compression rate is not affected by rotation to such a degree that deleptonization is significantly stronger for rapidly rotating models as we speculated in the previous section.

Of course, the effects of centrifugal braking are potentially much larger in the outer regions of the core than at the centre, as the specific angular momentum increases outwards. However, the deleptonization of the shells around the edge of the inner core proceeds in such a manner that the parameterization of Y_e as a function of ρ is still

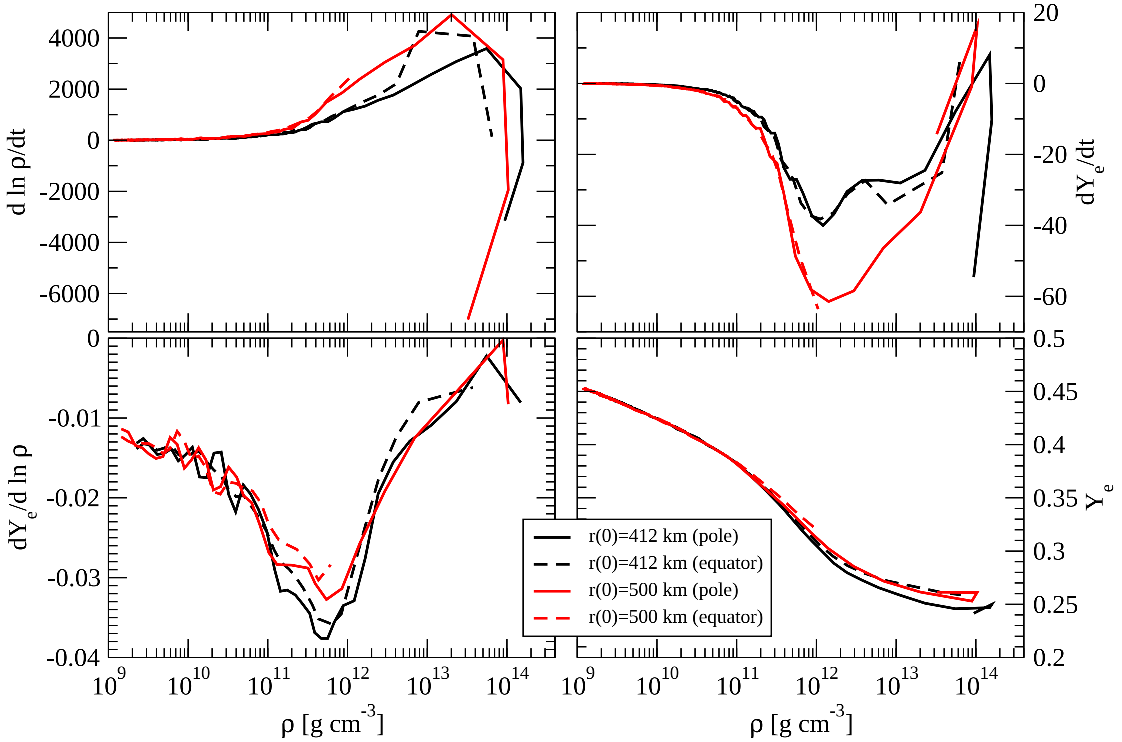

Figure 5.6.: Compression rate $\mathrm{d}\ln\rho/\mathrm{d}t$ (top left), electron capture rate $\mathrm{d}Y_e/\mathrm{d}t$ (top right), electron fraction Y_e (bottom right), and the derivative $\mathrm{d}Y_e/\mathrm{d}\ln\rho$ along the trajectories of different fluid elements in the strongly rotating model s15a2o9. The fluid elements are initially located at $r = 412$ km (black lines, corresponding to a mass coordinate of $m = 0.46M_\odot$) and $r = 500$ km (red lines, $m = 0.63M_\odot$, either in the equatorial plane (dashed lines) or 10° away from the polar axis (solid lines). The trajectories are shown right until bounce.

quite accurate. As an example, we consider four fluid elements from that region in the simulation of the strongly rotating model s15a2o9 (Fig. 5.6). Although the infall of the fluid elements in the equatorial plane is slowed down – the mass element initially located at 500 km has not even reached 10^{12} g cm^{-3} at bounce – the electron fraction for a given density does not differ grossly (by less than 0.02) from the fluid elements starting near the polar axis. Remarkably, even the compression rate as a function of density seems to be independent of latitude up to densities of a few 10^{12} g cm^{-3}, and the same applies to the electron capture rate. There is, however, a considerable difference in the electron capture rate between fluid elements starting at different radial positions: During the critical phase just before neutrino trapping (at $\rho \approx 10^{12}$ g cm^{-3}), it is about twice as large for the mass shell $m = 0.63M_\odot$ as for $m = 0.46M_\odot$.

It thus appears that the radial variation of the electron capture rate is as much a limiting factor for the proposed universality of the Y_e-ρ-relation during collapse as the dynamical effects of rotation. This conclusion is borne out by Fig. 5.7, which shows

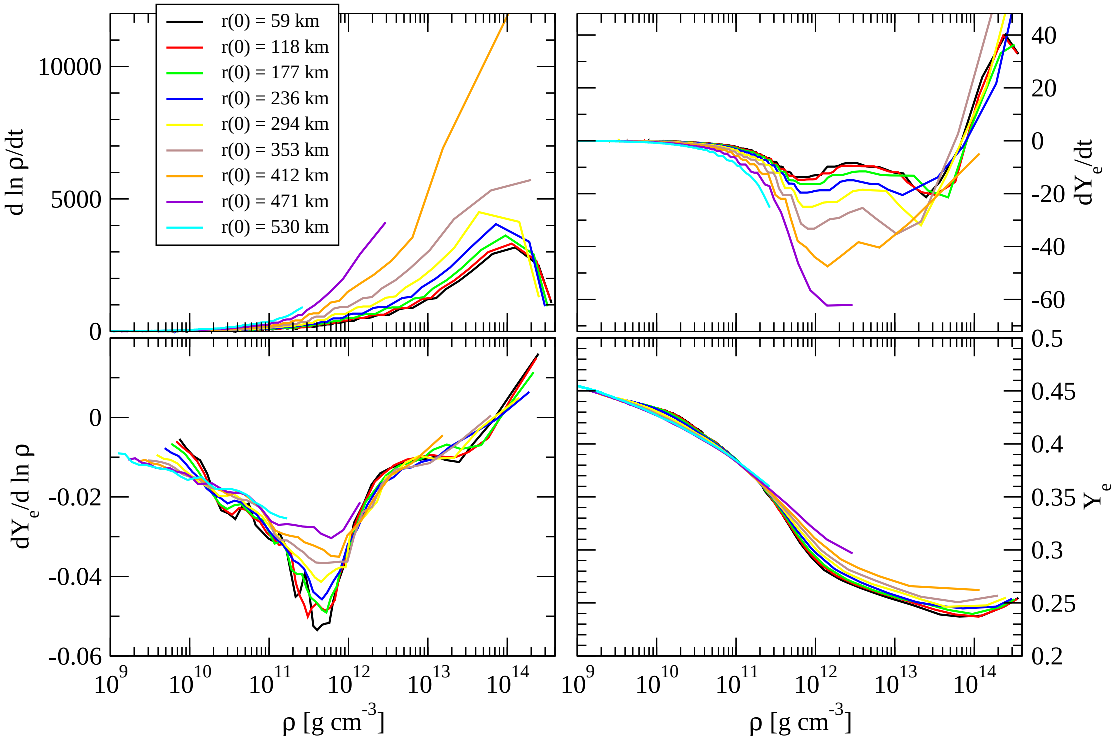

Figure 5.7.: Compression rate $\mathrm{d}\ln\rho/\mathrm{d}t$ (top left), electron capture rate $\mathrm{d}Y_e/\mathrm{d}t$ (top right), electron fraction Y_e (bottom right), and the derivative $\mathrm{d}Y_e/\mathrm{d}\ln\rho$ along the trajectories of fluid elements in the slowly rotating model s15a1o1. The initial radial position $r(0)$ of the fluid elements ranges from 58 km to the 530 km, i.e. to a mass shall ($m = 0.69 M_\odot$) located well outside the inner core at bounce.

the electron fraction, the compression rate, and the electron capture rate for a number of different mass shells in model s15a1o1, which rotates rather slowly and therefore remains close to spherical symmetry. Clearly, the compression rate at a given density is highest for the outermost mass shells, but the more rapid compression is compensated (albeit imperfectly) by higher electron capture rates, so that the different mass shells follow similar deleptonization curves in the ρ-Y_e-plane until bounce. This confirms our tentative explanation concerning the validity of the Liebendörfer scheme in Sec. 5.2. It rests on the (imperfect) cancellation of the radial variation of the electron capture rate and of the compression rate.

The conclusion that can be drawn from these observations is rather encouraging: Apparently, the application of a deleptonization scheme to rotational core collapse can be justified, at least for the rotation rates covered by our models. The influence of centrifugal forces seems to be insufficient to alter the dynamics of the infall to such an extent that deleptonization proceeds differently than during non-rotational collapse. At the present stage, it is not yet possible to determine whether this behaviour is merely incidental (because the rotation rates considered so far are too low to be of importance),

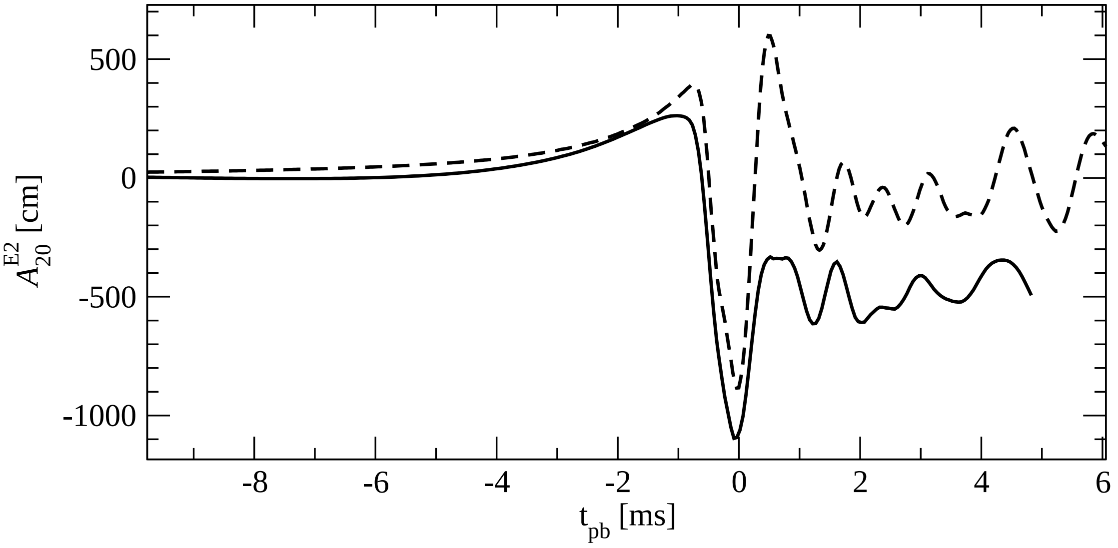

Figure 5.8.: Gravitational wave amplitude A_{20}^{E2} for model s15a2o9 as obtained with VERTEX-CoCoNuT (sold), and with the Liebendörfer scheme (data from [1]).

or the result of some feedback mechanism. There are arguments for either of these explanations: deleptonization is essentially finished at densities no higher than a few 10^{12} g cm^{-3}, and it is obvious that rotation is dynamically less relevant during this early collapse phase than at bounce, where the core is much more compact. On the other hand, a feedback mechanism can also be conceived: Slower compression due to centrifugal braking would result in stronger deleptonization, and hence in a reduction of the effective adiabatic index γ_{eff}, which would in turn accelerate the collapse, increase the compression rate $\mathrm{d}\ln\rho/\mathrm{d}t$, and reduce $|\mathrm{d}Y_e/\mathrm{d}\ln\rho|$ again.

5.4. Gravitational wave emission

We now finally turn to the discussion of gravitational wave signals from rotational core collapse. As the conformal-flatness condition constitutes a *waveless* approximation to general relativity, we determine the gravitational wave signal using the Einstein quadrupole formula[9] [40, 42, 43, 168] in its time-integrated version [9, 56]. In axisymmetry, it yields the quadrupole wave amplitude A_{20}^{E2} as,

$$A_{20}^{\mathrm{E2}} = \frac{32\pi^{3/2}}{\sqrt{15}} \frac{\mathrm{d}}{\mathrm{d}t} \int r^3 \sin\theta \rho \left[v_r (3\cos^2\theta - 1) - 3 v_\theta \sin\theta \cos\theta \right] \mathrm{d}\theta \, \mathrm{d}r, \tag{5.10}$$

---

[9] Although the quadrupole formula is derived in the slow-motion and weak-field limit, it yields results that are accurate to within 10% to 20% in astrophysical situations similar to stellar core collapse [135, 168].

from which the dimensionless gravitational wave strain h measured by an observer located at an angle θ with respect to the symmetry axis can be determined as,

$$h = \frac{1}{8}\sqrt{\frac{15}{\pi}} \sin^2\theta \frac{A^{E2}_{20}}{R}, \tag{5.11}$$

where R is the distance to the source. In the following, we shall assume the most optimistic case of an observer positioned in the equatorial plane, i.e. $\sin^2\theta = 1$. Using the time-integrated quadrupole formula, we have computed gravitational wave signals for the 14 models of the G15 and s15 series. These are shown, along with Fourier spectra, in Figs. 5.9 and 5.10, respectively.

As we find reasonably good agreement with Dimmelmeier et al. [46] concerning the mass of the inner core as a crucial quantity for the dynamics of the collapse, it can be expected that our gravitational wave signals are similar to theirs, and this is indeed the case. Specifically, we obtain waveform that are clearly of type I (except for model s15a1o1, which will be discussed below). Furthermore, our gravitational wave spectra also exhibit a peak with a rather stable location at a frequency of $f \approx 725$ Hz. The peak frequency is very similar to the one found by Dimmelmeier et al. [46], but significantly lower than in Müller et al. [132] and Scheidegger et al. [161] in the context of pseudo-Newtonian simulations of rotational collapse. This is a further indication that some dynamical properties (e.g. the eigenfrequencies) of proto-neutron stars are not correctly captured by effective pseudo-relativistic potentials. Although a direct comparison of our wave signals with Dimmelmeier et al. [46] is problematic, because of the different grid resolution, we point out that the waveforms agree quite well qualitatively. The first (and largest) negative peak of the type I waveform typically has a very similar amplitude, as demonstrated in Fig. 5.8 in the case of model s15a2o9. However, the ring-down signal can be quite different (see below).

Nevertheless, there are some peculiar features not hitherto seen in the relativistic simulations of [44–46, 143, 144]. First, the wave signals of the almost uniformly rotating models G15a1oX and s15a1oX all start with a (sometimes considerable) negative offset. This is the result of a strong contribution from expanding outer shells of the progenitor which are not in rotational equilibrium due to the choice of the rotation profile. Since these outer regions with densities $\rho \lesssim 10^6$ g cm^{-3} were omitted in earlier simulations, this offset has hitherto gone unnoticed. The very fact that the artificial imposition of rotation onto a progenitor leaves visible traces in the gravitational wave signal prompts us to sound a note of caution concerning this practise.

As noted before, model s15a1o1 deserves a few special remarks (Fig. 5.10). The first negative peak of the gravitational wave amplitude is not very pronounced, and the waveform might thus be classified as type III. However, this classification is doubtful for several reasons: Dynamically, the mass of the inner core at bounce ($0.45 M_\odot$) is too high for a type III signal to be produced. Moreover, the low-frequency background from shells outside the inner core that readjust themselves to establish rotational equilibrium (as explained in the last paragraph) would have to be subtracted to allow for a clear-cut determination of the signal type. The waveform for model s15a1o1 should more likely be interpreted as a "disguised" type I signal superimposed on a hump-like background signal as seen for model s15a1o5. In addition, the two-lobed structure of the incipient post-shock convection (right panel of Fig. 5.2) gives rise to a strong wave signal soon after bounce, and thus further contributes to the rather unusual shape of the waveform.

We also find a general tendency for the first peak of the ring-down phase to be much less pronounced than in [44–46, 143, 144] (cp. Fig. 5.8). Pending the outcome of a further detailed comparison of simulations with parameterized deleptonization and full spectral neutrino transport, with an identical grid setup and the same hydrodynamics solver, the origin of this feature remains ambiguous.

5.5. Summary

Considering the different aspects discussed in the previous sections (collapse dynamics, deleptonization, wave signals), our conclusions concerning the validity of the latest simulations of rotational collapse in general relativity are very encouraging. Obviously, the Liebendörfer scheme [103] is adequate for modelling the deleptonization of the core until bounce even in the case of relatively rapid rotation with similar accuracy as in spherical symmetry. Consequently, gross features of previous simulations, i.e. gravitational waveforms from the core bounce are uniformly of type I, and peak in a narrow frequency band in the region around ≈ 725 Hz, as claimed by Dimmelmeier et al. [44] (cf. [45, 46, 143, 144]), are confirmed by our results. From the point of view of gravitational wave astronomy, this implies that both the potential for enhancing the detection probability by narrow-banding future detectors and the signal inversion problem introduced by the frequency degeneracy remain, as discussed by Dimmelmeier et al. [44].

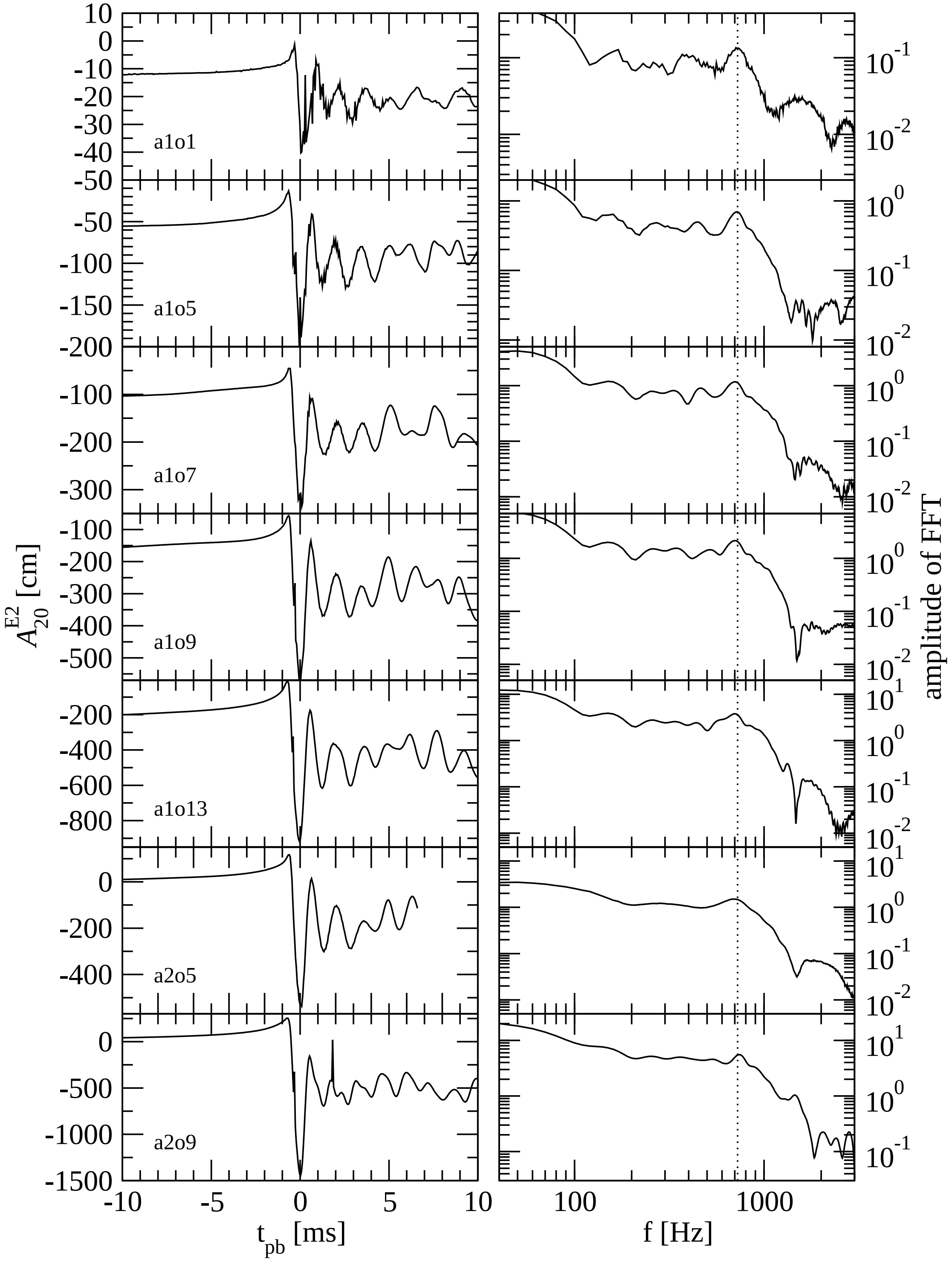

Figure 5.9.: Gravitational wave amplitude A_{20}^{E2} (left) and spectra (right, obtained with the Welch window function) for the model series G15aXoY. The spectral peak at $f \approx 725$ Hz is indicated by a dotted line.

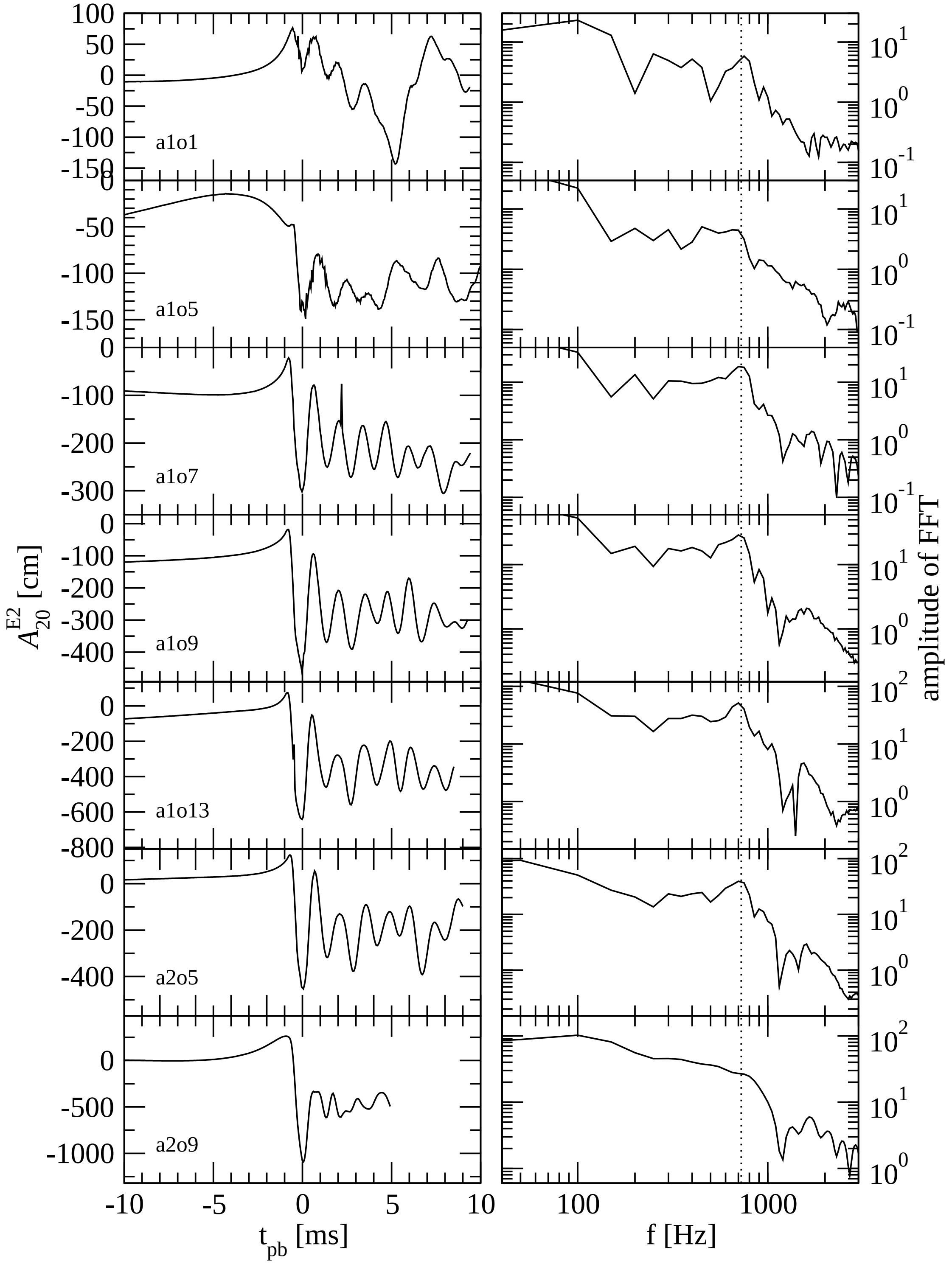

Figure 5.10.: Gravitational wave amplitude A^{E2}_{20} (left) and spectra (right, obtained with the Welch window function) for the model series s15aXoY. The spectral peak at $f \approx$ 725 Hz is indicated by a dotted line.

6. Applications II: Multidimensional Simulations of the Post-Bounce Phase

Having discussed the effects of rotation during the collapse phase, we now turn our attention to the post-bounce phase. Because of the failure of one-dimensional supernova models, multi-dimensional effects (like convection) during this phase have long been suggested as crucial ingredients for the explosion mechanism. The existence of a convectively unstable region inside the proto-neutron star was already recognized by Epstein [52]. For a while, it was hoped that "proto-neutron convection" in this region below the neutrinosphere might sufficiently boost the neutrino luminosities and thereby increase the energy deposition in the gain region to revive the stalled shock. Unfortunately, the assumptions of one-dimensional explosion models with parameterized convection [192] were not borne out by multi-dimensional simulations [20, 37, 86, 122]: Proto-neutron star convection does indeed occur, but according to the current Newtonian or pseudo-relativistic models the enhancement of the neutrino luminosities is rather modest. However, as Bethe [7] already pointed out, there is another region of convective instability in the so-called "hot-bubble" region between the shock and the proto-neutron star. Hot-bubble convection was found to increase the neutrino heating efficiency considerably in several simulations conducted in the 1990s [23, 72, 73, 80, 81], all of which obtained robust explosions. Today, the importance of hot-bubble convection remains undisputed, although the most up-to-date multi-dimensional supernova simulations with spectral neutrino transport [17, 20, 21, 26, 114] differ in many respects from these earlier studies. Most importantly, another hydrodynamic instability, known as "standing accretion shock instability" (SASI) [11], was identified during the last years. The SASI is a generic instability of the accretion shock to non-radial deformations, and can be understood in terms of an "advective-acoustic" feedback cycle [60, 64]: vorticity perturbations created at the shock are advected towards the proto-neutron star surface, where they are decelerated and create sound waves that couple back to the shock and create larger vorticity perturbations there[1]. The resulting non-radial oscillations of the shock front are dominated by low-order modes (i.e. the $l = 1$ dipole and the $l = 2$ quadrupole mode), and enhance neutrino energy deposition, since the material in the wake of the expanding shock remains in the heating region for a longer time before being advected towards the neutron star surface. In most recently published explosion models [17, 20, 26, 114], this plays a crucial role, although neutrino heating and the SASI are not universally

---

[1] Alternatively, the feedback might also be mediated by acoustic waves only, as suggested by Blondin and Mezzacappa [10].

recognized as the primary agent for the explosion. Energy deposition by acoustic waves emitted by core g-mode oscillations of the proto-neutron star [26] or magnetic fields [27] have been advocated as alternatives to the SASI-aided neutrino-driven mechanism; however, serious doubts have been cast on the viability the "acoustic mechanism" [189], and it is doubtful whether rotation rates and magnetic field strengths required for magnetohydrodynamic explosions are reached in the generic case. At any rate, the interplay of neutrino heating and cooling and multi-dimensional (magneto-)hydrodynamic effects has emerged as the central issue for supernova modelling during the recent years.

On the other hand, general relativity has received relatively little attention in the quest for the explosion mechanism during the recent years, although general relativistic supernova simulations in *spherical symmetry* with grey or multi-group flux-limited diffusion have been conducted since the 1980s [6, 15], and have been supplemented by simulations with Boltzmann neutrino transport [105, 106, 201]. This is rather surprising, as comparisons with the Newtonian case (see, e.g., Bruenn et al. [15]) in spherical symmetry revealed a sizable influence of general relativity on the mass of the inner core at shock formation, the initial shock strength, the long-term evolution of the shock position, the compactness of the proto-neutron star, and the neutrino luminosities and energies. However, generalizing the existing formulations of relativistic neutrino radiation hydrodynamics in spherical symmetry to the multi-dimensional case is indeed a formidable task, since some of the simplifying gauge choices (Lagrangian coordinates, Misner-Sharpe form of the metric [125]) are no longer available. To some extent, these complications can be avoided by resorting to a recipe that is both simple and astonishingly successful: Instead of treating general relativistic effects rigorously by working in a curved spacetime, one can mimic important relativistic effects (e.g. the greater compactness of the proto-neutron star) by introducing an *effective gravitational potential* [116, 128, 151] constructed from a solution of the Tolman-Oppenheimer-Volkov equation of stellar structure, while retaining the framework of Newtonian hydrodynamics. Despite its merits, this approach has some drawbacks: It cannot be derived in a systematic way like the post-Newtonian approximation, does not capture special relativistic effects, and predicts incorrect eigenfrequencies of neutron stars [128]. It is also impossible to formulate conservation laws for the total energy and momentum in this approach. Whether the existing "pseudo-Newtonian" multi-dimensional simulations [20, 21, 114, 117] capture the effects of general relativity with sufficient accuracy thus remains an open question. With VERTEX-CoCoNuT, which combines the elaborate treatment of neutrino transport with an accurate description of relativistic effects, we can now provide a few answers concerning this issue.

6.1. Aims and model setup

The first two-dimensional supernova simulations of the post-bounce phase with VERTEX-CoCoNuT need to address a number of different issues: First, the mere ability of the new code to evolve a core collapse model to post-bounce times of several hundreds of ms is not to be taken for granted since the hydrodynamics module CoCoNuT was only used in the past to study core collapse up to the time of bounce and a few tens of ms beyond. Provided that CoCoNuT proves up to the task, the analysis of multi-dimensional effects in the supernova problem (convection, standing-accretion shock instability) can be extended to the general relativistic case with a view to detecting quantitative or qualitative differences to existing Newtonian simulations. These two steps cannot be completely disentangled, however, since different results may either be caused by different physics (i.e. GR effects) or by differences in the codes. In our case this problematic ambiguity is somewhat mitigated by the fact that VERTEX-CoCoNuT shares most of its key components (neutrino transport scheme, interaction rates, equation of state) with the PROMETHEUS-VERTEX code; and we will therefore rely heavily on the work done in the framework of Newtonian hydrodynamics (with a pseudo-potential treatment of GR) with that particular code [18, 20, 21, 113, 114].

Ideally, an analysis of relativistic effects would be based on a comparison of relativistic and (pseudo-)Newtonian simulations with an identical model setup. Since fully-fledged multi-dimensional runs with VERTEX are computationally expensive, a repetition of the recently published simulations by Marek and Janka [114] within a reasonable time-frame is unfortunately out of reach at this stage. We have therefore confined ourselves to two less costly simulations (G15-2D and R15LS-2D), whose setup is still similar to model M15LS-2D of [114]. Both of these were launched from the same spherically symmetric progenitor model s15s7b2 [195] as the 1D runs of model G15 discussed in Sec. 4.2. Simulation G15-2D was carried out with the same set of neutrino interaction rates, the same EoS, and the same radial grid (400 zones) as model G15 in Chapter 4, a reduced energy resolution (12 zones), and a rather modest angular resolution of 64 zones (for 180°). As in model G15, nuclear burning in the low-density regime was switched off. Model R15LS-2D was simulated with the "improved" set of neutrino interaction rates in VERTEX [20, 21, 114] and the simplified burning description of Rampp and Janka [151] (known as "flashing"). Moreover, the hybrid HLLC/HLLE scheme, which has been switched on in run G15-2D only at $t_{\mathrm{pb}} \approx 120$ ms, has been used throughout. Apart from the different grid (600×64) and the treatment of general relativity, this model is identical to model M15LS-2D of Marek and Janka [114]. Although R15LS-2D is arguably a more sophisticated and reliable model than G15-2D, our analysis focuses on the latter, because it has been run to more than 300 ms after bounce, while the simulation of R15LS-2D presently covers only a few ms after bounce.

We emphasize that we consider only *non-rotating* models in this chapter: According to recent stellar evolution studies, magnetic braking is probably very effective in slowing down pre-collapse iron cores to such low rotation rates [71] that the dynamical effect of centrifugal forces is negligible for the collapse and the subsequent explosion. Non-rotating models are thus probably representative for the majority of core-collapse supernovae. This does not imply, however, that the case of rapid rotation discussed in Chapter 5 is not of relevance: Rapid rotation is an essential ingredient in some astrophysical scenarios connected to core collapse, such as accretion-induced collapse [38, 39], or in the collapsar scenario for long gamma-ray bursts [27, 112]. Furthermore, even if the recent models for magnetic torques are correct, rapidly rotating progenitor cores might still be formed at low galactic metallicities due to reduced mass loss rates [194], or as

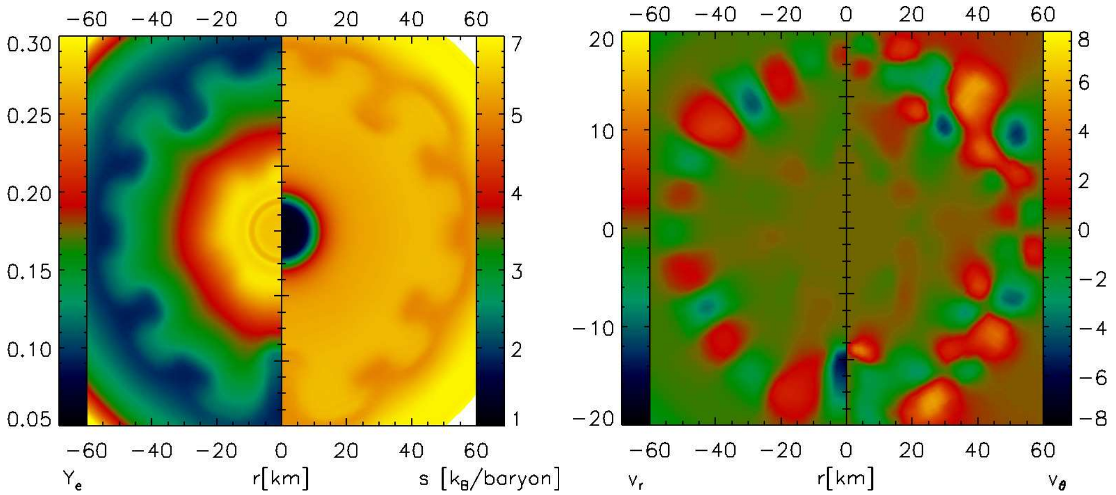

Figure 6.1.: Electron fraction Y_e, specific entropy s, radial velocity v_r and lateral velocity v_θ (from left to right) at a time of 17 ms after bounce for model G15-2D. Incipient convective motions are clearly visible in all four quantities. Velocities are given in units of 10^8 cm s^{-1}.

the result of accretion [28, 204] or even merger events [61] in binaries.

6.2. Development of convection

All recent multi-dimensional simulations [17, 18, 20, 21, 37, 113, 114, 177] with spectral neutrino transport give a rather homogeneous picture of convection during the post-bounce phase: convection occurs both inside the proto-neutron star (below/around the neutrinosphere) and in the gain region (hot-bubble/HB convection). It is identified as buoyancy-driven (Ledoux) convection also in the former case. Doubly diffusive instabilities [13, 14, 16] do no seem to play a role. In addition, prompt post-shock convection may occur [17, 117, 177]. There is some variation between the models concerning the size, location, and first appearance of the different convective regions, probably due to differences in the neutrino transport, the equation of state, and the treatment of gravity (Newtonian/pseudo-relativistic). Our results with VERTEX-CoCoNuT, which are described in some detail in this section, fit well into this context, albeit that they show some quantitative differences.

6.2.1. Prompt post-bounce and proto-neutron star convection

Both our simulations show the development of Ledoux convection shortly after bounce (see Fig. 6.1 for model G15-2D and Fig. 6.2 for model R15LS-2D). Convection starts a little earlier for model R15LS-2D, where plumes in the entropy and Y_e distribution are clearly visible at $t_{\mathrm{pb}} = 7$ms, while model G15-2D needs another 10 ms to reach a similar

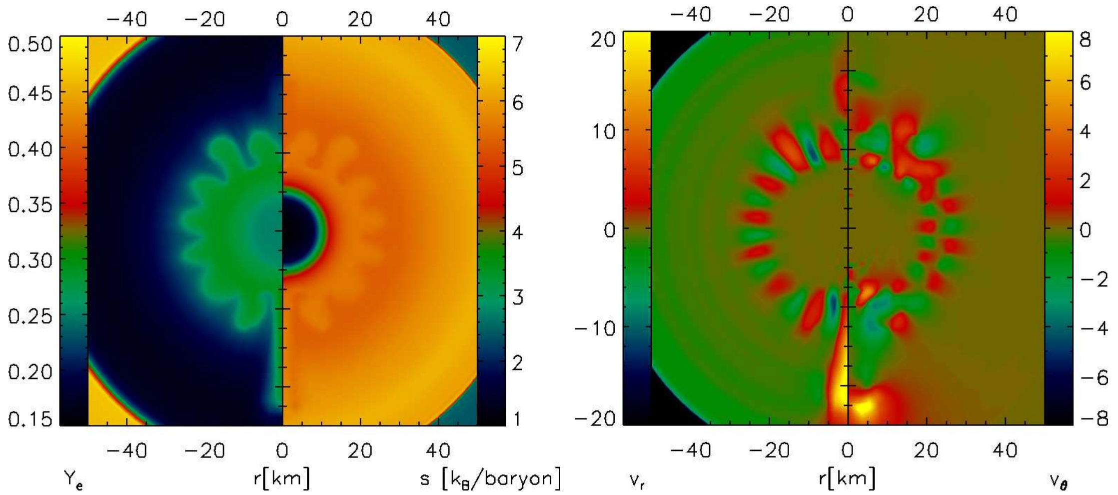

Figure 6.2.: Electron fraction Y_e, specific entropy s, radial velocity v_r and lateral velocity v_θ (from left to right) at a time of 7 ms after bounce for model R15LS-2D. Incipient convective motions are clearly visible in all four quantities. Velocities are given in units of 10^8 cm s^{-1}.

stage. The convectively unstable region also lies deeper inside the neutron star in the R15LS-2D run; it is located at a radius of $r \approx 25$ km, as opposed to $r \approx 45$ km in the G15-2D run. Fig. 6.3, which shows the value of the Ledoux criterion C_L at a time when the shock has reached an enclosed mass of $1.02 M_\odot$, demonstrates that both the time lag and the different location of the unstable layer result from a slightly different density stratification in both runs. In the case of R15LS-2D, C_L is positive for an enclosed mass in the range of $0.61 M_\odot \ldots 0.77 M_\odot$, while G15-2D is convectively unstable exterior to $m = 0.75 M_\odot$. Since the grid resolution is adequate in both runs (with more than 15 zones per decade in density), this difference is not likely to be a numerical artifact, but probably stems from the use of the "improved" neutrino opacities in simulation R15LS-2D, which alter the mass of the homologous inner core during collapse, and hence also the dynamics during the early post-bounce phase. The different location of the unstable region also offers a natural explanation for the time lag: As the local gravitational acceleration in the unstable layer in model G15-2D is considerably smaller than in the in the mass shells between $0.61 M_\odot$ and $0.77 M_\odot$ in model R15LS-2D, the Brunt-Väisälä frequency is smaller by a factor of two, which implies that the growth of convection is slowed by about the same factor. Otherwise the morphology of convection is quite similar in both simulations, with an angular size of the convective cells between 20° and 30° and a radial extension of approximately 10 km as in Buras et al. [21] and Keil [85].

A comparison to previous studies of prompt convection sheds some light on the role of GR effects during the early post-bounce phase: Although prompt convection develops in model M15LS-2D of Marek and Janka [114] (cf. [117]), the unstable region

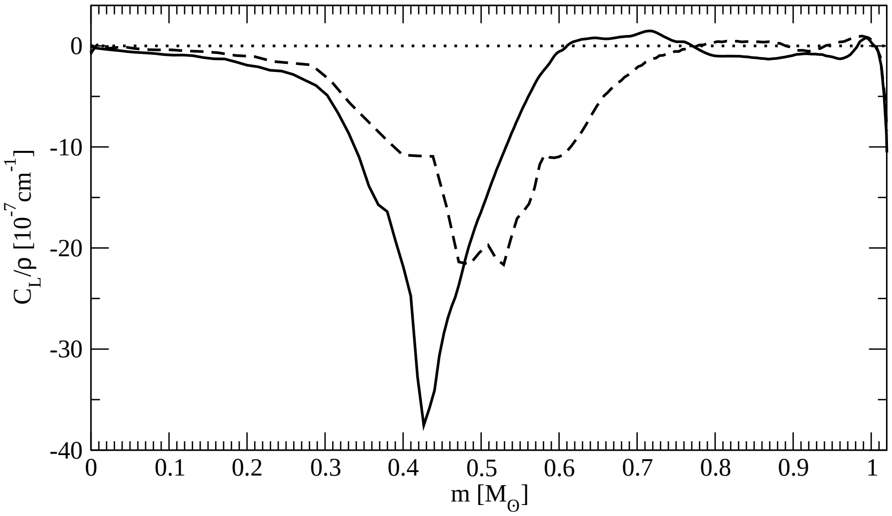

Figure 6.3.: Ledoux criterion C_L as a function of the enclosed mass m for model G15-2D (solid line) and R15LS-2D (dashed line) at the time when the shock has reached $m = 1.02 M_\odot$. For convenience, C_L is scaled to the local baryonic mass density ρ.

is significantly broader ($m = 0.61 M_\odot \dots 0.77 M_\odot$) in R15LS-2D than in M15LS-2D ($m = 0.6 M_\odot \dots 0.71 M_\odot$). Judging from Fig. 1 in Marek et al. [117], prompt post-shock convection also starts a few ms later (at least later than $t_{\mathrm{pb}} = 10$ ms) in M15LS-2D than in model R15LS-2D, where radial velocities of the order of 2×10^8 cm s^{-1} are already observed at $t_{\mathrm{pb}} = 7$ ms in the convective layer. The absence of a convectively unstable region in the pseudo-relativistic runs of the 1D model G15 (with different neutrino physics than R15LS-2D) has already been noted in Sec. 4.2. The proper inclusion of general relativity – as opposed to an effective potential approach – thus seems to favour the development of prompt convection. Where there is already an unstable region in the pseudo-Newtonian case (as for model M15LS-2D), the convective layer is apparently broadened, and convection grows more vigorously. As the proto-neutron star structure already changes tremendously by moving from Newtonian gravity to a pseudo-relativistic potential [116], this also suggests the disagreement concerning the onset of PNS convection in different studies need *not* be ascribed to different numerics, insufficient resolution, different seed perturbations [37], or the time of mapping from 1D to 2D [177]. This conclusion is also borne out by the fact that a modification of the neutrino opacities obviously affects the conditions for the development of prompt post-shock and PNS convection noticeably. A general analysis of these phenomena must take into account all the relevant factors, i.e. the equation of state, the treatment of gravity, and the neutrino physics.

The specific structure of the PNS convection layer in simulation G15-2D also has interesting consequences for the emission of neutrinos during the early post-bounce phase. As the convective layer reaches out quite far during the first tens of milliseconds after

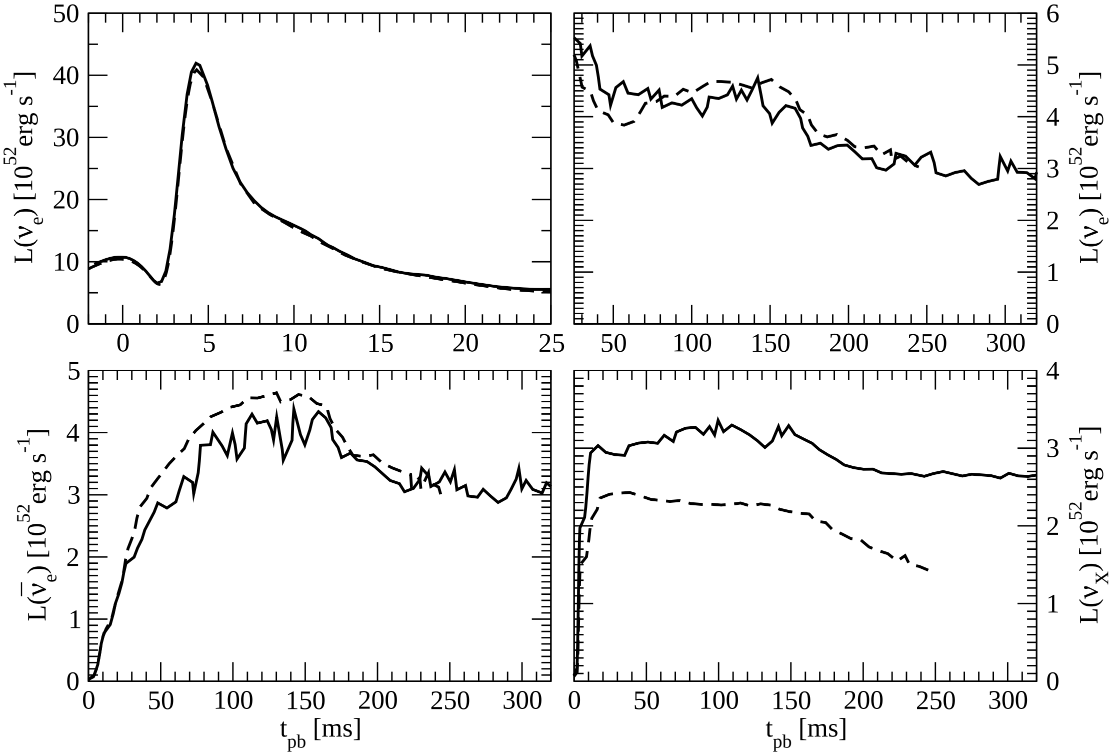

Figure 6.4.: Comparison of neutrino luminosities for models G15-2D (solid) and G15 (dashed). Electron neutrino luminosities are shown in the left and right upper panels, electron anti-neutrino and μ/τ luminosities in the left and right lower panels, respectively. In the 2D case, the ν_μ- and ν_τ-luminosities are enhanced by 20% to 40% throughout the entire evolution of the model. The $\bar{\nu}_e$-luminosity is slightly reduced from about 25 ms onward, but is again comparable to the 1D case for $t_{\mathrm{pb}} \gtrsim 200$ ms. For electron neutrinos the luminosities are similar in the 1D and 2D case throughout.

bounce, it comes very close to the neutrinospheres for all flavours (located at $r \approx 70$ km during this phase), and, more importantly coincides very well with the region where electron anti-neutrinos and μ/τ neutrinos thermally decouple from the fluid. This is in stark contrast to the situation recently described by other authors [20, 21, 37], where PNS convection occurred at a high transport optical depth τ (see [21] for the precise definition), with $\tau \geq 10$ for all flavours in the case of Buras et al. [21]: At the early stage depicted in Fig. 6.1, the convective plumes reach out to an optical depth as low as $\tau \approx 2$, which suggests that they may modify the neutrino emission considerably. Apart from the μ/τ neutrinos, for which we observe an enhancement of 20% to 40%, there is little effect on the luminosities (see Fig. 6.4). On the other hand, the mean energies of the emitted neutrinos of all flavours are systematically higher during the first ≈ 30 ms – with the exception of the μ/τ-neutrinos from the peak phase of the breakout burst ($t_{\mathrm{pb}} \approx 5$ ms$\ldots$10 ms). The differences before $t_{\mathrm{pb}} \approx 10$ ms are probably due to the lower

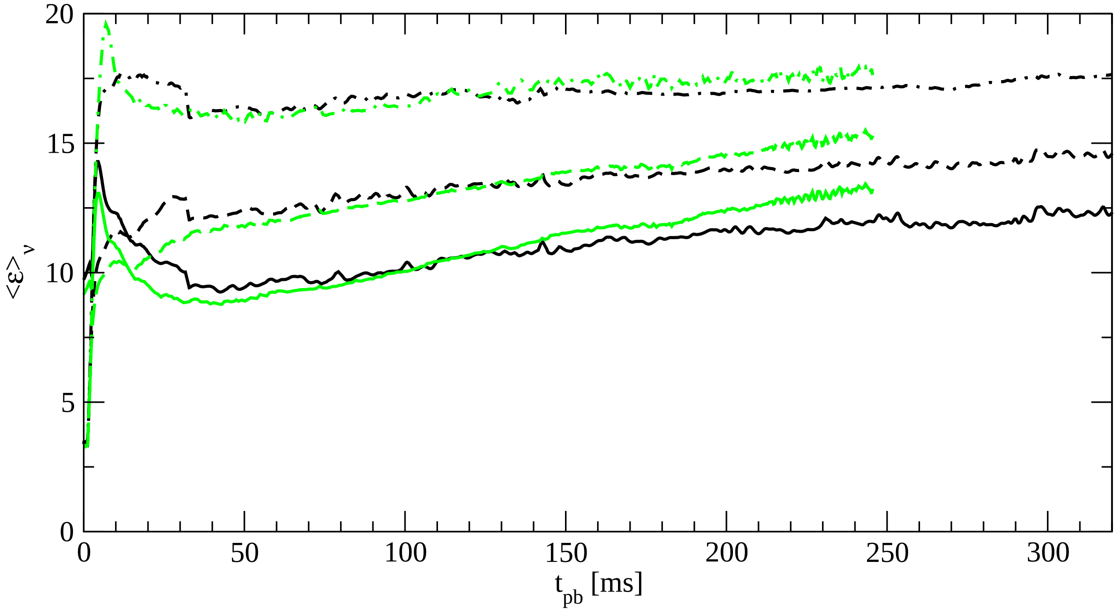

Figure 6.5.: Mean energies of emitted neutrinos, measured at $r = 400$ km in the lab frame, for the simulations G15-2D (black) and G15 (green). Solid lines are used for electron neutrino, dashed lines for electron anti-neutrinos, and dash-dotted lines for μ/τ neutrinos.

energy resolution in G15-2D (12 zones, as opposed to 17 in G15), since no significant growth of convection has taken place yet[2]. The slight transient increase of the mean energy may possibly be due to the convective motions near the neutrinosphere: Over the rising plumes, the neutrinosphere temperature is somewhat higher than above the sinking ones, while the angle-dependent neutrinosphere radius is more or less identical in both cases. This implies locally stronger emission of neutrinos with a slightly harder spectrum above the rising plumes. While the overall effect on the luminosities seems to cancel out except for ν_μ and ν_τ, the higher contribution of hot emitting region seems to result in a slight overall increase of the mean energies because the weighted contribution from the hot regions to the total luminosity is higher. However, since we observe the phenomenon at a time when neutrino emission cannot be appropriately modelled as (modified) black body emission from the neutrinosphere, our reasoning can only constitute a very tentative analysis of the observed phenomenon.

At later times ($t_{\mathrm{pb}} > 30$ ms, the PNS convection affects the neutrino luminosities in simulation G15-2D in exactly the same way as described by Buras et al. [20]. Convective transport of lepton number produces a broader and slightly more shallow Y_e-trough than in the 1D case, as shown in Fig. 6.6 at a time of 50 ms after bounce. The higher electron

---

[2] It should also be borne in mind that the higher energies in the 1D run are observed while the luminosities of μ/τ-neutrinos rapidly rises from a few percent to 50% of its peak value. As the luminosities are still low, a relatively small alteration of the spectral emission properties due to a different energy resolution may have a rather large effect on the mean energy.

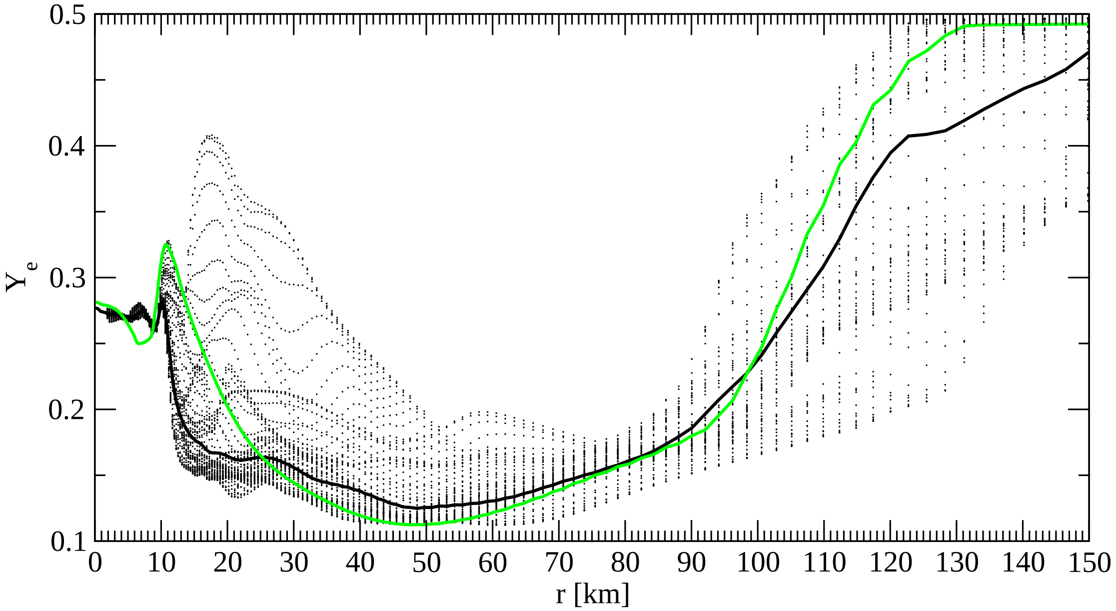

Figure 6.6.: Comparison of the angle-averaged profile of Y_e for model G15-2D (black line) and the Y_e-profile for model G15 (green line) at $t_{\mathrm{pb}} = 50$ ms. Values of Y_e for different latitudes in the 2D run are also given (black points). The broadening of the trough in Y_e and the scatter due to convection are clearly visible.

and lepton fraction at the bottom of the trough due to the convective transport of electrons from deeper layers to regions closer to the neutrinosphere implies a higher electron neutrino chemical potential and hence a suppression of the electron anti-neutrino abundance in this region. Consequently, we observe a reduction of the $\bar{\nu}_e$-luminosities during the first 200 ms. Convection also causes a slight inflation of the PNS, which results in an increase of the neutrinosphere radius and a decrease of the neutrinosphere temperature for all flavours. The overall effect of these changes of the PNS structure, together with the convective energy deposition below the neutrinosphere, is an enhancement of the neutrino luminosities, which, in our case, is strongest for μ/τ-neutrinos, weak at best for electron neutrinos, and cannot compensate the opposing effect of a different lepton number stratification for electron anti-neutrinos.

While PNS convection obviously affects the emission of neutrinos in very much the same way as in previous Newtonian or pseudo-relativistic simulations, its hydrodynamical morphology develops in a very interesting way in model G15-2D. The convective cells, initially of a size of 20° and 30°, soon merge to form larger structures, as can be seen from Fig. 6.7: Within 5 ms seven rising convective plumes have merged into only four which are still clearly discernible. No such smoothing seems to occur in the recent simulations of Buras et al. [20] or Dessart et al. [37], where the convective flow is still dominated by small-scale structure at late post-bounce times, and it was also absent in previous studies with a simplified neutrino treatment [81, 130]. For the high Reynolds numbers

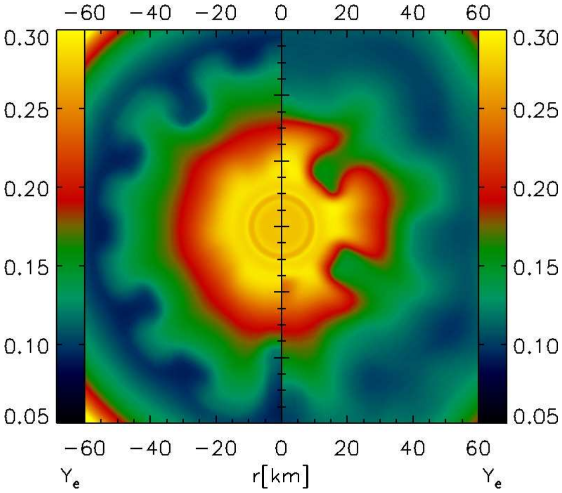

Figure 6.7.: Contour plot of Y_e for model G15-2D at times of $t_{\mathrm{pb}} = 17$ ms (left) and t_{pb} 22 ms (right). Within 5 ms seven convective plumes in the region of $r \approx 40$ ms have merged into four.

in the PNS environment, one would expect that the convective motions on scales of 20° to 30° should feed a turbulent cascade, and that small-scale structures should develop in the flow as it evolves. A very likely explanation for this apparent incongruity seen for model G15-2D is the relatively large effective diffusivity of the approximate HLLE Riemann solver used during this phase of the simulation. The numerical analysis in Appendix D provides a rule of thumb to estimate how the flow is affected by the use of the HLLE solver, based on the sound-crossing time of a specific flow feature: For a structure extending $\approx 30°$ in the angular direction, and with a sound speed of $2 \ldots 4 \times 10^9$ cm s^{-1} in the convective region of the proto-neutron star, the sound-crossing time is of the order of a few tenth of a ms; and since the structure is covered by about 10 zones, the estimated damping timescale should be around 10 sound-crossing times. Such a structure should therefore not survive significantly longer than ≈ 10 ms, which is what we indeed observe. The argument for ascribing the absence of short wavelength features to the HLLE solver is reinforced by the fact that large wavenumbers again dominate PNS convection in the later post-bounce phase once the hybrid HLLC/HLLE solver is switched on (at $t_{\mathrm{pb}} = 120$ ms), as shown by Fig. 6.8. Moreover, model R15LS-2D, for which the hybrid scheme has been used throughout, shows a flow pattern much more similar to previous simulations. The dominance of large-scale convective structures in model G15-2D may be relevant for the growth of the standing accretion shock instability (SASI), which is discussed in Sec. 6.3, and could therefore have considerable influence on the overall dynamics of the model. However, even if the specific morphology of convection in this model were a mere consequence of the employed Riemann solver, some important conclusions could be drawn from this: First, the resolution required in simulations of convection in core-collapse supernovae can depend strongly on the numerical

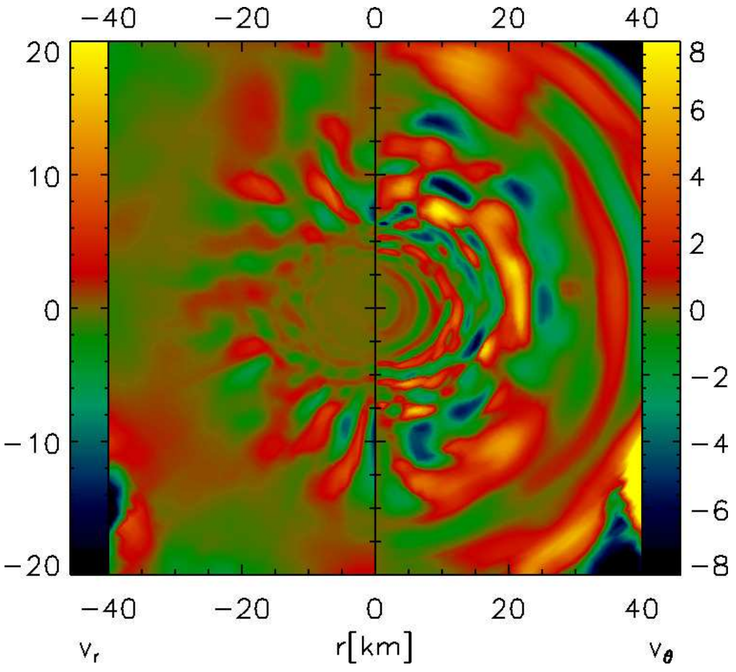

Figure 6.8.: Radial velocity v_r (left panel) and lateral velocity v_θ (right right panel) at a time of 300 ms after bounce for model G15-2D, in units of 10^8 cm s^{-1}. At this time, the convective cells (clearly visible in the left panel) in the region between $r \approx 10$ km and $r \approx 30$ km inside the proto-neutron star have a typical angular size of about 20°, i.e. they extend just over a few angular grid zones.

method for treating the equations of hydrodynamics (which is, admittedly, something of a commonplace). Second, one might speculate that model G15-2D is still representative of a situation where convective modes with short wavelengths are suppressed by some physical mechanism, e.g. magnetic tension in the magneto-convective regime identified by Obergaulinger et al. [140].

6.2.2. Hot-bubble convection

The further development of convection in model G15-2D also exhibits some interesting peculiarities. In recent studies [20, 21, 37, 114], a convective region in the gain layer behind the shock develops a few tens of ms after bounce as neutrino heating produces a negative entropy gradient, and this region is cleanly separated from the convective zone inside the PNS, at least at early times. Although this "hot bubble" (HB) convection is also observed in model G15-2D, there is no clearly identifiable quiescent zone between the regions of HB and PNS convection, as demonstrated by Fig. 6.9, where we show the cube root $\sqrt[3]{|v|}$ of the radial and lateral velocity components (in units of cm s^{-1}) in the equatorial plane as a function of time. Lateral velocities in excess of 7×10^7 cm s^{-1}

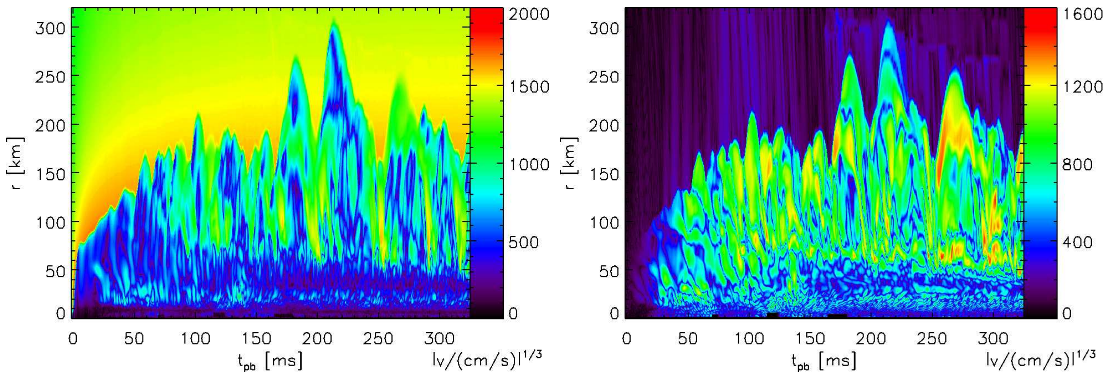

Figure 6.9.: Cube root of the absolute value of the radial velocity component (left panel) and of the lateral velocity component (right panel) in units of cm s^{-1} in the equatorial plane for model G15-2D during the simulation as a function of the radial coordinate r and the time t_{pb} after bounce. Values higher than $\sqrt[3]{|v|} \approx 400$ can be taken as indicative of convective activity. Convection persists almost throughout the entire post-shock region down to $r \approx 10$ km for the first ≈ 150 ms after bounce, when a convectively quiescent layer around $r \approx 30$ km … 40 km develops.

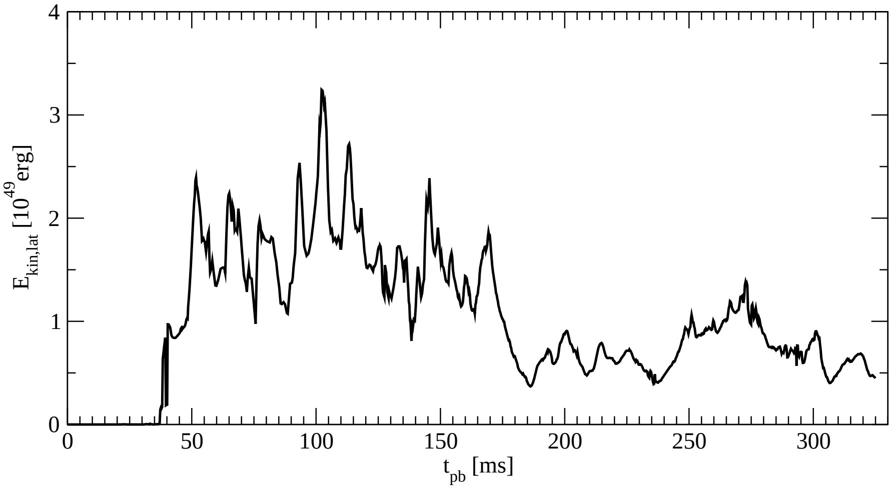

Figure 6.10.: Kinetic energy $E_{\mathrm{kin,lat}}$ associated with lateral velocities of material in the gain layer as a function of the post-bounce time t_{pb}. $E_{\mathrm{kin,lat}}$ is computed in the Newtonian approximation according to Eq. (6.1).

(taken as indicative of convective motion in [20, 21]) are observed in the entire region between the outer layers of the PNS and the shock. It is not completely clear whether this should be properly interpreted as convection or, alternatively, as g-mode activity: As soon as the deviation from spherical symmetry above the proto-neutron star are quite large, the Ledoux criterion (which *does* yields positive values in the relevant region) is no longer completely adequate to determine the extent of the convectively unstable layers. Only after $t_{\mathrm{pb}} = 150$ ms does a relatively quiet layer develop between $r \approx 30$ km and $r \approx 40$ km. However, bearing in mind the specifics of prompt post-shock convection in model G15-2D, this behaviour seems quite reasonable. As the region of prompt convection (which later wanders further inward and continuously evolves into the familiar convective layer inside the PNS) is initially located relatively far outside, contact between the zones of HB and PNS convection can easily be maintained by overshooting. This appears all the more likely as the cooling layer separating the two zones is marginally stable at best according to the Ledoux criterion. The convective flows in the HB region exhibit a similar morphology to that inside the PNS, with the conspicuous absence of small-structures during the first 100 ms after bounce. It is only at later times that the characteristic flow pattern as seen in earlier simulations using PROMETHEUS-VERTEX emerges, with several rising high-entropy bubbles separated by narrow downflows of cold material, as illustrated by the snapshots of the specific entropy in Fig. 6.11. It cannot be excluded that this is again due to the initial use the HLLE solver, but it is also conceivable that the structure of hot-bubble convection is due to "advective stabilization": Foglizzo et al. [59] showed that convective modes with a growth time larger than the advection time through the gain region are effectively suppressed, leading to a dominance of intermediate wavenumbers, and that the most unstable (linear) mode has a horizontal wavelength comparable to twice the vertical size of the gain region (≈ 60 km at $t_{\mathrm{pb}} = 50$ ms). The flow structures in the first panel of Fig. 6.11 are not inconsistent with this. Notwithstanding the peculiarities of the flow during the initial phase of convective activity in the HB region, the typical radial and lateral velocities are of the same order as those reported in the literature (up to ≈ 50000 km s^{-1}, see Fig. 6.9). Moreover, the kinetic energy associated with lateral velocities of matter in the gain region volume V_{gain} as calculated in the Newtonian approximation,

$$E_{\mathrm{kin,lat}} = \int_{V_{\mathrm{gain}}} \frac{1}{2} D v_\theta^2 \mathrm{d}V, \tag{6.1}$$

does not grow beyond a few 10^{49} erg (see Fig. 6.10), which is of the same order as the values reported by Buras et al. [20]. In that sense, HB convection in model G15-2D is not significantly stronger than in existing Newtonian simulations.

All in all, the convective activity observed in our relativistic model is qualitatively similar to that observed in pseudo-Newtonian simulations. Quantitative differences are partially due to genuinely relativistic effects (different shock propagation) on the density stratification behind the shock, and these effects have been firmly established in the 1D case. Some other features seen in our simulation, such as the early dominance of large-scale flow structure in the region of PNS convection, still lacks a definitive explanation – the Riemann solver is the likely culprit – and should probably be regarded with some caution.

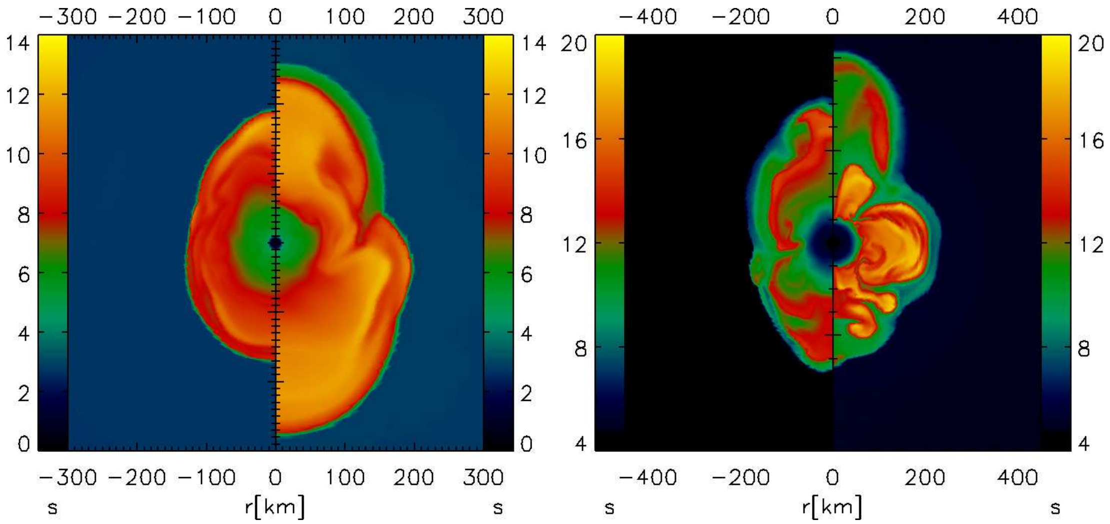

Figure 6.11.: Entropy per baryon (in units of k_B/baryon) at times of t_{pb} = 50 ms, 100 ms, 150 ms, 230 ms (from left to right). The shock front is visible as the colour discontinuity to the blue/black outer region of the infalling material. Its deformation due to large-scale convective motions and the standing-accretion shock instability is already quite pronounced at $t_{pb} = 50$ ms.

6.3. Shock propagation and the standing accretion shock instability (SASI)

Having focused on convective instabilities, we now turn to a discussion of the consequences of multi-dimensional effects on the propagation of the shock. Compared to the one-dimensional case, various additional factors now influence the shock propagation, viz. convective activity (both by improving the energy transfer from the region immediately outside the gain radius to the outer layers, and by modifying the emitted neutrino fluxes and energies), and the so-called standing-accretion shock instability (SASI [11]), which has already been described at the beginning of this chapter. In the more general case, which is not addressed by our post-bounce simulations, rotation and magnetic fields may also play a role.

6.3.1. Early growth of SASI activity

As discussed in Sec. 6.2, convection sets in rather early in model G15-2D, and shows some other peculiarities; but its effects in the neutron star on the emission of neutrinos from the PNS are qualitatively and quantitatively similar to those reported in earlier Newtonian and pseudo-relativistic studies, and neither is HB convection unexpectedly vigorous. The SASI therefore remains the one likely candidate that could make a crucial difference for the post-bounce evolution of model G15-2D. We do indeed find that the

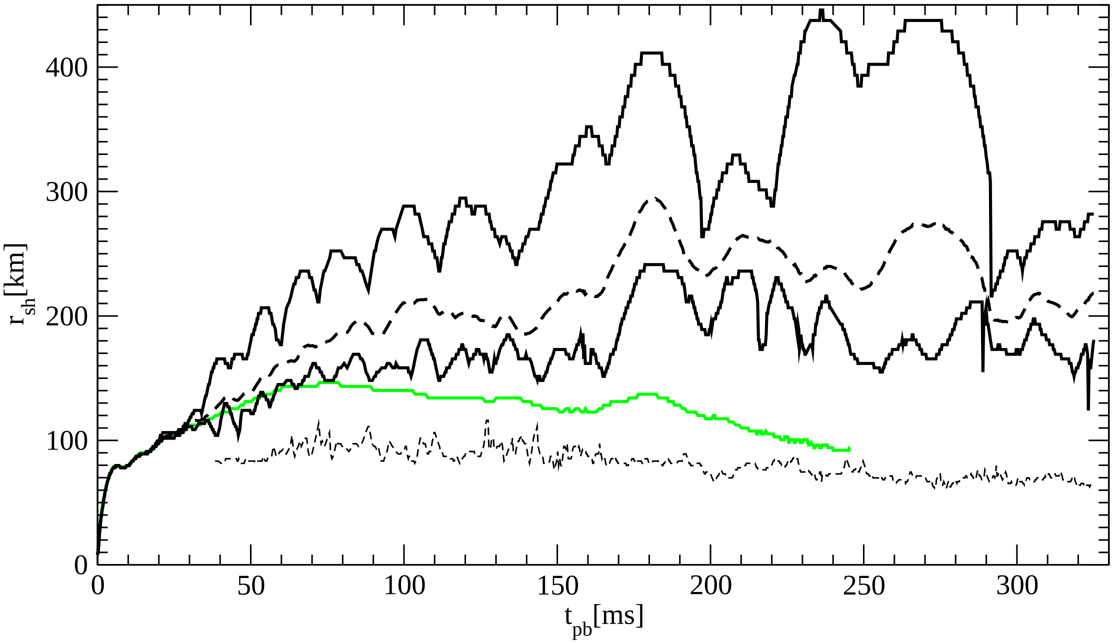

Figure 6.12.: Maximal, minimal (black solid lines), and average shock radius (black dashed line) for model G15-2D, compared to the shock radius of the 1D model G15 (green). We define the average shock radius as the radius of a sphere with volume V_{sh} (the total volume enclosed by the shock front). The laterally averaged gain radius is indicated by a thin dashed line.

SASI grows extremely rapidly in our simulation: Fig. 6.11 shows that the accretion shock is already strongly deformed 50 ms after bounce; its aspect ratio is close to 3 : 2 at that time. The strong SASI activity continues throughout the entire simulation and is accompanied by an expansion of the shock to rather large radii, culminating at slightly more than 400 km at $t_{\mathrm{pb}} \approx 230$ ms. Compared to the one-dimensional model G15, where the shock reaches out no further than $r \approx 150$ km, the shock propagation is significantly different from $t_{\mathrm{pb}} = 30$ ms onward (Fig. 6.12). Although there is a period of shock retraction comparable to the 1D model from 100 ms to 140 ms after bounce, the average shock radius $\bar{r}_{\mathrm{sh}}$ stays at around 200 km even during that phase. Once the Si-SiO-interface reaches the shock, $\bar{r}_{\mathrm{sh}}$ transiently grows to 300 km, and remains more than twice as high as in model G15 until the end of the 1D simulation. Such large average shock radii are not reached by the comparable pseudo-relativistic model of Marek and Janka [114] until 500 ms after bounce or more.

On the other hand, the dominance of low-l SASI modes in model G15-2D, which is clearly visible in Fig. 6.11, is a characteristic property which is shared by all Newtonian simulations, and which has a firm theoretical footing [10, 11, 59, 60, 64, 96, 202]. Whether the dipolar ($l = 1$) mode, the quadrupolar ($l = 2$) or octupolar ($l = 3$) grows fastest, and which of these actually reaches the non-linear stage, seems to depend on the

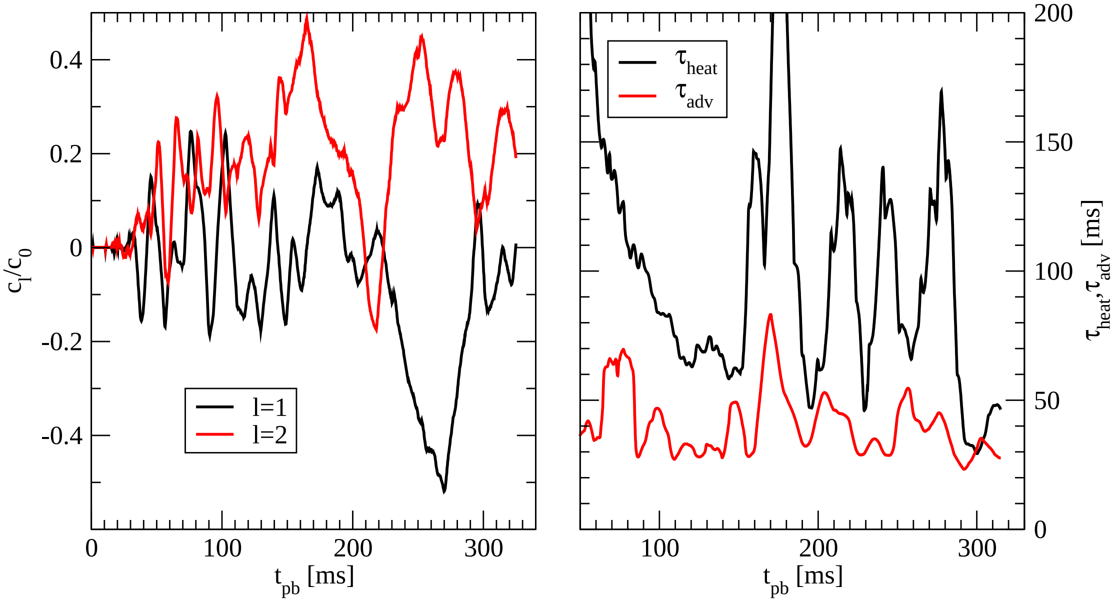

Figure 6.13.: Left panel: Normalized coefficients c_l/c_0 for the decomposition of the shock position in model G15-2D into Legendre polynomials. Only the lowest non-radial modes, i.e. the dipole ($l = 1$, black) and quadrupole (l=2, red) modes are shown. Right panel: The heating and advection time-scales τ_{heat} (black) and τ_{adv} (red) for model G15-2D. In order to eliminate high-frequency noise, running averages over 10 ms are shown.

neutrino heating conditions and the shock position. A first hint is given by the decomposition of the angle-dependent shock position $r_{\text{sh}}(\theta)$ into spherical harmonics Y_{lm} (or Legendre polynomials P_l in axisymmetry, i.e. for $m = 0$),

$$r_{\text{sh}}(\theta) = \sum_{l=1}^{\infty} c_l P_l(\cos\theta). \tag{6.2}$$

The coefficients for the dipole and quadrapole mode (normalized to the angle-averaged shock position c_0) are shown in Fig. 6.13. It is evident that the transition to the non-linear stage ($|c_l/c_0| \gtrsim 0.1c_0$) occurs within 40 ms after bounce for both modes. The dipole mode actually enters the non-linear regime somewhat earlier than the quadrupole mode, and may be responsible for instigating the latter mode in the first place via non-linear mode coupling; the absence of a clearly discernible higher-frequency component in the quadrapole mode compared to the dipole points to this hypothesis. In principle, the coefficient c_2 could also be "contaminated" by the dipole mode, if the angular dependence of the eigenfunction of the latter were not given by $P_1(\cos\theta)$ alone, which would make c_2 a bad indicator for the activity of the quadrupole mode; but the fact that c_1 and c_2 are not strictly correlated excludes this. Moreover, the shape of the shock front indicates the presence of a "real" quadrupole mode: it regularly displays either a bulge between two cusps in the equatorial region (cp. Fig.6.11) or a single cusp near the equator, with

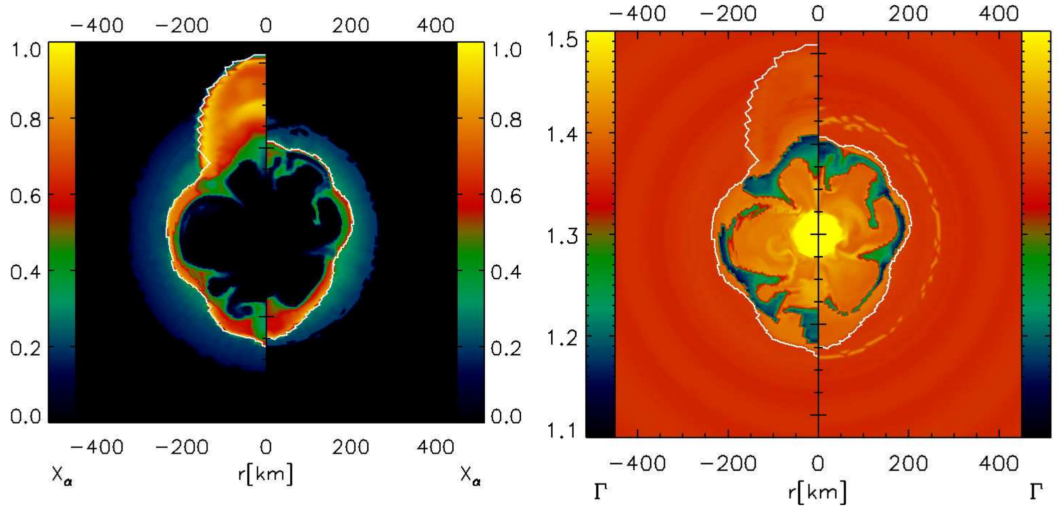

Figure 6.14.: Mass fraction X_α of α-particles (left panel) and the adiabatic index Γ (right panel) at $t_{\rm pb} = 230$ ms and $t_{\rm pb} = 300$ ms. The shock front is marked as white line. Note that yellow is used also for $\Gamma > 1.5$ in the right panel.

both patterns alternating quite regularly in a quasi-periodic manner[3].

6.3.2. Marginally failed SASI-driven explosion?

It is well known that SASI activity is conducive to shock expansion, both because it directly increases the time during which the accreted material is exposed to neutrino heating, and because it can trigger secondary convection [20, 160]. The propagation of the shock to more than 400 km in the polar direction in model G15-2D is therefore understandable, but in spite of this, the model fails to explode before the end of our simulation, and instead experiences a dramatic retraction of the shock almost to 200 km from $t_{\rm pb} = 270$ ms to $t_{\rm pb} = 290$ ms. Naturally, the question arises whether model G15-2D has come close to an explosion during the phase of extraordinarily strong SASI activity from $t_{\rm pb} = 150$ ms to $t_{\rm pb} =$ 290ms that had already pushed the shock to very large radii. This can be discussed quantitatively using the advection time-scale $\tau_{\rm adv}$ for the advection of matter from the shock to the gain radius (i.e. the “average” infall time behind the shock during which neutrino heating is effective), and the heating time-scale $\tau_{\rm heat}$, which is a measure for the time required to make the material in the gain region gravitationally unbound by neutrino energy deposition. $\tau_{\rm adv}/\tau_{\rm heat} > 1$ can be taken as a rough criterion [20, 79, 114, 160, 179] indicating favourable conditions for an expolsion, which can readily be applied to our model. We closely follow the definitions of Marek

---

[3] Irrespective of its precise shape, the eigenfunction of the dipole mode should have only one node in the equatorial plane and an anti-node on each polar half-axis.

and Janka [114] for τ_{adv} and τ_{heat}. The advection time-scale is defined as,

$$\tau_{\mathrm{adv}} = \int\limits_{r_{\mathrm{gain}}}^{r_{\mathrm{sh}}} \frac{\mathrm{d}r}{|\langle v_r \rangle (r)|}, \tag{6.3}$$

where r_{gain} and r_{sh} are the angle-averaged gain and shock radii, and $v_r(r)$ is the mass-weighted angular average of the radial velocity,

$$\langle v_r \rangle = \frac{\int D\phi^6 v_r \,\mathrm{d}\Omega}{\int D\phi^6 \,\mathrm{d}\Omega} = \frac{\int \rho W \phi^6 v_r \,\mathrm{d}\Omega}{\int \rho W \phi^6 \,\mathrm{d}\Omega}. \tag{6.4}$$

The heating time-scale is defined as the ratio of the binding energy E_{bind} of the material in the gain region, and the total neutrino heating rate Q_{heat},

$$\tau_{\mathrm{heat}} = \frac{E_{\mathrm{bind}}}{Q_{\mathrm{heat}}}, \tag{6.5}$$

$$Q_{\mathrm{heat}} = \int\limits_{r_{\mathrm{gain}}}^{r_{\mathrm{sh}}} Q_E \phi^6 \mathrm{d}V. \tag{6.6}$$

Some care must be exercised when defining the binding energy E_{bind}: In principle, it would be desirable to take merely the kinetic, internal and gravitational binding energy into account and to neglect contributions from the nuclear binding energy, but this cannot be done rigorously in general relativity. We therefore assume that the Newtonian limit[4] applies in the gain region (which is true to good accuracy), and then obtain the following expression for the binding energy,

$$E_{\mathrm{bind}} = \int\limits_{r_{\mathrm{gain}}}^{r_{\mathrm{sh}}} \left[\tau - \sum_i D X_i B_i + D\left(1 - \phi^2) c^2\right) \right] \phi^6 \mathrm{d}V. \tag{6.7}$$

Here, B_i is the nuclear binding energy[5] per baryon for species i, while τ and D are the conserved hydrodynamic quantities introduced at the beginning of Sec. 2.2. In the Newtonian limit, this expression correctly reduces to,

$$E_{\mathrm{bind}} \approx \int\limits_{r_{\mathrm{gain}}}^{r_{\mathrm{sh}}} \left[\rho \left(\frac{v^2}{2} + \epsilon \right) + \rho \Phi \right] \mathrm{d}V. \tag{6.8}$$

Both time-scales are shown in the right panel of Fig. 6.13. The time-scale ratio $\tau_{\mathrm{adv}}/\tau_{\mathrm{heat}}$ does indeed come close to 1 at post-bounce times of 150 ms, 200 ms and 260 ms, where it peaks at $\tau_{\mathrm{adv}}/\tau_{\mathrm{heat}} \approx 0.8$. At a time of 300 ms after bounce it even exceeds unity

---

[4] This implies: $D \to \rho$, $\tau \to \rho\epsilon + \frac{1}{2}\rho v^2$, $\phi^4 \to 1 - \frac{2\Phi}{c^2}$.

[5] The normalization of B (e.g. such that $B = 0$ for ^{56}Fe) has to be consistent with the definition of τ, but otherwise the choice is arbitrary in GR.

for a brief interval of 5ms. However, $\tau_{\mathrm{adv}}/\tau_{\mathrm{heat}}$ is a highly oscillatory function of time for model G15-2D, and the relatively high peak values are only reached shortly before and during the phase of maximal SASI-induced shock expansion, and then rapidly drop below the long-term average value of ≈ 0.5 again. All in all, the time-scale ratio provides some indications that G15-2D might already have come close to an explosion during the first 300 ms, but the evidence is ambiguous: The long-term average of $\tau_{\mathrm{adv}}/\tau_{\mathrm{heat}}$ during the simulations is not significantly higher than for the similar model M15LS-2D of Marek and Janka [114].

Recombination of free nucleons into α-particles behind the shock has also been advocated as a "point of no return" for the shock, and thus as an effective criterion for the onset of the explosion. Bethe [8] argued that the energy of 7 MeV per baryon released by recombination should be sufficient to unbind the newly accreted material, and estimated that this would occur as soon as the shock reaches about 300 km. Parameterized one- and two-dimensional simulations of the accretion and explosion phase by Fernández and Thompson [55] also suggested that recombination plays a crucial role for the developing explosion. We actually find large abundance of α-particles in our simulation at a radii larger than $r_\alpha \approx 200$ km, as can be seen in the left panel Fig. 6.14, which shows the mass fraction X_α of α-particles for the time of maximum shock expansion ($t_{\mathrm{pb}} = 230$ ms) and towards the end our simulation (at $t_{\mathrm{pb}} = 300$ ms). At least at $t_{\mathrm{pb}} = 230$ ms a value of $X_\alpha > 0.5$ is reached behind the entire shock front, but this does not seem to be connected with a significant boost to the post-shock velocities. This is to be expected, however, since recombination actually occurs only in the expanding convective bubbles behind the shock (e.g. the large bubbles around the north polar axis in the first panel of Fig. 6.14) that develop during the large-scale SASI oscillations, and the energy release in this regions competes with significant $\alpha-$dissociation losses in regions where the oscillating shock front is receding. Therefore, the mere fact that a model reaches the critical radius for α-recombination cannot be taken as a guarantee for an explosion. The competition between the recombination to and the dissociation of α-particles can also be interpreted in a slightly different manner, by considering the adiabatic index Γ, which is shown in the right panel of Fig. 6.14. Areas where recombination or dissociation occurs exhibit the well-known drop of Γ significantly below $4/3$. This drop of Γ affects post-shock material undergoing expansion or compression differently: Expanding material in the rising high-entropy bubbles will experience a less rapid fall-off of pressure with decreasing density, and hence undergo accelerated expansion (pushing the shock further out). Conversely, the *compression* of material in the receding plumes will also be accelerated, leading to a more rapid recession of the shock front. Based on these considerations, we do not view the fact that recombination occurs in *some* of the convective plumes as indicative of a developing explosion in our model.

To finish our discussion about the possible classification of model G15-2D as a marginally failed explosion, we note that a very small amount of material in the gain region is transiently unbound, in the sense that its total (i.e. internal, kinetic, and potential) energy becomes positive. However, the energy of the "nominally" unbound matter reaches only 1.3×10^{48} erg. In combination with the shock propagation, the ratio of the advection to the heating time-scale, we take this as weak circumstantial evidence that G15-2D may have missed an explosion only by a narrow margin.

6.3.3. Possible reasons for early SASI activity

As described in the preceding sections, the early SASI activity in model G15-2D has very interesting consequences, but it would be highly desirable to track down the reason for such a conspicuous difference to Newtonian and pseudo-Newtonian simulations in order to judge the validity and robustness of the results. Unfortunately, an analytic framework for understanding the SASI in general relativity in the context of core-collapse supernovae[6] is still lacking. Presently, any explanation must therefore be considered as speculative.

Considering possible reasons for the early growth of the SASI, we must first point out that numerical effects cannot be completely excluded at this stage, since the high-resolution model R15LS-2D, which is simulated with the improved HLLE/HLLC hybrid scheme from the very beginning has not yet been evolved to the point where the SASI grows significantly in model G15-2D. In the absence of a high-resolution reference model, it is indeed conceivable that numerical effects play a role. The influence of the grid resolution for the linear growth phase has already been discussed to some extent by Sato et al. [159], who concluded (based on planar toy-models) that the *radial* resolution near the shock is particularly crucial for obtaining the correct growth rates. However, the radial resolution of model G15-2D (400 zones) is comparable or even better than in many Newtonian simulations (e.g. those in [17, 26]); and the same applies to the angular resolution (64 zones), which is to be compared to 32 zones typically used in Bruenn et al. [17]. On the other hand, the grid resolution will not only influence the linear growth phase, but also the non-linear interaction between turbulence and the SASI. Fernández and Thompson [55] demonstrated that, if convection develops in the hot-bubble region (and is not suppressed by advective stabilization [59]), it becomes the forcing agent behind shock oscillations and determines the saturation amplitude of the $l = 1, 2$ modes of the SASI. In the non-linear regime the SASI oscillations are obviously driven directly by the alternating expansion and compression of convective bubbles behind the shock as suggested by Buras et al. [20]. Based on general physical arguments, it is reasonable to assume that convective modes with *low wavenumbers* are most efficient at driving the low-l SASI modes; and the fact that the HLLE scheme used for the first 100 ms of the post-bounce evolution of model G15-2D favours the development of such large-scale flow features (see Sec. 6.2.1) suggests that numerics might play a role in the growth of the SASI. However, as we pointed out before, the dominance of modes with low and intermediate wavenumbers in the hot-bubble region could also be the result of the advective stabilization discussed by Foglizzo et al. [59].

General relativity could also affect the linear phase of the SASI: Depending on whether the mechanism underlying the SASI is an advective-acoustic [60, 64, 141, 160] or a purely acoustic [10] feedback cycle (which may depend on the mode number and the conditions in the core collapse environment [96]), relativistic effects could influence several key

---

[6] However, a linear stability analysis has been carried out for accretion shocks around black holes by Nagakura and Yamada [134].

ingredients for the SASI, namely the interaction of acoustic perturbations with the (relativistic) shock, the propagation of acoustic waves (because the sound speed is different in the Newtonian approximation and in GR[7]), and the generation of acoustic feedback from vorticity perturbations near the PNS surface (for the same reason). Probably neither of these effects is very large; nonetheless a sizable effect on the growth rates of SASI modes in general relativity cannot be excluded. A relativistic generalization of the existing analytic or semi-numerical studies of the SASI is clearly called for to resolve this issue.

Based on these arguments, we conclude that the early growth of SASI in model G15-2D should neither be taken as final statement, nor be discounted as a numerical artifact prematurely pending the outcome of thorough resolution studies.

6.4. Gravitational wave emission

Before finishing our discussion of model G15-2D, we turn to some possible observational signatures of the multi-dimensional hydrodynamic instabilities described in the preceding sections. Broadly speaking, these signatures fall into three classes, namely, features that can be detected by classical astronomical observations of the explosion and the supernova remnant, the neutrino signal, and the gravitational wave signal from non-radial mass motion. Since the connection to classical observations can only by made via long-time simulations of the successful explosion (see [87–90] for the most ambitious studies and further references), only the neutrino and gravitational wave signals can be analysed on the basis of our available simulation data. To some extent the neutrino signal has already been discussed in Sec. 6.2.1, and we shall forgo a more detailed analysis of the anisotropy and the SASI-induced modulation of neutrino emission discussed by Ott et al. [145] and [117], because we find these effects to be comparable to or even weaker than in Newtonian simulations. However, as we shall demonstrate in this section, the gravitational wave signal is significantly stronger than those reported in the most advanced studies of gravitational wave emission during the post-bounce phase [117, 132], and therefore merits particular attention.

As in Chapter 5, we use the time-integrated quadrupole formula (5.10) to compute the gravitational wave signal,

$$A_{20}^{\mathrm{E2}} = \frac{32\pi^{3/2}}{\sqrt{15}} \frac{\mathrm{d}}{\mathrm{d}t} \int r^3 \sin\theta \rho \left[v_r (3\cos^2\theta - 1) - 3 v_\theta \sin\theta \cos\theta \right] \mathrm{d}\theta \, \mathrm{d}r. \tag{6.9}$$

The dimensionless gravitational wave strain h measured by an observer located at a distance R and at an angle θ with respect to the symmetry axis can be determined from A_{20}^{E2} as,

$$h = \frac{1}{8}\sqrt{\frac{15}{\pi}} \sin^2\theta \frac{A_{20}^{E2}}{R}. \tag{6.10}$$

---

[7] In the Newtonian limit, c_s is given by $c_s^2 = \left(\frac{\partial P}{\partial \rho}\right)$, while the relativistic sound speed is[97] $c_s = \left(\frac{\partial P}{\partial(\rho+\rho\epsilon)}\right) = \frac{1}{h}\left(\frac{\partial P}{\partial \rho}\right)$, where h is the specific relativistic enthalpy and ϵ is the specific internal energy.

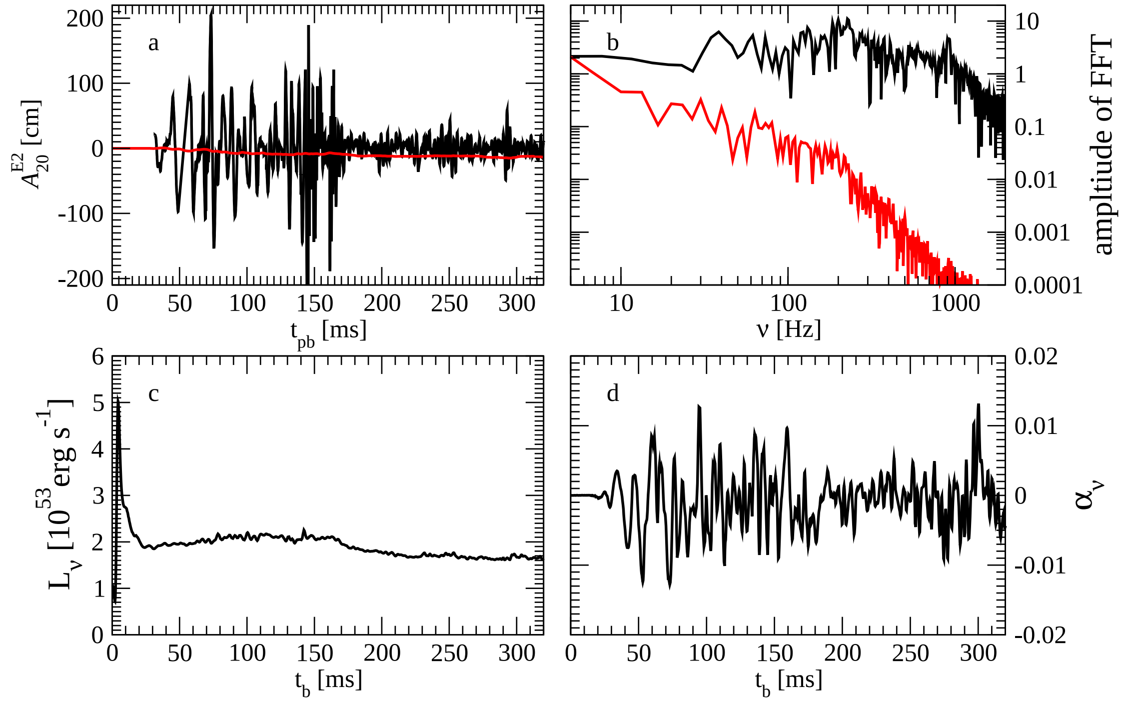

Figure 6.15.: Gravitational wave signal for model G15-2D Panel a) shows the matter signal (black) and the neutrino signal (red); the corresponding Fourier spectra are given in panel b). The total neutrino luminosity L_ν (panel c) and the neutrino anisotropy parameter α_ν (panel d) are also shown. Note that we began the automatic evaluation of the quadrupole formula in CoCoNuT was only switched on 32 ms after bounce, when the first prominent SASI oscillations developed.

In addition, we also consider the gravitational wave signal form anisotropic neutrino emission using the Epstein formula [51, 130], according to which the gravitational wave strain h_ν is given by,

$$h_\nu = \frac{2G}{c^4 R} \int_0^t L_\nu(t')\alpha_\nu(t')\,\mathrm{d}t', \tag{6.11}$$

in the most optimistic case of an observer positioned in the equatorial plane of the system. Here L_ν is the total neutrino luminosity, and the anisotropy parameter α_ν can be obtained as,

$$\alpha_\nu = \frac{1}{L_\nu} \int \pi \sin\theta \,(2|\cos\theta| - 1)\, \frac{\mathrm{d}L_\nu}{\mathrm{d}\Omega} \mathrm{d}\Omega, \tag{6.12}$$

in axisymmetry [94]. The inversion of Eq. (6.10) then yields the quadrupole amplitude A_{20}^{E2}.

The quadrupole wave amplitudes computed for model G15-2D are shown in Fig.6.15 (panel a), along with the associated Fourier spectra of the matter and neutrino signals (panel b), the total neutrino luminosity (panel c), and the anisotropy parameter (panel d). Compared to the pseudo-Newtonian PROMETHEUS-VERTEX simulations analysed by Müller et al. [132] and Marek et al. [117], we find a number of quantitative differences. During the first 180 ms after bounce, the quadrupole amplitude of the matter signal is rather high, easily reaching 100 cm and more during the oscillations. Afterwards the signal strength drops appreciably, and the root-mean square average of the amplitude (over 5 ms) typically remains between 10 cm and 20 cm. Obviously, the decrease of the accretion rate that occurs as the Si-SiO-interface reaches the shock results in weaker, less violent convection, which in turn produces a weaker gravitational wave signal. This conclusion is also supported by the fact that the turbulent energy shows a marked decrease precisely at the same time (see. Fig. 6.10). However, it is astonishing that the onset of the phase of reduced gravitational wave emission coincides closely with one of the most violent periods of SASI activity, when then shock first reaches 400 km along the polar axis. In that respect, our results for model G15-2D are completely inverse to those of Müller et al. [132] and Marek et al. [117], who found that strong gravitational wave emission was positively correlated with strong SASI activity, and tended to increase with time.

The neutrino signal, on the other hand, is not particularly strong; it decreases more or less monotonically to negative amplitudes with time and reaches a peak absolute value of around 15 cm. Considering the variation in the neutrino signals obtained in previous studies [117, 132], this is not very spectacular and well within the expected range. The small signal is a result of the rather isotropic neutrino emission, characterized by an anisotropy parameter whose absolute value rarely exceeds 0.01.

Concerning the gravitational wave spectra (panel b in Fig. 6.15), we also note some particularities of model G15-2D. While the neutrino signal exhibits a similar fall-off behaviour with increasing frequency as in Marek et al. [117], the matter signal is characterized by a peak at ≈ 900 Hz, which is not very pronounced, however. This is a slightly higher value than that reported by Marek et al. [117] for the same equation of state. We also see much stronger low-frequency contributions between 10 Hz and several 100 Hz than Marek et al. [117], particularly in the region around 200 Hz where the absolute peak of the spectrum is located. Such an enhancement of the low-frequency part is a natural consequence of the strong convective and SASI activity seen in our simulation.

6.5. Summary

The multi-dimensional simulation G15-2D presented in this chapter constitutes the first, largely successful attempt to model the complex, multi-dimensional supernova problem through the collapse and post-bounce phase with an up-to-date neutrino transport scheme and a sufficiently accurate treatment of general relativity. We have not only been able to stably evolve a two-dimensional model to more than 300 ms with VERTEX-CoCoNuT, but have qualitatively confirmed the findings of existing Newtonian and pseudo-Newtonian simulations, i.e. the development of prompt post-shock, proto-neutron star, and hot-bubble convection, and the growth of the SASI. We have also been able to extract observational signals, i.e. neutrino and gravitational wave signals from our simulation.

Quantitatively, our model shows a number of peculiarities, such as the dominance of convective modes of low wavenumber during the early post-bounce phase, and the extremely rapid growth of the $\ell = 1$ mode of the SASI, which may yet turn out to be numerical artifacts. Interestingly our analysis also suggests that model G15-2D has come rather close to an explosion, but the rather optimistic development of the model depends critically on the extremely vigorous SASI activity, and must therefore be viewed with caution. A short high-resolution simulation with an improved Riemann solver has already shed light on some open questions, but the reason of the early growth of the SASI remains unclear at this stage, and may be physical. Further numerical studies using our new code are thus clearly called for.

7. Conclusions

In this thesis, we have presented the first multi-dimensional models of core-collapse supernovae that combine a detailed, up-to-date treatment of neutrino transport, the equation of state, and — in particular — general relativistic gravity. Building on the well-tested neutrino transport code VERTEX [21, 151] and the GR hydrodynamics code CoCoNuT [40, 41], we developed and implemented a relativistic generalization of the ray-by-ray-plus method of Buras et al. [21] for energy-dependent neutrino transport. The result of these effort, the VERTEX-CoCoNuT code, also incorporates a number of improved numerical techniques that have not been used in the code components VERTEX and CoCoNuT before.

In order to validate the VERTEX-CoCoNuT code, we conducted several test simulations in spherical symmetry, most notably a comparison with the one-dimensional relativistic supernova code AGILE-BOLTZTRAN and the Newtonian PROMETHEUS-VERTEX code. CoCoNuT is in excellent agreement with the fully relativistic AGILE code, and has proved a reliable numerical tool up to more than 200 ms after bounce. We also found that, unlike PROMETHEUS, which includes some GR effects in a very approximate fashion , CoCoNuT captures the relativistic shock propagation during the early post-bounce phase accurately. Thus, the importance of a rigorous implementation of general relativistic effects already manifested itself in the one-dimensional test runs.

Encouraged by the results of our one-dimensional code tests, we turned to multi-dimensional problems, and used VERTEX-CoCoNuT to investigate the collapse and bounce of rotating iron cores, and compared our results to previous studies of the subject [44–46, 143, 144], in which the deleptonization of the core had been treated with a simple, parameterized approximation, the "Liebendörfer scheme" [103]. Our sophisticated neutrino transport simulations confirm the results obtained with this simple model for deleptonization during collapse qualitatively: The mass of the inner core, which is a key quantity for the dynamics of the collapse, shows a similar dependence on the initial rotation rate of the progenitor core; and the error incurred by using the Liebendörfer prescription is about as large as in spherical symmetry, where it can reach up to 6%. We also presented the first gravitational waveforms from rotational core collapse obtained with an up-to-date neutrino transport scheme: As suggested by relativistic simulations with the Liebendörfer scheme [44–46, 143, 144], the bounce signal from rotational core collapse is indeed generic, with a robust spectral peak at ≈ 725 Hz, at least for the rotation rates considered in this thesis. Thus, these findings no longer rest on an approximate deleptonization scheme that had never been tested in the case of rotational collapse.

Furthermore, VERTEX-CoCoNuT has been used to simulate the post-bounce evolution of the progenitor model s15s7b2 of Woosley and Weaver [195] in axisymmetry for more than 300 ms. Qualitatively, we confirmed the findings of all recent multi-dimensional Newtonian supernova simulations with spectral neutrino transport. However, our simulation "G15-2D" exhibits several peculiar features, the most spectacular of which is the extremely rapid growth of post-shock convection and of the standing-accretion shock instability. The violent SASI activity facilitates strong shock expansion, and our analysis suggests that the model fails to explode within the first 300 ms only by a narrow margin. Of course, some of these interesting results still require further confirmation in order to exclude numerical or resolution effects completely. At any rate, the first extended simulation of the post-bounce phase in general relativity paves the way for a future generation of relativistic supernova models: As the numerical methods required for the stable and accurate long-term evolution of the accreting proto-neutron star and its environment are now established, these new models will be used to address open issues like the surprisingly fast growth of the SASI. If it can be confirmed that relativistic effects precipitate the growth of the SASI, as observed in model G15-2D, a correct treatment of general relativistic hydrodynamics might be crucial for modelling the supernova explosion correctly. We emphasize, however, that we presently lack *unambiguous* evidence to support this interesting hypothesis. We also provided a first analysis of gravitational wave emission during the post-bounce phase, along with a brief discussion of qualitative differences to recent Newtonian studies [117, 132]: The violent convective activity and the large-amplitude bipolar shock oscillations produce a rather strong wave signal, particularly during the first 150 ms of the post-bounce phase. Taking all these findings into account with due reserve, it seems that general relativistic effects during the post-bounce phase may be appreciable.

All in all, VERTEX-CoCoNuT has emerged as a versatile and reliable tool for simulations of core-collapse supernovae, and there are clear perspectives for future applications of the new code. The work presented in this thesis needs to be extended to answer a number of open questions: The unexpected fast growth of the SASI will have to be confirmed by high-resolution simulations, one of which is already underway (model R15LS-2D). Rotational collapse, which was discussed in Chapter 5, should also be studied for rotation rates higher than those discussed in this thesis. Ideally, future relativistic simulations should address all the issues that have already been touched in Newtonian studies such as the progenitor dependence and the influence of the nuclear equation of state (EoS) in the neutron star. Here, VERTEX-CoCoNuT can be most useful in establishing the connection between supernova physics (e.g. details of the explosion mechanism, nuclear EoS) and gravitational wave astronomy, since it allows for a more accurate determination of gravitational wave signals than Newtonian codes. For some other future applications, the relativistic capabilities of CoCoNuT will also be a particular asset, e.g. for black hole formation [58], and – because of the increasing compactness of the central object – for the cooling phase of the contracting proto-neutron star [86, 148]. Such a broad spectrum of computationally demanding applications will of course require a highly efficient code, and significant efforts will have to be invested in the optimization of CoCoNuT, with a particular focus on increasing the parallel performance of the metric solver.

A. Derivation of the Boltzmann Equation in General Relativity

The formulation of kinetic theory within the framework of general relativity has been discussed at length in the literature [29, 49, 108, 173], but most of the work on this subject relies rather heavily on sophisticated concepts from differential geometry. In order to furnish the reader with the basic ingredients for understanding the derivation of the Boltzmann equation (2.27) in a CFC spacetime, we provide a brief sketch of the path from the Hamiltonian formulation of relativistic mechanics to the formulation of the Boltzmann equation for a specific spacetime and tetrad frame. We use only elementary concepts from Hamilton mechanics and general relativity to make this brief sketch as easily accessible as possible.

Let us consider the equation of motion for a relativistic particle,

$$\frac{\mathrm{d}^2 q^\mu}{\mathrm{d}\lambda^2} = -\Gamma^\mu_{\nu\xi} \left(\frac{\mathrm{d}q^\nu}{\mathrm{d}\lambda}\right)\left(\frac{\mathrm{d}q^\xi}{\mathrm{d}\lambda}\right), \tag{A.1}$$

where q^μ is the spacetime coordinate of the particle, λ is the affine parameter[1] or the proper time along the trajectory (depending on whether the particle is massless or not), and $\Gamma^\lambda_{\mu\nu}$ are the Christoffel symbols of the second kind. It is well known (see e.g. [126, 175]) that the equation of motion follows from a Lagrangian,

$$L = \frac{1}{2} g_{\mu\nu} \left(\frac{\mathrm{d}q^\mu}{\mathrm{d}\lambda}\right)\left(\frac{\mathrm{d}q^\nu}{\mathrm{d}\lambda}\right). \tag{A.2}$$

Equivalently, the equation of motion can be derived from a Hamiltonian, by introducing the canonical momentum p_μ,

$$p_\mu = \frac{\partial L}{\partial \dot{q}^\mu} = g_{\mu\nu}\frac{\mathrm{d}q^\nu}{\mathrm{d}\lambda} = \dot{q}_\mu, \tag{A.3}$$

and by choosing the Hamiltonian as the Legendre transform of L,

$$H = p_\mu \dot{q}^\mu - L = \frac{1}{2} g_{\mu\nu} p^\mu p^\nu. \tag{A.4}$$

---

[1] We remind the reader that the four-velocity u^μ of massless particles is a *null vector*, i.e. $u_\mu u^\mu = 0$. Therefore, their world lines cannot be parameterized by the proper time along the trajectory. However, there exists a preferred class of parameterizations by an "affine parameter" λ for light-like geodesics which leads to the same form of the geodesic equation as for massive particles.

Note that the dot notation is used to indicate the derivative with respect to the affine parameter λ. The equation of motion in phase space can then be written as,

$$\dot{q}^\mu = \frac{\partial H}{\partial p_\mu}, \quad \dot{p}_\mu = -\frac{\partial H}{\partial q^\mu}. \tag{A.5}$$

A first version of the collisionless relativistic Boltzmann equation can now be formulated by invoking Liouville's theorem (which states that the phase space volume is conserved by the Hamiltonian flows). As in the Newtonian case, this implies that the total derivative of the 1-particle distribution function f is conserved along phase space trajectories,

$$\frac{\mathrm{d}f}{\mathrm{d}\lambda} = \frac{\partial f}{\partial \lambda} + \frac{\mathrm{d}q^\mu}{\mathrm{d}\lambda}\frac{\partial f}{\partial q^\mu} + \frac{\mathrm{d}p_\mu}{\mathrm{d}\lambda}\frac{\partial f}{\partial p_\mu} = 0. \tag{A.6}$$

Since the metric $g_{\mu\nu}$ is independent of the momentum coordinates, this equation can also be formulated in terms of the contravariant momentum vector $p^\mu = g^{\mu\nu} p_\mu$, which allows some further simplifications,

$$\frac{\partial f}{\partial \lambda} + p^\mu \frac{\partial f}{\partial q^\mu} - \Gamma^\mu_{\nu\xi} p^\nu p^\xi \frac{\partial f}{\partial p^\mu} = 0. \tag{A.7}$$

We emphasize that we have only obtained the Boltzmann equation for the distribution function f in the 8-dimensional phase space (q^μ, p_ν), which is defined as the number of particles per phase space volume $\mathrm{d}^4 q\, \mathrm{d}^4 p$ for a given affine parameter of the Hamiltonian flow. Naturally, it is much more convenient to work with the distribution function $\hat{f}$ in the 6-dimensional phase space (q^i, p_i) in numerical radiation hydrodynamics. However, we defer the derivation of the Boltzmann equation for $\hat{f}$ to the end of this chapter, because the 8-dimensional Boltzmann equation can be specialized to a specific frame more easily without sacrificing the benefits of an explicitly covariant notation. We also disregard the collision term for the moment, because it only needs to be considered after specializing to the comoving frame, and then its treatment is straightforward.

So far, we have implicitly assumed that p^μ is given in the holonomic coordinate basis[2], but switching to a non-holonomic frame is conceptually easy. Changing to another basis in real space and to the associated dual base in momentum space conserves phase space volume, and hence f transforms as a scalar. We therefore need only to take care of the proper transformation of the partial derivatives according to the chain rule. In general, the Boltzmann equation in the transformed coordinates $(\tilde{q}, \tilde{p})$ reads,

$$\frac{\partial f}{\partial \lambda} + p^\mu \left(\frac{\partial \tilde{q}^\alpha}{\partial q^\mu}\frac{\partial f}{\partial \tilde{q}^\alpha} + \frac{\partial \tilde{p}^\alpha}{\partial q^\mu}\frac{\partial f}{\partial \tilde{p}^\alpha} \right) - \Gamma^\mu_{\nu\xi} p^\nu p^\xi \left(\frac{\partial \tilde{q}^\alpha}{\partial p^\mu}\frac{\partial f}{\partial \tilde{q}^\alpha} + \frac{\partial \tilde{p}^\alpha}{\partial p^\mu}\frac{\partial f}{\partial \tilde{p}^\alpha} \right) = 0. \tag{A.8}$$

However, since we are only interested in a change of the local tetrad basis and keep the space coordinates q fixed, the transformation is of a rather simple form,

$$\tilde{q^\alpha}(q, p) = q^\alpha, \quad \tilde{p}^\alpha = C_\mu{}^\alpha(q) p^\mu, \tag{A.9}$$

---

[2] The holonomic coordinate basis of the tangent vector space is given by the four coordinate derivatives $\partial/\partial x^\mu$. For further details on the interpretation of directional derivatives as vectors, the reader may consult introductory texts on general relativity [69, 126, 175].

i.e. it can be expressed as a linear transformation in momentum space. Using the inverse $\tilde{C}$ of the transformation matrix C, we thus arrive at the following equation,

$$\frac{\partial f}{\partial \lambda} + \tilde{C}^{\mu}{}_{\alpha}\tilde{p}^{\alpha}\frac{\partial f}{\partial q^{\mu}} + \tilde{C}^{\mu}{}_{\alpha}\tilde{p}^{\alpha}\frac{\partial \tilde{p}^{\beta}}{\partial q^{\mu}}\frac{\partial f}{\partial \tilde{p}^{\beta}} - \Gamma^{\mu}_{\nu\xi}\tilde{C}^{\nu}{}_{\beta}\tilde{C}^{\xi}{}_{\gamma}C_{\mu}{}^{\alpha}\tilde{p}^{\beta}\tilde{p}^{\gamma}\frac{\partial f}{\partial \tilde{p}^{\alpha}} = 0, \tag{A.10}$$

or equivalently,

$$\frac{\partial f}{\partial \lambda} + \tilde{C}^{\mu}{}_{\alpha}\tilde{p}^{\alpha}\frac{\partial f}{\partial q^{\mu}} + \left(\tilde{C}^{\mu}{}_{\beta}\tilde{C}^{\gamma}{}_{\xi}\frac{\partial C_{\gamma}{}^{\alpha}}{\partial q^{\mu}}\tilde{p}^{\beta}\tilde{p}^{\xi} - \Gamma^{\mu}_{\nu\xi}\tilde{C}^{\nu}{}_{\beta}\tilde{C}^{\xi}{}_{\gamma}C_{\mu}{}^{\alpha}\tilde{p}^{\beta}\tilde{p}^{\gamma}\right)\frac{\partial f}{\partial \tilde{p}^{\alpha}} = 0. \tag{A.11}$$

To obtain the collisionless Boltzmann equation in the comoving frame, the momentum space transformation must be written as the product of a linear transformation from the coordinate basis to the orthonormal Eulerian basis (see, e.g. Banyuls et al. [5]) and a Lorentz boost with the negative three-velocity $-\mathbf{v}$. Although this is conceptually easy, the algebra is rather cumbersome and is omitted here. A semi-automatic MATHEMATICA worksheet for such calculations is available from the author upon request.

Eq. (A.11) is still formulated for the 8-dimensional distribution function, but can be converted in to an equation for the 6-dimensional distribution function in a straightforward manner. In order to keep the derivation simple, we rewrite Eq. (A.11) in a more abstract form,

$$\frac{\partial f}{\partial \lambda} + A^{\mu}\frac{\partial f}{\partial q^{\mu}} + B^{\mu}\frac{\partial f}{\partial p^{\mu}} = 0, \tag{A.12}$$

where we have introduced the coefficients A^{μ} and B^{μ} for the sake of a more compact notation. Moreover, we use p^{μ} instead of $\tilde{p}^{\mu}$ to indicate the four-momentum in the specified frame, because the tilde will be needed otherwise. Eq. (A.12) has the form of an advection equation in phase space, and this has an interesting implication concerning B^{μ}. Since the Hamiltonian flow conserves the invariant mass $m = p^{\mu}p_{\mu}$ of the particles, B^{μ} must be orthogonal to p_{μ}, otherwise particles would move away from the mass-shell. We shall assume that Eq. (A.12) is already formulated in an orthonormal frame, which implies that indices can be raised and lowered using the flat-space metric $\eta_{\mu\nu} = \mathrm{diag}\,(-1, 1, 1, 1)$.

As a first step, we derive the governing equation for the 7-dimensional distribution function $\tilde{f}$, which we define as the number of particles per three-volume $\mathrm{d}^3 q$ and four-momentum-volume $\mathrm{d}^4 p$, measured by the observer associated with the frame in which the Boltzmann equation is formulated. In terms of f, $\tilde{f}$ is given by

$$\int\limits_{-\infty}^{\infty} p^0 f \,\mathrm{d}\lambda, \tag{A.13}$$

Here, the integrand $p^0 f$ can be interpreted as the "flux" through the space-like hypersurface associated with the specified frame. The governing equation for $\tilde{f}$ can be obtained by multiplying Eq. (A.12) by p^0 and integrating over the affine parameter,

$$\int\limits_{-\infty}^{\infty} p^0 \frac{\partial f}{\partial \lambda}\,\mathrm{d}\lambda + \int\limits_{-\infty}^{\infty} p^0 A^{\mu}\frac{\partial f}{\partial q^{\mu}}\,\mathrm{d}\lambda + \int\limits_{-\infty}^{\infty} p^0 B^{\mu}\frac{\partial f}{\partial p^{\mu}}\,\mathrm{d}\lambda = 0. \tag{A.14}$$

The first integral vanishes for any finite coordinate time: Since $\lambda \to \infty$ implies $t \to \infty$, the distribution function *must* vanish for $\lambda \to \infty$. By switching the order of integration and differentiation, we find an equation for $\tilde{f}$,

$$A^\mu \frac{\partial \tilde{f}}{\partial q^\mu} + B^\mu \frac{\partial \tilde{f}}{\partial p^\mu} - B^0 \frac{\tilde{f}}{p^0} = 0. \tag{A.15}$$

Note that A^μ, B^μ and the phase space coordinates q^μ and p^μ do not depend on λ.

We next express $\tilde{f}$ in terms of the six-dimensional distribution function $\hat{f}$, which gives the number of particles per three-volume $\mathrm{d}^3 q$ and three-momentum-volume $\mathrm{d}^3 p$, and depends only on q and the three-momentum p^i, but not on p^0,

$$\tilde{f}(q^\mu, p^\nu) = 2\hat{f}(q^\mu, p^i)\delta(p^\alpha p_\alpha - m^2) p^0 \theta(p^0). \tag{A.16}$$

This guarantees that the total number of particles per three-momentum volume obtained by integrating $\tilde{f}$ correctly reduces to $\hat{f}$,

$$\hat{f} = \int\limits_0^\infty \tilde{f}\, \mathrm{d}p^0 = \int\limits_0^\infty 2\hat{f}\delta(p^\alpha p_\alpha - m^2) p^0 \theta(p^0)\, \mathrm{d}p^0 = \hat{f}. \tag{A.17}$$

Using the relation between $\hat{f}$ and $\tilde{f}$, we obtain the equation governing the evolution of $\hat{f}$,

$$2\delta(p^\alpha p_\alpha - m^2) p^0 \theta(p^0) \left(A^\mu \frac{\partial \hat{f}}{\partial q^\mu} + B^i \frac{\partial \hat{f}}{\partial p^i} \right) + 2\theta(p^0) B^\mu \hat{f} \frac{\partial \delta(p^\alpha p_\alpha - m^2) p^0}{\partial p^\mu} = 0. \tag{A.18}$$

$$2\delta(p^\alpha p_\alpha - m^2) p^0 \theta(p^0) \left(A^\mu \frac{\partial \hat{f}}{\partial q^\mu} + B^i \frac{\partial \hat{f}}{\partial p^i} \right) + 4\theta(p^0) p^0 B^\mu \delta'(p^\alpha p_\alpha - m^2) p_\mu \hat{f} = 0 \tag{A.19}$$

As noted before, B^μ must be orthogonal to the four-momentum vector: $B^\mu p_\mu = 0$. Hence, the term outside the brackets vanishes, and the collisionless Boltzmann equation for $\hat{f}$ can finally be written down as,

$$A^\mu \frac{\partial \hat{f}}{\partial q^\mu} + B^i \frac{\partial \hat{f}}{\partial p^i} = 0, \tag{A.20}$$

or, using the specific form of A^μ and B^μ,

$$\tilde{C}^\mu{}_\alpha p^\alpha \frac{\partial \hat{f}}{\partial q^\mu} + \left(\tilde{C}^\mu{}_\beta \tilde{C}^\gamma{}_\xi \frac{\partial C_\gamma{}^i}{\partial q^\mu} p^\beta p^\xi - \Gamma^\mu_{\nu\xi} \tilde{C}^\nu{}_\beta \tilde{C}^\xi{}_\gamma C_\mu{}^i p^\beta p^\gamma \right) \frac{\partial \hat{f}}{\partial p^i} = 0. \tag{A.21}$$

When working in spherical polar coordinates, p^i can be re-expressed in terms of the absolute value $|\vec{p}|$ of the three-momentum (which is identical to the particle energy in the massless case), the cosine $\mu = \vec{p} \cdot \vec{e}_r / |\vec{p}|$ of the angle enclosed by $\vec{p}$ and the radial unit vector $\vec{e}_r$, and the angle ψ enclosed by $\vec{p}$ and the unit vector in θ-direction. In the special case of spherical symmetry, $\hat{f}$ will only depend on $|\vec{p}|$ and μ. To express the Boltzmann equation in terms of these momentum space coordinates $\hat{p}^i = (|p|, \mu, \psi)$ we need to plug in the Jacbobian matrix $\partial \hat{p}^j / \partial p^i$,

$$\tilde{C}^{\mu}{}_{\alpha} p^{\alpha} \frac{\partial \hat{f}}{\partial q^{\mu}} + \left(\tilde{C}^{\mu}{}_{\beta} \tilde{C}^{\gamma}{}_{\xi} \frac{\partial C_{\gamma}{}^{i}}{\partial q^{\mu}} p^{\beta} p^{\xi} - \Gamma^{\mu}_{\nu\xi} \tilde{C}^{\nu}{}_{\beta} \tilde{C}^{\xi}{}_{\gamma} C_{\mu}{}^{i} p^{\beta} p^{\gamma} \right) \frac{\partial \widehat{p^j}}{\partial p^i} \frac{\partial \hat{f}}{\partial \hat{p}^j} = 0. \tag{A.22}$$

If all momenta are expressed in terms of $\hat{p}^i$, and if both the Christoffel symbols in a spherically symmetric CFC spacetime and the transformation matrices C and $\tilde{C}$ are written out explicitly, one finally arrives at Eq. (2.27) after a considerable amount of algebra.

B. Reformulation of the Relativistic Momentum Equation

One of the guiding principles in formulating the equations of GR hydrodynamics (2.5, 2.6,2.7) as in Banyuls et al. [5] has been to choose a form of the equations that eliminates geometric source terms on the right-hand side as far as possible, so that, by virtue of a flux-conservative discretization, analytical conservation laws can also be fulfilled numerically. Unfortunately, this approach has its limitations: Moving the square root of the three-metric determinant $\sqrt{\gamma}$ into the time derivative eliminates source terms in the continuity equation (2.5) , but not in the momentum and energy equations (2.6) and (2.7). It can easily be verified that the source term in the energy equation vanishes at least in the limit of a flat spacetime (in arbitrary coordinates), but the situation is worse for the momentum equation. Once we expand the stress-energy tensor as $T^{\mu\nu} = \rho h u^\mu u^\nu$ in the source term,

$$\frac{\partial \sqrt{\gamma} \rho h W^2 v_j}{\partial t} + \frac{\partial \sqrt{g} \left(\rho W v_j \hat{v}^i + \delta^i_j P \right)}{\partial x^i} = \frac{\sqrt{g}}{2} \left(\rho h u^\mu u^\nu + P g^{\mu\nu} \right) \frac{\partial g_{\mu\nu}}{\partial x^j}, \tag{B.1}$$

it is evident that in general curvilinear coordinates the source term contains contributions from the pressure even in the case of a stationary fluid with $u^\mu \propto (1,0,0,0)$.

Thus, a naive "conservative" formulation introduces geometric source terms that contain the pressure even in the limit of vanishing velocities! This is *not* a relativistic effect, as can be illustrated by considering the Newtonian limit of the equation for the momentum component $S_2 = \rho v_2$ in spherical polar coordinates, which reads,

$$\frac{\partial r^2 \sin\theta \rho v_2}{\partial t} + \frac{\partial r^2 v_2 v^1 \sin\theta}{\partial r} + \frac{\partial r^2 v_2 v^2 \sin\theta}{\partial r} + \frac{\partial r^2 v_2 v^3 \sin\theta}{\partial r} + \frac{\partial r^2 P \sin\theta}{\partial \theta} = P r^2 \cos\theta + \rho r^2 \cos\theta\, v_3^2 - \rho \nabla \Phi. \tag{B.2}$$

The source term $-P r^2 \cos\theta$ is clearly an artifact of the adopted coordinates: Unlike the "conserved quantity" $r^2 \sin\theta \rho v_2$ it does not vanish on the axis, and this may lead to unwanted side effects in a numerical code as the effective "acceleration" resulting from this term becomes infinite for $\theta \to 0$ and $\theta \to \pi$. More specifically, the spherical symmetry of a fluid configuration with $\rho = \rho(r)$, $v_1 = v_1(r)$, $P = P(r)$, $\Phi = \Phi(r)$, $v_2 \equiv 0$ and $v_3 \equiv 0$ will inevitably be broken, unless the *discretized* (symbolized by "D") flux and source terms containing P cancel,

$$\left(\frac{\partial r^2 P \sin\theta}{\partial \theta} \right)_D - \left(P r^2 \cos\theta \right)_D = 0. \tag{B.3}$$

At the origin, a similar problem with a coordinate singularity occurs. Since such coordinate artifacts should in general be avoided in any finite-difference representation, this is a rather unsatisfactory situation. It is important to note that these source terms are most harmful for quasi-static configurations (e.g. a slowly accreting proto-neutron star), since velocity-dependent fictitious forces are unavoidable in highly dynamical flows anyway.

Fortunately, there is a way to eliminate the offending source terms from the relativistic Euler equations, which has been extensively used and tested in the Newtonian case in the codes PROMETHEUS [62] and FLASH [63]. The crucial ingredient is the identity (cp. §86 in [98])

$$\frac{\partial g}{\partial x^j} = g^{\mu\nu}\sqrt{g}\frac{\partial g_{\mu\nu}}{\partial x^j}, \tag{B.4}$$

whereby the flux and source terms containing P in Eq. (2.6) can be rearranged into a gradient:

$$\frac{\partial\sqrt{\gamma}\rho h W^2 v_j}{\partial t} + \frac{\partial\sqrt{g}\left(\rho W v_j \hat{v}^i\right)}{\partial x^i} + \frac{\partial P}{\partial x^j} = \frac{\sqrt{g}}{2}\rho h u^\mu u^\nu g^{\mu\nu}\frac{\partial g_{\mu\nu}}{\partial x^j}. \tag{B.5}$$

By pulling $\sqrt{\gamma}$ out of the derivatives everywhere and applying standard high-resolution shock-capturing methods to solve the resulting equation[1], one could thus get rid of source terms in P. However, this is achieved at the expense of introducing additional source terms containing v, and is therefore not an optimal solution.

On the other hand, it is possible to discretize Eq. (B.5) directly *provided that the pressure and the velocities on the cell interfaces are known.* Normally one would obtain the flux contribution to the time derivative of the conserved variable $S_j = \rho h W^2 v_j$ in a cell volume V by integrating the numerical fluxes F^i_j over all cell interfaces A_i,

$$\left(\frac{\partial}{\partial t}\int_V \sqrt{\gamma}\rho h W^2 v_j \,\mathrm{d}V\right)_{\text{flux}} = -\int_{\partial V}\sqrt{g}\left(\rho W v_j \hat{v}^i + P\delta^i_j\right)\mathrm{d}A_i = -\int_{\partial V}\sqrt{g}F^i_j \mathrm{d}A_i, \tag{B.6}$$

but if the flux components $\rho W v_j \hat{v}^i$ and $P\delta^i_j$ are known independently, the pressure term can be split off and combined with the source term to form a pure gradient,

$$\begin{aligned}\left(\frac{\partial}{\partial t}\int_V \sqrt{\gamma}\rho h W^2 v_j \,\mathrm{d}V\right)_{\text{flux}} &= -\int_{\partial V}\sqrt{g}\left(\rho W v_j \hat{v}^i\right)\mathrm{d}A_i - \nabla P\int_V \mathrm{d}V \\ &= -\int_{\partial V}\sqrt{g}\left(\rho W v_j \hat{v}^i\right)\mathrm{d}A_i - \nabla P\int_V \mathrm{d}V. \end{aligned} \tag{B.7}$$

Since the integration of the "advective" flux component $\tilde{F}^i_j = \rho h W^2 v_j$ over V is not reformulated, no new source terms in v appear.

Splitting the pressure and advection terms in the flux F^i_j obviously requires a Riemann solver that yields an interface state consistent with the interface flux, and therefore the method explained cannot be incorporated into any given GR hydrodynamics code,

---

[1] Such a formulation of the relativistic Euler equations was used in [40], but the improvement in some collapse situations was (probably erroneously) ascribed to a higher "effective viscosity".

since many of the popular approximate Riemann solvers (Marquina [47], HLLE [68, 184], Kurganov-Tadmor [95]) do not fulfil this condition. However, with the new HLLC scheme the implementation in CoCoNuT has been straightforward. It should be pointed out that adaptive schemes as proposed by [150] to avoid odd-even decoupling can also be easily constructed, despite the fact that they rely on the HLLE solver: It suffices to compute the HLLE flux only for the "advective" component $\tilde{F}^i_j$ near shocks, while retaining the pressure gradient term obtained from the "companion" Riemann solver (such as HLLC). Several tests performed with CoCoNuT have shown that this leads to a robust and accurate numerical scheme that greatly reduces unphysical stirring of the flow near the axis or the origin.

C. Equations of Newtonian Radiation Hydrodynamics

In Chapter 2, our main focus was on the equations of general relativistic radiation hydrodynamics, and only a few references were made to the corresponding Newtonian case. Since we employed the (pseudo-)Newtonian code PROMETHEUS-VERTEX extensively for our tests in Chapter 4, we give a very brief overview of the equations of radiation hydrodynamics used in that code for reference purposes. In particular, we provide the neutrino moment equations in the form actually implemented in the pseudo-relativistic 2D version of PROMETHEUS-VERTEX, thereby supplementing the works of Rampp and Janka [151] and Buras et al. [21], where some algebraic manipulations of the moment equations were not worked out completely. In order to facilitate a comparison with the relativistic case, we also refer to the corresponding equations in Chapter 2. All the equations are given for the special case of axisymmetry, and spherical polar coordinates are used throughout.

As in the relativistic case, the evolution of a perfect fluid in the Newtonian approximation is governed by the continuity equation (cp. Eq. (2.5)),

$$\frac{\partial \rho}{\partial t} + \frac{1}{r^2}\frac{\partial}{\partial r}\left(r^2 \rho v_r\right) + \frac{1}{r\sin\theta}\frac{\partial}{\partial \theta}\left(\rho \sin\theta v_\theta\right) = 0, \tag{C.1}$$

and the Euler equations for momentum conservation (corresponding to Eq. (2.6)),

$$\frac{\partial \rho v_r}{\partial t} + \frac{1}{r^2}\frac{\partial}{\partial r}\left(r^2 \rho v_r^2\right) + \frac{1}{r\sin\theta}\frac{\partial}{\partial \theta}\left(\rho \sin\theta v_\theta v_r\right) - \rho\frac{v_\theta^2 + v_\varphi^2}{r} + \frac{\partial P}{\partial r} = -\rho\frac{\partial \Phi}{\partial r} + Q_M, \tag{C.2}$$

$$\frac{\partial \rho v_\theta}{\partial t} + \frac{1}{r^2}\frac{\partial}{\partial r}\left(r^2 \rho v_r v_\theta\right) + \frac{1}{r\sin\theta}\frac{\partial}{\partial \theta}\left(\rho \sin\theta v_\theta^2\right) + \rho\frac{v_r v_\theta - v_\varphi^2 \cot\theta}{r} + \frac{1}{r}\frac{\partial P}{\partial \theta} = -\frac{\rho}{r}\frac{\partial \Phi}{\partial \theta} + Q_P, \tag{C.3}$$

$$\frac{\partial \rho r \sin\theta v_\varphi}{\partial t} + \frac{1}{r^2}\frac{\partial}{\partial r}\left(r^2 \rho r \sin_\theta v_r v_\varphi\right) + \frac{1}{r\sin\theta}\frac{\partial}{\partial \theta}\left(\rho r \sin^2\theta v_\theta^2\right) = 0, \tag{C.4}$$

and energy conservation (corresponding to Eq. (2.7)),

$$\frac{\partial e}{\partial t} + \frac{1}{r^2}\frac{\partial}{\partial r}\left[r^2\left(e+P\right)v_r\right] + \frac{1}{r\sin\theta}\frac{\partial}{\partial \theta}\left[\left(e+P\right)\sin\theta v_\theta\right] = -\rho\left(v_r\frac{\partial \Phi}{\partial r} + \frac{v_\theta}{r}\frac{\partial \Phi}{\partial \theta}\right) + Q_E + v_r Q_M + v_\theta Q_P. \tag{C.5}$$

Here, ρ is the baryonic rest mass density, v_i is the velocity component along the i-th coordinate direction, P is the pressure, e is the total energy density $e = \rho\left(\epsilon + v^2/2\right)$ (ϵ being the specific internal energy), and Φ is the gravitational potential.

As Eqs. (2.6) and (2.7), the momentum and energy equation contain source terms due to neutrino interactions. The momentum and energy source terms Q_M and Q_E are given by Eqs. (2.39) and (2.40) also in the Newtonian case, but enter the equations of hydrodynamics in a slightly different way than in general relativity, cp. Eqs. (2.43,2.44,2.52, 2.53,2.54). The source terms Q_P accounting for the acceleration of the fluid in the optically thick regime is given by the lateral component of the neutrino pressure gradient,

$$Q_M = -\frac{1}{r}\frac{\partial P_\nu}{\partial \theta}, \tag{C.6}$$

where P_ν is the neutrino pressure.

The equations of hydrodynamics are supplemented by continuity equations for the electron fraction Y_e,

$$\frac{\partial \rho Y_e}{\partial t} + \frac{1}{r^2}\frac{\partial}{\partial r}\left(r^2 \rho Y_e v_r\right) + \frac{1}{r\sin\theta}\frac{\partial}{\partial\theta}\left(\rho Y_e \sin\theta v_\theta\right) = Q_{Y_e}, \tag{C.7}$$

and the mass fractions X_i,

$$\frac{\partial \rho X_i}{\partial t} + \frac{1}{r^2}\frac{\partial}{\partial r}\left(r^2 \rho X_i v_r\right) + \frac{1}{r\sin\theta}\frac{\partial}{\partial\theta}\left(\rho X_i \sin\theta v_\theta\right) = Q_i^{\mathrm{nuc}}. \tag{C.8}$$

These correspond to Eqs. (2.8) and (2.9). The neutrino source term Q_{Y_e} is given by Eq. (2.38) as in the relativistic case. Nuclear reactions are taken into account by introducing source terms Q_i^{nuc} for the mass fractions X_i.

The gravitational potential Φ is determined by the Poisson equation,

$$\hat{\Delta}\Phi = 4\pi G\rho, \tag{C.9}$$

which replaces the much more complicated non-linear system of equations (2.10,2.11,2.12). As described in Marek et al. [116], pseudo-relativistic corrections to the monopole component of Φ may be added to mimic the effect of relativistic gravity. Along with such an "effective relativistic potential", one obtains a lapse function α for the underlying Misner-Sharp metric [125] from which the potential is constructed. Using this lapse function, time dilation and gravitational redshift can be approximately taken into account in the neutrino transport.

Finally, the monochromatic neutrino moment equations corresponding to Eqs. (2.28) and (2.29) read,

$$\begin{aligned}
&\frac{\partial J}{\partial t} + \frac{1}{r^2}\frac{\partial\left(r^2 v_r J\right)}{\partial r} + \boldsymbol{\frac{1}{r\sin\theta}\frac{\partial\left(\sin\theta v_\theta J\right)}{\partial r}} + \frac{1}{r^2}\frac{\partial\left(r^2\alpha H\right)}{\partial r} + \frac{\partial\alpha}{\partial r}H \\
&-\frac{\partial}{\partial\varepsilon}\left[\frac{\varepsilon v_r}{r}\left(J-K\right) + \varepsilon\alpha\frac{\partial\left(e^{-\alpha}v_r\right)}{\partial r}K + \varepsilon\frac{\partial\alpha}{\partial r}H + \boldsymbol{\frac{\varepsilon}{2r\sin\theta}\frac{\partial\left(\sin\theta v_\theta\right)}{\partial\theta}K}\right] \\
&+v_r\frac{J-K}{r} + \alpha\frac{\partial\left(\alpha^{-1}v_r\right)}{\partial r}K - \boldsymbol{\frac{1}{2r\sin\theta}\frac{\partial\left(\sin\theta v_\theta\right)}{\partial\theta}K} = \alpha C_0,
\end{aligned} \tag{C.10}$$

$$\begin{aligned}
&\frac{\partial H}{\partial t} + \frac{1}{r^2}\frac{\partial\left(r^2 v_r H\right)}{\partial r} + \boldsymbol{\frac{1}{r\sin\theta}\frac{\partial\left(\sin\theta v_\theta H\right)}{\partial r}} + \frac{1}{r^2}\frac{\partial\left(r^2\alpha K\right)}{\partial r} + \frac{\partial\alpha}{\partial r}K \\
&-\frac{\partial}{\partial\varepsilon}\left[\frac{\varepsilon v_r}{r}\left(H-L\right) + \varepsilon\alpha\frac{\partial\left(e^{-\alpha}v_r\right)}{\partial r}L + \varepsilon\frac{\partial\alpha}{\partial r}K + \boldsymbol{\frac{\varepsilon}{2r\sin\theta}\frac{\partial\left(\sin\theta v_\theta\right)}{\partial\theta}L}\right] \\
&+\alpha\frac{K-J}{r} + \alpha\frac{\partial\left(\alpha^{-1}v_r\right)}{\partial r}H - \boldsymbol{\frac{1}{2r\sin\theta}\frac{\partial\left(\sin\theta v_\theta\right)}{\partial\theta}L} = \alpha C_1.
\end{aligned} \tag{C.11}$$

Here, J, H, K, and L denote the zeroth to fourth moment of the neutrino distribution function, C_0 and C_1 are zeroth and first moment of the collision integral, and ε is the neutrino energy. The moment equations contain terms marked in boldface for the lateral advection of neutrinos and the concomitant compressional heating. Note that the advection terms corresponding to Eqs. (2.46) and (2.47),

$$\left(\frac{\partial J}{\partial t}\right)_{\mathrm{adv}} = -\frac{1}{r\sin\theta}\frac{\partial\left(\sin\theta v_\theta J\right)}{\partial r}, \tag{C.12}$$

$$\left(\frac{\partial H}{\partial t}\right)_{\mathrm{adv}} = -\frac{1}{r\sin\theta}\frac{\partial\left(\sin\theta v_\theta H\right)}{\partial r}, \tag{C.13}$$

are treated in an operator-split fashion before the radial transport sweep, just as described in Chapter 2.

D. Diffusivity of Approximate Riemann Solvers in the Subsonic Regime

In our discussion of convection in Chapter 6 we claimed that the HLLE solver may spuriously damp convective modes with high wavenumbers. The diffusive character of the HLLE solver has been mentioned repeatedly in the literature (e.g. [123, 146, 183]), but we nevertheless provide the reader with a simple analysis of the issue in this chapter. Two important points are addressed: first, we demonstrate how diffusive terms arise naturally from the HLLE flux formula. Furthermore, we present quantitative estimates for the effects of numerical diffusion on certain flow features depending on their typical length scale.

Our analysis does not cover the full range of hydrodynamic regimes, and is intended to be applicable only to the case of subsonic convection. We therefore confine ourselves to the limit of a static fluid, i.e. to the "extremely subsonic" case. Although this not a perfect approximation for proto-neutron star and hot-bubble convection, the numerical diffusivity of the HLLE solver can be analysed most conveniently in this regime, and the essential points can be brought out more clearly than in the general case. For the same reason, we work in the Newtonian approximation and not in full GR. Furthermore, we assume that the pressure P is constant throughout the fluid, which is reasonable, since convective bubbles are more or less in pressure equilibrium with their environment. Under these assumptions, the only discontinuities in the flow (and the only kind of discontinuities for which we need to discuss the HLLE solver) are *contact discontinuities* and *tangential discontinuities*, which share the same mathematical structure.

Let us now consider the HLLE flux formula for the one-dimensional Euler equations. In terms of the state vectors $\mathbf{U}_{L,R} = (\rho_{L,R}, v_{L,R}, e_{L,R})^T$ to the left and right of a cell interface, the HLLE flux is given by [68, 184],

$$\mathbf{F}_{\mathrm{HLLE}} = \begin{cases} \mathbf{F}_L, & \lambda_- > 0 \\ \frac{\lambda_+ \mathbf{F}_L - \lambda_- \mathbf{F}_R}{\lambda_+ - \lambda_-} + \frac{\lambda_+ \lambda_-}{\lambda_+ - \lambda_-} \left(\mathbf{U}_R - \mathbf{U}_L\right), & \lambda_+ \geq 0 \geq \lambda_- \\ \mathbf{F}_R, & \lambda_+ < 0 \end{cases} \tag{D.1}$$

Here λ_+ and λ_- are the maximal and minimal signal speeds at the cell interface, and $\mathbf{F}_{L,R} = \left(\rho v, \rho v^2 + P, (e+P)\, v\right)^T$. Under the assumptions made in the last paragraph, the state and flux vectors read,

$$\mathbf{U} = \begin{pmatrix} \rho \\ 0 \\ e \end{pmatrix}, \quad \mathbf{F} = \begin{pmatrix} 0 \\ P \\ 0 \end{pmatrix}, \tag{D.2}$$

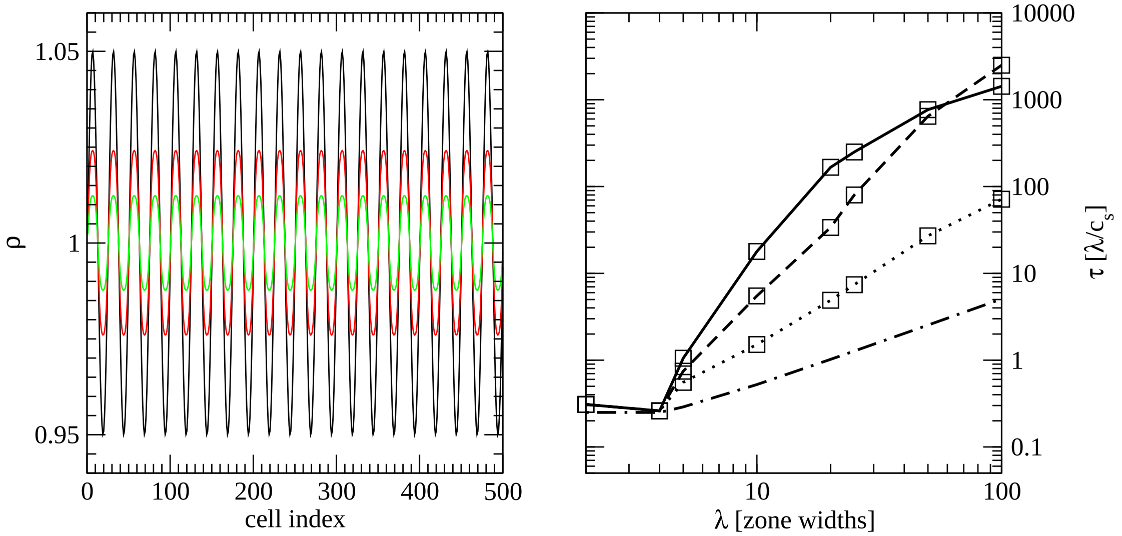

Figure D.1.: Left panel: Snapshots of the evolution of a plane-wave density perturbation, showing the density ρ as a function of the cell index. Right panel: Damping time-scale τ as a function of wavelength λ in units of the sound-crossing time λ/c_S for different reconstruction schemes: PPM (solid line), MC (dashed line), Minmod (dotted line), and first-order Godunov reconstruction (dashed-dotted line).

and the maximal and minimal signal speeds are given by the local sound speed c_s[1],

$$\lambda_+ = c_s, \quad \lambda_- = -c_s. \tag{D.3}$$

We therefore obtain the following numerical flux $\mathbf{F}_{\mathrm{HLLE}}$ at the interface,

$$\mathbf{F}_{\mathrm{HLLE}} = \begin{pmatrix} -\frac{\rho_R - \rho_L}{2} c_s \\ P \\ -\frac{e_R - e_L}{2} c_s \end{pmatrix}. \tag{D.4}$$

The momentum flux is given by the pressure P, which is the analytically correct result. However, the mass and total energy fluxes F^{ρ}_{HLLE} and F^{e}_{HLLE} do not vanish as they ought to, and can be interpreted as diffusive fluxes,

$$F^{\rho}_{\mathrm{HLLE}} = -\frac{c_s \Delta x}{2} \frac{\partial \rho}{\partial x}, \quad F^{e}_{\mathrm{HLLE}} = -\frac{c_s \Delta x}{2} \frac{\partial e}{\partial x}, \tag{D.5}$$

with a diffusion coefficient $c_s \Delta x/2$ that depends on the zone width Δx.

Using the analytic result for the HLLE flux, we can explicitly calculate the numerical damping time-scale for a wavelike perturbation of the density ("entropy wave") for the

---

[1] For the sake of simplicity, we assume that the sound speed is identical on both sides of the interface. As long as the density discontinuity is small, this is a valid approximation.

special case of first-order reconstruction and a uniform grid. The initial conditions for an entropy wave with wavelength λ and amplitude $\delta\rho$ can be written as,

$$\rho_n = \bar{\rho} + \delta\rho\, e^{\frac{2\pi i n \Delta x}{\lambda}}. \tag{D.6}$$

Here, ρ_n is the density in zone n, Δx is the zone width, and $\bar{\rho}$ is the background density on which the wavelike perturbation is superposed. We again assume that the velocity v vanishes, and that the pressure is constant on the entire grid.

For these initial conditions, the HLLE mass flux $F^{\rho}_{n+1/2}$ between cell n and $n+1$ reads,

$$F^{\rho}_{n+1/2} = \left(e^{\frac{2\pi i n \Delta x}{\lambda}} - e^{\frac{2\pi i (n+1) \Delta x}{\lambda}}\right)\frac{c_s \delta\rho}{2}, \tag{D.7}$$

and the density in cell n therefore evolves according to,

$$\begin{aligned}\frac{\partial \rho_n}{\partial t} &= \frac{F^{\rho}_{n-1/2} - F^{\rho}_{n+1/2}}{\Delta x} = \frac{c_s \delta\rho}{2\Delta x} e^{\frac{2\pi i n \Delta x}{\lambda}} \left(e^{\frac{2\pi i \Delta x}{\lambda}} + e^{-\frac{2\pi i \Delta x}{\lambda}} - 2\right) \\ &= \frac{c_s \delta\rho}{\Delta x} e^{\frac{2\pi i n \Delta x}{\lambda}} \left(\cos\frac{2\pi\Delta x}{\lambda} - 1\right) = -\frac{2c_s}{\Delta x}\left(\rho_n - \bar{\rho}\right)\sin^2\frac{\pi \Delta x}{\lambda}.\end{aligned} \tag{D.8}$$

Eq. (D.8) can be integrated directly,

$$\rho_n(t) = \bar{\rho} + \left(\rho_n(0) - \bar{\rho}\right) e^{-\frac{2 c_s t}{\Delta x}\sin^2\frac{\pi\Delta x}{\lambda}}. \tag{D.9}$$

In other words, the initial perturbation is damped exponentially, and the decay time-scale being given by,

$$\tau = \frac{\Delta x}{2\lambda \sin^2 \frac{\pi \Delta x}{\lambda}} \frac{\lambda}{c_s}. \tag{D.10}$$

Eq. (D.10) shows that numerical damping is strongest for short wavelength perturbations.

First-order schemes, of course, are rarely used in practise, and Eq. (D.10) therefore cannot be immediately applied to estimate damping time-scales for features in convective flows. However, it suggests that τ can be related to the sound-crossing time λ/c_s for one wavelength by a function f that depends only on the ratio $\Delta x/\lambda$,

$$\tau(\lambda) = f(\Delta x/\lambda)\frac{\lambda}{c_s}. \tag{D.11}$$

Here, f depends only on the reconstruction method, and can be determined by extracting the eigenvalues of entropy waves from numerical simulations instead of solving Eq. (D.8). We have carried out such simulations for different higher-order reconstruction methods on a grid of 500 zones, using periodic boundary conditions and a Γ-law equation of state (with $\Gamma = 5/3$). However, different from the case of first-order reconstruction, the eigenfunctions of the non-linear time-evolution operator are *not* plane waves, and the initial conditions corresponding to Eq. (D.6) are not known *a priori*; but since high wavenumber modes decay fastest, any plane wave with wavelength λ will evolve into the corresponding eigenfunction anyway. f can therefore be extracted from the *asymptotic* decay rate of plane wave perturbations. To this end, we compute the logarithmic time derivative $\partial \ln \delta\rho/\partial t$ of the perturbation amplitude $\delta\rho(t)$ numerically. $\partial \ln \delta\rho/\partial t$ reaches a constant value after a while (indicating that higher eigenmodes have already decayed), from which τ can be calculated as,

$$\tau = -\frac{1}{\frac{\partial \ln \delta\rho}{\partial t}}. \tag{D.12}$$

In Fig. D.1 we show the damping time-scale τ extracted from our simulations along with the analytical result for first-order reconstruction. Fig. D.1 can be used to estimate the damping time-scale for convective flow features, using their length scale as a "typical" wavelength. It should be borne in mind, of course, that one can only obtain a rough estimate, since such flow features are obviously not one-dimensional entropy waves.

Finally, we note that the diffusivity of other approximate Riemann solvers can be analysed in exactly the fashion as for the HLLE solver. For the modified Marquina solver of Aloy et al. [2] (which is widely used in numerical relativistic hydrodynamics) the numerical diffusivity in the subsonic regime is rather similar to HLLE. On the other hand Marquina's original flux formula [47], the Roe solver [153], and the HLLC solver [123, 183] do not introduce numerical diffusivity in the extremely subsonic case.

Bibliography

[1] `http://www.mpa-garching.mpg.de/rel_hydro/wave_catalog.shtml`.

[2] M. A. Aloy, J. A. Pons, and J. M. Ibáñez. An efficient implementation of flux formulae in multidimensional relativistic hydrodynamical codes. *Computer Physics Communications*, 120:115–121, 1999.

[3] W. Baade and F. Zwicky. On Super-novae. *Proceedings of the National Academy of Science*, 20:254–259, 1934.

[4] W. Baade and F. Zwicky. Cosmic Rays from Super-novae. *Proceedings of the National Academy of Science*, 20:259–263, 1934.

[5] F. Banyuls, J. A. Font, J. M. A. Ibanez, J. M. A. Martí, and J. A. Miralles. Numerical {3+1} general relativistic hydrodynamics: A local characteristic approach. *Astrophys. J.*, 476:221–231, 1997.

[6] E. Baron, E. S. Myra, J. Cooperstein, and L. J. van den Horn. General relativistic neutrino transport in stellar collapse. *Astrophys. J.*, 339:978–986, 1989.

[7] H. A. Bethe. Supernova mechanisms. *Reviews of Modern Physics*, 62:801–866, 1990.

[8] H. A. Bethe. Breakout of the Supernova Shock. *Astrophys. J.*, 469:737–739, 1996.

[9] L. Blanchet, T. Damour, and G. Schaefer. Post-Newtonian hydrodynamics and post-Newtonian gravitational wave generation for numerical relativity. *Mon. Not. R. Astron. Soc.*, 242:289–305, 1990.

[10] J. M. Blondin and A. Mezzacappa. The Spherical Accretion Shock Instability in the Linear Regime. *Astrophys. J.*, 642:401–409, 2006.

[11] J. M. Blondin, A. Mezzacappa, and C. DeMarino. Stability of Standing Accretion Shocks, with an Eye toward Core-Collapse Supernovae. *Astrophys. J.*, 584:971–980, 2003.

[12] S. W. Bruenn. Stellar core collapse - Numerical model and infall epoch. *Astrophys. J. Suppl.*, 58:771–841, 1985.

[13] S. W. Bruenn and T. Dineva. The Role of Doubly Diffusive Instabilities in the Core-Collapse Supernova Mechanism. *Astrophys. J. Lett.*, 458:L71–L74, 1996.

[14] S. W. Bruenn, A. Mezzacappa, and T. Dineva. Dynamic and diffusive instabilities in core collapse supernovae. *Phys. Rep.*, 256:69–94, 1995.

[15] S. W. Bruenn, K. R. De Nisco, and A. Mezzacappa. General Relativistic Effects in the Core Collapse Supernova Mechanism. *Astrophys. J.*, 560:326–338, 2001.

[16] S. W. Bruenn, E. A. Raley, and A. Mezzacappa. Fluid Stability Below the Neutrinospheres of Supernova Progenitors and the Dominant Role of Lepto-Entropy Fingers. *ArXiv Astrophysics e-prints*, astro-ph/0404099, 2004.

[17] S. W. Bruenn, C. J. Dirk, A. Mezzacappa, J. C. Hayes, J. M. Blondin, W. R. Hix, and O. E. B. Messer. Modeling core collapse supernovae in 2 and 3 dimensions with spectral neutrino transport. *Journal of Physics Conference Series*, 46:393–402, 2006.

[18] R. Buras. *Multi-dimensional simulations of core-collapse supernovae with a variable Eddington factor technique for energy-dependent neutrino transport.* PhD thesis, Technische Universtiät München, 2005.

[19] R. Buras, H.-T. Janka, M. T. Keil, G. G. Raffelt, and M. Rampp. Electron Neutrino Pair Annihilation: A New Source for Muon and Tau Neutrinos in Supernovae. *Astrophys. J.*, 587:320–326, 2003.

[20] R. Buras, H.-T. Janka, M. Rampp, and K. Kifonidis. Two-dimensional hydrodynamic core-collapse supernova simulations with spectral neutrino transport. II. Models for different progenitor stars. *Astron. Astrophys.*, 457:281–308, 2006.

[21] R. Buras, M. Rampp, H.-T. Janka, and K. Kifonidis. Two-dimensional hydrodynamic core-collapse supernova simulations with spectral neutrino transport. I. Numerical method and results for a 15 Mȯ star. *Astron. Astrophys.*, 447:1049–1092, 2006.

[22] A. Burrows and R. F. Sawyer. Effects of correlations on neutrino opacities in nuclear matter. *Phys. Rev. C*, 58:554–571, 1998.

[23] A. Burrows, J. Hayes, and B. A. Fryxell. On the Nature of Core-Collapse Supernova Explosions. *Astrophys. J.*, 450:830–850, 1995.

[24] A. Burrows, T. Young, P. Pinto, R. Eastman, and T. A. Thompson. A New Algorithm for Supernova Neutrino Transport and Some Applications. *Astrophys. J.*, 539:865–887, 2000.

[25] A. Burrows, T. Young, P. Pinto, R. Eastman, and T. A. Thompson. A New Algorithm for Supernova Neutrino Transport and Some Applications. *Astrophys. J.*, 539:865–887, 2000.

[26] A. Burrows, E. Livne, L. Dessart, C. D. Ott, and J. Murphy. A New Mechanism for Core-Collapse Supernova Explosions. *Astrophys. J.*, 640:878–890, 2006.

[27] A. Burrows, L. Dessart, E. Livne, C. D. Ott, and J. Murphy. Simulations of Magnetically Driven Supernova and Hypernova Explosions in the Context of Rapid Rotation. *Astrophys. J.*, 664:416–434, 2007.

[28] M. Cantiello, S.-C. Yoon, N. Langer, and M. Livio. Binary star progenitors of long gamma-ray bursts. *Astron. Astrophys.*, 465:L29–L33, 2007.

[29] C. Cardall and A. Mezzacappa. Conservative formulations of general relativistic kinetic theory. *Phys. Rev. D*, 68(2):023006:1–26, 2003.

[30] C. Y. Cardall. Liouville equations for neutrino distribution matrices. *Phys. Rev. D*, 78(8):085017:1–17, 2008.

[31] M. Caspar, editor. *Johannes Kepler, Gesammelte Werke*, volume II., Mysterium Cosmographicum. De Stella Nova. C.H.Beck, München, 2. edition, 1938.

[32] J. I. Castor. Radiative Transfer in Spherically Symmetric Flows. *Astrophys. J.*, 178:779–792, 1972.

[33] P. Cerdá-Durán, G. Faye, H. Dimmelmeier, J. A. Font, J. M. Ibáñez, E. Müller, and G. Schäfer. CFC+: improved dynamics and gravitational waveforms from relativistic core collapse simulations. *Astron. Astrophys.*, 439:1033–1055, 2005.

[34] P. Cerdá-Durán, J. A. Font, and H. Dimmelmeier. General relativistic simulations of passive-magneto-rotational core collapse with microphysics. *Astron. Astrophys.*, 474:169–191, 2007.

[35] P. Colella and P. R. Woodward. The piecewise parabolic method (PPM) for gas-dynamical simulations. *J. Comp. Phys.*, 54:174–201, 1984.

[36] G. B. Cook, S. L. Shapiro, and S. A. Teukolsky. Testing a simplified version of Einstein's equations for numerical relativity. *Phys. Rev. D*, 53:5533–5540, 1996.

[37] L. Dessart, A. Burrows, E. Livne, and C. D. Ott. Multidimensional Radiation/Hydrodynamic Simulations of Proto-Neutron Star Convection. *Astrophys. J.*, 645:534–550, 2006.

[38] L. Dessart, A. Burrows, C. D. Ott, E. Livne, S.-C. Yoon, and N. Langer. Multidimensional Simulations of the Accretion-induced Collapse of White Dwarfs to Neutron Stars. *Astrophys. J.*, 644:1063–1084, 2006.

[39] L. Dessart, A. Burrows, E. Livne, and C. D. Ott. Magnetically Driven Explosions of Rapidly Rotating White Dwarfs Following Accretion-Induced Collapse. *Astrophys. J.*, 669:585–599, 2007.

[40] H. Dimmelmeier. *General Relativistic Collapse of Rotating Stellar Cores in Axisymmetry.* PhD thesis, Technische Universtiät München, 2001.

[41] H. Dimmelmeier, J. A. Font, and E. Müller. Relativistic simulations of rotational core collapse I. Methods, initial models, and code tests. *Astron. Astrophys.*, 388: 917–935, 2002.

[42] H. Dimmelmeier, J. A. Font, and E. Müller. Relativistic simulations of rotational core collapse II. Collapse dynamics and gravitational radiation. *Astron. Astrophys.*, 393:523–542, 2002.

[43] H. Dimmelmeier, J. Novak, J. A. Font, J. M. Ibáñez, and E. Müller. Combining spectral and shock-capturing methods: A new numerical approach for 3D relativistic core collapse simulations. *Phys. Rev. D*, 71:064023:1–30, 2005.

[44] H. Dimmelmeier, C. D. Ott, H.-T. Janka, A. Marek, and E. Müller. Generic Gravitational-Wave Signals from the Collapse of Rotating Stellar Cores. *Physical Review Letters*, 98(25):251101:1–4, 2007.

[45] H. Dimmelmeier, C. D. Ott, H.-T. Janka, A. Marek, and E. Muller. Generic Gravitational Wave Signals from the Collapse of Rotating Stellar Cores: A Detailed Analysis. *ArXiv e-prints*, astro-ph/0705.2675, 2007.

[46] H. Dimmelmeier, C. D. Ott, A. Marek, and H.-T. Janka. Gravitational wave burst signal from core collapse of rotating stars. *Phys. Rev. D*, 78(6):064056:1–28, 2008.

[47] R. Donat and A. Marquina. Capturing Shock Reflections: An Improved Flux Formula. *Journal of Computational Physics*, 125:42–58, 1996.

[48] H. Duan, G. M. Fuller, J. Carlson, and Y.-Z. Qian. Flavor Evolution of the Neutronization Neutrino Burst From an O-Ne-Mg Core-Collapse Supernova. *Physical Review Letters*, 100(2):021101:1–4, 2008.

[49] J. Ehlers. General relativity and kinetic theory. In *General Relativity and Cosmology*, pages 1–70, 1971.

[50] B. Einfeldt. On Godunov-type methods for gas dynamics. *SIAM J. Numer. Anal.*, 25:294–318, 1988.

[51] R. Epstein. The generation of gravitational radiation by escaping supernova neutrinos. *Astrophys. J.*, 223:1037–1045, 1978.

[52] R. I. Epstein. Lepton-driven convection in supernovae. *Mon. Not. R. Astron. Soc.*, 188:305–325, 1979.

[53] Y. Eriguchi and E. Müller. A general computational method for obtaining equilibria of self-gravitating and rotating gases. *Astron. Astrophys.*, 146:260–268, 1985.

[54] B. D. Farris, T. K. Li, Y. T. Liu, and S. L. Shapiro. Relativistic radiation magnetohydrodynamics in dynamical spacetimes: Numerical methods and tests. *Phys. Rev. D*, 78(2):024023:1–20, 2008.

[55] R. Fernández and C. Thompson. Dynamics of a Spherical Accretion Shock with Neutrino Heating and Alpha-Particle Recombination. *ArXiv e-prints*, astro-ph/0812.4574, 2008.

[56] L. S. Finn. Supernovae, gravitational radiation, and the quadrupole formula. In C. R. Evans, L. S. Finn, and D. W. Hobill, editors, *Frontiers in Numerical Relativity*, pages 126–145, Cambridge (UK), 1989. Cambridge University Press.

[57] L. S. Finn and C. R. Evans. Determining gravitational radiation from Newtonian self-gravitating systems. *Astrophys. J.*, 351:588–600, 1990.

[58] T. Fischer, S. C. Whitehouse, A. Mezzacappa, F. . Thielemann, and M. Liebendörfer. The neutrino signal from protoneutron star accretion and black hole formation. *ArXiv e-prints*, astro-ph/0809.5129, 2008.

[59] T. Foglizzo, L. Scheck, and H.-T. Janka. Neutrino-driven Convection versus Advection in Core-Collapse Supernovae. *Astrophys. J.*, 652:1436–1450, 2006.

[60] T. Foglizzo, P. Galletti, L. Scheck, and H.-T. Janka. Instability of a Stalled Accretion Shock: Evidence for the Advective-Acoustic Cycle. *Astrophys. J.*, 654: 1006–1021, 2007.

[61] C. L. Fryer and A. Heger. Binary Merger Progenitors for Gamma-Ray Bursts and Hypernovae. *Astrophys. J.*, 623:302–313, 2005.

[62] B. A. Fryxell, E. Müller, and D. Arnett. Hydrodynamics and Nuclear Burning. *Max-Planck-Institut für Astrophysik, Preprint*, 449, 1989.

[63] B. A. Fryxell, K. Olson, P. Ricker, F. X. Timmes, M. Zingale, D. Q. Lamb, P. MacNeice, R. Rosner, J. W. Truran, and H. Tufo. FLASH: An Adaptive Mesh Hydrodynamics Code for Modeling Astrophysical Thermonuclear Flashes. *Astrophys. J. Suppl.*, 131:273–334, 2000.

[64] P. Galletti and T. Foglizzo. The Advective-Acoustic instability in type II Supernovae. In F. Casoli, T. Contini, J. M. Hameury, and L. Pagani, editors, *SF2A-2005: Semaine de l'Astrophysique Francaise*, page 487, 2005.

[65] P. Goldreich and S. V. Weber. Homologously collapsing stellar cores. *Astrophys. J.*, 238:991–997, 1980.

[66] H. Dimmelmeier, private communication.

[67] S. Hannestad and G. Raffelt. Supernova Neutrino Opacity from Nucleon-Nucleon Bremsstrahlung and Related Processes. *Astrophys. J.*, 507:339–352, 1998.

[68] B. Harten, P. D. Lax, and B. van Leer. On upstream differencing and Godunov-type schemes for hyperbolic conservation laws. *SIAM Review*, 25:35–61, 1983.

[69] S. W. Hawking and G. F. R. Ellis. *The Large-Scale Strucutre of Space-Time.* Cambridge University Press, Cambridge (UK), 1973.

[70] A. Heger, N. Langer, and S. E. Woosley. Presupernova Evolution of Rotating Massive Stars. I. Numerical Method and Evolution of the Internal Stellar Structure. *Astrophys. J.*, 528:368–396, 2000.

[71] A. Heger, S. E. Woosley, and H. C. Spruit. Presupernova Evolution of Differentially Rotating Massive Stars Including Magnetic Fields. *Astrophys. J.*, 626:350–363, 2005.

[72] M. Herant, W. Benz, and S. Colgate. Postcollapse hydrodynamics of SN 1987A - Two-dimensional simulations of the early evolution. *Astrophys. J.*, 395:642–653, 1992.

[73] M. Herant, W. Benz, W. R. Hix, C. L. Fryer, and S. A. Colgate. Inside the supernova: A powerful convective engine. *Astrophys. J.*, 435:339–361, 1994.

[74] W. Hillebrandt and R. G. Wolff. Models of Type II Supernova Explosions. In W. D. Arnett and J. W. Truran, editors, *Nucleosynthesis : Challenges and New Developments*, page 131, 1985.

[75] R. D. Hoffman, B. Müller, and H.-T. Janka. Nucleosynthesis in O-Ne-Mg Supernovae. *Astrophys. J. Lett.*, 676:L127–L130, 2008.

[76] E. P. Hubble. Novae or Temporary Stars. *Leaflet of the Astronomical Society of the Pacific*, 1:55–58, 1928.

[77] J. A. Isenberg. Waveless approximation theories of gravities. University of Maryland Preprint, ArXiv e-print gr-qc/0702113, 1978.

[78] N. Itoh, R. Asahara, N. Tomizawa, S. Wanajo, and S. Nozawa. Ion-Ion Correlation Effect on the Neutrino-Nucleus Scattering in Supernova Cores. *Astrophys. J.*, 611: 1041–1044, 2004.

[79] H.-T. Janka. Conditions for shock revival by neutrino heating in core-collapse supernovae. *Astron. Astrophys.*, 368:527–560, 2001.

[80] H.-T. Janka and E. Müller. The First Second of a Type II Supernova: Convection, Accretion, and Shock Propagation. *Astrophys. J. Lett.*, 448:L109–L113, 1995.

[81] H.-T. Janka and E. Müller. Neutrino heating, convection, and the mechanism of Type-II supernova explosions. *Astron. Astrophys.*, 306:167–198, 1996.

[82] H.-T. Janka, B. Müller, F. S. Kitaura, and R. Buras. Dynamics of shock propagation and nucleosynthesis conditions in O-Ne-Mg core supernovae. *Astron. Astrophys.*, 485:199–208, 2008.

[83] H.-Th. Janka, Th. Zwerger, and R. Mönchmeyer. Does artificial viscosity destroy prompt type-II supernova explosion. *Astron. Astrophys.*, 268:360–368, 1993.

[84] M. H. Johnson and C. F. McKee. Relativistic hydrodynamics in one dimension. *Phys. Rev. D*, 3:858–863, 1971.

[85] W. Keil. *Konvektive Instabilitäten in entstehenden Neutronensternen.* PhD Thesis, Technische Universtiät München, 1997.

[86] W. Keil, H.-T. Janka, and E. Müller. Ledoux Convection in Protoneutron Stars—A Clue to Supernova Nucleosynthesis? *Astrophys. J. Lett.*, 473:L111–L114, 1996.

[87] K. Kifonidis, T. Plewa, H.-T. Janka, and E. Müller. Nucleosynthesis and Clump Formation in a Core-Collapse Supernova. *Astrophys. J. Lett.*, 531:L123–L126, 2000.

[88] K. Kifonidis, E. Müller, and T. Plewa. Non-spherical core collapse supernovae and nucleosynthesis. *Nuclear Physics A*, 688:168–171, 2001.

[89] K. Kifonidis, T. Plewa, H.-T. Janka, and E. Müller. Non-spherical core collapse supernovae. I. Neutrino-driven convection, Rayleigh-Taylor instabilities, and the formation and propagation of metal clumps. *Astron. Astrophys.*, 408:621–649, 2003.

[90] K. Kifonidis, T. Plewa, L. Scheck, H.-T. Janka, and E. Müller. Non-spherical core collapse supernovae. II. The late-time evolution of globally anisotropic neutrino-driven explosions and their implications for SN 1987 A. *Astron. Astrophys.*, 453: 661–678, 2006.

[91] F. S. Kitaura, H.-T. Janka, and W. Hillebrandt. Explosions of O-Ne-Mg cores, the Crab supernova, and subluminous type II-P supernovae. *Astron. Astrophys.*, 450: 345–350, 2006.

[92] W. Kley and G. Schäfer. Relativistic dust disks and the Wilson-Mathews approach. *Phys. Rev. D*, 60(2):027501:1–4, 1999.

[93] H. Komatsu, Y. Eriguchi, and I. Hachisu. Rapidly rotating general relativistic stars. I - Numerical method and its application to uniformly rotating polytropes. *Mon. Not. R. Astron. Soc.*, 237:355–379, 1989.

[94] K. Kotake, N. Ohnishi, and S. Yamada. Gravitational Radiation from Standing Accretion Shock Instability in Core-Collapse Supernovae. *Astrophys. J.*, 655:406–415, 2007.

[95] A. Kurganov and E. Tadmor. New High-Resolution Central Schemes for Nonlinear Conservation Laws and Convection-Diffusion Equations. *Journal of Computational Physics*, 160:241–282, 2000.

[96] J. M. Laming. Analytic Approach to the Stability of Standing Accretion Shocks: Application to Core-Collapse Supernovae. *Astrophys. J.*, 659:1449–1457, 2007.

[97] L. D. Landau and E. M. Lifschitz. *Lehrbuch der theoretischen Physik*, volume VI, Hydrodynamik. Akademie Verlag, Berlin, 5. edition, 1991.

[98] L. D. Landau and E. M. Lifschitz. *Lehrbuch der theoretischen Physik*, volume II, Klassische Feldtheorie. Verlag Harri Deutsch, Thun und Frankfurt am Main, 12. edition, 1997.

[99] K. Langanke, G. Martínez-Pinedo, B. Müller, H.-T. Janka, A. Marek, W. R. Hix, A. Juodagalvis, and J. M. Sampaio. Effects of Inelastic Neutrino-Nucleus Scattering on Supernova Dynamics and Radiated Neutrino Spectra. *Physical Review Letters*, 100(1):011101:1–4, 2008.

[100] J. M. Lattimer and F. D. Swesty. A generalized equation of state for hot, dense matter. *Nuclear Physics A*, 535:331–376, 1991.

[101] R. J. LeVeque. Nonlinear Conservation Laws and Finite Volume Methods. In *Saas-Fee Advanced Course 27: Computational Methods for Astrophysical Fluid Flow.*, pages 1–159, Berlin, 1998. Springer.

[102] A. Lichnerovicz. L'integration des équation de la gravitation relativiste et le problème des n corps. *J. Math. Pures Appl.*, 23:37–63, 1944.

[103] M. Liebendörfer. A Simple Parameterization of the Consequences of Deleptonization for Simulations of Stellar Core Collapse. *Astrophys. J.*, 633:1042–1051, 2005.

[104] M. Liebendörfer, A. Mezzacappa, and F.-K. Thielemann. Conservative general relativistic radiation hydrodynamics in spherical symmetry and comoving coordinates. *Phys. Rev. D*, 63(10):104003:1–14, 2001.

[105] M. Liebendörfer, A. Mezzacappa, F.-K. Thielemann, O. E. Messer, W. R. Hix, and S. W. Bruenn. Probing the gravitational well: No supernova explosion in spherical symmetry with general relativistic Boltzmann neutrino transport. *Phys. Rev. D*, 63(10):103004:1–13, 2001.

[106] M. Liebendörfer, O. E. B. Messer, A. Mezzacappa, S. W. Bruenn, C. Y. Cardall, and F.-K. Thielemann. A Finite Difference Representation of Neutrino Radiation Hydrodynamics in Spherically Symmetric General Relativistic Spacetime. *Astrophys. J. Suppl.*, 150:263–316, 2004.

[107] M. Liebendörfer, M. Rampp, H.-T. Janka, and A. Mezzacappa. Supernova simulations with boltzmann neutrino transport: A comparison of methods. *Astrophys. J.*, 620:840–860, 2005.

[108] R. W. Lindquist. Relativistic transport theory. *Annals of Physics*, 37:487–518, 1966.

[109] M.-S. Liou. Mass Flux Schemes and Connection to Shock Instability. *Journal of Computational Physics*, 160:623–648, 2000.

[110] E. Livne, A. Burrows, R. Walder, I. Lichtenstadt, and T. A. Thompson. Two-dimensional, Time-dependent, Multigroup, Multiangle Radiation Hydrodynamics Test Simulation in the Core-Collapse Supernova Context. *Astrophys. J.*, 609:277–287, 2004.

[111] C. Lunardini, B. Müller, and H.-T. Janka. Neutrino oscillation signatures of oxygen-neon-magnesium supernovae. *Phys. Rev. D*, 78(2):023016:1–13, 2008.

[112] A. I. MacFadyen and S. E. Woosley. Collapsars: Gamma-Ray Bursts and Explosions in “Failed Supernovae”. *Astrophys. J.*, 524:262–289, 1999.

[113] A. Marek. *Multi-dimensional simulations of core collapse supernovae with different equations of state for hot proto-neutron stars.* PhD thesis, Technische Universtiät München, 2007.

[114] A. Marek and H. T. Janka. Delayed neutrino-driven supernova explosions aided by the standing accretion-shock instability. *ArXiv e-prints*, astro-ph/0708.3372, 2007.

[115] A. Marek, H.-T. Janka, R. Buras, M. Liebendörfer, and M. Rampp. On ion-ion correlation effects during stellar core collapse. *Astron. Astrophys.*, 443:201–210, 2005.

[116] A. Marek, H. Dimmelmeier, H.-T. Janka, E. Müller, and R. Buras. Exploring the relativistic regime with Newtonian hydrodynamics: an improved effective gravitational potential for supernova simulations. *Astron. Astrophys.*, 445:273–289, 2006.

[117] A. Marek, H. . Janka, and E. Müller. Equation-of-State Dependent Features in Shock-Oscillation Modulated Neutrino and Gravitational-Wave Signals from Supernovae. *ArXiv e-prints*, astro-ph/0808.4136, 2008.

[118] M. M. May and R. H. White. Hydrodynamic Calculations of General-Relativistic Collapse. *Physical Review*, 141:1232–1241, 1966.

[119] N. U. Mayall and J. H. Oort. Further Data Bearing on the Identification of the Crab Nebula with the Supernova of 1054 A.D. Part II. The Astronomical Aspects. *PASP*, 54:95–104, 1942.

[120] A. Mezzacappa and R. A. Matzner. Computer simulation of time-dependent, spherically symmetric spacetimes containing radiating fluids - Formalism and code tests. *Astrophys. J.*, 343:853–873, 1989.

[121] A. Mezzacappa and O. E. B. Messer. Neutrino transport in core collapse supernovae. *Journal of Computational and Applied Mathematics*, 109:281–319, 1999.

[122] A. Mezzacappa, A. C. Calder, S. W. Bruenn, J. M. Blondin, M. W. Guidry, M. R. Strayer, and A. S. Umar. An Investigation of Neutrino-driven Convection and the Core Collapse Supernova Mechanism Using Multigroup Neutrino Transport. *Astrophys. J.*, 495:911–926, 1998.

[123] A. Mignone and G. Bodo. An HLLC Riemann solver for relativistic flows - I. Hydrodynamics. *Mon. Not. R. Astron. Soc.*, 364:126–136, 2005.

[124] D. Mihalas and B. Weibel Mihalas. *Foundations of radiation hydrodynamics*. Oxford University Press, New York, 1984.

[125] C. W. Misner and D. H. Sharp. Relativistic equations for adiabatic, spherically symmetric gravitational collapse. *Phys. Rev.*, 136:B571–B576, 1964.

[126] C. W. Misner, K. S. Thorne, and J. A. Wheeler. *Gravitation*. W.H. Freeman, San Francisco, 1973.

[127] R. Mönchmeyer, G. Schaefer, E. Müller, and R. E. Kates. Gravitational waves from the collapse of rotating stellar cores. *Astron. Astrophys.*, 246:417–440, 1991.

[128] B. Müller, H. Dimmelmeier, and E. Müller. Exploring the relativistic regime with Newtonian hydrodynamics. II. An effective gravitational potential for rapid rotation. *Astron. Astrophys.*, 489:301–314, 2008.

[129] E. Müller and W. Hillebrandt. The collapse of rotating stellar cores. *Astron. Astrophys.*, 103:358–366, 1981.

[130] E. Müller and H.-T. Janka. Gravitational radiation from convective instabilities in Type II supernova explosions. *Astron. Astrophys.*, 317:140–163, 1997.

[131] E. Müller and M. Steinmetz. Simulating self-gravitating hydrodynamic flows. *Computer Physics Communications*, 89:45–58, 1995.

[132] E. Müller, M. Rampp, R. Buras, H.-T. Janka, and D. H. Shoemaker. Toward Gravitational Wave Signals from Realistic Core-Collapse Supernova Models. *Astrophys. J.*, 603:221–230, 2004.

[133] J. W. Murphy and A. Burrows. BETHE-Hydro: An Arbitrary Lagrangian-Eulerian Multidimensional Hydrodynamics Code for Astrophysical Simulations. *Astrophys. J. Suppl.*, 179:209–241, 2008.

[134] H. Nagakura and S. Yamada. General Relativistic Hydrodynamic Simulations and Linear Analysis of the Standing Accretion Shock Instability around a Black Hole. *Astrophys. J.*, 689:391–406, 2008.

[135] A. Nagar, O. Zanotti, J. A. Font, and L. Rezzolla. Accretion-induced quasinormal mode excitation of a Schwarzschild black hole. *Phys. Rev. D*, 75(4):044016:1–17, 2007.

[136] K. Nomoto. Evolution of 8-10 solar mass stars toward electron capture supernovae. I - Formation of electron-degenerate O + NE + MG cores. *Astrophys. J.*, 277:791–805, 1984.

[137] K. Nomoto. Evolution of 8-10 solar mass stars toward electron capture supernovae. II - Collapse of an O + NE + MG core. *Astrophys. J.*, 322:206–214, 1987.

[138] T. W. Noonan. The gravitational contribution to the stress-energy tensor of a medium in general relativity. *General Relativity and Gravitation*, 16:1103–1118, 1984.

[139] I. D. Novikov. Gravitational radiation from a star collapsing into a disk. *Soviet Astronomy*, 19:398–399, 1976.

[140] M. Obergaulinger, P. Cerdà-Duràn, E. Müller, and M. A. Aloy. Semi-global simulations of the magneto-rotational instability in core collapse supernovae. *ArXiv e-prints*, astro-ph/0811.1652, 2008.

[141] N. Ohnishi, K. Kotake, and S. Yamada. Numerical Analysis of Standing Accretion Shock Instability with Neutrino Heating in Supernova Cores. *Astrophys. J.*, 641: 1018–1028, 2006.

[142] J. R. Oppenheimer and G. M. Volkoff. On Massive Neutron Cores. *Physical Review*, 55:374–381, 1939.

[143] C. D. Ott, H. Dimmelmeier, A. Marek, H.-T. Janka, I. Hawke, B. Zink, and E. Schnetter. 3D Collapse of Rotating Stellar Iron Cores in General Relativity Including Deleptonization and a Nuclear Equation of State. *Physical Review Letters*, 98(26):261101:1–4, 2007.

[144] C. D. Ott, H. Dimmelmeier, A. Marek, H.-T. Janka, B. Zink, I. Hawke, and E. Schnetter. Rotating collapse of stellar iron cores in general relativity. *Classical and Quantum Gravity*, 24:S139–S154, 2007.

[145] C. D. Ott, A. Burrows, L. Dessart, and E. Livne. Two-Dimensional Multiangle, Multigroup Neutrino Radiation-Hydrodynamic Simulations of Postbounce Supernova Cores. *Astrophys. J.*, 685:1069–1088, 2008.

[146] S. H. Park and J. H. Kwon. On the dissipation mechanism of Godunov-type schemes. *Journal of Computational Physics*, 188:524–542, 2003.

[147] T. Plewa and E. Müller. The consistent multi-fluid advection method. *Astron. Astrophys.*, 342:179–191, 1999.

[148] J. A. Pons, S. Reddy, M. Prakash, J. M. Lattimer, and J. A. Miralles. Evolution of Proto-Neutron Stars. *Astrophys. J.*, 513:780–804, 1999.

[149] J. Pruet, R. D. Hoffman, S. E. Woosley, H.-T. Janka, and R. Buras. Nucleosynthesis in Early Supernova Winds. II. The Role of Neutrinos. *Astrophys. J.*, 644: 1028–1039, 2006.

[150] J. J. Quirk. A contribution to the great Riemann solver debate. *International Journal for Numerical Methods in Fluids*, 18:555–574, 1994.

[151] M. Rampp and H.-T. Janka. Radiation hydrodynamics with neutrinos. Variable Eddington factor method for core-collapse supernova simulations. *Astron. Astrophys.*, 396:361–392, 2002.

[152] E. C. Reifenstein, III, W. D. Brundage, and D. H. Staelin. Crab nebula pulsar NP 0527. *Physical Review Letters*, 22:311–311, 1969.

[153] P. L. Roe. Approximate riemann solvers, parameter vectors and difference schemes. *Journal of Computational Physics*, 43:357–372, 1981.

[154] J. V. Romero, J. M. A. Ibanez, J. M. A. Marti, and J. A. Miralles. A New Spherically Symmetric General Relativistic Hydrodynamical Code. *Astrophys. J.*, 462:839–854, 1996.

[155] R. A. Saenz and S. L. Shapiro. Gravitational radiation from stellar collapse - Ellipsoidal models. *Astrophys. J.*, 221:286–303, 1978.

[156] R. A. Saenz and S. L. Shapiro. Gravitational and neutrino radiation from stellar core collapse Improved ellipsoidal model calculations. *Astrophys. J.*, 229:1107–1125, 1979.

[157] R. A. Saenz and S. L. Shapiro. Gravitational radiation from stellar core collapse. III - Damped ellipsoidal oscillations. *Astrophys. J.*, 244:1033–1038, 1981.

[158] I. Sagert, T. Fischer, M. Hempel, G. Pagliara, J. Schaffner-Bielich, A. Mezzacappa, F.-K. Thielemann, and M. Liebendörfer. Signals of the QCD Phase Transition in Core-Collapse Supernovae. *Physical Review Letters*, 102(8):081101:1–4, 2009.

[159] J. Sato, T. Foglizzo, and S. Fromang. A simple toy model of the advective-acoustic instability. II. Numerical simulations. *ArXiv e-prints*, astro-ph/0809.2303, 2008.

[160] L. Scheck, H.-T. Janka, T. Foglizzo, and K. Kifonidis. Multidimensional supernova simulations with approximative neutrino transport. II. Convection and the advective-acoustic cycle in the supernova core. *Astron. Astrophys.*, 477:931–952, 2008.

[161] S. Scheidegger, T. Fischer, S. C. Whitehouse, and M. Liebendörfer. Gravitational waves from 3D MHD core collapse simulations. *Astron. Astrophys.*, 490:231–241, 2008.

[162] P. J. Schinder. General-relativistic radiation hydrodynamics and neutrino transport in polar-sliced space-time. *Phys. Rev. D*, 38:1673–1683, 1988.

[163] M. Schwarzschild. *Structure and evolution of the stars.* Princeton, Princeton University Press, 1958.

[164] S. L. Shapiro. Gravitational radiation from stellar collapse - The initial burst. *Astrophys. J.*, 214:566–575, 1977.

[165] S. L. Shapiro and S. A. Teukolsky. *Black Holes, White Dwarfs, and Neutron Stars: The Physics of Compact Objects.* Wiley-Interscience, New York, 1983.

[166] S. T. Shapiro and A. P. Lightman. Rapidly rotating, post-Newtonian neutron stars. *Astrophys. J.*, 207:263–278, 1976.

[167] H. Shen, H. Toki, K. Oyamatsu, and K. Sumiyoshi. Relativistic Equation of State of Nuclear Matter for Supernova Explosion. *Progress of Theoretical Physics*, 100: 1013–1031, 1998.

[168] M. Shibata and Y.-I. Sekiguchi. Gravitational waves from axisymmetrically oscillating neutron stars in general relativistic simulations. *Phys. Rev. D*, 68(10): 104020:1–14, 2003.

[169] M. Shibata and Y.-I. Sekiguchi. Gravitational waves from axisymmetric rotating stellar core collapse to a neutron star in full general relativity. *Phys. Rev. D*, 69: 084024:1–30, 2004.

[170] M. Shibata and Y.-I. Sekiguchi. Three-dimensional simulations of stellar core collapse in full general relativity: Nonaxisymmetric dynamical instabilities. *Phys. Rev. D*, 71:024014:1–32, 2005.

[171] F. H. Shu. *Physics of Astrophysics, Vol. II.* University Science Books, 1992.

[172] D. H. Staelin and E. C. Reifenstein. Pulsating radio sources near the Crab Nebula. *Science*, 162:1481–1483, 1968.

[173] J. M. Stewart, editor. *Non-equilibrium relativistic kinetic theory*, volume 10 of *Lecture Notes in Physics, Berlin Springer Verlag*, 1971.

[174] P. Strack and A. Burrows. Generalized Boltzmann formalism for oscillating neutrinos. *Phys. Rev. D*, 71(9):093004:1–8, 2005.

[175] N. Straumann. *General Relativity with Applications to Astrophysics.* Springer, Berlin, 2004.

[176] R. S. Sutherland, D. K. Bisset, and G. V. Bicknell. The Numerical Simulation of Radiative Shocks. I. The Elimination of Numerical Shock Instabilities Using a Local Oscillation Filter. *Astrophys. J. Suppl.*, 147:187–195, 2003.

[177] F. D. Swesty and E. S. Myra. Multigroup models of the convective epoch in core collapse supernovae. *Journal of Physics Conference Series*, 16:380–389, 2005.

[178] J.-L. Tassoul. *Theory of Rotating Stars.* Princeton University Press, Princeton, 1978.

[179] C. Thompson. Accretional Heating of Asymmetric Supernova Cores. *Astrophys. J.*, 534:915–933, 2000.

[180] K. S. Thorne. Validity in General Relativity of the Schwarzschild Criterion for Convection. *Astrophys. J.*, 144:201–205, 1966.

[181] T. X. Thuan and J. P. Ostriker. Gravitational Radiation from Stellar Collapse. *Astrophys. J. Lett.*, 191:L105–L107, 1974.

[182] R. C. Tolman. Static Solutions of Einstein's Field Equations for Spheres of Fluid. *Physical Review*, 55:364–373, 1939.

[183] E. F. Toro, M. Spruce, and W. Speares. Restoration of the contact surface in the HLL-Riemann solver. *Shock Waves*, 4:25–34, 1994.

[184] B. J. van Leer. Towards the ultimate conservative difference scheme. v. a second order sequel to godunov's method. *J. Comp. Phys.*, 32:101–136, 1979.

[185] K. A. van Riper and J. M. Lattimer. Stellar core collapse. I - Infall epoch. *Astrophys. J.*, 249:270–289, 1981.

[186] R. M. Wald. *General Relativity.* The University of Chicago Press, Chicago, 1984.

[187] S. Wanajo, K. Nomoto, H. . Janka, F. S. Kitaura, and B. Mueller. Nucleosynthesis in Electron Capture Supernovae of AGB Stars. *ArXiv e-prints*, astro-ph/0810.3999, 2008.

[188] J. Weber. Observation of the Thermal Fluctuations of a Gravitational-Wave Detector. *Physical Review Letters*, 17:1228–1230, 1966.

[189] N. N. Weinberg and E. Quataert. Non-linear saturation of g-modes in protoneutron stars: quieting the acoustic engine. *Mon. Not. R. Astron. Soc.*, 387: L64–L68, 2008.

[190] J. A. Wheeler. Superdense Stars. *Ann. Rev. Astron. Astrophys.*, 4:393–432, 1966.

[191] J. R. Wilson. Supernovae and Post-Collapse Behavior. In J. M. Centrella, J. M. Leblanc, and R. L. Bowers, editors, *Numerical Astrophysics*, pages 422–434, 1985.

[192] J. R. Wilson and R. W. Mayle. Report on the progress of supernova research by the Livermore group. *Phys. Rep.*, 227:97–111, 1993.

[193] J. R. Wilson, G. J. Mathews, and P. Marronetti. Relativistic numerical model for close neutron-star binaries. *Phys. Rev. D*, 54:1317–1331, 1996.

[194] S. E. Woosley and A. Heger. The Progenitor Stars of Gamma-Ray Bursts. *Astrophys. J.*, 637:914–921, 2006.

[195] S. E. Woosley and T. A. Weaver. The evolution and explosion of massive stars. II. Explosive hydrodynamics and nucleosynthesis. *Astrophys. J. Suppl.*, 101:181–235, 1995.

[196] S. E. Woosley, A. Heger, and T. A. Weaver. The evolution and explosion of massive stars. *Reviews of Modern Physics*, 74:1015–1071, 2002.

[197] A. Yahil. Self-similar stellar collapse. *Astrophys. J.*, 265:1047–1055, 1983.

[198] A. Yahil and J. M. Lattimer. Supernovae for pedestrians. In V. L. Trimble, editor, *NATO ASIC Proc. 90: Supernovae: A Survey of Current Research*, pages 53–70, 1982.

[199] S. Yamada. Boltzmann equations for neutrinos with flavor mixings. *Phys. Rev. D*, 62(9):093026:1–12, 2000.

[200] S. Yamada and K. Sato. Numerical study of rotating core collapse in supernova explosions. *Astrophys. J.*, 434:268–276, 1994.

[201] S. Yamada, H.-T. Janka, and H. Suzuki. Neutrino transport in type II supernovae: Boltzmann solver vs. Monte Carlo method. *Astron. Astrophys.*, 344:533–550, 1999.

[202] T. Yamasaki and S. Yamada. Stability of Accretion Flows with Stalled Shocks in Core-Collapse Supernovae. *Astrophys. J.*, 656:1019–1037, 2007.

[203] S.-C. Yoon and N. Langer. Presupernova evolution of accreting white dwarfs with rotation. *Astron. Astrophys.*, 419:623–644, 2004.

[204] S.-C. Yoon and N. Langer. On the evolution of rapidly rotating massive white dwarfs towards supernovae or collapses. *Astron. Astrophys.*, 435:967–985, 2005.

[205] H. W. Yorke. Numerical solution of the equation of radiation transfer in spherical geometry. *Astron. Astrophys.*, 86:286–294, 1980.

[206] T. Zwerger and E. Müller. Dynamics and gravitational wave signature of axisymmetric rotational core collapse. *Astron. Astrophys.*, 320:209–227, 1997.

Danksagung

Am Ende dieser Arbeit gebührt es sich einige Menschen zu erwähnen, die nicht unwesentlich zu ihrem Entstehen beigetragen haben. Zunächst gilt mein Dank natürlich meinem Doktorvater, Hans-Thomas Janka, der die Anregung für das Thema dieser Dissertation geliefert und meine Bemühungen jederzeit mit großem Interesse begleitet hat. Die Möglichkeit zur regelmäßigen und intensiven fachlichen Diskussion meiner Ergebnisse, welche er mir stets geboten hat, war von enormer Bedeutung für das Gelingen dieser Arbeit. Auch für die kritische Durchsicht meiner Entwürfe will ich mich besonders bedanken.

Besonderen Dank verdienen ebenfalls Harald Dimmelmeier und Andreas Marek: Harald hat als einer der Betreuer meiner Diplomarbeit mit der Einführung in seinen CoCoNuT-Code einen wichtigen Grundstein für meine Doktorarbeit gelegt; und Andreas hat mir als gewissenhafter Verwalter und kundiger Nutzer des VERTEX-Codes nicht nur in der Anfangsphase meiner Promotion sehr geholfen. Auch weitere momentane und ehemalige Mitglieder unserer Arbeitsgruppe will ich erwähnen, namentlich Almudena Arcones, Andreas Bauswein, Ewald Müller, Francisco Kitaura, Konstantinos Kifonidis, Leonhard Scheck, Lorenz Hüdepohl, Martin Obergaulinger, Nicolay Hammer, Pablo Cerda-Duran, Reiner Birkl, Robert Buras und Roland Öchslin. Ihnen gebührt Dank für die angenehme Arbeitsatmosphäre und die fruchtbare Zusammenarbeit in verschiedener Form. Besonders hervorheben will ich hierbei Nicolay Hammer als Bürokollegen, sowie Reiner Birkl für die zahlreichen mit ihm geführten philosophischen Diskussionen. Auch Katharina Benkert vom Höchstleistungsrechenzentrum Stuttgart soll nicht unerwähnt bleiben; sie hat enorm viel Zeit in die Optimierung von VERTEX auf den dortigen Rechnern investiert.

Ein allgemeiner Dank für die Arbeitsausstattung, die anregende wissenschaftliche Umgebung und zahlreiche lohnende Dienstreisen geht an das Max-Planck-Institut für Astrophysik, die Sonderforschungsbereiche "Neutrinos and Beyond" und "Gravitational Wave Astronomy", den Exzellenzcluster "Origin and Structure of the Universe" und den Deutschen Akademischen Austauschdienst.

Um Wissenschaft betreiben zu können bedarf es freilich auch der Unterstützung "von außen". Am Ende gilt mein Dank daher den beiden Menschen, welche mir diese Unterstützung immer in einzigartigem Maß zukommen haben lassen: meinen Eltern.